

The ParC/ParP system in the  
localization and segregation of  
chemotaxis signaling arrays in *Vibrio  
cholerae* and *Vibrio parahaemolyticus*

**DISSERTATION**

zur  
Erlangung des Doktorgrades  
der Naturwissenschaften  
(Dr. rer. nat.)

dem Fachbereich Biologie  
der Philipps-Universität Marburg  
vorgelegt

von

ALEJANDRA GUADALUPE  
ALVARADO RODRIGUEZ  
aus Torreón, Coahuila/Mexiko

Marburg/Lahn im Oktober 2018

Die Untersuchungen zur vorliegenden Arbeit wurden von Oktober 2014 bis Oktober 2018 am Max-Planck-Institut für Terrestrische Mikrobiologie unter der Leitung von Dr. Simon Ringgaard durchgeführt.

Vom Fachbereich Biologie der Philipps-Universität Marburg als Dissertation  
angenommen am: 09.10.2018

Erstgutachter: Dr. Simon Ringgaard

Zweitgutachter: Prof. Dr. Martin Thanbichler

Weitere Mitglieder der Prüfungskommission:

Prof. Dr. Victor Sourjik

Prof. Dr. Michael Bölker

Prof. Dr. Johann Heider

Tag der mündlichen Prüfung am: 07.12.2018

Die während der Promotien erzielten Ergebnisse wurden zum Teil in folgenden  
Originalpublikationen veröffentlicht:

Alvarado, A., Kjær, A., Yang, W., Mann, P., Briegel, A., Waldor, M. K., & Ringgaard, S. (2017).  
Coupling chemosensory array formation and localization. *eLife*, 6.

Unpublished works:

Yang, W.\*, Alvarado, A.\*, Glatter, T., Ringgaard, S. & Briegel, A. (2018). Variability of  
chemosensory arrays. *In revision, PNAS* (\*equal contribution)

Alvarado, A., Turkowyd, B., Endesfelder, U. & Ringgaard, S. Differential diffusion rates of distinct  
protein states drive ParC gradient formation. *Submitted*.

*A mi familia*

# TABLE OF CONTENTS

TABLE OF CONTENTS .....	I
LIST OF FIGURES.....	V
LIST OF TABLES.....	VII
ABBREVIATIONS .....	VIII
ABSTRACT.....	X
ZUSAMMENFASSUNG .....	XI
1. CHAPTER 1: INTRODUCTION .....	1
1.1 Bacterial chemotaxis and chemotactic signaling arrays .....	1
1.2 Chemosensory systems .....	3
1.2.1 <i>E.coli</i> .....	3
1.2.1.1 Adaptation as molecular memory.....	4
1.2.2 <i>Bacillus subtilis</i> .....	5
1.2.3 <i>Rhodobacter sphaeroides</i> .....	7
1.3 <i>Vibrio cholerae</i> and <i>Vibrio parahaemolyticus</i> as model organisms.....	10
1.3.1 Chemotaxis in <i>Vibrio cholerae</i> and <i>Vibrio parahaemolyticus</i> .....	11
1.3.1.1 Genetic organization of chemosensory genes.....	13
1.3.1.2 Chemotaxis proteins from different clusters form independent arrays in <i>V. cholerae</i> .....	15
1.3.1.3 The role of chemotaxis in infection of <i>V. cholerae</i> and <i>V.</i> <i>parahaemolyticus</i> .....	17
1.4 Components of the chemosensory arrays.....	18
1.4.1 Chemoreceptors or MCPs .....	19
1.4.1 The histidine kinase CheA .....	21
1.4.2 The adaptor protein CheW .....	22
1.4.3 Chemosensory array assembly .....	23
1.5 Mechanisms for the subcellular localization of chemotaxis signaling arrays in bacteria .....	24
1.5.1 Stochastic self-assembly in the placement of chemosensory arrays in <i>E. coli</i> .....	25
1.5.2 Importance of the curved zones for the placement of chemosensory arrays in <i>B. subtilis</i> .....	27
1.5.3 Localization of chemosensory arrays by ParA homologues .....	28
1.5.3.1 ParA-like proteins .....	28
1.5.3.1.1 Min system.....	28
1.5.3.1.2 MipZ.....	29
1.5.3.1.3 PomXYZ complex .....	29

1.5.3.2 PpfA-mediated localization of cytoplasmic arrays in <i>R. sphaeroides</i> .....	30
1.5.4 Localization of chemosensory arrays in <i>Vibrio</i> spp.: the ParC/ParP system.....	32
1.5.4.1 The ParA-like protein ParC.....	35
1.5.4.2 The coupling protein ParP.....	37
1.5.4.3 HubP marks the old pole.....	38
2. CHAPTER 2: SCOPE.....	42
3. CHAPTER 3: RESULTS.....	44
3.1 <b>PART I</b> - Coupling chemosensory array formation and localization.....	44
3.1.1 ParP contributes in the formation of chemotaxis signaling arrays.....	45
3.1.2 ParP interacts with the signaling domain of methyl-accepting-chemotaxis proteins.....	47
3.1.3 The MCP protein interaction tip mediates interaction with ParP.....	49
3.1.4 A conserved hydrophobic pocket within the AIF domain of ParP mediates interaction with MCP signaling domains.....	51
3.1.5 Distinct ParP interfaces mediate its interaction with MCPs and CheA2.....	55
3.1.6 Interaction with MCPs or CheA2 is required for association of ParP with the chemotaxis signaling arrays.....	56
3.1.7 The AIF domain of ParP is responsible for promoting signaling array formation.....	58
3.1.8 ParP's N-terminal ParC interaction domain couples array localization and formation.....	58
3.1.9 Integration of ParP within signaling arrays is required for their polar localization and inheritance.....	60
3.1.10 Interactions between ParP, CheA2 and MCPs regulate polar localization of ParP.....	61
3.1.11 Integration of ParP within signaling arrays promotes ParP's retention at the cell pole.....	64
3.1.12 Integration of ParP into signaling arrays influences ParC localization.....	66
3.2 <b>PART II</b> – Base plate variability of chemoreceptor arrays in <i>V. cholerae</i> .....	67
3.2.1 Formation and localization of chemoreceptor arrays from cluster II are independent of CheA proteins.....	67
3.2.2 Variability of array base plates in <i>V. cholerae</i> decreases ultrastability of chemotaxis arrays.....	71
3.2.3 <i>V. cholerae</i> cluster II arrays show a high degree of instability.....	73
3.2.4 The composition of the <i>V. cholerae</i> cluster II array is variable and it exhibits a distinct stoichiometry of chemotaxis proteins.....	74
3.3 <b>PART III</b> - Differential diffusion rates of distinct protein states drive protein gradient formation.....	79

---

3.3.1	ParC forms a gradient extending from the cell pole towards mid-cell ..80
3.3.2	DNA binding by ParC is required for its function in mediating polar array localization.....81
3.3.3	DNA binding by ParC is regulated by its nucleotide-bound state .....82
3.3.4	ParC's polar localization is regulated by its ATP-cycle and DNA association .....85
3.3.5	ParC's gradient formation is regulated by its ATP-cycle and is required for ParC's function .....87
3.3.6	Differential diffusion rates of distinct protein states drive protein gradient formation.....88
4.	CHAPTER 4: DISCUSSION .....94
4.1	<b>PART I</b> - Coupling chemosensory array formation and localization.....94
4.2	<b>PART II</b> - Base plate variability of chemoreceptor arrays in <i>V. cholerae</i> ....99
4.3	<b>PART III</b> - Differential diffusion rates of distinct protein states drive protein gradient formation .....103
5.	CHAPTER 5: CONCLUSIONS AND FUTURE PROSPECTS .....107
6.	CHAPTER 6: MATERIALS AND METHODS .....110
6.1	Chemicals, equipment and software .....110
6.2	Media, buffers and solutions .....113
6.3	Microbiological methods .....113
6.3.1	Growth conditions.....113
6.3.2	Strains .....113
6.3.3	Swimming assays.....115
6.3.4	Growth curves .....115
6.3.5	Bacterial-two-hybrid assays.....116
6.3.6	Protein interaction-partner screening based on the bacterial-two-hybrid system.....117
6.4	Molecular biology methods .....117
6.4.1	Preparation of competent cells .....117
6.4.2	Transformation of competent cells .....118
6.4.3	Construction of strains and domains exchange.....118
6.4.4	Plasmids and oligonucleotides.....118
6.4.4.1	Construction of plasmids.....124
6.4.5	Site-directed mutagenesis .....128
6.4.6	Polymerase chain reaction (PCR) and agarose gel electrophoresis..128
6.4.7	Restriction digestion and ligation .....129
6.5	Biochemical and proteomics methods.....130
6.5.1	Immunoblot analyses.....130

---

6.5.2	Determination of isotopically labeled reference peptides for CheA, CheW, ParP and CheV proteins .....	130
6.5.3	Targeted Liquid chromatography-mass spectrometry (LC-MS).....	131
6.6	Microscopy methods.....	131
6.6.1	Fluorescence microscopy .....	131
6.6.1.1	Sample preparation.....	131
6.6.1.2	Image acquisition.....	132
6.6.1.3	Sample size and image analysis .....	133
6.6.2	Photobleaching time-lapse experiments .....	133
6.6.3	Cryo-electron microscopy .....	134
6.6.3.1	Tomogram Reconstruction and Subtomogram Averaging.....	135
6.6.4	sptPALM microscopy .....	135
6.6.4.1	Sample preparation.....	135
6.6.4.2	Agarose slide preparation .....	135
6.6.4.3	Microscope set-up .....	135
6.6.4.4	sptPALM image acquisition.....	136
6.6.4.5	sptPALM data analysis .....	136
6.6.4.5.1	Extracting diffusive states, their occupancies and apparent diffusion coefficients.....	137
6.6.4.5.2	Generation of average cellular distribution heatmaps.....	138
6.7	Bioinformatic analyses.....	138
6.7.1	Multiple sequence alignment .....	138
6.7.2	Phylogenetic tree.....	139
6.7.3	Lists of sequences.....	139
7.	REFERENCES .....	145
	ACKNOWLEDGEMENTS.....	156
	CURRICULIM VITAE .....	158
	ERKLÄRUNG.....	159
	EINVERSTÄNDNISERKLÄRUNG .....	160



# LIST OF FIGURES

Figure 1. Chemosensory system of <i>E. coli</i> .....	3
Figure 2. Chemosensory system of <i>B. subtilis</i> .....	6
Figure 3. Chemosensory system of <i>R. sphaeroides</i> .....	9
Figure 4. Clusters of <i>che</i> genes in <i>V. cholerae</i> .....	12
Figure 5. Distribution of <i>che</i> genes in <i>V. parahaemolyticus</i> .....	13
Figure 6. The MCPs of <i>V. cholerae</i> .....	15
Figure 7. Chemotaxis proteins of <i>V. cholerae</i> form arrays.....	16
Figure 8. Chemosensory arrays and the core unit.....	20
Figure 9. Components of the core unit.....	22
Figure 10. Localization of chemosensory arrays in <i>E. coli</i> .....	26
Figure 11. Localization of chemosensory arrays in <i>B. subtilis</i> .....	28
Figure 12. Localization of chemosensory arrays in <i>R. sphaeroides</i> .....	31
Figure 13. Localization of proteins of the ParC/ParP system in <i>Vibrio cholerae</i> and <i>Vibrio parahaemolyticus</i> .....	33
Figure 14. The ParC/ParP system in <i>Vibrio</i> species.....	41
Figure 15. ParP contributes to the formation of chemotaxis signaling arrays.....	46
Figure 16. Cryo-EM microscopy revealed the presence of chemotaxis arrays at the poles near the flagellum.....	47
Figure 17. Genomic library screening revealed MCPs as potential ParP interaction partners.....	48
Figure 18. The protein interaction tip of the MCPs is a highly conserved region.....	49
Figure 19. ParP interacts with the protein interaction tip of MCP proteins.....	50
Figure 20. YFP-ParP is diffusely localized in the cytoplasm of <i>E. coli</i> .....	51
Figure 21. YFP-ParP forms clusters when co-expressed with mCherry-MCP in <i>E. coli</i> .....	52
Figure 22. The AIF domain is a conserved region in ParP proteins.....	53
Figure 23. AIF domains form their own distinct clade.....	54
Figure 24. Two distinct interfaces of ParP-AIF mediate its interaction with MCP and CheA2.....	56
Figure 25. ParP's interactions with CheA2 and MCPs favor array formation.....	57
Figure 26. The ParP-AIF and CheA2-P5 domains promote chemotaxis array formation.....	59
Figure 27. Only CheA2-P5 is involved in signaling.....	61
Figure 28. Interactions between ParP, MCPs and CheA2 ensure polar placement and inheritance of chemotaxis arrays.....	62
Figure 29. ParP's interaction with CheA2 and MCPs are important for clustering of CheW.....	63
Figure 30. Integration of ParP within arrays influences ParP polar recruitment.....	64
Figure 31. Integration of ParP within signaling arrays stabilizes recruitment of ParP to the cell pole.....	65
Figure 32. Integration of ParP within signaling arrays influences ParC polar retention.....	66
Figure 33. Chemotaxis signaling arrays of proteins from cluster II form in <i>V. cholerae</i> without CheA proteins.....	69
Figure 34. CheA proteins from clusters I, II or III do not influence formation of arrays.....	70
Figure 35. YFP-CheA2 fluorescent fusion is functional.....	71
Figure 36. Polar retention of YFP-CheW1 clusters is independent of CheA proteins at the base plate of arrays.....	72

---

Figure 37. Hexagonal packing of chemoreceptor arrays in wild-type <i>V. cholerae</i> and <i>E. coli</i> cells. ....	74
Figure 38. Cellular stoichiometry and variability of <i>V. cholerae</i> base plate proteins. ....	76
Figure 39. Methyl-accepting chemotaxis proteins identified in proteomics assay.....	77
Figure 40. ParC forms a protein concentration gradient extending from the cell pole to mid-cell. ....	80
Figure 41. ParC associates non-specifically to DNA.....	83
Figure 42. Association of ParC with nsDNA influences polar placement of chemosensory arrays.. ....	84
Figure 43. ParC's polar localization and gradient formation is regulated by its ATP-cycle and DNA association.....	86
Figure 44. ParC's nucleotide ATP-dependent cycle influences localization of ParP and CheW. ....	87
Figure 45. Differential diffusion rates of distinct ParC protein states. ....	91
Figure 46. sptPALM showing the localization and fraction of immobile polar ParC .....	93
Figure 47. Model of ParP's integration within the core unit of the chemotactic arrays..	97
Figure 48. Different arrangement of CheA dimer occupancy in different arrays. ....	102
Figure 49. Differential diffusion rates of distinct protein states in a diffusion-and-capture mechanism drive protein gradient formation. ....	105
Figure 50. Scheme summarizing the current model of the ParC/ParP system.....	109

---

# LIST OF TABLES

Table 1. Reagents.....	110
Table 2. Commercial kits and assays .....	111
Table 3. Software and on-line resources .....	111
Table 4. Essential equipment .....	112
Table 5. Media, buffers and solutions.....	113
Table 6. Strains .....	114
Table 7. Plasmids.....	119
Table 8. Primers.....	121
Table 9. Components of the PCR mix .....	129
Table 10. Standard PCR program .....	129
Table 11. sptPALM data and statistics of different PA-mcherry ParC variants .....	138
Table 12. Methyl-accepting chemotaxis proteins of <i>V. cholerae</i> .....	139
Table 13. ParP sequences employed for alignment.....	140
Table 14. Sequences employed for phylogenetic tree .....	142
Table 15. ParA sequences .....	144
Table 16. Other sequences used in this work .....	144

---

# ABBREVIATIONS

---

+Att	Addition of an attractant
μ-	Micro
aa	Amino acid
AIF	Array Integration and Formation (ParP domain)
-Att	Removal of attractant
BACTH	Bacterial Adenylate Cyclase-based Two Hybrid
bp	Base pair
C	Cytoplasmic
CA	Cytoplasmic bound arrays
CCW	Counterclockwise
CDF	Cumulative distribution function
CFP	Cyan fluorescent protein
Chr	Chromosome
CL	Classical
Cryo-EM	Cryo-electron microscopy
CW	Clockwise
D	Diffusion coefficient
ET	EI Tor
EZRDM	EZ rich defined medium
FRAP	Fluorescence recovery after photobleaching
h	Hour
HAMP	Histidine kinases, adenylate cyclases, methyl-accepting chemotaxis proteins and phosphatases
Hz	Hertz
IM	Inner membrane
IPTG	Isopropyl β-D-1-thiogalactopyranoside
JD	Jumping distance
LB	Luria-Bertani medium
LBD	Ligand binding domain
LC-MS	Liquid chromatography mass spectrometry
LID	Localization and Inheritance Domain (CheA domain)
M	Molar
MA	Membrane bound arrays
mCherry	Monomeric Cherry (fluorescent protein)
MCP	Methyl-accepting chemotaxis protein

---

min	Minutes
MLP	MCP-like protein
ms	Millisecond
N/A	Not applicable
nsDNA	Non-specific DNA
OM	Outer membrane
P-	Phosphorylated (next to a protein name, for example CheY-P)
PAmCherry	Photoactivatable mCherry
PF	Polar flagellum
pH	Negative decimal logarithmic of the hydrogen ion activity
REC	Response regulator domain (in CheV)
SD	Signaling domain
SEM	Standard Error of the Mean
sptPALM	Single particle tracking photoactivated localization microscopy
T	Transmembrane
Tlp	Transducer-like protein(s)
v/v	Volume per volume
w/v	Weight per volume
Xgal	5-Bromo-4-chlor-3indoxyl- $\beta$ -D-galactopyranosid
YFP	Yellow fluorescent protein

---

---

# ABSTRACT

Chemotaxis proteins organize into large, highly ordered arrays. Particularly, in the enteric bacteria *Vibrio cholerae* and *Vibrio parahaemolyticus*, chemotaxis arrays are found at the cell pole, and their distribution follows a cell cycle dependent localization. The ParC/ParP system mediates this localization pattern and without either ParC or ParP, arrays are no longer positioned at the cell poles and fail to segregate upon division. Localization of arrays in these bacteria follow a hierarchical process, where arrays are tethered by ParP, which in turn links them to ParC, an ATPase that serves as a cell pole determinant in *Vibrios*. Here, we analyze the mechanism behind ParP's ability to access the chemotaxis arrays and positions them at the cell pole. Furthermore, we show that even in the absence of histidine kinase CheA proteins, the arrays still exhibit the native spatial localization and the iconic hexagonal packing of the receptors. We show that the *V. cholerae* Cluster II array is versatile in respect of array composition for auxiliary chemotaxis proteins, such as ParP and that these arrays are structurally less stable due to their lower CheA occupancy in comparison to the ultrastable arrays found in *E.coli*. Additionally, we examine the dynamic localization of ParC and evaluate its influence in the overall localization of the arrays and ParP. We show that ParP's C-terminus integrates into the core unit of signaling arrays through interactions with MCP proteins and the histidine kinase CheA. Our results indicate that ParP's intercalation within the core units facilitates array formation, whereas its N-terminal interaction domain enables polar recruitment of arrays and promotes ParP's own polar localization. Moreover, the data provides evidence that ParP serves as a critical nexus between the formation of the chemotactic arrays and their proper polar recruitment. Additionally, our data revealed that arrays in *V. cholerae* have the capacity to include several scaffolding proteins, displaying a previously uncharacterized variability. In turn, we demonstrate that this variability explains the high degree of structural instability shown by *V. cholerae* chemotaxis arrays. Finally, we show that ParC forms a protein gradient in *V. parahaemolyticus* cells. This protein gradient extends in a decreasing concentration from the cell pole towards mid-cell, and it is essential for ParC's function in positioning ParP and consequently the chemosensory arrays. Similarly, gradient maintenance requires a continuous cycle of ParC between the cell pole and the cytoplasm, as well as ParC's ability to associate with DNA and transition into different protein states in a nucleotide dependent manner. The data shows that ParC's localization dynamics relies upon differential diffusion rates of its distinct protein states. Altogether, this work studies the complexity of the ParC/ ParP system and highlights the importance of each component in the correct placement of the chemotactic signaling arrays.

---

# ZUSAMMENFASSUNG

Chemotaxisproteine organisieren sich zu großen, übergeordneten Arrays. Bei den Darmbakterien *Vibrio cholerae* und *Vibrio parahaemolyticus* befinden sich Chemotaxisarrays am Zellpol, und ihre Lokalisation variiert abhängig vom Zellzyklus. Das ParC/ParP-System vermittelt dieses Lokalisationsmuster, und ohne die Proteine ParC oder ParP sind die Arrays nicht mehr an den Zellpolen positioniert und können sich bei der Zellteilung nicht mehr aufteilen. Die Lokalisierung von Arrays in diesen Bakterien folgt einem hierarchischen Prozess, bei dem die Arrays via ParP und der ATPase ParC, welche als Zellpol-Determinante in *Vibrios* dient, am Zellpol verankert werden. In dieser Arbeit analysieren wir den Mechanismus wie sich ParP Zugang zu den Chemotaxis-Array verschafft um sie am Zellpol zu positionieren. Darüber hinaus zeigen wir, dass die Arrays auch in Abwesenheit der Histidin-Kinase CheA weiterhin die native räumliche Lokalisation und die ikonische hexagonale Anordnung der Rezeptoren aufweisen. Wir zeigen außerdem, dass die Zusammensetzung des *V. cholerae* Cluster II Arrays variabel ist und zusätzliche Proteine wie ParP enthalten können. Diese Arrays sind dann aufgrund ihrer geringeren CheA-Einbindung strukturell weniger stabil als die in *E. coli* vorkommenden ultrastabilen Arrays. Darüber hinaus untersuchen wir die dynamische Lokalisierung von ParC und bewerten ihren Einfluss auf die Gesamtlokalisierung der Arrays und ParP. Wir zeigen, dass sich der C-Terminus von ParP durch Wechselwirkungen mit MCP-Proteinen und der Histidin-Kinase CheA in die Signal-Arrays integriert. Unsere Ergebnisse zeigen, dass die Interkalation von ParP die Arraybildung erleichtert. Desweiteren ermöglicht ParPs N-terminale Interaktionsdomäne die Rekrutierung von Arrays zu den Zellpolen und fördert seine eigene polare Lokalisation. Darüber hinaus liefern die Daten den Beweis, dass ParP als kritischer Knotenpunkt zwischen der Bildung der chemotaktischen Arrays und ihrer richtigen polaren Rekrutierung dient. Zusätzlich zeigen unsere Daten, dass Arrays in *V. cholerae* die Fähigkeit haben, mehrere Gerüstproteine aufzunehmen, die eine bisher nicht charakterisierte Variabilität aufweisen. Wir zeigen außerdem, dass diese Variabilität für den hohen Grad der strukturellen Instabilität von *V. cholerae* Chemotaxis-Arrays verantwortlich ist. Schließlich zeigen wir, dass ParC einen Proteingradienten in *V. parahaemolyticus* Zellen bildet. Die ParC-Proteinkonzentration nimmt vom Zellpol zur Zellmitte hin ab, und dieser Gradient ist für die Funktion von ParC bei der Positionierung von ParP und damit auch der chemosensorischen Arrays unerlässlich. Auch erfordert die Erhaltung des Gradienten einen kontinuierlichen Austausch von ParC zwischen Zellpol und Zytoplasma, sowie die Fähigkeit von ParC, mit der DNA zu assoziieren und nukleotidabhängig in verschiedene Proteinzustände überzugehen. Die

Lokalisierungsdynamik von ParC beruht auf unterschiedlichen Diffusionsraten dieser Proteinzustände. Insgesamt untersucht die Arbeit die Komplexität des ParC/ ParP-Systems und betont die Bedeutung jeder Komponente für die korrekte Lokalisierung der chemotaktischen Signal-Arrays.



---

# CHAPTER 1: INTRODUCTION

## 1.1 Bacterial chemotaxis and chemotactic signaling arrays

Evolution grants selective advantage to those organisms that are best at adapting to changes in their environment. Since most natural niches have an extraordinarily diverse community of microorganisms, it is clear that microorganisms must be very well equipped to detect and face changes in their surroundings. In the particular case of bacteria, it is well known that they are capable of sensing a wide range of external cues such as changes in pH (Kihara & Macnab, 1981; Repaske & Adler, 1981), temperature (Maeda et al., 1976), varied chemicals at different concentrations (Adler, 1966a, 1966b, 1976), oxygen levels and even changes in light wavelength (Armitage, 1997; Engelmann, 1883). Additionally, there are different resources a bacterium employs to deal with these changes, for instance when encountering toxic compounds or in the face of a lack of resources, bacteria can simply move towards more favorable conditions.

Amongst a vast diversity of motility mechanisms in bacteria, rotation of the flagellum, a semi-rigid helical filament projecting from the cell, is the most widespread mechanism for movement in aqueous environments. Flagellum rotation, powered by an electrochemical ion force generated across the membrane, allows bacterial swimming. Although rotation of the flagellum is a common resource for displacement in liquids, bacteria display several swimming strategies. For instance, in the peritrichously flagellated *Escherichia coli*, each flagella is powered by a reversible rotary motor, and when all motors rotate in a counterclockwise (CCW) direction, the flagella forms a bundle that propels *E. coli* forward in a nearly straight swimming direction (normally called “run”). But when one or more motors change direction and rotate clockwise (CW), the bundle comes apart, leading to cellular realignments (commonly referred to as “tumbles”), before a new “run” begins. This “run-and-tumble” pattern is common among peritrichous bacteria, including *Salmonella enterica* and *Bacillus subtilis* (Berg & Berry, 2005; Kearns, 2010).

In contrast, cells with one single flagellum located at the cell pole, such as several species of *Vibrio*, *Pseudomonas*, *Aeromonas* and *Shewanella*, employ another strategy known as “run-reverse-flick”. In this swimming pattern, the spinning of the motor in a CCW sense leads to forward motion, while during CW rotation the cell is pulled backwards. Once the CCW rotation is resumed, the flagellum undergoes a kink, whose angle is amplified by flagellar rotation. Ultimately, this causes a flick of the flagellum that

induces a fast reorientation of the cell body (Berg, 1991; Son et al., 2013; Stocker, 2011; Xie et al., 2011). Meanwhile, other single flagellated bacteria, such as *Rhodobacter sphaeroides*, follow a strategy known as “run-stop-run”. In this case the motor is unidirectional and only rotates CW. Rotation of the flagellum drives the cell forward, while periodic stops of the motor permit cell reorientation through the change of the flagellum from a helical to a relax coiled form (Armitage et al., 1999).

Despite all these variations in the turning activity, number and position of the flagella, all swimming patterns have in common the presence of smooth or straight swimming events (or “runs”) combined with periodic interruptions (namely tumbles, reversals or stops) that permit cell reorientation. In general, during “run-and-tumble”, reorientation angle during tumbles is random, while in “run-reverse-flick”, reversals permit a 180° reorientations, while flicks result in varied reorientation angles, with an average of 90° (Xie et al., 2011). In homogenous environments, these variations translate in bacteria swimming randomly (Wadhams & Armitage, 2004). However, in the presence of chemical gradients, bacteria are able to bias the frequency of tumbles, reversals or stops as well as the length of the runs. Over time, the average frequency of these events leads to swimming towards more favorable environments. It is precisely this biasing of movement up a gradient of a beneficial compound, or away from harmful chemical substances, that is defined as *bacterial chemotaxis* (Adler, 1966a; Alon et al., 1999; Armitage, 1999; Macnab & Koshland, 1972; Sourjik & Wingreen, 2012; Wadhams & Armitage, 2004).

In order to regulate and coordinate chemotactic response, chemotactic microorganisms employ several well-characterized proteins, generally termed the *chemotaxis proteins*. These proteins associate in highly organized structures known as *chemotaxis, chemotactic or chemosensory signaling arrays* (Briegel et al., 2014a; Hazelbauer et al., 2008; Wadhams & Armitage, 2004; Zhang et al., 2007). Evidence suggests that most motile microorganisms are chemotactic, especially all motile bacteria (Briegel et al., 2015; Faguy & Jarrell, 1999). In accordance, the formation of chemotaxis arrays has been reported in many bacteria as well as some archaea species (Briegel et al., 2009; Szurmant & Ordal, 2004). Furthermore, previous research indicates that for some organisms, chemotactic as well as swimming behavior, play important roles in biofilm formation and host infection (Matilla & Krell, 2018). Altogether, these observations highlight the importance of bacterial chemotaxis in the overall understanding of microbial physiology.

## 1.2 Chemosensory systems

### 1.2.1 *E.coli*

The signaling pathway involved in chemotaxis of bacteria has been most extensively studied in *E. coli*. This pathway initiates when an array of transmembrane proteins named chemoreceptors, or as they are more commonly known, methyl-accepting chemotaxis proteins (MCPs), detect extracellular substances or chemoeffectors, namely attractants or repellents. Upon binding of a chemoeffector to the MCPs, mechanical signals are transferred to the protein CheA, a histidine kinase located in the cytoplasm. In this place, the adaptor protein CheW aids linkage between CheA and the MCPs. The MCPs arranged in large structures, usually termed the chemoreceptor arrays, and interactions between MCPs, CheA and CheW form the chemotactic signaling arrays. The binding events between chemoeffectors and the MCPs promote trans-autophosphorylation of CheA, which then transfers a phosphoryl group to the response regulator CheY. In turn, phosphorylation of CheY (CheY-P) stimulates its interaction with FliM/FliN complexes at the flagellar motor. Ultimately, CheY-P interaction with the flagellar motor proteins induces a change in the direction of flagellar rotation (Figure 1A).

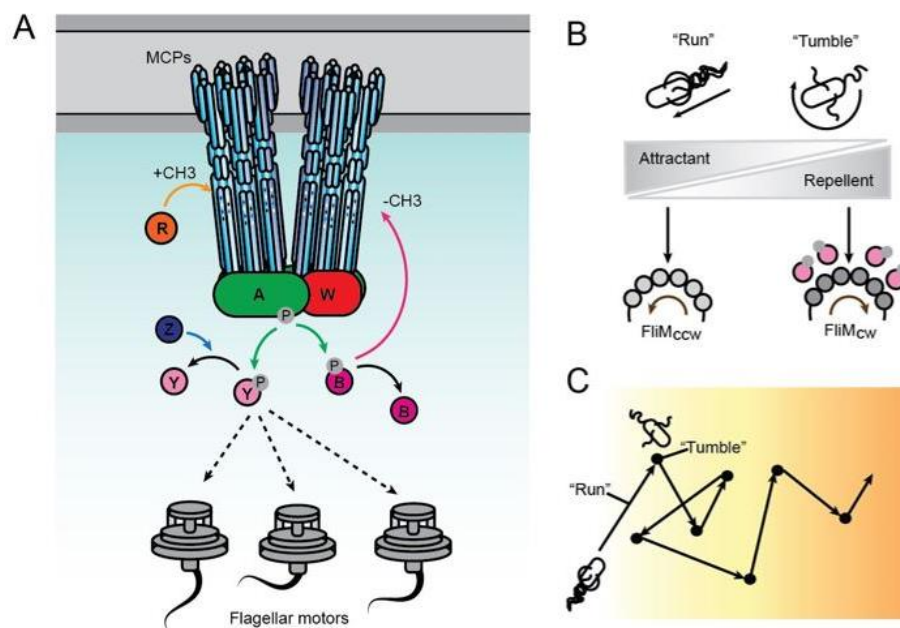


**Figure 1. Chemosensory system of *E. coli*.** (A) Methyl-accepting chemotaxis proteins (or MCPs) activate kinase CheA (green) in response to repellent chemoeffector molecules. Active CheA transfers a phosphoryl group to the response regulator CheY (pink), which exists as a phosphorylated (CheY-P) or non-phosphorylated form, both diffused within the cell. While phosphorylation of CheY is regulated by CheA, dephosphorylation depends in CheZ (dark blue), a CheY-P specific phosphatase. Adaptation proteins CheB (dark pink) and CheR (orange) add or remove methyl groups to and from the MCPs in order to tune sensitivity of the MCPs. As CheY-P diffuses in the cell, it interacts with the flagellar motors. Protein CheW (red) serves a scaffolding structure and mediates signal transfer between MCPs and CheA. (B) Interaction between FliM in the motor and CheY is facilitated when CheY is phosphorylated. Counterclockwise (CCW) rotating motors have a decreased affinity towards CheY-P, while clockwise

(CW) rotating motors allow CheY-P binding. Motor switching in a CCW sense occurs in presence of attractant or decrease of a repellent molecule, promoting straight swimming behavior or “runs”. In the opposite scenario, i.e. in the presence of a repellent, CheY-P interacts with FliM, causing motor rotation in a CW direction, eliciting episodic tumbling swimming, which ultimately allows the cell body to reorient. (C) Switching of “runs” and “tumbles” over time permit bacteria biased swimming up a gradient of a beneficial chemical compound. Adapted from (Fukuoka et al., 2014; Jones & Armitage, 2015; Micali & Endres, 2016).

For *E. coli*, a decrease in the concentration of attractant or increase in repellent molecules allows MPCs to stimulate CheA autophosphorylation. Consequently, levels of CheY-P increase, favoring CheY-P interaction with FliM/FliN. In turn, this interaction allows the change in the direction of flagellar rotation to CW sense, which disrupt the flagellar bundle and causes cell tumbling. On the other hand, an increase in the concentration of attractant causes a decrease in the autophosphorylation activity of CheA, rendering lower levels of CheY-P and thus allowing the rotation of the flagella in a CCW direction (Figure 1B-C). This in turn decreases the frequency of motor switching and causes the bacterium to swim smoothly (Borkovich et al., 1989). Finally, CheY-P signal is terminated by the phosphatase CheZ. Overtime, the regulation of the frequency of smooth swimming and tumbling episodes, results in the net movement towards more favorable conditions (Figure 1C).

### 1.2.1.1 Adaptation as molecular memory

Although the opposite has been argued (Thar & Kuhl, 2003), there is a growing consensus indicating that for bacteria, cell size is a limiting factor when moving up or down a chemical gradient, which means that the cell is too small to detect varied concentrations of chemicals along its length (Alon et al., 1999; Wadhams & Armitage, 2004). Hence, to overcome this constrain, chemotactic bacteria have evolved the ability to tune and adapt to variations in stimuli gradient through what is defined as *adaptation*, a property that has also been referred as “short-term molecular memory”. Adaptation is given by the receptors’ methylation system, which involves the methyltransferase CheR (Springer & Koshland, 1977) and the methylesterase CheB (Stock & Koshland, 1978). When CheA is activated (i.e. when autophosphorylation takes place using ATP as the phosphodonor), not just CheY but also CheB is phosphorylated (CheB-P). CheB-P removes methyl groups from specific glutamate residues on the chemoreceptors (Figure 1A). Demethylated MCPs have a lower ability to induce CheA autophosphorylation, hence the levels of CheY-P and CheB-P decrease and so does the frequency of motor switching, which in turn elicits straight swimming. Meanwhile, CheR adds methyl groups to the MCPs, and since CheR is constitutively active, MCPs remain in their methylated state even when CheB-P levels reduce. Eventually, highly methylated MCPs are better at stimulating CheA autophosphorylation, even in the continuous presence of an

attractant. Ultimately, when CheA is active, CheY-P will induce a tumbling episode (Figure 1B-C). Overall, this adaptation strategy guarantees that the sensitivity of the chemoreceptors is tuned and primed for subsequent changes while kinase activity is controlled depending on the current environmental conditions (Wadhams & Armitage, 2004).

However, while the chemotaxis model in *E. coli* is very well understood; several studies point to the existence of a wide variety of chemosensory systems. For instance, an analysis of 206 complete bacterial genomes showed that although 51% of bacteria had five of the chemotaxis (or *che*) genes found in *E. coli* (*cheA*, *B*, *R*, *W* and *Y*), 30% had multiple homologues too (Collins et al., 2014; Hamer et al., 2010). For example, *R. sphaeroides*, *Myxococcus xanthus*, *P. aeruginosa* and *Vibrio cholerae* have several sets of *che* genes. In addition, several bacterial species have chemotaxis proteins that are not homologues of any of the ones in *E. coli*, such as CheV, CheD, CheC and CheX (Wuichet & Zhulin, 2010). Moreover, while *E. coli* has five chemoreceptor genes, other species have a vast repertoire of putative genes encoding for MCPs (Morgan et al., 1993).

### 1.2.2 *Bacillus subtilis*

A very interesting example of a chemosensory system that greatly differs from the paradigm of *E. coli*, is offered by the gram-positive bacterium *B. subtilis* (Bischoff & Ordal, 1992; Rao et al., 2008). In *E. coli*, attractant addition decreases CheA autophosphorylation, which favors methylation of the MCPs. However, in *B. subtilis* attractant addition promotes CheA activity, and in turn demethylation of the MCPs (Bischoff & Ordal, 1991; Thoelke et al., 1989; Zimmer et al., 2000). This means that for *B. subtilis* an attractant-bound MCP increases the levels of CheY-P, as opposed to *E. coli*'s process, where an attractant-bound MCP decreases CheY-P levels. In *B. subtilis*, CheY-P binding to the flagellar motor elicits a change in rotation from CW to CCW, whereas in *E. coli*, CheY-P interactions with the motor cause a change from CCW to CW rotation (Kirsch et al., 1993a, 1993b). Although these two responses are reciprocal, it is important to notice that in both bacteria the CCW rotation of the flagella induces smooth swimming events (Figure 2A-B) (Bischoff & Ordal, 1991, 1992).

Another important difference between the chemosensory systems of *E. coli* and *B. subtilis* is their adaptation mechanisms. In *E. coli*, adaptation is provided only by the integrated activities of CheB and CheR, and there is only one CheY phosphatase (CheZ). Meanwhile, *B. subtilis* is known for its three adaptation systems and the presence of two

phosphatases, CheC and FliY (Figure 2C) (Mauriello et al., 2018; Rao et al., 2008; Szurmant et al., 2004; Walukiewicz et al., 2014).

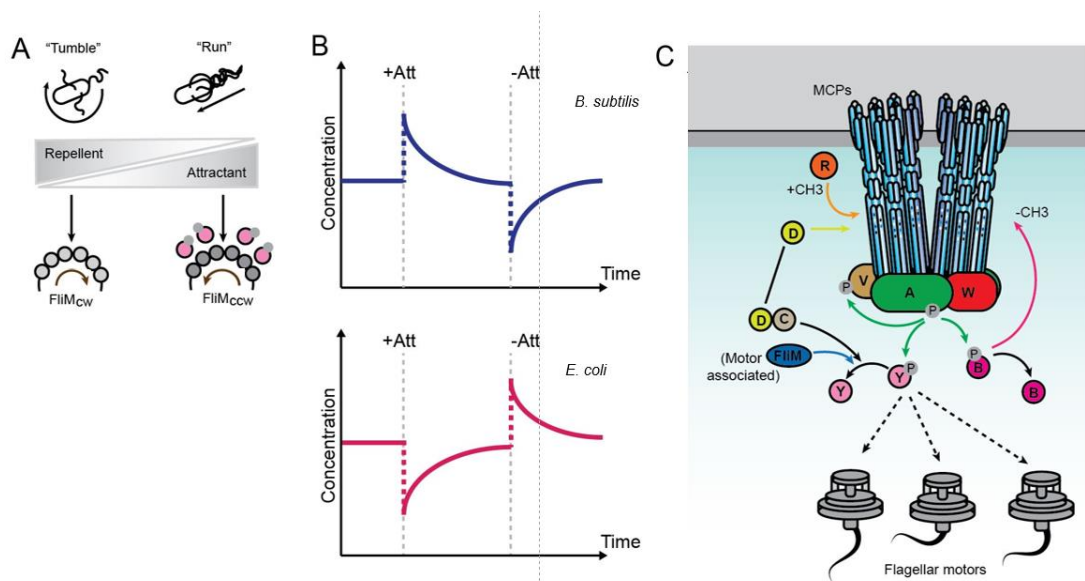


**Figure 2 Chemosensory system of *B. subtilis*.** (A) Swimming behavior. Unlike *E. coli*, in *B. subtilis* binding of CheY-P to the flagellar motors increases straight swimming or “runs”. Notably, “runs” and “tumbles” correlate with CW and CCW flagella rotation in both organisms. (B) Adaptation of CheY-P levels. For *E. coli* addition of an attractant (+Att) causes a smooth “run”, which translates in a transient decrease of CheY-P levels (pink line); however, the levels of CheY-P return to pre-stimulus level due to adaptation. Removal of attractant (-Att) increases CheY-P levels, leading to the increment in the likelihood of a reorienting “tumbling” episode. The pathway eventually adapts the levels of CheY-P. For *B. subtilis* follows a reciprocal response, +Att causes an increase in CheY-P, and -Att leads to a decrease of CheY-P levels. Adapted from (Mauriello et al., 2018; Rao et al., 2008). (C) Detection of chemoeffector attractant molecules causes activation of kinase CheA (green). CheA phosphorylates CheY (pink), CheV (brown) and CheB (dark pink). CheY-P binds to the flagellar motors to modulate swimming behavior. Dephosphorylation of CheY-P requires the concerted action of FliM (dark blue), located at the flagellar motor and CheD (light green) complexed with CheC (light brown). Importantly, adaptation of the methylation state of the MCPs in *B. subtilis* requires several proteins. CheR (orange) and CheB perform analogous functions to the namesake proteins in *E. coli*. Additionally, *B. subtilis* employs CheD, which is bound to the MCPs prior attractant detection. Upon detection of an attractant, an increase in the cellular concentration of CheY-P causes formation of CheD-CheC complexes and these can dephosphorylate CheY-P. Protein CheV is found in association with MCPs and CheA, attractant binding not only activates CheA but also CheV. CheV-P inhibits CheA activity depending on the methylation state of the MCPs. For more details see main text.

The three adaptation systems in *B. subtilis* are (1) the methylation, (Goldman & Ordal, 1984), (2) the CheC/CheD/CheY-P (Muff & Ordal, 2007) and (3) the CheV system (Karatan et al., 2001). The methylation system also involves CheB and CheR to demethylate and methylate chemoreceptors, respectively. Meanwhile, as its name indicates, the CheC/CheD/CheY-P system involves CheC and CheD, two proteins without homologues in *E. coli* (Rosario et al., 1994, 1995). The activity of this system relies on CheC’s ability to bind CheY-P (Szurmant et al., 2004), and the subsequent binding between the CheC-CheY-P complexes to CheD (Rosario & Ordal, 1996). Briefly, CheD is bound to the chemoreceptors until an attractant is added, increasing CheA activity. In turn, the levels of CheY-P raise, which then favors the chances of CheC to interact with CheY-P. The formation of CheC-CheY-P complexes provide an alternative

target to CheD, which is then removed from the MCPs. In consequence, CheA activity decreases, and so the levels of CheY-P decrease too. Ultimately, CheD will be released and free to bind MCPs again (Figure 2C) (Muff & Ordal, 2007; Rao et al., 2008). Although CheC is a phosphatase, previous studies indicate that it does not exhibit a significant influence on CheY-P dephosphorylation (Szurmant et al., 2004; Yuan et al., 2012). Instead, it functions as a regulator of adaptation, while FliY, a component of the C-ring of the flagellar motor, appears to have a more similar role to CheZ from *E. coli* (Szurmant et al., 2004). Even though there are still many open questions regarding the interplay between CheD, CheC and CheY, it is clear that this system plays a role in the CheY-P dependent modulation of flagellar rotation and thus in the chemotactic response of *B. subtilis* (Walukiewicz et al., 2014).

Lastly, the CheV system makes use of the C-terminus region of CheV, this region is a response regulator domain, also known as REC or CheY-like domain, that can be phosphorylated by CheA (Fredrick & Helmann, 1994; Rosario et al., 1994). When CheA is activated, it phosphorylates the REC of CheV. CheV-P then inhibits CheA activity by rendering CheA unresponsive to the chemoreceptor's signal relay (Figure 2C) (Karatan et al., 2001). Moreover, CheV has a CheW-like domain at the N-terminus (Hanlon et al., 1992), which as its name indicates shares structural similarities with the protein CheW. The CheW-like domain of CheV in *B. subtilis* allows CheV to interact with CheA and the MCPs (Rosario et al., 1994).

Interestingly, these three adaptation systems are functionally redundant and it is largely unclear how they coordinate to mediate chemotaxis (Bischoff & Ordal, 1992; Rao et al., 2008; Walukiewicz et al., 2014). Earlier, it was proposed that *B. subtilis* employs these three systems to selectively methylate certain residues in the MCPs with specific activity over CheA function (Rao et al., 2008). Recent work shows that CheD and CheV affect CheA activity as a function of the receptor methylation state, and suggest that these three different adaptation systems may be used to sense gradients of different magnitudes in the diverse habitats where *B. subtilis* is commonly found (Walukiewicz et al., 2014).

### **1.2.3 *Rhodobacter sphaeroides***

The complexity offered by the chemosensory system of this  $\alpha$ -proteobacterium resides in the presence of more than one set of *che* genes (Porter et al., 2008) and the formation of two distinct types of chemosensory arrays, classified based on their cellular placement as transmembrane and cytoplasmic (Hamblin et al., 1997; Porter et al., 2002). Chemotaxis genes in *R. sphaeroides* are distributed in three major operons (*cheOp1*,

*cheOp2* and *cheOp3*) and two minor ones with fewer genes (*cheBRA* and *cheY4-mcpG* operons) (Figure 3) (Hamblin et al., 1997; Mackenzie et al., 2001; Porter et al., 2002; Wadhams et al., 2003; Ward et al., 1995). Interestingly, the genes in these operons encode proteins with diverse roles and different subcellular localizations (Porter et al., 2008; Sourjik & Armitage, 2010). Additionally, it has been shown that the loss of any type of array, either transmembrane or cytoplasmic, abolishes chemotaxis (Hamblin et al., 1997; Porter et al., 2002). Particularly, deletion of *cheOp2* and *cheOp3* impairs chemotaxis altogether (Leonard et al., 2005; Porter et al., 2002), while deletion of *cheOp1* or *cheBRA* alone showed no effect (Ward et al., 1995).

Genes in *cheOp2* encode proteins responsible for the formation of transmembrane arrays (Wadhams et al., 2000, 2003), while proteins synthesized by *cheOp3* genes are responsible for the formation of arrays in the cytoplasm (Wadhams et al., 2002, 2003). Like in *E. coli*, when extracellular stimuli are perceived by the MCPs at the transmembrane arrays, CheA2 autophosphorylation is induced, and then a phosphoryl group is transferred to CheY6 (Porter & Armitage, 2002, 2004). However, the resemblance between *E. coli* and *R. sphaeroides*' cascades ends here, because CheY6-P alone is unable to bring about a change in flagellar movement, it needs the activity of either CheY5 from *cheOp1* or CheY4 from *cheBRA*, indicating that minimum two CheYs are needed to support chemotaxis (Porter et al., 2006).

Interestingly, while CheY3 and CheY4 are phosphorylated only by CheA2, which is in the transmembrane arrays, they can also interact with proteins in the cytoplasmic arrays (Porter & Armitage, 2004). These observations suggest that CheAs in *R. sphaeroides* can discriminate between CheYs (and also CheBs) for phosphotransfer (Porter et al., 2008; Porter & Armitage, 2004). Nevertheless, although structural differences have been documented in all CheAs of *R. sphaeroides* (Porter & Armitage, 2002, 2004), it is unknown how they can differentiate between response regulators.

On the other hand, it has been reported that cytoplasmic arrays in *R. sphaeroides* integrate their activity to transmembrane arrays in order to coordinate chemotaxis. Cytoplasmic arrays consist of CheW4 and CheA from *cheOp2* and a series of cytoplasmic chemoreceptors known as Tlps (for transducer like proteins) (Figure 3 A-B). It has been hypothesized that cytoplasmic arrays can detect extra and intracellular stimuli (Porter et al., 2008), a theory that leads to speculate that *R. sphaeroides* is capable of detecting changes in the concentration of intracellular compounds, which in turn might reflect the metabolic state of the cell (Packer & Armitage, 2000a, 2000b). However, this remains largely unclear and the reasons behind the presence of two types of arrays (cytoplasmic and transmembrane) within the cell are still incompletely understood. A



suggestion is that having two arrays ensures the correct placement of all chemotaxis proteins, which in turn prevents their crosstalk, so that each one can independently sense and respond to their specific chemoeffectors. Nevertheless, the exact stimuli that cytoplasmic chemoreceptors detect is unknown, nor is it clear how they integrate their responses to the activity of transmembrane arrays (Porter et al., 2008, 2011).

Another interesting aspect in *R. sphaeroides* signaling cascade is the lack of a phosphatase (Figure 3). While *B. subtilis* has two CheZ-like proteins (CheC and FliY) (Szurmant et al., 2004; Yuan et al., 2012), *R. sphaeroides* uses phosphate sinks instead. Interestingly, in *R. sphaeroides* all CheYs with the exception of CheY6, are capable of complementing a  $\Delta cheZ$  *E. coli* strain (Shah et al., 2000). Additionally, CheA3 has showed phosphatase activity for CheY6 (Porter & Armitage, 2002), and all together these proteins control signal termination in *R. sphaeroides* (Porter & Armitage, 2002).

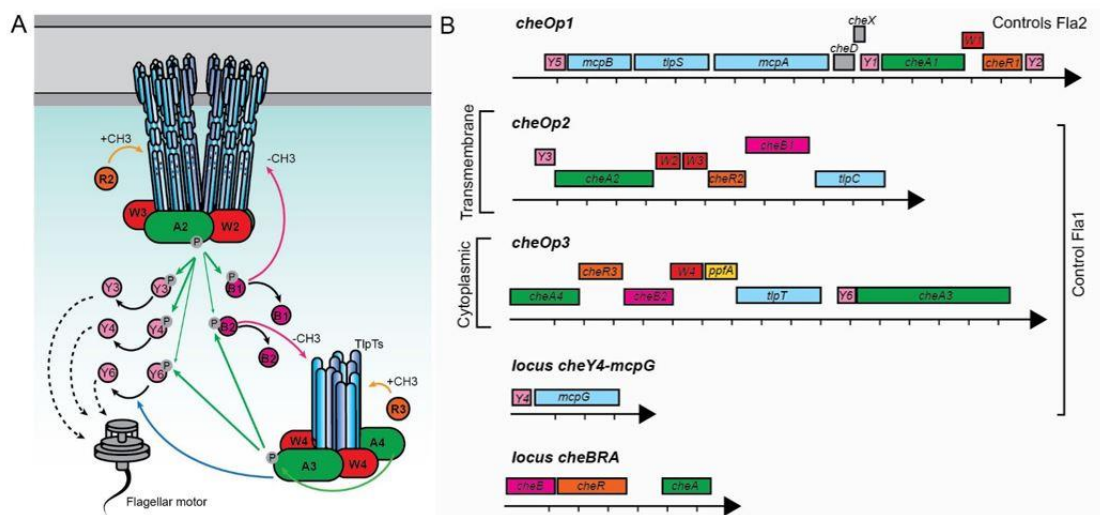


**Figure 3. Chemotaxis system of *R. sphaeroides*.** (A) MCPs (blue) detect extracellular signals, while TlpTs, cytoplasmic receptors, are believed to detect metabolic signals. Transmembrane MCPs transfer signals to CheA2, while TlpTs induce accumulation (or clustering) of CheA3-P and CheA4-P (kinases are shown in green). Phosphotransfer to three response regulators increases their concentration, ultimately, modulation of flagella rotation requires CheY3-P, CheY4-P and CheY6-P (all CheYs appear in pink). The targeting of CheB proteins (dark pink) to different receptors remains hypothetical. The central signaling output is CheY6, because it can be phosphorylated by CheA3 and CheA2. CheR proteins (orange) methylate receptors, while CheW proteins (red) act as coupling proteins for array formation and facilitate signal transduction. (B) Organization of chemotaxis genes in *R. sphaeroides*. The main operons (1, 2 and 3) and *cheBRA* are located in the larger chromosome, while the smaller operon (*cheY4-mcpG*) is in the smaller chromosome. Response regulators in *cheOp1* coordinate function with the Fla2 system. Operons 2 and 3 mediate the formation and function of transmembrane and cytoplasmic arrays, respectively, and their activity associates with the master regulator *fla1*. Arrows indicate transcription direction. Color conventions are kept same in (A) and (B). Adapted from (Hernandez-Valle et al., 2017; Porter et al., 2008).

---

### 1.3 *Vibrio cholerae* and *Vibrio parahaemolyticus* as model organisms

In this thesis, the microorganisms *V. cholerae* and *Vibrio parahaemolyticus* were employed as model organisms to study the formation and localization of chemotaxis signaling arrays. Hence an overview of their physiology becomes relevant before dwelling on the chemosensory system of these bacteria.

*V. cholerae* is a marine gram-negative  $\gamma$ -proteobacteria. It is a motile curved rod with one single polar flagellum and the causative agent of the disease cholera. Since 1817, cholera has caused seven pandemics. Currently, it is endemic to several countries in Asia, Africa and America (Nelson et al., 2009). The incidence of cholera is correlated to poverty and lack of proper sanitation. Every year, about 5 to 7 million cases of cholera are reported worldwide (Ali et al., 2015; Clemens et al., 2017; Harris et al., 2012; Sack et al., 2004). The disease manifests as a profuse diarrhea, sometimes accompanied by vomiting, which can lead to severe dehydration, metabolic acidosis and in the absence or delayed treatment, it can be fatal. Transmission of cholera occurs by consumption of contaminated food or water (Clemens et al., 2017). Upon consumption, *V. cholerae* colonizes the epithelium of the small intestine via a complex mechanism involving intra-intestinal signals that induce ToxR, required for transcriptional activation of the *toxT* gene, whose protein product activates numerous virulence related genes. This regulatory cascade consists of several inner membrane proteins that detect environmental signals present in the intestine and ultimately coordinate the production of the cholera toxin (Gill & Meren, 1978; Mekalanos, 1985; Peterson & Mekalanos, 1988). The cholera toxin is largely responsible for the diarrheal symptoms, since it stimulates fluid secretion by activating adenylate cyclase in epithelial cells. This in turn leads to an increase in the levels of cyclic adenosine monophosphate that is responsible for increased chloride and water secretion and the subsequent decreased uptake of sodium in the cells (Gill & Meren, 1978). Eventually, epithelial cells loss water and electrolytes, which in extreme cases can cause severe dehydration leading to death within hours of the onset of diarrhea (Mekalanos, 1985).

*V. cholerae* cells are found in large numbers in the diarrheal fluid, thereby if means of sanitation are not available, the disease can spread to other individuals and become pandemic (Peterson & Gellings, 2018). The majority of cholera outbreaks were caused by *V. cholerae* serotype O1, which is divided into classical (CL) and El Tor (ET) biotypes (Sang et al., 2009). These biotypes differ in that the CL biotype generally causes more severe diarrhea because it produces higher amounts of cholera toxin, while the ET

biotype has the greater ability to survive in the environment and cause infection (Sack et al., 2004). In the present study, two strains of biotype ET (N16961 and C6706) were employed.

Like *V. cholerae*, *V. parahaemolyticus* is also a marine bacterium and as such thrives in estuarine environments. *V. parahaemolyticus* is a gram-negative rod-shaped bacterium that is commonly found as a free-swimming cell, attached to underwater surfaces, or commensally associated with different shellfish species (McCarter, 1999).

Diseases associated with *V. parahaemolyticus* include wound infections, septicemia and more commonly acute gastroenteritis, usually acquired via consumption of raw or undercooked seafood. While some strains of *V. parahaemolyticus* are strictly environmental, many are pathogenic to humans, and since its isolation in 1950, pathogenic *V. parahaemolyticus* has become a leading cause of seafood-driven food poisoning worldwide (Su & Liu, 2007; Yeung & Boor, 2004). *V. parahaemolyticus* infections have been associated with three serotypes, namely O3:K6, O4:K68 and O1:K. The strain used in this work, the RimD 221063, belongs to the serotype O3:K6, and was the first *V. parahaemolyticus* strain to be sequenced (Morris & Acheson, 2003; Nair et al., 2007).

*V. parahaemolyticus* has two different types of flagella. As a swimmer cell, it has one single polar flagellum that is sheathed. Nonetheless, *V. parahaemolyticus* has the ability to differentiate into a large, peritrichously flagellated swarmer cell, and as a swarmer, *V. parahaemolyticus* produces non-sheathed lateral flagella, which allow it to swarm over solid or semi-solid surfaces. Lateral flagella rotation is powered by proton motive force, unlike the single polar flagellum, where the energy is given by sodium motive force (McCarter, 1999; McCarter et al., 1988; Shinoda & Okamoto, 1977). In this study, both strains, *V. cholerae* and *V. parahaemolyticus* (particularly, the swimmer cell type), are employed to address several questions concerning the intracellular positioning of proteins involved in chemotaxis.

### **1.3.1 Chemotaxis in *Vibrio cholerae* and *Vibrio parahaemolyticus***

Similar to *R. sphaeroides* (Figure 3), the enteric human pathogen *V. cholerae* has several sets of *che* genes in its genome. *V. cholerae* has three chemotaxis operons known as operon or cluster I, II and III, distributed in its two chromosomes. Cluster I locates in chromosome one and contains *cheY1*, *cheA1*, *cheY2*, *cheR1*, *cheB1*, *cheW0*; cluster II also on chromosome one includes *cheW1*, *cheB2*, *cheA2*, *cheZ*, *cheY3* and two genes known as *parC* and *parP*; cluster III on chromosome two contains *cheB3*,

*cheD*, *cheR3*, *cheW2*, *cheW3*, *cheA3* and *cheY4*. Cluster II does not have a *cheR* gene, and instead *cheR2* is found in the *fla* gene operon adjacent to cluster II (Figure 4). Moreover, *V. cholerae*'s genome has four predicted *cheV* genes simply termed *chev1*, *chev2*, *chev3* and *chev4*. Not one of these is placed within a *che* gene cluster, and only *cheV3* is placed relatively close in the genome to *cheR2* (Boin et al., 2004).

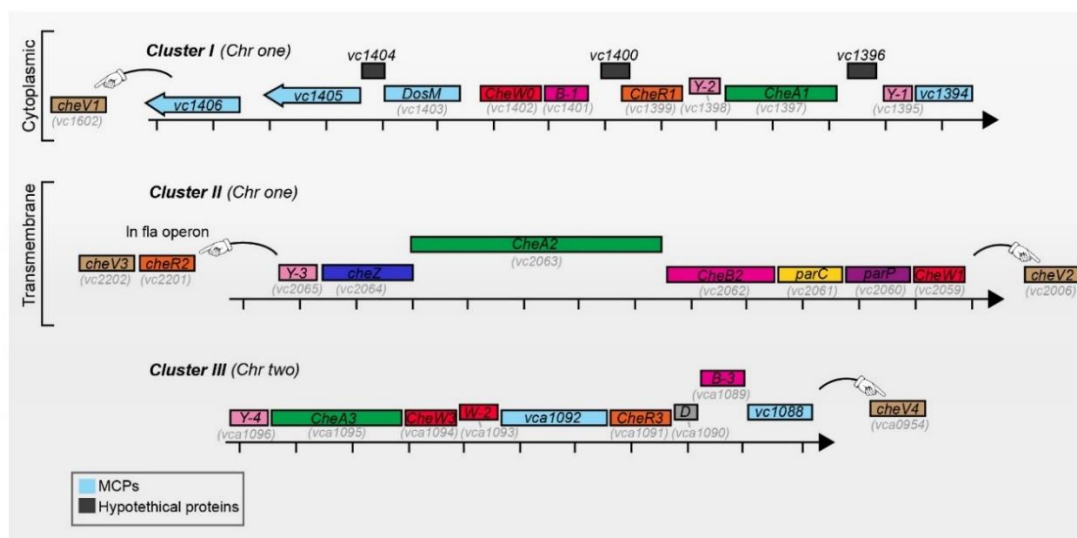


**Figure 4. Clusters of *che* genes in *V. cholerae*.** Chemotaxis genes in *V. cholerae* organize in three operons or clusters (I, II and III). Cluster I and II are found in the larger chromosome (Chr one), while cluster III is in the small chromosome (Chr two). Each cluster contains a kinase CheA (green). Kinases of clusters I, II and III are referred to as CheA1, CheA2 and CheA3, respectively. There are four CheW proteins (red), CheW0 in cluster I, CheW1 in cluster II and CheW2 and CheW3 in cluster III. Genes encoding for MCPs (light blue) are scattered through the genome with only few found within a cluster. For instance, the gene encoding for MCP *DosM* is found in cluster I. Gene encoding for *CheR2* (orange), is found outside cluster II, in the adjacent *fla* operon. The genes that encode for CheV proteins (brown) are also found outside the *che* gene clusters (pointing hands). Cluster I CheA1 and CheW0 proteins form arrays that localize in the cytoplasm, while CheA2 and CheW1 cluster II proteins form transmembrane arrays. It is unknown which CheV protein assembles in transmembrane or cytoplasmic arrays. Proteins of unknown function located within cluster I are shown in dark gray. Gene numbers are shown for all cases. Chr = chromosome.

Meanwhile, *V. parahaemolyticus* has only one set of *che* genes with homology to the ones in cluster II of *V. cholerae*. However, most of *V. parahaemolyticus*' *che* genes are located in close proximity to a large flagella operon, these genes are *cheY*, *cheZ*, *cheA*, *cheB*, the genes *parC* and *parP* followed by *CheW* and an open reading frame annotated as *vp2224*. Two other *che* genes are found in another genomic region, these genes are *cheV* and *cheR* (Figure 5) (Kim & McCarter, 2000).

On the other hand, genes encoding for MCP proteins in both, *V. cholerae* and *V. parahaemolyticus*, are scattered in the genome. In the case of *V. cholerae* only a few are found in proximity to a chemotaxis cluster (Figure 4). Furthermore, the number of putative *mcp* genes in these microorganisms, more than 40 for both *Vibrio* species, greatly surpasses that of *E. coli*, where there are only five *mcp* genes.

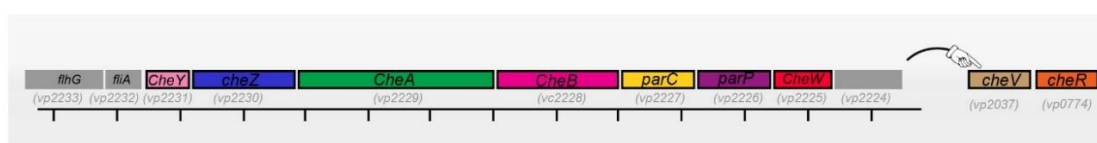


**Figure 5. Distribution of *che* genes in *V. parahaemolyticus*.** Unlike *V. cholerae*, there is only one set of chemotaxis genes in *V. parahaemolyticus*. These are found within an operon of flagella related genes. Genes *cheR* and *cheV* are located somewhere else (pointing hand). Product of gene *vp2224* is annotated as a hypothetical protein. Gene numbers are indicated.

### 1.3.1.1 Genetic organization of chemosensory genes

In *V. cholerae*, the proteins encoded by the *che* genes in each chemotaxis cluster (Figure 4) are hypothesized to represent three distinct signaling systems (Peterson & Gellings, 2018). Earlier research showed that only CheA2 from cluster II is required for chemotactic response in standard conditions, that is in soft LB agar plates (Gosink et al., 2002). Furthermore, it was indicated that *cheA2* is a homolog of *cheA* from *E. coli*, and cross-species complementation of a swimming phenotype of  $\Delta cheA$  *E. coli* was achieved by overexpression of *cheA2* (Gosink et al., 2002). Furthermore, other studies have shown that introducing mutations in *cheY3* from cluster II rendered non-chemotactic *V. cholerae* cells (Lee et al., 2001), and the same result was obtained later from an in frame deletion of *cheY3* (Hyakutake et al., 2005). Meanwhile, single deletions of each of the other three *cheY* genes from cluster I and III had no effect on chemotactic ability under standard laboratory conditions (Boin et al., 2004). Moreover, from all *cheR* paralogues, only the absence of *cheR2* decreased chemotactic activity (Butler & Camilli, 2004). Hence, cluster II is deemed the one responsible for chemotactic behavior in *V. cholerae* (Boin et al., 2004; Butler & Camilli, 2004; Lee et al., 2001), regulating a similar signaling pathway as *E. coli*'s. Furthermore, the fact that genes in cluster II are constitutively expressed (Ringgaard et al., 2015), has guided the idea that genes in cluster II direct chemotactic activity not only in laboratory conditions but in most environmental scenarios.

Meanwhile, earlier studies demonstrated that *V. cholerae* proteins encoded in cluster I are specifically produced under low oxygen conditions, either induced by growing cells in standing liquid cultures or by the addition of reducing compounds (Hiremath et al., 2015). Based on these observations, showing that energy-limiting conditions regulate expression of genes in cluster I (Briegel et al., 2016; Hiremath et al., 2015), it was proposed that proteins produced from cluster I genes are responsible for chemotactic activity and survival in host environments, such as host intestine (Hiremath et al., 2015). The importance of chemotaxis during infection will be discussed in further detail below.

More recently it was observed that production of cluster III proteins was determined by the growth phase, this is cluster III proteins were observed in microscopy experiments only during stationary phase (Ringgaard et al., 2015). While these studies suggest that expression of genes from all clusters are induced in different growth conditions, it has not been reported whether cluster I and III proteins coordinate any chemotactic-related behavior. Other studies have shown that some chemosensory systems have outputs other than mediating a chemotactic response (i.e. modulation of flagella rotation) (Wuichet & Zhulin, 2010), and instead they regulate alternative functions, such as type IV-pili mediated motility or the modulation of intracellular levels of secondary messengers (Hickman et al., 2005; Wuichet & Zhulin, 2010; Zusman et al., 2007). However, it remains unclear if this is the case for *V. cholerae*'s cluster I and III.

Interestingly, it was shown that expression of cluster III genes occurred even in the absence of cluster I and II genes (Ringgaard et al., 2015). This observation complies with a model where the three systems in *V. cholerae* do not require crosstalk and instead act independently of each other, possibly coordinating varied outputs. Drawing inspiration from the current knowledge of *B. subtilis* (Figure 2) or *R. sphaeroides* (Figure 3), the presence of three clusters could respond to the need of detect and respond to a wide variety of stimuli. This would require the assembly of arrays with distinct MCPs, which in turn would have the capacity to sense different environmental cues.

In support of this theory, is the fact that *V. cholerae* encodes 45 putative *mcp* genes. Their classification and predicted or experimentally determined localization is shown in Figure 6. Some published works refer to MCPs in *V. cholerae* as MLPs, for (MCP)-like proteins, but for consistency, the denomination MCP will be used in this thesis, and when conflicted with the literature the corresponding gene number will be given. Briefly, MCPs have been classified based on the number of heptads present in the signaling domain (SD) region, the most conserved part of MCP proteins that locates at their most distal tip towards the cytoplasm (Figure 5) (Alexander & Zhulin, 2007; Salah Ud-Din & Roujeinikova, 2017). This classification has in total 12 categories, and MCPs in *V. cholerae* belong to four of them, although the majority fall into the 40H group (Figure 6).

Meanwhile, no as much information is available for the genetic organization of *che* genes in *V. parahaemolyticus* as there is for *V. cholerae*. However, there is experimental evidence showing that deletion strains of genes involved in both flagella systems, lateral and polar, experienced a decreased chemotactic behavior in capillary assays (McCarter & Silverman, 1990). These observations were later confirmed in experiments where strains defect in varied *che* genes affected both, swimming and

swarming motility. Thereby, the current hypothesis is that a common chemotaxis system directs both forms of displacement (Boles & McCarter, 2002). Nevertheless, it is unknown how chemotactic control is shared by the two flagella systems (McCarter, 1999).

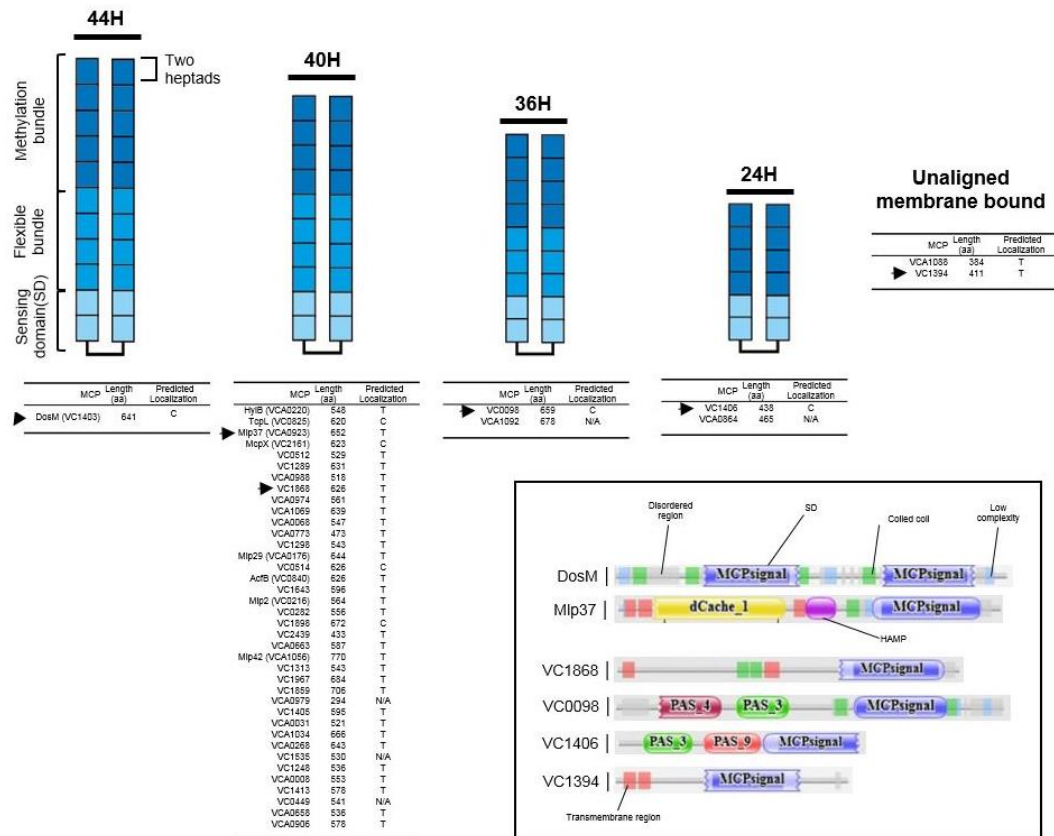


**Figure 6. The MCPs of *V. cholerae*.** Classification of all MCP proteins of *V. cholerae* indicate the majority belong to the 40H class. Based on the presence of predicted transmembrane regions, cellular localization is transmembrane (T) or cytoplasmic (C). Black arrows point at the MCPs whose domain architecture retrieved from Pfam is shown inside the box. (aa)= amino acids. N/A = not applicable or known. Classification data taken from (Alexander & Zhulin, 2007).

### 1.3.1.2 Chemotaxis proteins from different clusters form independent arrays in *V. cholerae*

Much like *R. sphaeroides*, *V. cholerae* forms polar as well as cytoplasmic arrays. Proteins from cluster II form polar membrane-bound arrays (Figure 7A-B), these arrays are composed by the receptors of the class 40H (Figure 6) (Briegel et al., 2016). Meanwhile, recent evidence shows that cluster III proteins also form membrane-bound arrays, but in this case arrays include the MCP of category 44H (Figure 6) (Mann and Ringgaard, unpublished). Interestingly, formation as well as localization of cluster III arrays is independent of cluster I or cluster II genes (Ringgaard et al., 2015).

Localization of YFP-CheW0, that is CheW from cluster I (Figure 4), showed that cluster I proteins form cytoplasmic arrays, and these arrays formed independently of proteins from cluster II. Similarly, cryo-electron microscopy (cryo-EM) studies revealed that formation of cluster I arrays does not require proteins from cluster III (Figure 7B) (Briegel et al., 2016). Thus, like gene expression, array formation and localization of proteins from all chemotaxis clusters is independent of one another, regardless whether the arrays are polar or cytoplasmic.

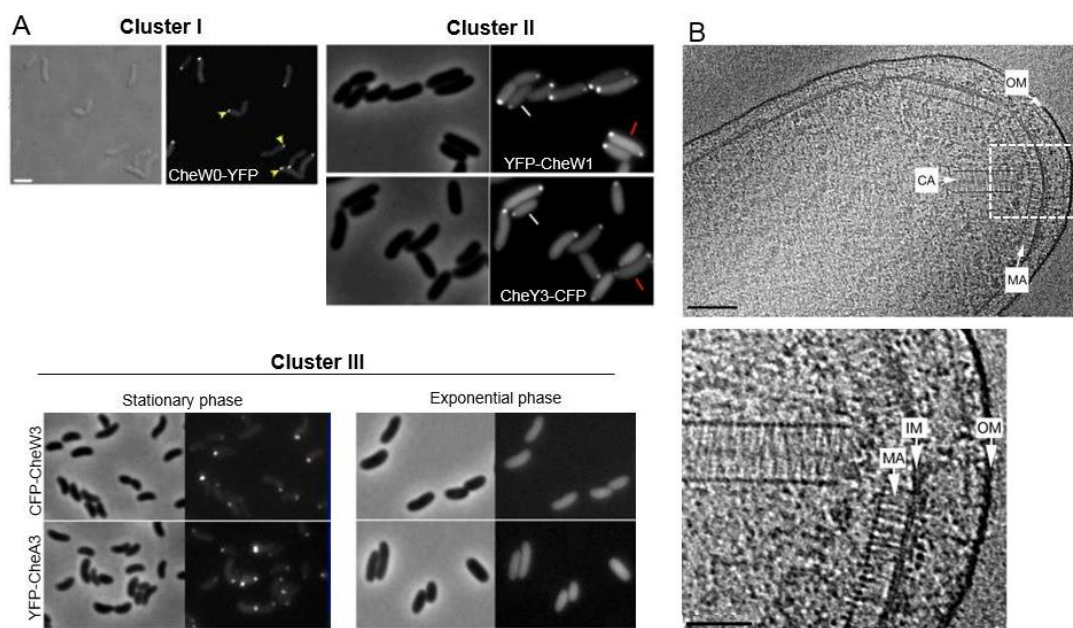


**Figure 7. Chemotaxis proteins of *V. cholerae* form arrays.** (A) Fluorescence microscopy of proteins from cluster I, II and III in *V. cholerae*. Array from clusters I and III form under specific environmental conditions (see text for details). Cluster III proteins form arrays when cells have reached stationary phase. Meanwhile, arrays from cluster II are deemed the ones responsible for chemotactic behavior in most scenarios. (B) Top panel, electron tomography of cytoplasmic (CA) and membrane-bound arrays (MA) (scale bar 100nm). Lower panel shows magnified view of the area inside the white dotted square (scale bar 50nm). Importantly, fluorescence microscopy of cluster I and II proteins appears similar because CA form near the polar region. IM= inner membrane, OM= outer membrane. Images taken from (Briegel et al., 2016; Ringgaard et al., 2011, 2015).

In the case of *V. parahaemolyticus* the chemosensory arrays have not been directly visualized as is the case of *V. cholerae* (Figure 7B). However, due to the universality of the chemosensory array structure (Briegel et al., 2009), it is likely arrays in *V. parahaemolyticus* do not differ much from the ones observed in *V. cholerae*. Indirect visualization of the arrays, on the other hand, has been reported recently. Microscopy studies of fluorescent protein fusions of YFP-CheW show that arrays form at the cell poles in swimmer cells, but are located throughout the cell membrane when the cells exist in the swarming stage (Hearing & Ringgaard, 2016). Although it is likely these arrays are membrane anchored, there is no experimental evidence to back this claim.



### 1.3.1.3 The role of chemotaxis in infection of *V. cholerae* and *V. parahaemolyticus*

Studies to determine attractants and repellents for *V. cholerae* date to more than 30 years ago, and they place important emphasis on the influence of chemotaxis in colonization and infection of the small intestine (Almagro-Moreno et al., 2015; Boin et al., 2004; Freter et al., 1981; Freter & O'Brien, 1981a, 1981b; Guentzel & Berry, 1975). Literature shows contradictory findings when it comes to determining the link between *V. cholerae* infection capabilities and chemotaxis (Matilla & Krell, 2018; Peterson & Gellings, 2018). Some studies have found positive correlation between chemotaxis and infection (Banerjee et al., 2002; Hang et al., 2003), while others indicate that chemotaxis is important only for the distribution and colonization of the bacterium in the intestine but not necessarily for infection (Butler & Camilli, 2004; Lee et al., 2001; Millet et al., 2014). Currently, a few chemoreceptors and their physiologically relevant signals that are associated with *V. cholerae*'s pathogenicity have been identified. These MCPs are Mlp7 (sometimes referred to as Tcpl; gene number *vc0825*) (Chaparro et al., 2010; Harkey et al., 1994), Mpl8 (or AcfB; *vc0840*) (Chaparro et al., 2010; Everiss et al., 1994), Mlp24 (or McpX; *vc2161*) (Lee et al., 2001), Mlp37 (*vcA0923*) (Pasupuleti et al., 2014), Mlp30 (or HlyB; *vca0220*) (Alm & Manning, 1990), Mlp2 (*vc0216*), Mlp29 (*vca0176*) and Mlp42 (*vca1056*) (Hang et al., 2003) (Figure 6).

Earlier studies indicate that *V. cholerae* requires chemotaxis to penetrate the mucus layer and access the intestinal space at the base of the villi (Freter et al., 1981). Based on these observations, a more recent study showed that deletions of *tcpI* and *acfB* do not show chemotactic behavior towards a gradient of intestinal mucus using a capillary tube assay (Selvaraj, P., Gupta, R., Peterson, 2015). Furthermore, other studies showed that the ToxR-ToxT regulatory cascade, which regulates virulence in *V. cholerae*, controls expression of both, *tcpI* and *acfB* (Everiss et al., 1994; Harkey et al., 1994). In agreement with these findings, it has been observed that a double deletion of *tcpI* and *acfB*, decreases intestinal colonization in infant mice (Chaparro et al., 2010).

Similarly, earlier studies identified McpX as a regulator for the production of the cholera toxin (responsible for inducing cholera disease) upon mouse infection (Lee et al., 2001). This study showed that McpX was required for induction of the *ctxAB* operon, essential for toxin production. Later studies showed that wild-type *V. cholerae* exhibits chemotactic behavior towards multiple amino acids (Nishiyama et al., 2012), and a deletion of *mcpX* decreased chemotaxis towards many of them. The authors of this study concluded that McpX is required for chemotaxis towards amino acids in the host intestine, but that other chemoreceptors must exist for amino acid detection.

In accordance with these data, the deletion of gene *mlp37* (*vca0923*), the closest paralogue of *mcpX*, resulted in a decreased chemotactic response towards amino acids which were not recognized by *mcpX* (Nishiyama et al., 2016). In this study, it was also reported that *V. cholerae* exhibits chemotactic activity towards bile, and previous evidence suggested that bile enhances motility of *V. cholerae in vivo* (Gupta & Chowdhury, 1997; Nishiyama et al., 2016). Protein crystallization studies showed that Mlp37 binds directly to L-amino acids and most interestingly, to taurine, the main component of bile. This observation led the authors to suggest that chemotaxis towards taurine might play a role in *V. cholerae* colonization (Nishiyama et al., 2016). However, as mentioned earlier, it is unclear whether chemotaxis has significant influence in *V. cholerae* pathogenicity. Other experiments showed that disruption of *cheA2*, *cheY3* and *cheZ* delayed expression of *toxT*, an essential gene for the production of cholera toxin (Lee et al., 2001). This is in agreement with a later study showing that mutants of *cheY3* and *cheY4* reduced production of cholera toxin *in vitro* (Bandyopadhyaya & Chaudhuri, 2009). Hence, while chemotaxis appears to play a role in *V. cholerae* infection, the details remain largely unclear. More research is still needed to determine how each component of the chemotactic machinery in *V. cholerae* influences host infection.

In the case of *V. parahaemolyticus*, there are not studies directly addressing the link between chemotaxis and virulent activity. One study earlier reported that at high cell density, a strain of *V. parahaemolyticus* produced a transcriptional regulator pertinent to quorum sensing, whose targets for regulation include several virulence related genes as well as nine *mcp* genes (Burke et al., 2015). However, there is no experimental evidence of the correlation between these nine MCPs and the identified transcriptional regulator. Therefore, like in *V. cholerae*, more research is required.

## 1.4 Components of the chemosensory arrays

In terms of the chemosensory system itself, the interactions between the involved proteins (namely MCPs, CheA and CheW) have been studied extensively. Interactions between the histidine kinase CheA, the chemoreceptors and the adaptor protein CheW, are quite literally the core of the chemotaxis signaling response. Indeed, in *E. coli* the so-called core unit of the chemotactic apparatus, i.e. the smallest structure capable of kinase control and activation, consist of one CheA dimer, two adaptor proteins CheW and two chemoreceptor trimers of receptor dimers (Figure 8A) (Greenfield et al., 2009; Li & Hazelbauer, 2011).

---

### 1.4.1 Chemoreceptors or MCPs

Within the core unit of chemotaxis signaling complex each of the components has extremely specific structural features. For instance, all transmembrane receptors have a sensing or ligand binding domain (LBD), consisting of an amino-terminal extracellular domain that interacts with ligands or chemoeffectors (Figure 9A-B) (Falke & Hazelbauer, 2001; Kim et al., 1999). Additionally, although sensing domains vary among MCPs, all transmembrane chemoreceptors share a similar architecture (Figure 9A-B) (Alexander & Zhulin, 2007; Falke & Hazelbauer, 2001; Hazelbauer et al., 2008). This means that they all form dimers with four helices that extend throughout the cell membrane, linking the sensing domains by a HAMP (histidine kinases, adenyl cyclases, methyl-accepting and phosphatases) domain, a key component in signal transmission, to a well conserved carboxyl-terminal cytoplasmic domain (Ferris et al., 2011; Hulko et al., 2006). Following the HAMP, there is an adaptation region, or methylation helix bundle, where glutamate residues undergo methylation and demethylation when activation of the receptor is being tuned by CheB or CheR (Bornhorst & Falke, 2000; Li & Weis, 2000). Finally, there comes the cytoplasmic region, the most distal to the membrane, which is an unstructured linker segment at the C-terminus of every subunit. This region is known as the protein interaction region, kinase control module or signaling domain (SD), because it is the one that interacts with the two other components of the core, i.e. CheA and CheW (Figure 8A-B) (Mowery et al. 2008; Li & Weis 2000; Krembel et al. 2015).

As mentioned earlier, MCPs could be classified based on the structure of the SDs (Figure 6). Overall, there are seven major (44, 40, 38, 36, 28 and 24H) and five minor categories (48, 42, 52, 58 and 64H) (Alexander & Zhulin, 2007; Salah Ud-Din & Roujeinikova, 2017).

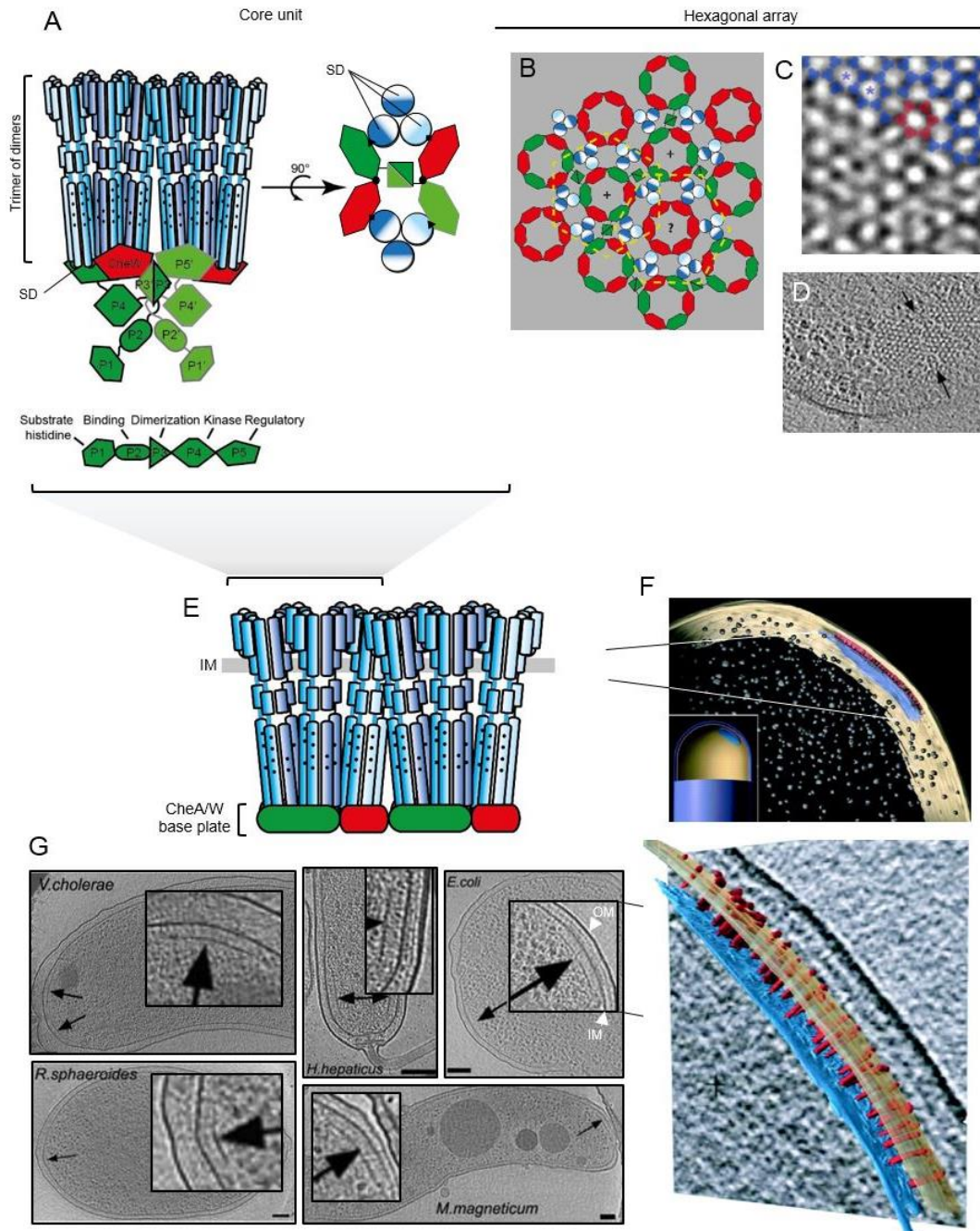


**Figure 8. Chemosensory arrays and the core unit.** (A) Schematic of the chemotaxis core unit, the smallest structure capable of kinase activity. It consists of two receptor MCP trimers of dimers, two CheW adaptor proteins and a CheA dimer. CheA cartoon in green shows its five different domains. MCPs employ their conserved interaction tip located the signaling domain (SD) to interact with the P5 domain of CheA and CheW as shown when the core is flipped 90°. (B) Scheme showing how core units assemble to form the classical hexagonal array (dotted yellow line and plus symbols). Computational analyses predict the existence of CheW only hexagons (question mark). (C) Cryo-tomography of *V. cholerae*, where trimers of dimers are shadowed in blue, they fit into the vertices of the hexagonal lattice in a chemoreceptor array. The image shows in red six trimers of dimers that enclose one hexagon. The spacing from the center of the hexagon to the center of an adjacent one (blue asterisk) is 12 nm. (D) Cryo-tomography of the top view of the array of *Termotoga maritima* pointed by the two black arrows. (E) MCPs orient with their SD towards the base plate composed of CheA/CheW proteins. (F) (Top) Schematic displaying array positioning relative to the cell pole (inset) in *E. coli*. (Bottom) In this scheme imposed over a cryo-tomograph of *E. coli*, a side view of the receptors in red shows how they are inserted in the CheA/CheW base plate in blue. (G) Chemoreceptor arrays of different bacteria, insets show a magnification of the arrays. Scale bars 100nm. OM= outer membrane, IM= inner membrane. Cryo-tomography pictures and 3D representation of arrays of *E. coli* taken from (Briegel et al., 2009; Zhang et al., 2007).

On average, chemotactic bacteria have about 14 chemoreceptors (Lacal et al., 2010), but the variation is enormous, with some having more than 80 or as little as one (Alexandre et al., 2004). Additionally, most of the chemoeffectors recognized by the LBDs are unknown, mostly because there is great sequence variation among LBDs themselves, which complicates the extrapolation of the findings from one bacterium to another. Moreover, within one bacterial species, chemoreceptors or MCPs differ in topology and have varied LBDs, which permits the recognition of a varied range of chemoeffectors (Matilla & Krell, 2018; Ortega et al., 2017; Salah Ud-Din & Roujeinikova, 2017). In general, many of the identified chemoeffectors serve as carbon or nitrogen sources, required for growth or electron acceptors. Some examples include sugars, amino and organic acids, dipeptides, aromatic and aliphatic hydrocarbons, nucleotide bases, polyamines and oxygen (Matilla & Krell, 2017; Parales et al., 2015; Sampedro et al., 2015). Also, some chemoreceptors permit the response to plant hormones (Antúñez-Lamas et al., 2009; Kim et al., 2007), hormones in the human-gut (Lopes & Sourjik, 2018), metal ions (Englert et al., 2010), neurotransmitters (Pasupuleti et al., 2014) and quorum sensing signals (Hegde et al., 2011; Laganenka et al., 2016).

#### 1.4.1 The histidine kinase CheA

Meanwhile, the histidine kinase CheA is a multi-domain protein, consisting of five separate domains with different functions (P1 to P5). P1 is the domain that contains the substrate histidine for autophosphorylation; P2 binds CheY for phosphotransfer from P1 (Bilwes et al., 1999; Morrison & Parkinson, 1994; Swanson et al., 1993); P3 is the dimerization domain, whose interaction with the receptors is suggested to be of major importance for chemotactic function (Cassidy et al., 2015; Park et al., 2006); while P4 is the kinase or ATP binding domain and the P5 is the regulatory domain (Figure 8A) (Bilwes et al., 1999; Borkovich et al., 1989; Gegner et al., 1992; Zhao & Parkinson, 2006). Several organisms, including *V. cholerae* and *R. sphaeroides*, have more than one *cheA* gene in their genomes (Figure 3 and Figure 4), and normally the number of CheAs is a good indication of the putative number of chemotactic signaling pathways in a given organism.

CheA activity is ATP-dependent and its interactions with the MCPs mediate signaling. A recent study in *E. coli* revealed that while the P5 domain has an essential role in chemoreceptor signaling, the receptors do not control CheA activity through their direct contacts with the P5 region, instead they manipulate CheW, and thus indirectly influence CheA-P5 to direct autophosphorylation (Piñas et al., 2018).

### 1.4.2 The adaptor protein CheW

The core unit also includes the adaptor protein CheW, which is structurally similar to the P5 regulatory domain of CheA (Avram Sanders et al., 1989; Gegner & Dahlquist, 1991; Griswold et al., 2002). CheW consists of two  $\beta$ -sheet domains, also referred to as interfaces 1 and 2, and each one is made up by a five-stranded  $\beta$ -barrel that forms a hydrophobic core for protein-protein interactions (Figure 9C-D) (Griswold et al., 2002; Vu et al., 2012). While CheW has been named the universal adaptor, the N-terminus of CheV has a similar structure to CheW (Ortega & Zhulin, 2016). Most of the research of CheV's role in chemotaxis has been done in *B. subtilis*, where it contributes to signaling relay through its REC domain at the C-terminus (Figure 2) (Fredrick & Helmann, 1994; Rosario et al., 1994). Phylogenetic analyses indicate that organisms with CheV, employ it as an extra adaptor to link CheA to chemoreceptors that cannot be effectively accommodated by CheW (Ortega & Zhulin, 2016).

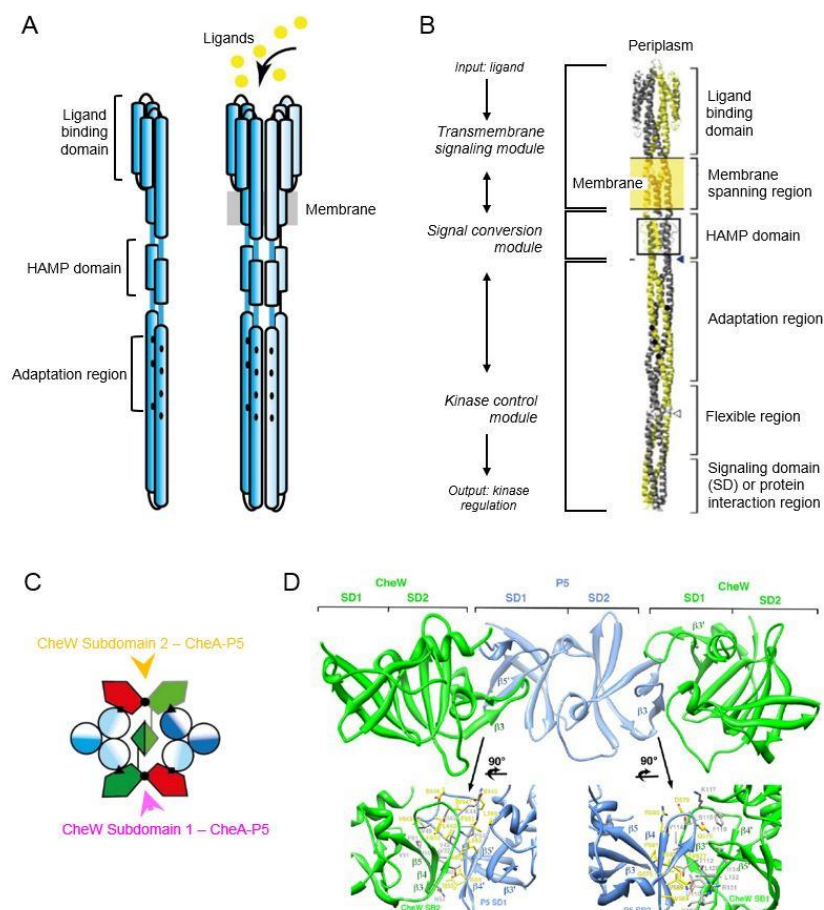


**Figure 9. Components of the core unit.** (A) Scheme showing a monomer subunit of a MCP, where different protein domains are indicated. When they form homodimers MCPs response to changes in ligand occupancy to modulate CheA activity. (B) Model of the three distinct modules that regulate signaling in the homodimeric structure of an aspartate receptor. (C) Cartoon showing the contacts that keep MCPs, CheW and CheA in the core unit together, these contacts are (i) CheW subdomain 1 or 2 interaction with P5 (black circle), (ii) P5 interaction with the SD region of the MCPs (black triangles) and MCPs interaction with CheW subdomain 1 or 2 (black squares). (D) Pseudo symmetric contacts made by CheW

subdomains and P5 domain. (Top) Half of one P5-CheW ring viewed from the center. (Bottom) The interfaces formed between CheW-subdomain 2 and the P5 or P5-subdomain 2 and CheW subdomain 1 rotated 90° relative to their orientation above. The two contacts are very similar, with both involving close associations of conserved hydrophobic residues on the respective domains. Protein structure images reproduced from (Li et al., 2013; Swain & Falke, 2007). MCP scheme based on (Falke & Hazelbauer, 2001).

### 1.4.3 Chemosensory array assembly

Despite the tremendous achievements made towards the definition of the structural features of chemoreceptors, CheA and the coupling proteins CheW and CheV alone (Bilwes et al., 1999; Griswold et al., 2002; Li et al., 2007), the study of assembly and activity of the arrays is a rich field for additional investigation. Importantly, although there is variation in the different chemosensory mechanisms, or the number of *che* genes, all arrays, regardless of the organism or the conditions where they form, share common features. An earlier study characterized the dimensions of chemosensory arrays in 13 bacteria species and found that there is a universally conserved 12-nm hexagonal arrangement of chemoreceptors, CheA and CheW proteins (Figure 8B-C) (Briegel et al., 2009). Currently, the model of array architecture depicts a single core unit arranged in a hexagonal structure, which is kept together by three defined contacts, (i) CheA-MCPs, (ii) CheW-MCPs and (iii) CheA-CheW (Piasta & Falke, 2014). Subsequently, more hexagonal structures join together to form a superlattice-like structure, which is more commonly called, the chemosensory array (Figure 8B-C) (Briegel et al., 2009, 2014a, 2014b). Formation of chemosensory arrays is essential for chemotactic activity, because this arrangement favors heightened sensitivity of the chemoreceptors (Duke & Bray, 1999), as well as their signal gain (Sourjik & Berg, 2002), cooperativity (Li & Weis, 2000; Sourjik & Berg, 2004) and adaptation capabilities (Endres & Wingreen, 2006; Li & Hazelbauer, 2005).

So far, it is known that within the core complex in *E. coli* a CheA dimer joins two receptor trimers of dimers through interactions with the P5 domain, while two CheW proteins bind to an MCP trimer of dimers in each core unit. Then, the helix formed by the dimerization of the P3 domains of the CheA dimer positions itself between the two receptor dimers (Figure 8A) (Briegel et al., 2011, 2012, 2014b; Li & Hazelbauer, 2011; Li et al., 2013). Moreover, the P5 domains of each CheA bind to the CheW interfaces (Figure 9C-D). These interactions between CheA and CheW, form what is known as the *base plate* for the chemoreceptor arrays (Figure 8E) (Briegel et al., 2009).

Moreover, it is also known that CheA-CheW interactions are the ones that bridge the two receptors trimers of every core and it seems clear too, that these interactions give the array its characteristic lasting stability (Briegel et al., 2009; Erbse & Falke, 2009; Liu

et al., 2012; Piasta & Falke, 2014; Zhao & Parkinson, 2006) and high sensitivity (Hazelbauer et al., 2008; Sourjik & Wingreen, 2012) even when reconstituted *in vitro* (Briegel et al., 2014a; Erbse & Falke, 2009; Li & Hazelbauer, 2011; Slivka & Falke, 2012). Moreover, recent experiments suggest that the superlattice structure has hexagons filled with CheWs only (Figure 8B) (Cassidy et al., 2015), which possibly contribute to array stability as well. However, some questions still persist, for instance, the mechanism behind array assembly is not entirely understood, and it remains unclear how each contact within the core unit contributes to the stability and ultimate activity of the entire array.

More interestingly, the core unit is asymmetric in the way signal transduction occurs. As it can be observed from the current structure model (Figure 8B-C), from the three receptor dimers in the core, only one interacts with CheA, one with CheW and the other one either has no interaction partner or interacts with CheW in the CheW-only hexagon of the lattice (Briegel et al., 2012; Li & Hazelbauer, 2014; Li et al., 2013; Liu et al., 2012). This would mean that only one of the dimers has the ability to influence kinase activity. Yet again, not much is known of how this asymmetry affects the overall activity and assembly of the array.

Furthermore, even though the general hexagonal arrangement is conserved among bacteria (Figure 8D-G), a previous study reports differences between the structures of cytoplasmic arrays of two distantly related organisms. While *V. cholerae* displayed flat arrays, the arrays in *R. sphaeroides* were much more curved or even round (Briegel et al., 2014a). More recently, it was observed that cytoplasmic arrays in *V. cholerae* have two, instead of one base plate. As previously shown, *V. cholerae* has different classes of MCPs (Figure 6), and recently, it was shown that cytoplasmic arrays in *V. cholerae* (Figure 7) include a chemoreceptor with an unusual architecture. These cytoplasmic arrays are formed by two layers of an MCP from cluster I known as DosM (Figure 4 and Figure 6). DosM has two signaling domains and is then sandwiched between two layers of CheA and CheW (Briegel et al., 2014a, 2016). Altogether, these observations suggest that there could be variations in arrays from different species that have not been studied.

## **1.5 Mechanisms for the subcellular localization of chemotaxis signaling arrays in bacteria**

It is important to notice that chemosensory arrays not only differ in their architectural features and composition, but also in their intracellular localization. For instance, *E. coli* has large chemosensory arrays at the cell poles, and small ones that form throughout the lateral cell membrane, while in *B. subtilis* arrays exist only in the



---

polar regions of the cell. In the case of *R. sphaeroides* and *V. cholerae*, chemosensory arrays form at the poles as well as in the cytoplasm (Figure 3 and Figure 7). This variation in the localization of chemosensory arrays between bacteria species is attributed to distinct mechanisms driving these intracellular positioning patterns.

### **1.5.1 Stochastic self-assembly in the placement of chemosensory arrays in *E. coli***

In *E. coli*, arrays localize primarily at the cell poles (Maddock & Shapiro, 1993), but there are also small lateral arrays formed along the cell length (Greenfield et al., 2009; Thiem & Sourjik, 2008). The stochastic model of array assembly arises from competition between nucleation of new arrays and growth of the existing ones with different rates and protein concentration dependence (Thiem & Sourjik, 2008). In this model, receptors are embedded into the cell membrane (Shiomi et al., 2006) but can either nucleate a new array or join an existing one. Arrays grow in size as more proteins are absorbed while the formation of new protein clusters near places where one already exists is prevented (Thiem & Sourjik, 2008). Thereby, the number of observable arrays in a given cell depends on its size, as well as the concentration and diffusion coefficient of the receptors; in fact, it has been shown that the number of arrays increases linearly as the cell length increases (Greenfield et al., 2009; Thiem & Sourjik, 2008). Correspondingly, simulations of stochastic self-assembly systems have reproduced the positioning patterns documented through *in vivo* microscopy experiments of *E. coli* (Figure 10) (Wang et al., 2008).

Similarly, photoactivated localization microscopy (PALM) experiments revealed that large arrays are indeed formed by absorption of smaller arrays and single proteins (Greenfield et al., 2009). These experiments confirmed stochastic assembly for chemotaxis clusters in *E. coli*, showing that arrays do not have a specific size but grow as more proteins are added maintaining a critical distance between one another. The presence of a limiting distance in array formation is supported by the fact that, when the expression levels of the chemoreceptors are increased, the number of arrays reaches saturation (Greenfield et al., 2009; Thiem & Sourjik, 2008). In this model for localization of arrays (Figure 10), protein clusters formed throughout the cell length ensure that after division, each daughter cell inherits small lateral arrays as well as one large polar array. Eventually, and after several rounds of division, lateral arrays become polar ones. This ensures that in long *E. coli* cells, the regulation of distant flagellar motors is not limited to the diffusion of CheY-P.

Importantly, the stochastic self-assembly model does not exclude the possibility that other factors may play a role in array formation and localization. Recent studies indicate that transmembrane regions of the two major MCPs in *E. coli*, Tar and Tsr, can alone mediate the formation of polar and lateral clusters (Pollard & Sourjik, 2018), which could explain why these receptors form clusters even without CheA (Saaki et al., 2018). Moreover, it has been indicated that chemoreceptors are sensitive to membrane curvature, suggesting that curvature sensitivity is intrinsic of the trimer of dimer conformation of the MCPs (Figure 8A) (Draper & Liphardt, 2017). Additionally, it has been reported that the Tol/Pal system also affects array stability and influences array localization (Saaki et al., 2018; Santos et al., 2014).

The Tol/Pal protein complex is a conserved component of the cell envelope in gram-negative bacteria (Lazzaroni et al., 1999). Previous research showed that the chemoreceptors interact with the Tol/Pal complex, and disruption of the complex rendered mislocalization of chemoreceptors as well as cells with chemotactic and motility defects (Santos et al., 2014). Nevertheless, recent experiments indicate that the Tol/Pal system affects polar clustering primarily by reducing average cluster size, but it does not affect curvature sensitivity (Draper & Liphardt, 2017).

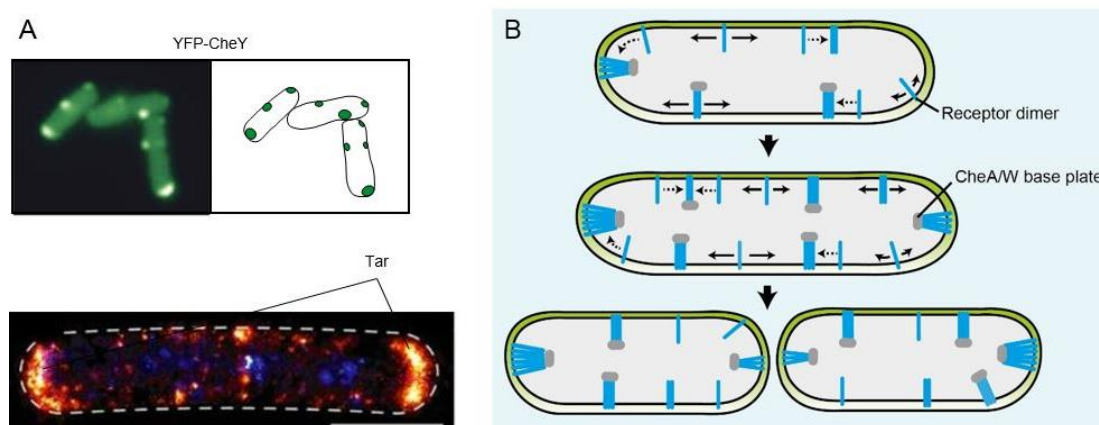


**Figure 10. Localization of chemosensory arrays in *E. coli*.** (A) (Top) Localization of receptor clusters in *E. coli* obtained by expressing YFP-CheY. (Bottom) Super resolution microscopy image of *E. coli*, where the receptor Tar formed large lateral clusters and small ones around the cell boundary. Scale bar 1  $\mu\text{m}$ . (C) Stochastic self-assembly model for the localization of chemosensory signaling arrays in *E. coli*. Receptors are inserted into the membrane and form small complexes, consisting of receptors and CheA/CheW. These complexes stochastically nucleate cluster assembly, and attach to one of the pre-division sites. Once attached, clusters do not move, but constantly grow by addition of smaller receptors or smaller complexes until they become polar in later division cycles. Microscopy pictures taken from (Greenfield et al., 2009; Sourjik & Armitage, 2010). Model adapted from (Thiem & Sourjik, 2008). For more details see main text.

### 1.5.2 Importance of the curved zones for the placement of chemosensory arrays in *B. subtilis*

Localization of arrays in *B. subtilis* shows a similar distribution to *E. coli*'s, i.e. large arrays are formed at the cell poles, and smaller arrays are seen in the lateral membrane (Figure 11). However, an earlier study showed that stochastic nucleation likely does not drive array placement in *B. subtilis*, but instead arrays accumulate at the areas of the membrane with strong curvature that are generated during cell division (Strahl et al., 2015). Microscopy experiments of a fluorescently tagged chemoreceptor in *B. subtilis* revealed that arrays do not form by clustering, or direct recruitment to the poles, instead, polar localization is the result of recruitment of the receptors to the cell division site when the membrane starts to invaginate (Figure 11). After completion of cell division, chemoreceptors remain at each side of the division plane, at the level of maximum curvature, and are not found at the central region of the septum where curvature is absent (Figure 11) (Strahl et al., 2015). This study argues that in case of lateral clusters, they are likely formed by stochastic nucleation, but differently from what *E. coli* follows, because lateral clusters in *B. subtilis* do not accumulate or show any periodicity in their spacing. Furthermore, authors in this study observed that localization of the chemoreceptors at the strongly curved regions occurs thanks to the physical conformation of the receptor trimers or dimers. This means that, each dimer is not parallel but forms a tripod-like structure with a precise curvature similar to the one measured for the base of the cell division septum (Strahl et al., 2015).

It was discussed that these differences in array localization between *E. coli* (Figure 10) and *B. subtilis* (Figure 11), are a consequence of the way these two bacteria strains divide. In most gram-positive bacteria, including *B. subtilis*, cell division leads to the formation of cross-wall, which in turn creates a strongly curved cell membrane at mid-cell. Meanwhile, *E. coli* constricts during division, resulting in a more moderate curvature of the cell (Strahl et al., 2015). Recent studies in *E. coli* showing that polar receptor clustering is influenced by the interaction between the receptors and the membrane (Pollard & Sourjik, 2018), indicate that possibly both models, stochastic nucleation as well as the properties of the cellular membrane, influence the placement of arrays, though differences are expected to exist between microorganisms (Mauriello et al., 2018).

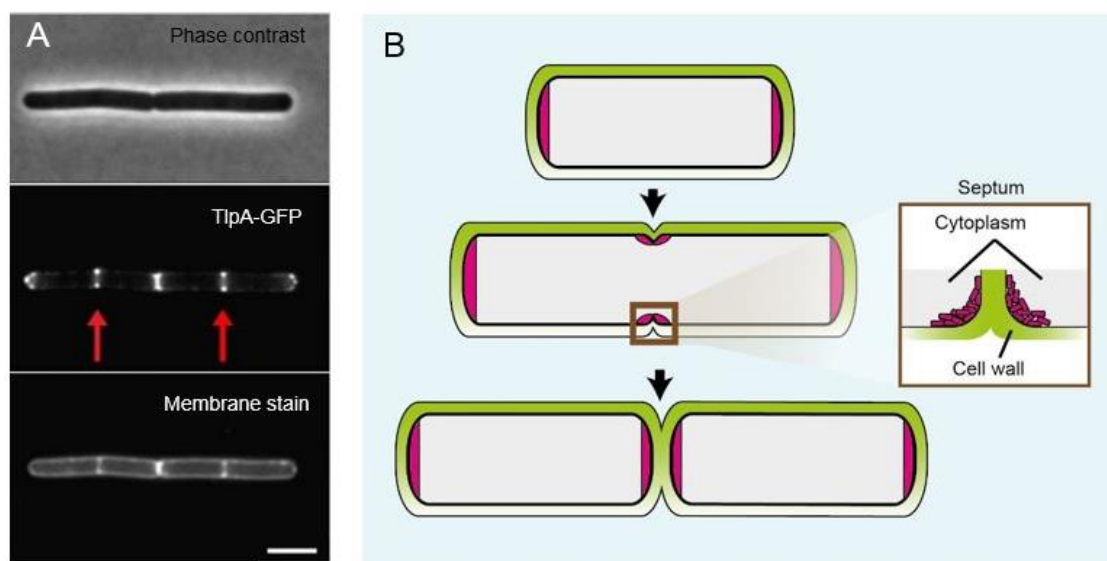


**Figure 11. Localization of chemosensory arrays in *B. subtilis*.** (A) Localization of TlpA-GFP (an MCP from *B. subtilis*). Arrows point at the active cell division sites. Scale bar 3  $\mu\text{m}$ . (B) Schematic showing the localization of TlpA. Membrane curvature influences its accumulation at the poles and at the cell division septum. Modified from (Strahl et al., 2015).

### 1.5.3 Localization of chemosensory arrays by ParA homologues

#### 1.5.3.1 ParA-like proteins

Among the mechanisms used for the positioning of chemosensory arrays are those mediated by homologous of ParA proteins or as they are commonly called, *ParA-like proteins*. ParA-like proteins belong to a group of P-loop NTPases from the Mrp/MinD family, which includes proteins widely distributed among bacteria (Lutkenhaus, 2012). These proteins are characterized for their ability to switch between a nucleoside diphosphate (NDP)-bound form to a nucleoside triphosphate (NTP)-bound form, which permits reversible binding to a surface, such as the membrane, nucleoid DNA or partner proteins (Lutkenhaus, 2012). The classical example in bacteria is MinD, which is involved in spatial regulation of the Z-ring (Lutkenhaus, 2012). Other important ParA-like proteins include MipZ and PomZ, which are briefly presented below.

##### 1.5.3.1.1 Min system

As mentioned above, the classical example is the Min system, best studied in *E. coli*, which directs the assembly of the Z-ring division machinery (FtsZ) to mid-cell. The Min system consists of the proteins MinC, MinD and MinE. MinC, the inhibitor of Z-ring formation, is recruited to the membrane by the ParA-like protein MinD where they form a complex. MinC and MinD together form an inhibitor complex that prevents Z-ring assembly anywhere but at mid-cell by a mechanism in which MinE-stimulated oscillation

of MinD from pole to pole ensures that the time averaged concentration of the MinCD complex is lowest at mid-cell and highest at the cell poles. MinE promotes ATP hydrolysis of MinD, which triggers the detachment of both MinD-ADP and MinE from the membrane. Subsequently, MinD-ADP undergoes nucleotide exchange in the cytosol such that its ability to bind to the membrane is restored. The combined function of MinD and MinE drives the oscillatory behavior of the system. Particularly, MinD-ATP dimers accumulate at the inner membrane at one cell pole, where they in turn recruit MinE, which stimulates ATP hydrolysis. This results in the formation of MinD-ADP monomers, which detach from the membrane, diffuse and accumulate at the opposite pole (de Boer et al., 1989; De Boer et al., 1992; Hu et al., 1999, 2002; Lackner et al., 2003; Lutkenhaus, 2012; Meinhardt & de Boer, 2001; Raskin & de Boer, 1999).

#### **1.5.3.1.2 MipZ**

Another important example, is the ParA-like protein MipZ of *Caulobacter crescentus*. MipZ is an inhibitor of Z-ring formation and forms a gradient with concentration maxima at the cell poles and a minimum at the cell center, which ensures that Z-ring formation only occurs at this site (Kiekebusch et al., 2012; Thanbichler & Shapiro, 2006). Similar to MinD, MipZ switches between monomeric and dimeric states depending on its nucleotide-bound state, and each conformation directs its interaction partner in the cell. This suggests a model where MipZ monomers are recruited to the cell pole by the chromosome segregation protein ParB (Kiekebusch et al., 2012). Then in the cell pole, ParB acts as a sink for freely diffusing MipZ monomers, raising their local concentration, which stimulates MipZ-ATP dimer formation. MipZ-ATP dimers are excluded from the cell pole and released into the cytoplasm where they bind nucleoid DNA with decreasing concentration as the distance to the pole increases. The intrinsic ATPase activity of MipZ eventually leads to dissociation of the dimer, generating monomers that detach from the DNA, undergo nucleotide exchange, and then restart the cycle, resulting in a concentration gradient on the nucleoid that diminishes towards mid-cell. ATP hydrolysis of the MipZ dimer on the nucleoid results in MipZ monomer formation and its release from the nucleoid into the cytoplasm where they are allowed faster diffusion and recapture by ParB at the cell pole. These repeated interactions and transitions between distinct stages, form a gradient of MipZ that regulates the formation of the Z-ring (Kiekebusch et al., 2012).

#### **1.5.3.1.3 PomXYZ complex**

More recently the characterization of another ParA-like protein was reported, PomZ, and its network constituents PomX and PomY, which form a complex on the

nucleoid that positively regulates Z-ring formation at mid-cell in *M. xanthus* (Schumacher et al., 2017; Treuner-Lange et al., 2013). This led to the proposed model of PomXYZ function which states that PomZ-ATP dimers bind the nucleoid where they diffuse rapidly. The diffusive flux of nucleoid bound PomZ into the PomXYZ cluster correlates with the amount of nucleoid on each side of the cluster. But when the cluster is asymmetrically localized on the nucleoid, the difference in PomZ flux into the cluster generates a concentration gradient across the cluster. This gradient has a concentration maximum on the side of the cluster that is positioned towards the largest nucleoid region. In consequence, interactions between PomXY and nucleoid bound PomZ results in biased random walk in the direction towards the largest nucleoid region and the highest PomZ diffusive flux. This ultimately results in the positioning of the PomXYZ cluster at mid-cell, where it in turn recruits FtsZ (Schumacher et al., 2017).

While the proteins mentioned so far participate in the segregation of genetic material and the regulation of cell division, it is well known that ParA-like ATPases display a wide diversity in their functions. For instance, the precise placement and segregation of carboxysomes in the cyanobacterium *Synechococcus elongates* PCC7942 is regulated by a ParA homologue, which locates over the nucleoid and oscillates from pole to pole (MacCready et al., 2018; Savage et al., 2010). Furthermore, PpfA and ParC, two ParA-like proteins, have been shown to mediate the intracellular localization of arrays in *R. sphaeroides* (Roberts et al., 2012) as well as *V. cholerae* and *V. parahaemolyticus* (Ringgaard et al., 2011), respectively.

### **1.5.3.2 PpfA-mediated localization of cytoplasmic arrays in *R. sphaeroides***

Positioning of chemosensory arrays in *R. sphaeroides* displays major complexity, this purple bacterium places its transmembrane arrays at the poles (Wadhams et al., 2005), while its cytoplasmic array, placed in the middle of the cell, is actively segregated by the activity of the ParA-like protein PpfA (Thompson et al., 2006).

PpfA segregates the cytoplasmic array during cell division. Specifically, it associates with TlpT, the major cytoplasmic chemoreceptor in *R. sphaeroides* (Figure 3A) (Wadhams et al., 2002, 2003, 2005). TlpT is known as the major cytoplasmic receptor because cells deleted of *tlpC*, the gene that encodes for TlpC (a minor cytoplasmic receptor), retain the capacity to form arrays. However, in the absence of *tlpT*, arrays no longer form (Jones & Armitage, 2017; Wadhams et al., 2002). Thereby, ensuring the proper location of TlpT is crucial for cytoplasmic array formation in *R. sphaeroides*.

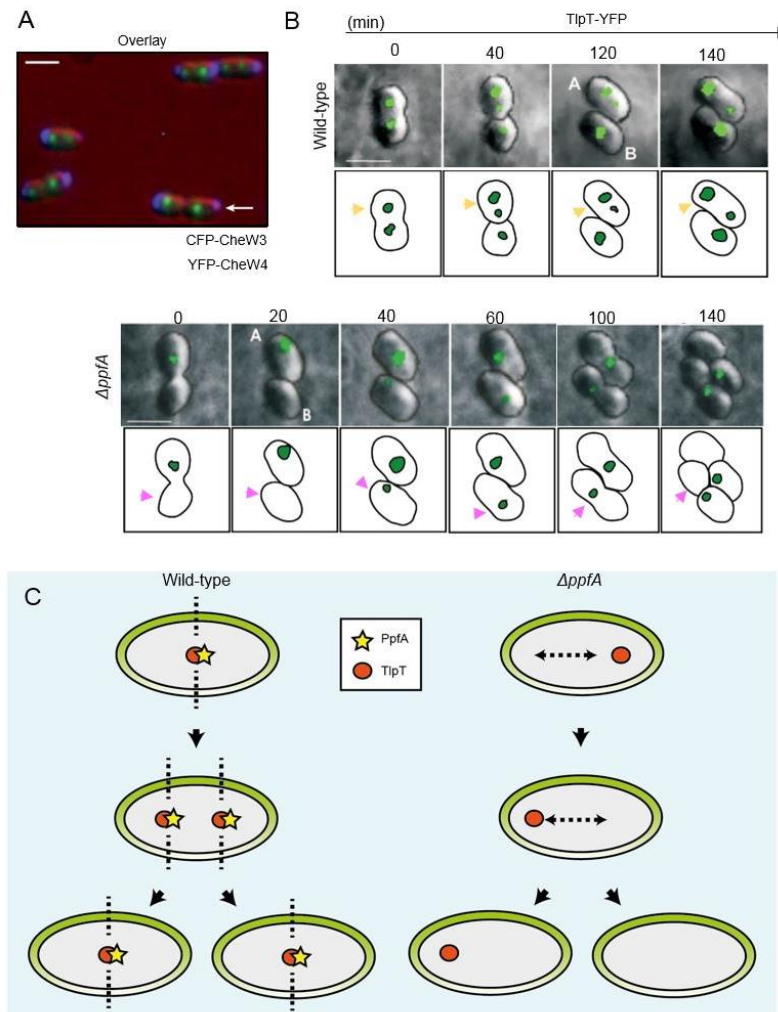


**Figure 12. Localization of chemosensory arrays in *R. sphaeroides*.** (A) There are cytoplasmic as well as polar arrays (white arrow). PpfA mediates localization of cytoplasmic arrays. (B) Time-lapse showing localization of receptor TipT-YFP in wild-type and  $\Delta ppfA$ . In wild-type arrays split into two and are kept at approximately 1/4 and 3/4 positions (yellow arrows) for their inheritance upon cell division. Without PpfA, arrays do not segregate, and cells do not inherit a cluster upon division (pink arrows). Therefore, cells take some time to create a new cluster, which fails to localize and segregate. (C) Schematic representation of the PpfA-mediated localization of cytoplasmic chemosensory arrays. Adapted from (Porter et al., 2011; Thompson et al., 2006). See main text for details.

The gene encoding for PpfA is located within the *CheOp3*, where the genes responsible for the majority of components of the cytoplasmic arrays, including *tipT*, are also located (Figure 3B). Fluorescently tagged TipT-YFP shows that in young cells there is one cluster in the cytoplasm at mid-cell, and as the cell grows, the single centered array splits into two, which prior to cell division become localized at one-quarter and three-quarter positions along the cell length (Figure 12) (Thompson et al., 2006). This localization pattern ensures that after division, both daughter cells inherit a complete set of chemotaxis proteins required for the assembly of cytoplasmic arrays (Mauriello et al., 2018). In a  $\Delta ppfA$  strain, clusters of TipT-YFP do not duplicate, and after completion of cell division one daughter cell does not inherit a cluster, and thus is non-chemotactic until

it forms a new cluster *de novo* (Roberts et al., 2012). Since it has been shown that without *ppfA* arrays still form, it is acknowledged that the main role of PpfA is mediating segregation and inheritance of cytoplasmic arrays (Roberts et al., 2012). However, recent evidence suggest that while it is not essential for arrays to form, PpfA has some influence in the time that *R. sphaeroides* takes to create a cytoplasmic array (Jones & Armitage, 2017). Through time-lapse experiments, it was shown that in the double deletion strain  $\Delta ppfA/ \Delta tlpT$ , arrays take more time to form upon induction of *tlpT* than in the single deletion of  $\Delta tlpT$ . Furthermore, the double mutant had on average less clusters than the single deletion mutant did. Additionally, it was reported that when cells were artificially elongated with cephalixin, the number of clusters increased as the cell length did in both strains,  $\Delta ppfA/ \Delta tlpT$  and  $\Delta tlpT$ . However, in long cells of the double mutant ( $\Delta ppfA/ \Delta tlpT$ ) the number of arrays in long cells was lower than in the single deletion ( $\Delta tlpT$ ) (Jones & Armitage, 2017). These observations led the authors to conclude that cytoplasmic array formation in *R. sphaeroides* might follow a stochastic assembly mechanism like in *E. coli* (Figure 10), where cell length determines the number of arrays that are formed, where PpfA not only is required for segregation and positioning of arrays, but also for their faster formation (Jones & Armitage, 2017).

Earlier studies showed that PpfA interacts with DNA non-specifically, and introducing amino acid substitutions in PpfA that prevented DNA binding hindered segregation of cytoplasmic clusters (Roberts et al., 2012). Similarly, it has been shown that segregation of arrays requires a 120 amino acids long region at the N-terminus of TlpT. This region is rich in basic residues, and thus it is speculated this particular stretch of TlpT acts as a ParB analogue to promote PpfA ATPase activity (Roberts et al., 2012). Nevertheless, it remains unknown how TlpT influences PpfA activity; similarly, it is unclear how PpfA splits the chemosensory cluster into two before cell division or even how PpfA access the arrays to mediate their positioning.

#### **1.5.4 Localization of chemosensory arrays in *Vibrio* spp.: the ParC/ParP system**

Another example of the influence of a ParA-like ATPase in the localization of chemotaxis arrays has also been seen in *V. cholerae* and *V. parahaemolyticus*. In these organisms, the protein ParC (for partitioning chemotaxis) mediates the polar localization and inheritance of chemosensory signaling arrays.

In *V. cholerae* and in *V. parahaemolyticus* swimming cells, the chemotaxis arrays are found exclusively at the cell poles (Figure 13A), and their placement depends on the proteins ParC and ParP, whose coordinated activities is described as the ParC/ParP



system. In *V. cholerae* only arrays formed by proteins encoded by genes in cluster II (Figure 4) are positioned by the ParC/ParP system, while cluster I and III arrays localize independently of this system. In recently divided cells, the chemotactic signaling arrays are located uni-polarly at the old flagellated cell pole (Figure 14–time lapse). As the cell cycle progresses, a second array is formed which is localized at the opposite cell pole, resulting in a bi-polar distribution. As a consequence, each daughter cell inherits an array at their respective old poles after completion of cell division.

The placement of the arrays to the cell pole is regulated by the ParA-like ATPase ParC and its partner protein ParP. Both *parC* and *parP* genes are part of the chemotaxis gene operon in *V. cholerae* (Figure 4) and in *V. parahaemolyticus* (Figure 5), where *parP* is always found immediately downstream of *parC*. In the absence of either *parC* or *parP*, arrays are not placed at the cell poles and are instead positioned randomly along the cell length. As a result, in the absence of either gene (*parC* or *parP*), bi-polar array localization is not established prior to cell division, and consequently only one daughter cell inherits an array upon division (Figure 13C). Even though the other daughter cell starts out without any chemotaxis array, a new array is, however, formed with a short delay after division, again at a random position along the cell length.

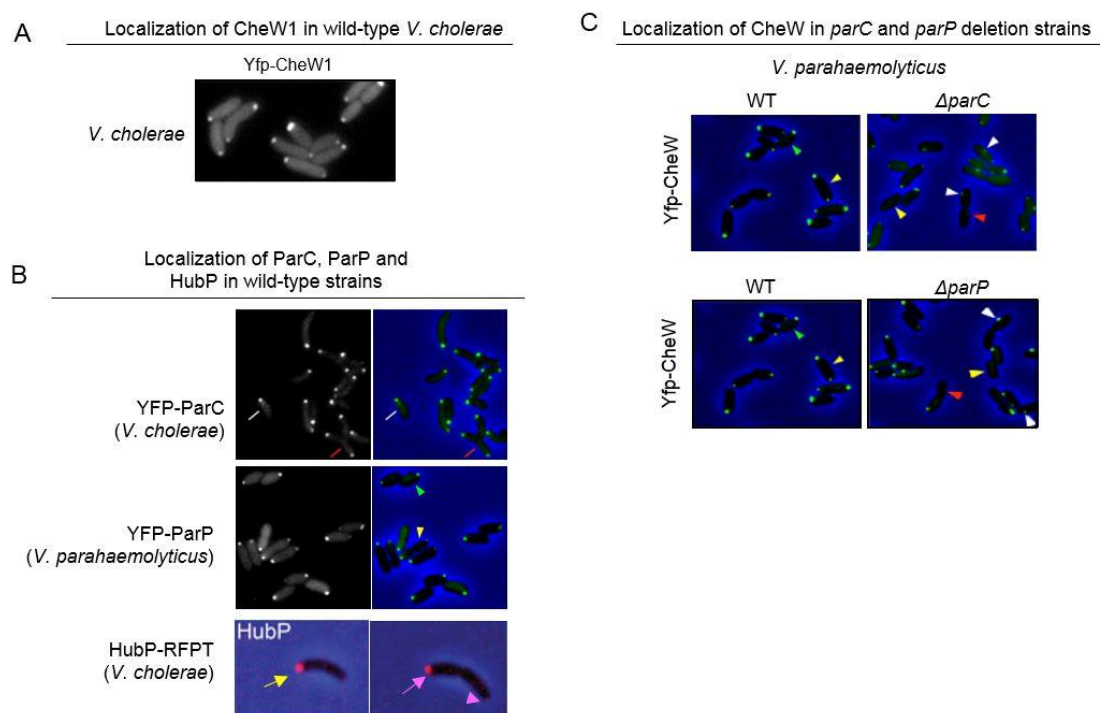


**Figure 13. Localization of proteins of the ParC/ParP system in *Vibrio cholerae* and *Vibrio parahaemolyticus*.** (A) Localization of chemosensory arrays represented by YFP-CheW1 in *V. cholerae* wild-type show a uni- and bi-polar distribution. (B) Localization of ParC, ParP and HubP. Similar to chemotaxis arrays, these proteins localize at the cell poles and are either bi-polar or uni-polar. (C) Chemotaxis arrays mislocalized in the absence of ParC and ParP. Images taken from (Galli et al., 2017; Ringgaard et al., 2011, 2014).

ParC and ParP themselves display a localization pattern similar to that of the chemotaxis arrays, this is uni-polarly at the old flagellated cell pole in young newborn cells, and bi-polarly later in the cell cycle (Figure 14B). Double labeling fluorescence microscopy in *V. parahaemolyticus* showed that localization of ParC and ParP to the new pole precedes that of the chemotaxis protein CheW. Moreover, in the same study it was shown that recruitment of ParP to the cell pole is dependent on ParC, and in its absence *parP* forms non-polar clusters that co-localize with chemotaxis arrays (Ringgaard et al., 2014).

In addition, polar localization of ParC is dependent on the marker of the cell pole HubP (Yamaichi *et al.*, 2012), which follows a similar localization pattern than ParC, ParP and the chemotaxis arrays (i.e. uni-polar in recently divided cells and bi-polar in longer cells) (Figure 13B) (Galli et al., 2017). In a  $\Delta hubP$  *V. cholerae* strain, ParC was mislocalized and formed non-polar clusters that co-localized with the chemotaxis arrays randomly along the cell length. However HubP and ParC did not show direct interaction, suggesting the existence of another partner of ParC allowing its interaction with HubP, ultimately directing ParC polar targeting (Yamaichi *et al.*, 2012).

ParP, on the other hand, has a CheW-like domain at the C-terminus, linked by a proline-rich region to the N-terminus of the protein that contains a highly conserved region of about 8 to 10 amino acids (Ringgaard *et al.*, 2014). Previously, the direct interaction between ParP and ParC was observed, and it was demonstrated that the conserved region at the N-terminus of ParP was essential to mediate ParP-ParC interaction. Hence, this protein region was termed the ParC interaction domain. Furthermore, it was demonstrated that ParP interacts with CheA specifically through the LID region (for localization and inheritance domain) of the kinase, and that ParP alone stabilizes CheA within the signaling arrays (Ringgaard *et al.*, 2014). Thus, positioning of the chemotactic arrays in the cell pole by the ParC/ ParP system relies on ParC's interaction with ParP (Ringgaard *et al.*, 2014). In this way, ParC positions ParP at the pole, while ParP in turn captures chemotaxis proteins at this site and prevents dissociation of the chemotaxis proteins from formed signaling arrays, resulting in their sequestration at the cell pole (Figure 14B). However, the mechanism behind ParC and ParP mediated localization of signaling arrays is not yet fully understood. To this end, available research pertinent to each component of the ParC/ParP system is summarized below.

#### 1.5.4.1 The ParA-like protein ParC

In the absence of *parC*, more than 25% of *V. cholerae* cells formed non-polar foci of chemotaxis proteins (Ringgaard et al., 2011), while that percentage has been reported to vary between the two different life styles of *V. parahaemolyticus* (swimming and swarmer cells). For *V. parahaemolyticus*, 25 to 30% in cells during the swimming stage (Heering & Ringgaard, 2016; Ringgaard et al., 2011) and up to 77% for cells in the swarming stage, formed non-polar chemotactic arrays (Heering & Ringgaard, 2016). Furthermore, it was also shown that a  $\Delta parC$  *V. cholerae* strain reverses swimming direction more than three times less frequently than the wild type, indicating a bias for straight swimming, which in turn correlates with this strain's ability to hypercolonize certain areas of the intestine in suckling mice (Ringgaard et al., 2011). Interestingly, ParC has no influence in the localization of proteins encoded by genes in the other two chemotaxis clusters (I and III) of *V. cholerae*'s genome (Figure 4) (Ringgaard et al., 2011).

Furthermore, ParC's localization pattern depends on its dynamic nature. Photoactivation fluorescence microscopy using ParC-PAmCherry revealed that recruitment of ParC to the new pole is the result of redistribution of ParC molecules from the old pole to the new pole. Additionally FRAP (fluorescence recovery after photobleaching) experiments showed that ParC undergoes a continuous cycle between the cell pole and the cytoplasm and that early in the cell cycle this exchange only occurs at the old pole. Based on these localization studies, a diffusion-and-capture model for ParC localization dynamics was proposed: early in the cell cycle ParC is recruited to HubP at the old cell pole via a HubP-dependent anchor that at this point in the cell cycle is exclusively found at this site. A continuous exchange of ParC between the cell pole and the cytoplasm ensures that there is a constant pool of cytosolic ParC at any given time. Then, later in the cell cycle HubP localizes to the new cell pole, making the HubP-dependent ParC anchor available at this site. ParC molecules from the cytoplasmic pool can then be captured at both poles. In consequence, a redistribution of ParC from the old to the new cell pole occurs. Eventually, equilibrium is reached, resulting in an equal distribution of ParC accumulating at both poles (Ringgaard et al., 2011).

The mechanism underlying ParC's cycle between its localization to the cell pole and the cytoplasm has not been characterized yet. However, it is at least partially regulated by ParC's ability to bind and hydrolyze ATP. ParC belongs to the superfamily of Walker-type ATPases, and ParCs from both *V. cholerae* and *V. parahaemolyticus* has weak intrinsic ATPase activity *in vitro*, reminiscent to that of ParA-type DNA partitioning proteins (Ringgaard et al., 2011). In the case of ParC, this cycle presumably directs a "diffusion and capture" mechanism that controls the exchange of protein between the

polar zone and the cytoplasm (Ringgaard et al., 2011). Interestingly, amino acid substitutions that are predicted to block ATP binding or block ATP hydrolysis result in non-functional ParC variants. Such cells are defective in recruitment of ParP and chemotaxis arrays to the cell poles. A ParC variant unable to bind ATP is diffusely localized in the cytoplasm, and a ParC that binds ATP but is defective for hydrolysis localizes to the cell pole in a uni- and bi-polar manner similar to wild-type ParC. Thus, the ParC mediated recruitment of chemotaxis arrays to the cell pole is an active process that requires ATP binding and hydrolysis. It is possible that ParC's ATP-cycle secures a constant turn-over of ParC at the cell pole, which ensures the presence of a constant cytoplasmic pool of ParC, needed for its immediate recruitment to the new cell pole once its polar anchor develops at this site.

Nonetheless, ParC does not have a known ParB-like partner similar to other ParA ATPases, and neither the dedicated ParA in *V. cholerae* (ParA1), nor FlhG (another polarly localized ParA-like in *V. cholerae*), influence ParC's localization or mediated placement of the chemosensory arrays (Ringgaard et al., 2011). Actually, other than disrupting its ATP binding or hydrolysis, the only case when ParC's localization and activity is affected, is in the absence of the polar determinant HubP (Yamaichi *et al.*, 2012). In the absence of *hubP*, 25 to 40% of cells display non-polar ParC foci. However, since direct interaction between ParC and HubP has not been documented, the hypothesis that there must be additional factors mediating ParC's localization still stands.

ParC proteins form an entire new family within the ATPases, separate from proteins that regulate chromosome and plasmid segregation, and a phylogenetic analysis revealed that ParC proteins are highly conserved among Vibrionacea and well conserved between other  $\gamma$ -proteobacteria (Ringgaard et al., 2011). Interestingly, all organisms with putative ParC's have polar flagella, which certainly offers a clue to the rationale behind ParC mediated localization of chemosensory arrays (Davis & Waldor, 2013; Ringgaard et al., 2011). Unlike *E. coli*, polarly flagellated organisms with ParC evolved to have an active rather than stochastic mechanism of array positioning that likely limits the diffusion of the response regulator CheY to the polar region, near enough to the flagellum. In an intriguing observation, a later study found that the placement of lateral clusters of chemotaxis proteins formed in *V. parahaemolyticus* long swarmer cells did not require ParC and rather, followed a stochastic process (Gestwicki et al., 2000; Heering & Ringgaard, 2016), indicating that *V. parahaemolyticus* may have two localization mechanisms of chemosensory arrays depending on its morphological state. However, more research is still needed to understand the role of ParC during differentiation, since the lack of ParC impaired swarming activity in soft-agar swarming plate assays (Heering & Ringgaard, 2016).

Notably, although ParC's cell cycle-dependent localization could be attributed to the need to segregate arrays in time before division and flagellum synthesis, it is not clear what regulates placement of arrays from proteins encoded by genes in clusters I and III in the case of *V. cholerae*. Similarly, the mechanism controlling ParC's own localization it is not yet fully understood.

#### 1.5.4.2 The coupling protein ParP

ParP is the only known protein to interact directly with ParC (Ringgaard et al., 2014). However, ParP itself also interacts with two components of the chemotaxis core unit, the histidine kinase CheA and the MCPs. ParP's role is to promote gradual retention of CheA and ParC at the cell pole while linking arrays to ParC for proper localization and inheritance (Alvarado et al., 2017; Ringgaard et al., 2014). Fluorescent microscopy experiments demonstrated that without *parP*, *V. parahaemolyticus* displayed similar defects as the  $\Delta parC$  mutant, including aberrant localization of fluorescent fusions of chemotaxis proteins, that is 25 to 30% of cells with non-polar foci and 25% with no foci altogether of YFP-CheW, YFP-CheA and mCherry-MCP. Additionally, in  $\Delta parP$  up to 50% of cells depicted biased forward swimming. Furthermore, FRAP microscopy showed that ParP was essential to prevent dissociation of CheA, since the fluorescent fusion YFP-CheA did not recover to wild-type levels in a  $\Delta parP$  background. Interestingly, ParC did not influence YFP-CheA recovery, indicating that its only contribution to chemotaxis is the placement of ParP (Ringgaard et al., 2014).

ParP's localization is similar to the chemosensory arrays, and as such, to ParC's (Figure 13B). Uni-polar foci are observed in newborn cells, and as the cell elongates ParP becomes bi-polar. ParC and ParP arrive at the new pole simultaneously, thus preceding the arrival of the arrays. Fluorescent fusions of YFP-ParP were observed to form non-polar clusters in approximately 25% of cells in the  $\Delta parC$  background, while 25% had no foci at all, confirming ParP's localization dependency on ParC (Ringgaard et al., 2014). Interestingly, in the  $\Delta parP$  *V. parahaemolyticus* dynamics of YFP-ParC was affected, this is the intensity of the fluorescent protein did not recover after photobleaching (Ringgaard et al., 2014). Additionally, it has been observed that ParC's ability to bind and hydrolyze ATP disrupted ParP's localization and rendered ParC variants with a decreased affinity for ParP in bacterial adenylate cyclase two-hybrid system (BACTH) assays (Ringgaard et al., 2014). Despite the evidence showing cooperativity between ParC and ParP, it is unknown if ParP has any effect on ParC's ATPase activity. Furthermore, the biased straight swimming phenotype of the  $\Delta parP$  strain suggest a decrease in CheY-P, inciting even more questions as to the exact nature

of ParP activity and its influence on the other components of the core unit of the chemotaxis apparatus.

#### 1.5.4.3 HubP marks the old pole

One of the most important components for the establishment of the cell pole in *Vibrios* is the pole-organizing protein HubP. First characterized in *Vibrio cholerae*, this protein earned its denomination as the polar hub because it directs the polar placement of three members of the ParA family involved in DNA segregation, chemotaxis and flagellum growth (Yamaichi *et al.*, 2012). It has also been shown that in *Shewanella putrefaciens* the ortholog of *V. cholerae* *hubP* mediates the polar recruitment of flagellar proteins (Rossmann *et al.*, 2015). More recently, it was observed that HubP coordinates its localization with ParB1 and *oriC1* in *V. cholerae* (Galli *et al.*, 2017), while another recent study reported that HubP also coordinates polar localization of a newly identified protein required for flagella number regulation in *Vibrio alginolyticus* (Inaba *et al.*, 2017).

In *V. cholerae* it was observed that HubP localizes at both cell poles while displaying a transient mid-cell localization before cell division (Yamaichi *et al.*, 2012). However, later experiments in the same bacterium revealed that only when overproduced, HubP is bi-polar, while a functional chromosomal insertion of HubP-sfGFP follows a localization pattern that more closely resembles ParC, ParP and the chemotaxis arrays. In newly divided cells HubP was predominantly found at the old pole, and as the cells grow, HubP adopts a bi-polar localization pattern, thus HubP is a marker of the old pole (Figure 13B) (Galli *et al.*, 2017). Similar localization of HubP was observed earlier in *S. putrefaciens* (Rossmann *et al.*, 2015), indicating that localization of HubP homologues of other organisms may follow this pattern. Additionally, fluorescent microscopy experiments revealed that HubP does not transition from the old to the new pole as a complex, suggesting that HubP dissociates and associates to migrate from the old to the new pole, ensuring that the same amount of protein is kept at each side (Galli *et al.*, 2017). This exchange between poles and equilibrium maintenance, was earlier seen in FRAP experiments of bi-polarly localized HubP-GFP in *V. cholerae*, where after bleaching one focus, the recovery occurred in less than three minutes with a concomitant decrease in the intensity of the non-bleached focus at the opposite pole (Yamaichi *et al.*, 2012). Similarly, this trend was also observed in *S. putrefaciens*, where the focus at the new pole of a chromosomal HubP-mCherry gained intensity over one generation time, until the intensity of both polar foci was the same (Rossmann *et al.*, 2015).

Furthermore, it was observed that HubP of *V. cholerae* arrives at mid-cell in the latest stages of the cell cycle, after the divisome is assembled and before septation (Galli

et al., 2017). Although it is unclear what mediates HubP's own placement at the cell pole, it has been noted that curvature of the cell is not required (Galli et al., 2017). Others have proposed the involvement of cell wall synthesis proteins (Davis & Waldor, 2013; Yamaichi et al., 2012), or proteins associated with later stages of cell division (Galli et al., 2017). While it was observed HubP-GFP localized mostly at the membrane of the heterologous system *E.coli* (Yamaichi et al., 2012), there is no substantial experimental evidence to support either theory.

In *V. cholerae* polar localization of ParA1, FlhG, and ParC is affected in the absence of *hubP* (Yamaichi et al., 2012). As a consequence, in the  $\Delta hubP$  strain *oriC1* (the replication origin of the larger chromosome in *V. cholerae*) does not target the cell pole, there are motility defects and the chemotaxis arrays are non-polar in a large fraction of the population (Yamaichi et al., 2012). YFP-ParA1 is mostly diffuse in all cells lacking *hubP*, while the localization pattern of ParB1-CFP resembles the one in a  $\Delta parA1$  strain, clearly indicating the importance of HubP in the localization of ParA1. Nonetheless, HubP does not show evident influence in the localization of ParA2 (important for segregation of the second chromosome) (Yamaichi et al., 2012), as this protein is normally diffused in wild-type *V. cholerae* (Fogel & Waldor, 2006). In *S. putrefaciens*, HubP is also important for the placement of *oriC* to the cell pole, in this organism the absence of *hubP* rendered mCherry-ParB foci at one-quarter and three-quarter positions, and did not manage to reach the pole (Rossmann et al., 2015). In *V. cholerae*, microscopy experiments and BACTH assays indicate that HubP directly interacts with ParA1, and at the same time that ParA1 dimerization inhibits its interaction with HubP (Yamaichi et al., 2012). This indicates that direct interaction between HubP and ParA1 is required for proper segregation.

Both FlhG and FlhF are known to mediate flagella localization, assembly and number in different organisms (Correa et al., 2005; Kusumoto et al., 2008). In *Vibrios* FlhG localizes as clusters in the cell poles as well as diffuse in the cytoplasm (Kusumoto et al., 2008; Yamaichi et al., 2012), and without *hubP* polar clusters do not form. Similar effects have been observed for FlhG in  $\Delta hubP$  *V. alginolyticus* (Takekawa et al., 2016) and *S. putrefaciens* (Rossmann et al., 2015). Furthermore, lack of HubP rendered a decrease of about 50% in the swimming diameter in soft agar of *V. cholerae* while *S. putrefaciens* swimming speed decreased from 52.7  $\mu\text{m/s}$  in wild type to 29.5  $\mu\text{m/s}$  for  $\Delta hubP$  (Rossmann et al., 2015). Similarly, in *V. cholerae* 6% of the population of  $\Delta hubP$  had an increase in the number of flagella, comparable with an 8% in the  $\Delta flgH$ . A similar phenotype was observed in *V. alginolyticus*, but here the amount of cells in a population of  $\Delta hubP$  with multiple flagella amounted to 55%, while 20% had no flagella at all

(Takekawa et al., 2016). The influence of HubP on FlhG is attributed to direct interaction, at least in *V. cholerae*, where heterologous expression of FlhG and HubP as well as BACTH assays indicated direct HubP-FlhG interaction (Yamaichi et al., 2012). However, in *V. alginolyticus* direct interaction between HubP and FlhG could not be resolved in pull-down or BACTH assays (Takekawa et al., 2016).

HubP also regulates proper localization of ParC. In a  $\Delta hubP$  *V. cholerae* strain, approximately 25% of cells have non-polar ParC clusters. This translates in an increase of cells with mislocalized chemosensory arrays, a phenotype also observed in *S. putrefaciens*  $\Delta hubP$  (Rossmann et al., 2015; Yamaichi et al., 2012). Nevertheless, while the influence of HubP on ParA1 and FlhG seem to be due to direct interaction, BACTH assays and microscopy experiments indicate that ParC and HubP do not interact (Yamaichi et al., 2012). Moreover, microscopy analyses revealed that HubP clusters lay farther apart from the ones formed by ParC, leading to the hypothesis that there are more interaction partners for ParC, which link it to HubP for its proper polar recruitment. Until today, there is no available information as to what this interaction partner or partners are.

Altogether, *Vibrio cholerae* and *Vibrio parahaemolyticus* follow a hierarchical mechanism for placement of chemotaxis arrays, where the marker of the old pole HubP, ensures polar placement of ParC through yet unknown proteins. In turn, ParC tethers ParP at the cell pole, which sequesters chemotaxis proteins, ultimately permitting their localization at the flagellated cell pole. Recently, the role of the ParC/ParP system was explored in the  $\gamma$ -proteobacterium *P. aeruginosa* (Reinhardt & Bardy, 2018). Like in *Vibrio* strains, ParC and ParP of *P. aeruginosa* interact with chemotaxis proteins, and in the absence of both genes, *parC* and *parP*, *P. aeruginosa* swimming motility decreases. However, there were some important differences, for instance, the authors noticed that clustering of CheA was only partially dependent on ParP, and interestingly, ParP also showed interaction with DipA, a protein involved in biofilm dispersal (Reinhardt & Bardy, 2018). This work, the first one to explore the role of the ParC/ParP system in another organism outside Vibrionacea, suggest that both proteins, ParC and ParP, have analogous roles among  $\gamma$ -proteobacteria, but their activity is likely involved in other physiological roles. Thereby, gathering more information about the mechanisms underlying the function of the system becomes relevant to understand how it could affect other cellular processes.



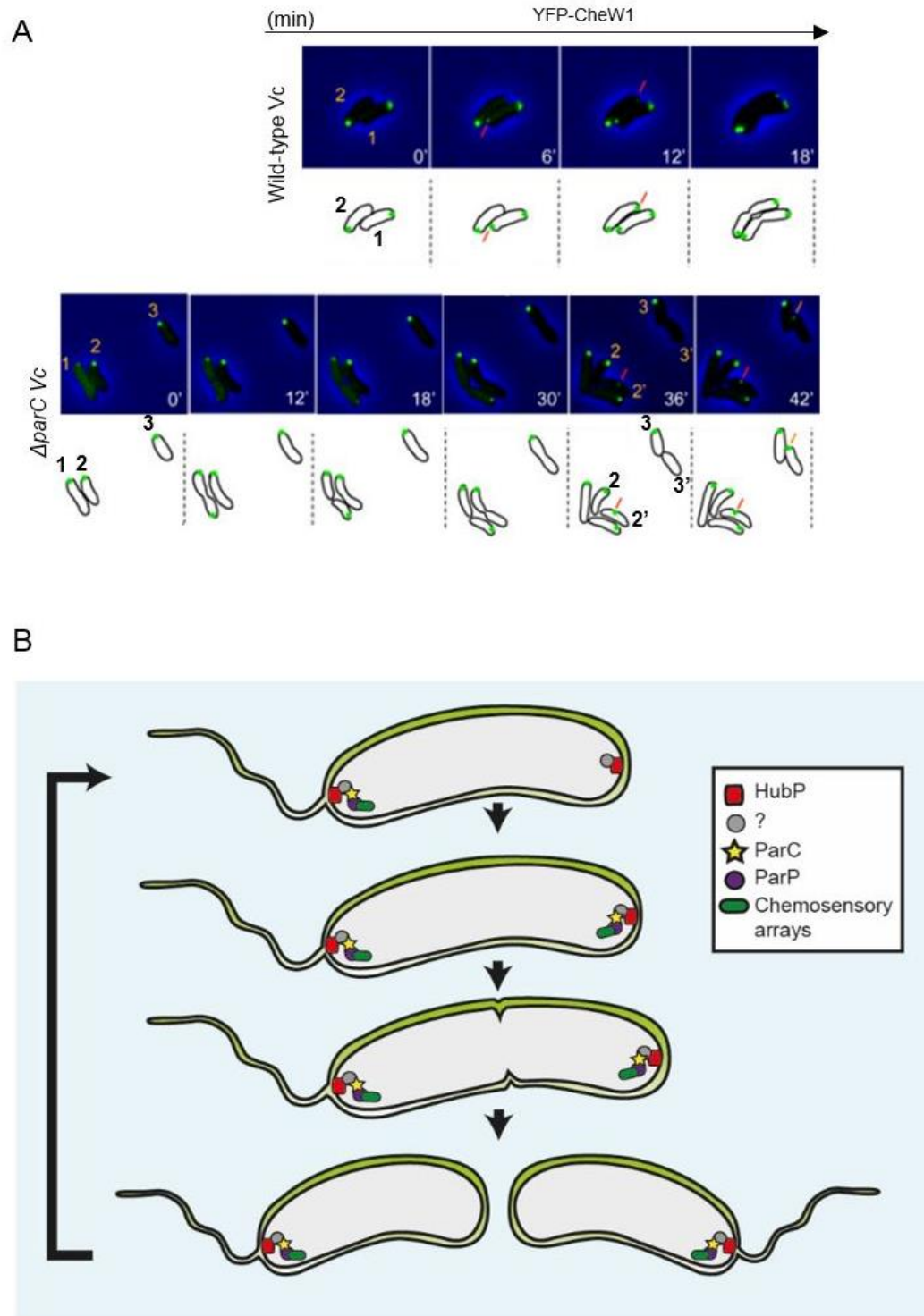


**Figure 14. The ParC/ParP system in *Vibrio* species.** (A) Time lapse showing localization of arrays represented by YFP-CheW1 in wild-type and  $\Delta parC$  *Vibrio cholerae* (Vc). Cells 1 and 2 in wild-type initiate with one polarly localized cluster, which later becomes bi-polar before cell division. The  $\Delta parC$  fail to inherit clusters (cell 2 and 3) or have off-pole clusters (cell 1). (B) Scheme depicting the hierarchical mechanism for the placement and segregation of chemotaxis arrays in *V. cholerae* and *V. parahaemolyticus*. Images taken and modified from (Ringgaard et al., 2011).

---

## CHAPTER 2: SCOPE

For several processes important for bacterial growth and survival, the ability to target proteins to specific cellular locations at the right time is essential. However, in most cases there is not a complete understanding of the mechanisms underlying intracellular spatiotemporal localization. Swimming motility and chemotaxis are some of these processes. In the case of the human pathogenic bacteria *V. cholerae* and *V. parahaemolyticus*, the presence of a polar flagellum permits swimming in liquid environments, and chemotaxis proteins allow the biased movement towards specific stimuli. The proteins responsible for the formation of chemotactic signaling arrays are located at the flagellated cell pole in both strains, and as the cell grows the arrays become bi-polar, and by the time the cell divide, each daughter inherits an array. Earlier research showed that the proteins ParC and ParP coordinate the placement and distribution of the chemotaxis arrays, and in their absence, arrays were no longer at the poles, thus daughter cells failed to acquire an array upon division. Consequently, deletion strains of *parC* and *parP* displayed swimming as well as chemotactic defects. Nonetheless, several questions remained open. Using *V. cholerae* and *V. parahaemolyticus* as model organisms, this work aims to analyze the molecular mechanisms by which the ParC/ParP participates in the formation and localization of chemotaxis signaling arrays.

Several studies prove that the chemotaxis arrays are formed by the complexing of MCPs with CheA, CheW and in some bacteria other scaffolding proteins. One of the most remarkable features of these arrays is their uniform structure, which in turn enables their sensitivity, cooperativity, signal gain and adaptation capabilities. Moreover, several microorganisms, including *V. cholerae* have more than one homologue of the *che* genes present in the model organism *E. coli* and form arrays with varied intracellular localization. In *V. cholerae* there are three operons (termed cluster I, II and III) of *che* genes, including three *cheA*, four *cheW* and four *cheV* genes. Proteins from cluster I form cytoplasmic arrays, while cluster II and III form transmembrane polar arrays. Interestingly, the ParP/ParC system only mediates positioning of arrays formed by proteins encoded by genes from cluster II.

In this work, we study (1) how ParP, the link between the arrays and ParC, access the chemotaxis arrays without affecting their structure. We explore the role of ParP in array formation, localization and segregation through fluorescence as well as cryo-electron microscopy (cryo-EM). Additionally, we look into the importance of the different CheA proteins in *V. cholerae* and try to understand (2) how they, as well as the different

coupling proteins, affect array stability and formation. Furthermore, considering previous works showing that ParC's ATP binding and hydrolysis influence its role in the positioning of chemosensory arrays in *V. cholerae*, we now look at (3) how ParC's ATP-dependent cycle affects ParC's own localization in *V. parahaemolyticus*. We employ fluorescence microscopy as well as single particle tracking photoactivation localization microscopy (sptPALM) in order to understand what drives ParC's cellular placement and how this process ultimately influences the localization of the chemotaxis arrays.

---

## CHAPTER 3: RESULTS

### 3.1 *PART I* - Coupling chemosensory array formation and localization

Chemotaxis proteins organize into large, highly ordered, chemotactic signaling arrays, which in *Vibrio* species are found at the cell poles. Proper localization of signaling arrays in these microorganisms is mediated by the ParC/ParP system. Previous studies show that ParP interaction with the LID domain of CheA2 prevents the dissociation of the kinase from the cell pole. Similarly, it is well known that ParP tethers arrays to the cell pole by interacting with ParC, and disruption of either interaction, namely ParP-CheA2 or ParP-ParC, results in defective recruitment of chemotaxis arrays to the cell poles (Ringgaard et al., 2011, 2014). However, the detailed mechanisms by which this protein interaction network governs the dynamic localization of the chemotaxis arrays remain to be elucidated. Notably, there is little knowledge of how factors that promote array positioning are able to access and guide localization of chemotaxis proteins. In particular, it is unclear how such factors integrate within the widely conserved structure of the arrays.

This work analyzes how ParP is able to gain access to the arrays and interact with the chemotaxis proteins that are present in the highly ordered structure of the arrays. Similarly, in this section we explore how ParP interaction network influences the polar placement of the chemotaxis arrays. Most data in this results' section was published earlier (Alvarado et al., 2017). Cryo-EM data shown here was obtained in collaboration with Prof. Ariane Briegel and Wen Yang from Leiden University, Netherlands.

Importantly, the data in this thesis refers specifically to arrays formed by proteins encoded by genes in the chemotaxis cluster II of *V. cholerae*'s genome (see Figure 4), and therefore when referring to genes or proteins in this organism the established nomenclature for proteins or genes from cluster II, although counterintuitive, will be used. For instance, proteins CheW1 and CheA2, quite contrary to what their designation suggest, are both components of arrays from cluster II (see Figure 4). When referring to proteins or genes from other organisms or not disambiguation is needed, simply "CheA" and "CheW" alone will be employed.

### 3.1.1 ParP contributes in the formation of chemotaxis signaling arrays

In order to understand how does ParP access the chemotaxis proteins within the arrays in *V. cholerae*, the localization of arrays was analyzed in wild-type,  $\Delta cheA2$  (the *cheA* gene from cluster II- see Figure 4),  $\Delta parP$  and the double mutant strain  $\Delta cheA2/\Delta parP$ . For these studies, a functional (Ringgaard et al., 2011) YFP-CheW1 fusion was used as a marker for array localization and formation. In wild-type cells the protein fusion YFP-CheW1 localized mainly in clusters at the cell poles (Figure 15A-C). In contrast, in  $\Delta parP$  strain, clusters were not recruited to the cell poles, but instead were mislocalized along the cell or completely absent in 74% of the population (Figure 15A-C). Meanwhile, in the absence of *cheA2*, YFP-CheW1 still formed clusters at the cell poles in a similar manner to that observed in the wild-type strain (Figure 15A-C), suggesting that formation of chemotaxis arrays does not require the presence of CheA2.

These data are further supported by cryo-EM studies where arrays that formed at the flagellated cell poles of different strains were quantified (Figure 16). In these experiments, chemotaxis arrays in  $\Delta cheA2$  were detectable and impossible to differentiate from arrays in wild-type, as in both cases the characteristic inner membrane-anchored MCPs and their corresponding cytoplasmic base plate were easily spotted (Figure 16). These data confirmed that indeed, arrays form in the absence of *cheA2*. Cryo-EM imaging revealed a 60% reduction in the number of cells with observable arrays in the  $\Delta cheA2$  background compared to wild-type – consistent with a role of CheA2 in stimulating array formation. Furthermore, the cryo-EM experiments revealed that ordered signaling arrays can still form in the absence of CheA2. In addition, these cryo-EM images (Figure 16) strongly suggest that the YFP-CheW1 clusters reflect the localization and formation of properly structured arrays in the absence of CheA2, although it is not possible to exclude the possibility that YFP-CheW1 clusters may reflect malformed or variant states of supramolecular complexes in some cells.

Meanwhile, in the double deletion  $\Delta cheA2/\Delta parP$ , YFP-CheW1 did not form clusters but was diffused in the cytoplasm (Figure 15A). Immunoblot analyses showed that these different localization patterns are not due to variations in expression level of the fusion proteins or cleavage of the YFP moiety from the YFP-CheW1 construct (Figure 15D). These data indicate that formation of signaling arrays is severely compromised in the absence of both ParP and CheA2. These data are further supported by cryo-EM analyses of the  $\Delta cheA2/\Delta parP$  strain, in which there was an 85% reduction in the number of cells with detectable signaling arrays compared to wild-type. Altogether, these

observations suggest that besides its previously known role in promoting the polar localization of arrays (Ringgaard et al., 2014), ParP also participates in array formation.

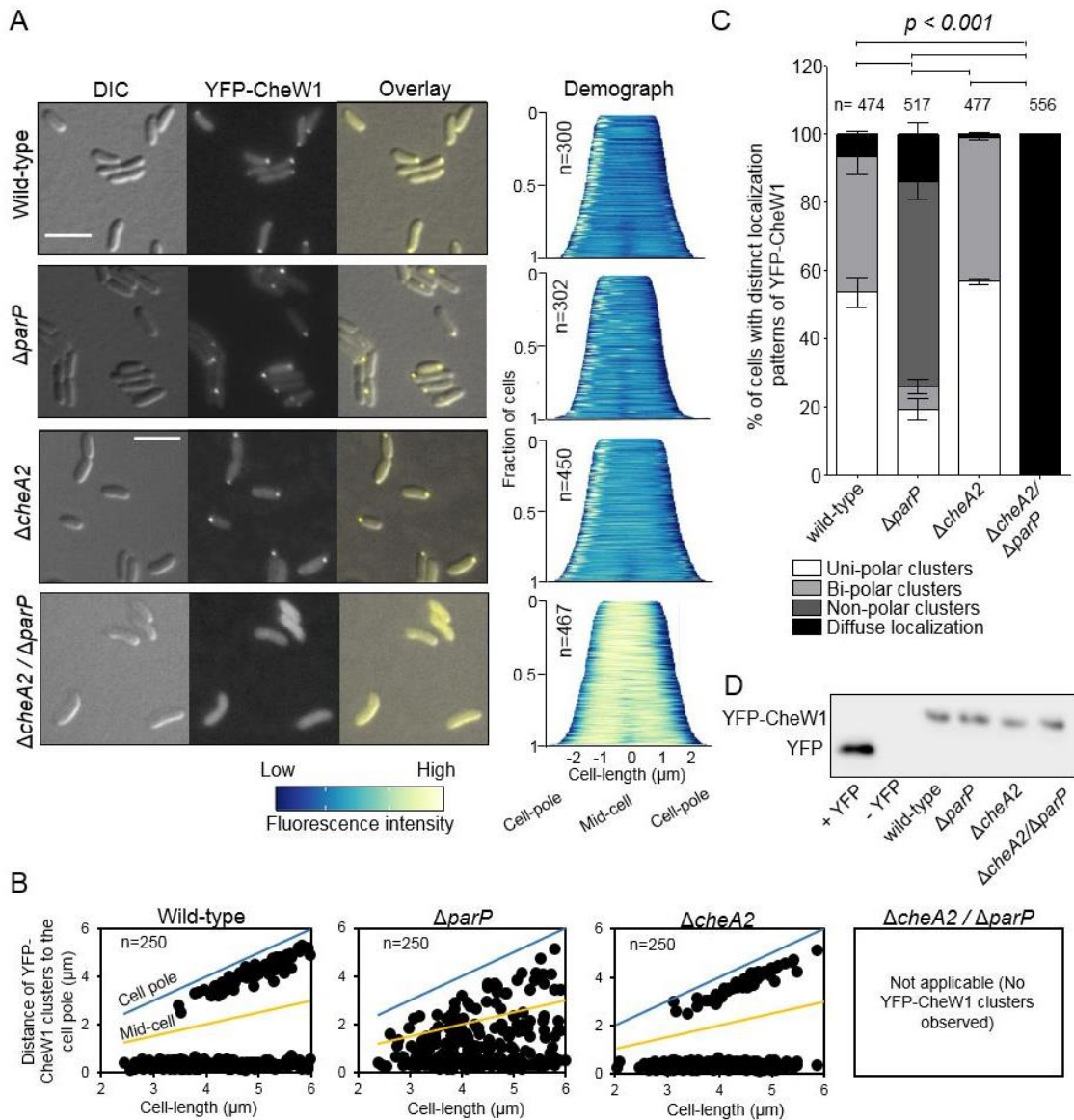


**Figure 15. ParP contributes to the formation of chemotaxis signaling arrays.** (A) Fluorescence microscopy showing the intracellular localization of YFP-CheW1 as a marker for array formation in *V. cholerae* wild-type and deletion backgrounds. Demographs show the fluorescence intensity of YFP-CheW1 along the cell length in the population. (B) Distance of YFP-CheW1 foci from the cell poles as a function of cell length. (C) Fraction of cells with distinct localization patterns. Error bars indicate standard error of the mean (SEM). (D) Immunoblot using JL8 anti-YFP antibodies to detect YFP-CheW1 in the indicated *V. cholerae* strains. As a positive control, a strain expressing YFP alone from plasmid pMF390 was included (+YFP). Similarly, a strain not expressing YFP, that is with plasmid pBAD33, was used as negative control (-YFP). The n-values indicate the total number of cells analyzed from three independent experiments. Scale bar is 5  $\mu m$ .

### 3.1.2 ParP interacts with the signaling domain of methyl-accepting-chemotaxis proteins

To gather more information about ParP's role in the formation of arrays, a genomic library screening based on the BACTH system was developed (Figure 17A). In this blue-and-white colony screen, *E. coli* was employed to use *parP* as bait against a chromosomal library from *V. cholerae* genome (Figure 17B). It is important to notice that *E. coli* lacks homologous of ParP and ParC, and thus it is likely that the identified candidate protein directly interacts with ParP. In this screening, one hundred blue colonies were selected and the candidate interacting partners were then identified by sequencing. Of the 100 sequenced plasmids, 95 corresponded to genes encoding MCP proteins; particularly they included 15 distinct MCPs (Figure 17C).

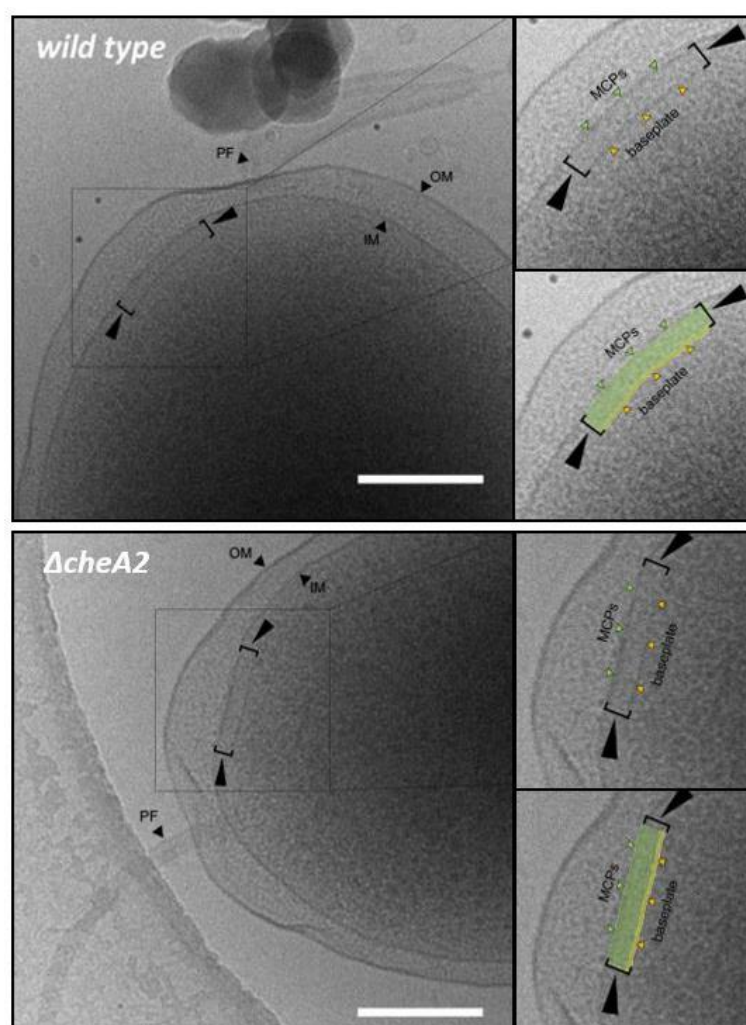


**Figure 16. Cryo-EM microscopy revealed the presence of chemotaxis arrays at the poles near the flagellum.** Images of the flagellated cell pole of wild-type and  $\Delta cheA2$  *V. cholerae* strains. Arrays are shown between brackets pointed by arrows. PF = polar flagellum; OM = outer membrane; IM = inner membrane. Green highlights MCPs and yellow the base plate. Scale bars are 200 nm.

While the fragments of all the *mcp* genes that were found in the screening covered varied regions, all hits included the region corresponding to the SD (signaling domain) of the MCPs (Figure 18). Therefore, we evaluated whether SDs, including the conserved interaction tip of four MCPs, were sufficient to mediate interactions with ParP. Interestingly, all four MCP signaling domains interacted with ParP (Figure 19A), confirming that MCPs are interaction partners of ParP, and that this interaction occurs via the MCP signaling domain. Additionally, no interaction between ParC and MCPs was observed (Figure 19A). Furthermore, although there was no interaction between the MCPs and CheA2, previous studies observed that interactions between these chemotaxis proteins are favored by the presence of all components of the core unit (Briegel et al., 2012, 2014b; Studdert & Parkinson, 2005). Accordingly, a three-hybrid assay when CheW1 was co-expressed along with CheA2 and the MCP VC1898, suggests that interaction between these three proteins takes place (Figure 19B).

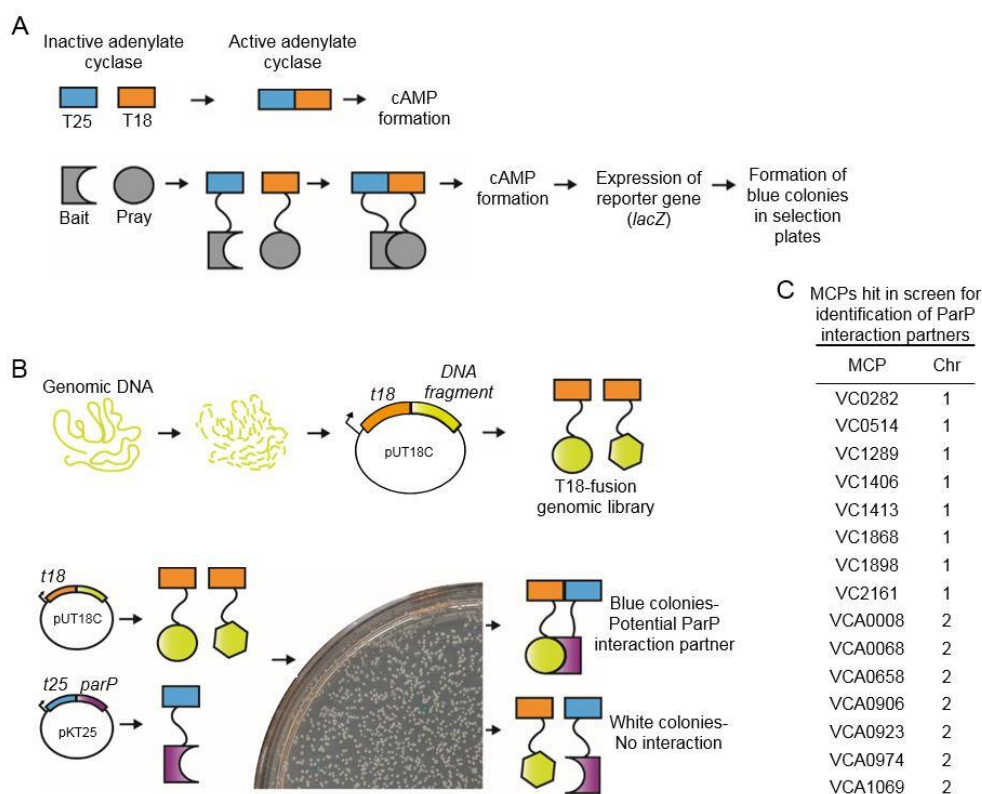


**Figure 17. Genomic library screening revealed MCPs as potential ParP interaction partners.** (A) Schematic depicting the principle behind bacterial two-hybrid based on adenylate cyclase reconstitution (BACTH) assay. (B) Schematic of genomic library screening using BACTH system with ParP as bait. (C) Summary of the MCP proteins identified as ParP interaction partners in the BACTH screen. Chromosome.

To further assay if ParP and the MCPs could interact independently of other chemotaxis proteins (Figure 19A), a co-expression assay was set up in an *E. coli* strain deleted of all native chemotaxis genes (strain VS269;



$\Delta cheR/\Delta cheB/\Delta cheW/\Delta cheA/\Delta cheY/\Delta cheZ/\Delta tar/\Delta tsr/\Delta tap$ ). In this background, functional fusions of YFP-ParP (Ringgaard et al., 2014) and mCherry-MCP-VC1898 (denoted mCherry-MCP) were assayed for their co-localization. When expressed alone, YFP-ParP was diffusely localized in the cytoplasm in the entire population, while mCherry-MCP localized as distinct clusters (Figure 20). Strikingly, when YFP-ParP was co-expressed along mCherry-MCP, YFP-ParP formed distinct clusters that always co-localized with mCherry-MCP (Figure 21A-B). These findings corroborated previous data, indicating that ParP is capable of associating with the MCPs. With this information, and considering previous evidence of the interaction between ParP and CheA2 (Ringgaard et al., 2014), we hypothesized that if ParP interacts with two components of the core unit, namely the kinase CheA2 and the MCPs, then it could form part of the core unit itself.

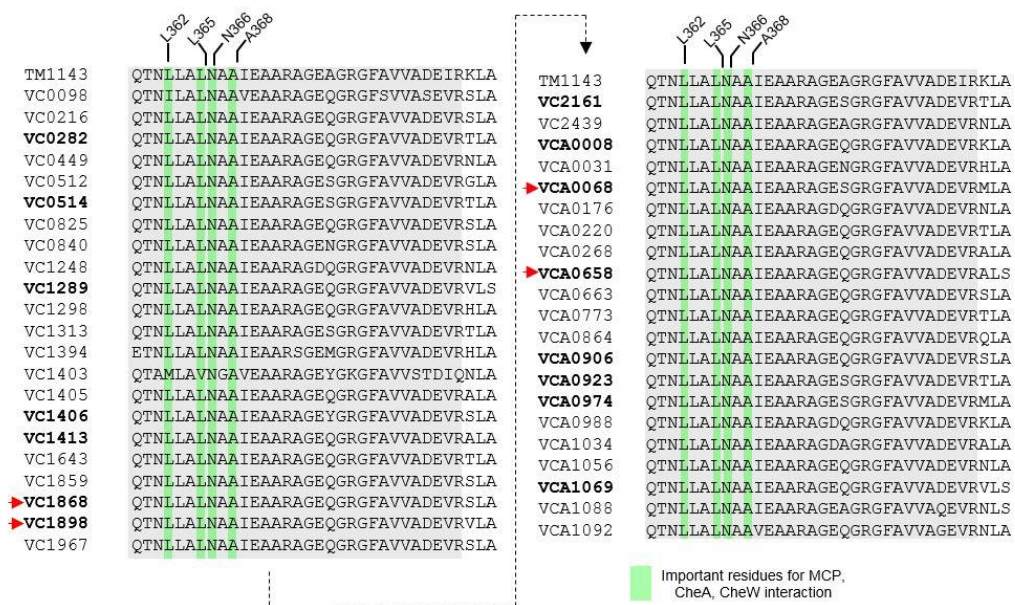


**Figure 18. The protein interaction tip of the MCPs is a highly conserved region.** Alignment of the protein interaction tip of all MCPs from *V. cholerae* against MCP TM1143 of *Thermotoga maritima* (Park et al., 2006). Gray area indicates a highly conserved region and in green are the residues known to be responsible for interaction with CheW and CheA-P5, i.e. L362, L365, N366 and A368 in TM1143 (Griswold et al., 2002; Kim et al., 1999; Li et al., 2011, 2013; Li & Hazelbauer, 2011). Bold letters indicate the MCPs of *V. cholerae* identified in the BACTH genomic library screening, red arrows point at the MCPs chosen for subsequent BACTH assays. Accession number of TM1143 is NP\_228949.1, accession numbers of all *V. cholerae* MCPs can be found in Table 12.

### 3.1.3 The MCP protein interaction tip mediates interaction with ParP

To test if indeed ParP forms part of the core unit, an analysis of the interaction between the MCPs and other proteins in the core was carried out. We took advantage of the fact that the tip of the MCPs is highly conserved, as previous studies have shown, this is the region responsible for MCP's interaction with CheW and CheA-P5 at the base

plate of the arrays (Briegel et al., 2012; Cassidy et al., 2015; Kim et al., 1999; Kremer et al., 1996; Li et al., 2011, 2013, 2007; Liu et al., 2012). Earlier studies of the protein TM1143, a MCP of *T. maritima*, identified those residues at the tip that are important to mediate MCP-CheW and MCP-CheA, namely L362, L365, N366 and A368 (Griswold et al., 2002; Kim et al., 1999; Li et al., 2011, 2013; Li & Hazelbauer, 2011). Multiple sequencing alignment between TM1143 and all putative MCPs of *V. cholerae*, revealed that these residues are conserved in all but two predicted MCPs of *V. cholerae*, including the ones identified in the genomic library screening (Figure 18). We then created amino acid substitution variants of *V. cholerae* MCP VC1898 (VC1898-L518R, L512R, N522R, A524R), to test their capabilities to associate with ParP. VC1898 was chosen precisely for its strong signal in previous assays for interaction with ParP (Figure 19A).

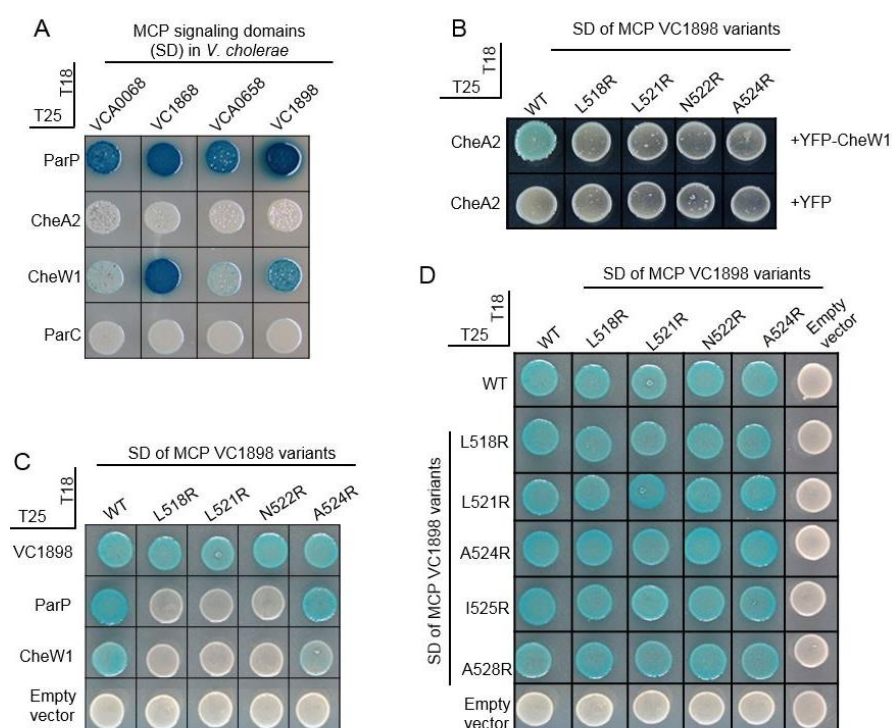


**Figure 19. ParP interacts with the protein interaction tip of MCP proteins.** BACTH experiments evaluating (A) interactions of *V. cholerae* MCP signaling domains of four different MCPs and ParP, CheA2, CheW1 and ParC; (B) Assay between the signaling domain of MCP VC1898, CheA2 and CheW1 in a bacterial three-hybrid set-up where plasmid containing YFP-CheW1 was also employed; (C) MCP VC1898 variants interaction with ParP and CheW1 and (D) self-interactions of MCP VC1898 variants. Blue colonies indicate a positive interaction.

Results showed that three of the four substitutions (L518R, L512R and N522R) disrupted VC1898 capacity to interact with ParP but not with itself (Figure 19C). Interestingly, the same substitutions also abolished VC1898 interaction with CheW1. Since all VC1898 variants retained their ability to self-interact (Figure 19D), the effect on their interactions with CheW1 and ParP is likely not due to decreased expression levels. Notably, YFP-ParP no longer formed foci co-localizing with mCherry-MCP-L518R, but

instead localized diffusely in the cytoplasm in 95% of cells, indicating that the L518R substitution abrogates the capacity of YFP-ParP and mCherry-MCP to interact (Figure 21A-B). Altogether, these observations suggest that ParP targets the same residues on the MCPs that are required for MCP-CheW and MCP-CheA interactions, thus lending support to the idea that ParP is a component of the chemotaxis core unit of signaling arrays.

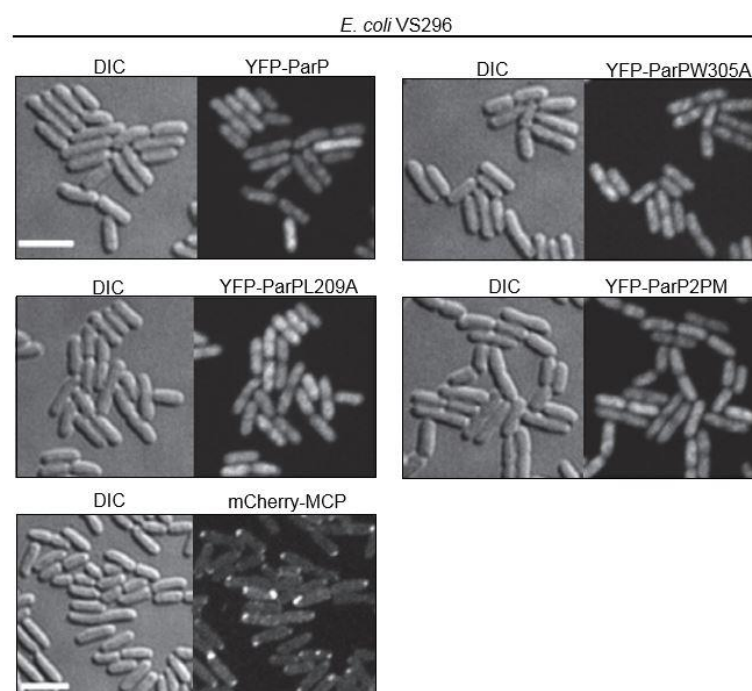


**Figure 20. YFP-ParP is diffusely localized in the cytoplasm of *E. coli*.** Fluorescence microscopy of YFP-ParP variants and mCherry-MCP (mCherry-VC1898) in *E. coli* strain VS269. Scale bars are 5  $\mu$ m.

### 3.1.4 A conserved hydrophobic pocket within the AIF domain of ParP mediates interaction with MCP signaling domains

Besides the evidence of ParP's ability to interact with two components of the core, i.e. CheA2 (Ringgaard et al., 2014) and the MCPs (Figure 21 and Figure 19), another important observation driving the hypothesis of ParP being part of the array, was the presence of a predicted CheW-like domain at the C-terminal end of ParP. This region is highly conserved among ParPs (Figure 22), it is approximately 135 amino acids long and hereafter it will be referred to as the *AIF domain* (for array integration and formation).

The AIF domain has a predicted similar architecture to that of CheWs and the P5 domains of CheA proteins. Nevertheless, ParP-AIF domains form their own distinct clade; separate from the P5 domains and CheWs (Figure 23A). CheA-P5 and CheW are each composed of two subdomains (1 and 2), and the junction between the two

subdomains contains branched hydrophobic residues that form a groove mediating interaction with the MCP interaction tip of the signaling domain (in CheW from *T. maritima* MSB8: L14, V27, I30, V33; Figure 23B, red residues) (Briegel et al., 2012; Griswold et al., 2002; Li et al., 2013; Park et al., 2006).

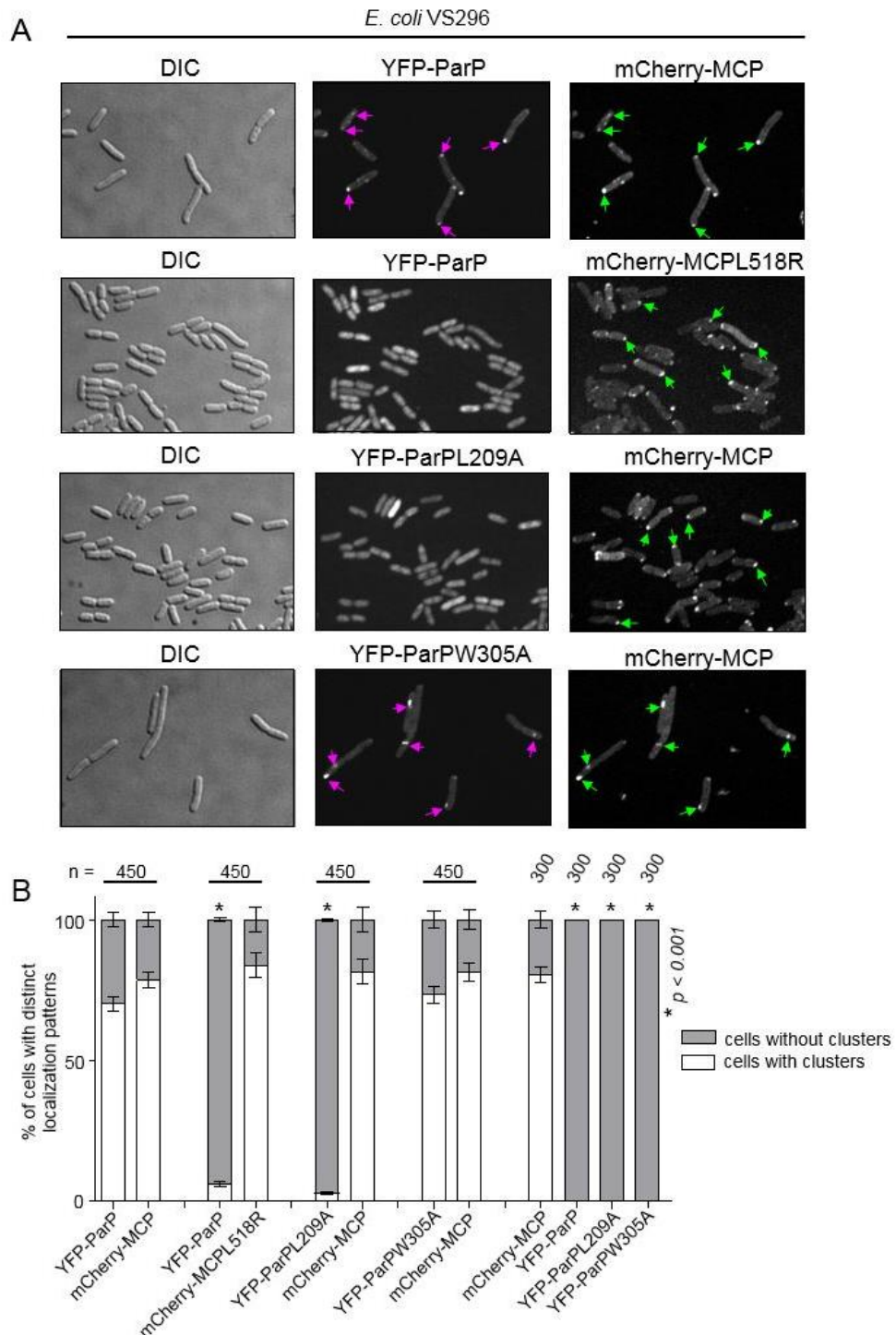


**Figure 21. YFP-ParP forms clusters when co-expressed with mCherry-MCP in *E. coli*.** Fluorescence microscopy of YFP-ParP variants and mCherry-MCP (mCherry-VC1898) in *E. coli* strain VS269. Error bars indicate SEM. The n-values depict the total number of cells analyzed in three independent experiments. Asterisks indicate  $p < 0.001$  compared to VS269 co-expressing YFP-ParP and mCherry-MCP. Purple arrows indicate clusters of YFP-ParP and its variants while green arrows indicate clusters formed by mCherry-MCP derivatives.

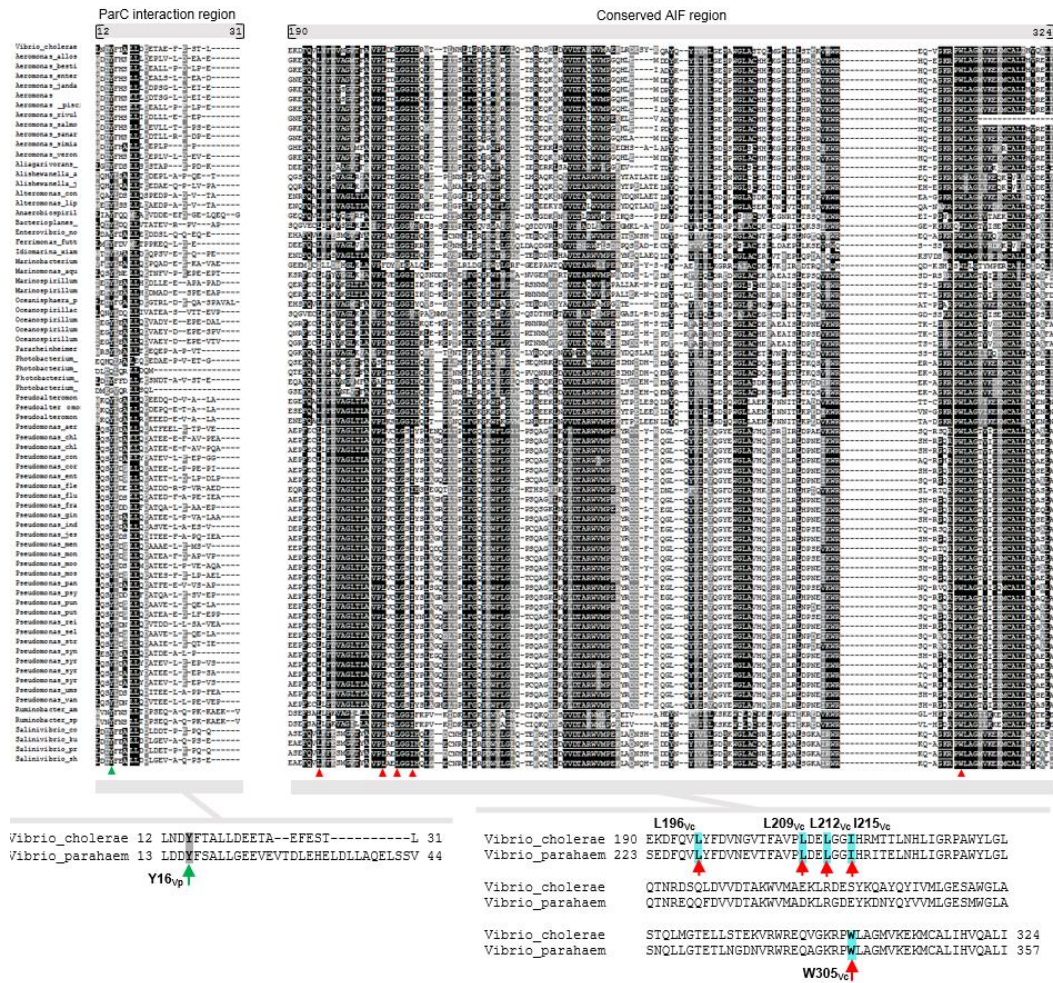


**Figure 22. The AIF domain is a conserved region in ParP proteins.** Multiple sequence alignment of ParP's of several organisms (for names and accession numbers see Table 13) against CheW of *T. maritima* (accession number AHD17545.1). Above the alignment, the length of the two ParP regions is shown between parentheses based on *V. cholerae*'s ParP amino acid sequence. Dark and gray highlight indicate high degree of conservation. Alignment between *V. cholerae* and *V. parahaemolyticus* ParP sequences is shown below. Blue highlight and red arrows point at residues in the AIF region selected for replacement in subsequent experiments. Green arrow indicates residue shown in an early study to be important for ParP-ParC interaction (Ringgaard et al., 2014).

Since the AIF domain of ParP shares similarities with CheW and the P5 domain of CheA proteins (Figure 23A), likewise the corresponding hydrophobic amino acids between the putative subdomains of the AIF region (L196, L209, L212 and I215; Figure 23B, white residues), may promote ParP's interaction with the MCPs. To evaluate this premise, several ParP variants were created by substituting those residues in the AIF region with alanine and then, their ability to interact with the signaling domain of MCP VC1898 was tested. Candidate residues in the AIF domain were chosen based on an alignment of the AIF region of *V. cholerae* against CheW of *T. maritima* (Figure 23C).

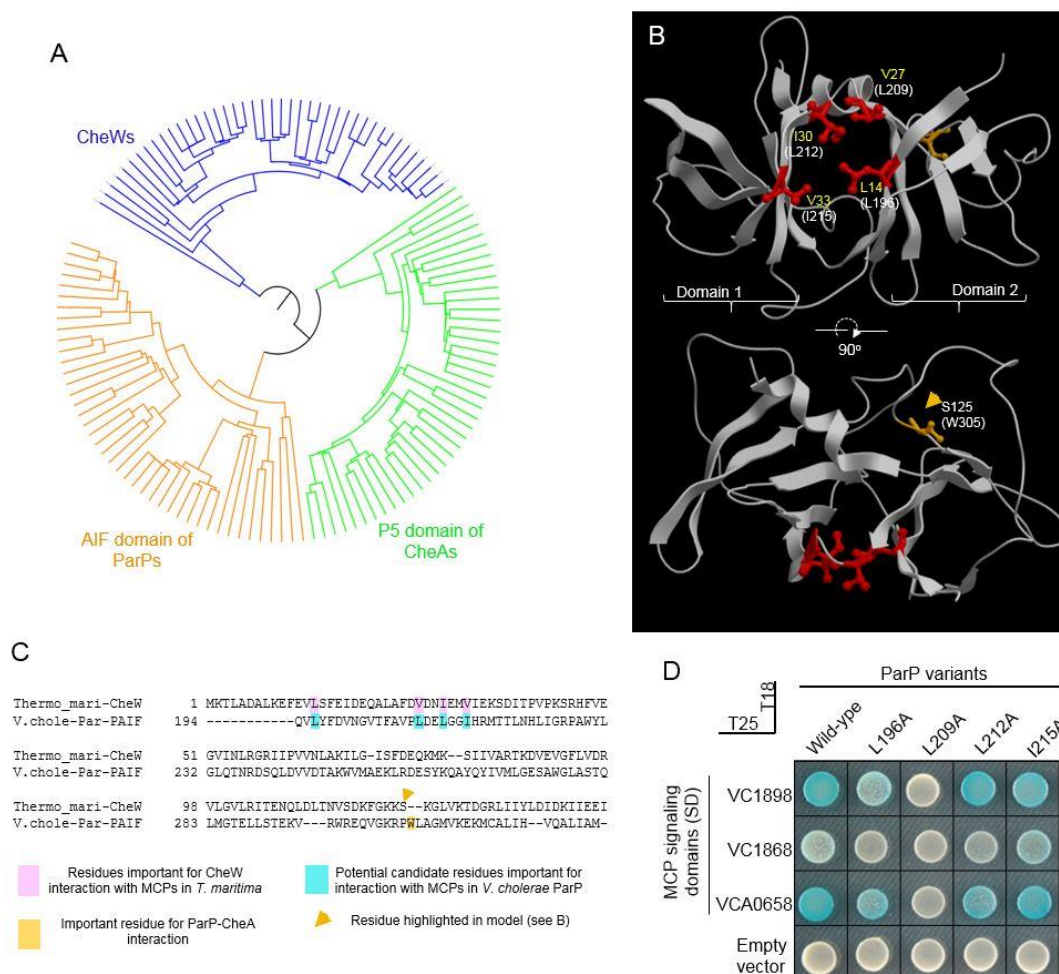


**Figure 23. AIF domains form their own distinct clade.** (A) Phylogenetic tree of CheWs, ParP-AIF and CheA-P5 protein domains (for details see

Table 14). (B) Structure of *T. maritima* MSB8 CheW under PDB 3UR1 (Griswold et al., 2002). Branched hydrophobic residues between subdomains 1 and 2 are highlighted in red. The corresponding amino acids in ParP-AIF of *V. cholerae* are noted between parentheses. Amino acid S125 is shown in orange. (C) Alignment between *T. maritima* MSB8 CheW and ParP-AIF region of *V. cholerae*, amino acid S125 corresponds to the position of W305 in ParP-AIF (orange square and arrow). Other important residues are highlighted accordingly. (D) BACTH assay testing interaction between ParP variants with amino acid substitutions in the predicted MCP binding pocket and MCP proteins VC1898, VC1868 and VCA0658.

ParP-L196A, L209A, L212A and I215A showed a slight decrease in their ability to interact with the MCP signaling domains (Figure 23D), suggesting that residues in the AIF putative interaction groove mediate ParP interaction with the MCPs, much similar to the way in which CheW and the P5 domain interact with the MCPs. It is important to notice that this BACTH assay rendered a ParP variant whose interaction with MCPs seemed greatly affected (ParPL209A, Figure 23D). This suggests that ParP-L209A is impaired in its interaction with the MCPs. Additionally, the co-expression assays in the *E. coli* strain deleted of *che* genes supported these observations, because YFP-

ParPL209A did not co-localized with mCherry-MCP clusters and was instead diffused in the cytoplasm (Figure 21). Thus, ParP appears to rely on analogous residues to CheW and the P5 domain to interact with MCPs. Interestingly, the studied residues on ParP-AIF (L196, L209, L212 and I215) are extremely conserved (Figure 22) among ParP proteins, suggesting that ParPs in other organisms also interact with MCPs, and possibly their AIF domains associate with arrays employing similar contacts.

### 3.1.5 Distinct ParP interfaces mediate its interaction with MCPs and CheA2

Earlier, it was shown that a single amino acid in ParP of *V. parahaemolyticus* was critical for ParP-CheA interaction (Ringgaard et al., 2014). The corresponding amino acid in *V. cholerae* ParP is W305, and it can be found within the AIF domain (Figure 22 and Figure 23B-C). Similarly to previous observation, ParPW305A did not interact with CheA2 of *V. cholerae*, but it showed interaction with the MCPs in BACTH assays (Figure 24A) or in co-expression assays in *E. coli* (Figure 21). Conversely, although ParPL209A did not interact with MCPs, it was still capable of interacting with CheA2 (Figure 24A). A ParP variant with both substitutions (ParPL209A-W305A, denoted henceforth ParP2PM) did not interact with either CheA2 or the MCP SD (Figure 24A). Neither variant, single substitutions nor combined, impaired ParP's ability to interact with ParC (Figure 24A), indicating that the effect of each substitution on ParP-MCP and ParP-CheA2 interactions are not likely explained by the variants decreased expression.

Previously, ParP-ParC interaction was attributed to a region located at the N-terminus of ParP, described as the ParC interaction domain (Ringgaard et al., 2014). This region consists of a stretch of about 10 amino acids and is linked to the AIF domain by a variable region (Figure 22) (Ringgaard et al., 2014). Based on the similarity between ParP and CheW of *T. maritima* MSB8, residues L209 and W305 are predicted to be on opposite sides of the AIF domain (Figure 23B-C), supporting the claim that ParP-AIF contains distinct interfaces that direct interactions with CheA2 and MCPs. Since ParP's N-terminus mediates interaction with ParC (Ringgaard et al., 2014), ParP has now at least three distinct interaction interfaces (Figure 24B and Figure 22). Furthermore, self-interaction of ParP was observed in BACTH assays (Figure 24C), suggesting that ParP has the capacity to interconnect arrays. These interfaces potentially allow ParP to simultaneously couple two signaling components, namely CheA2 and the MCPs, to the polar determinant ParC (Figure 24D). Therefore, ParP is an important component for both, the chemotactic machinery as well as the system responsible for cell pole development.

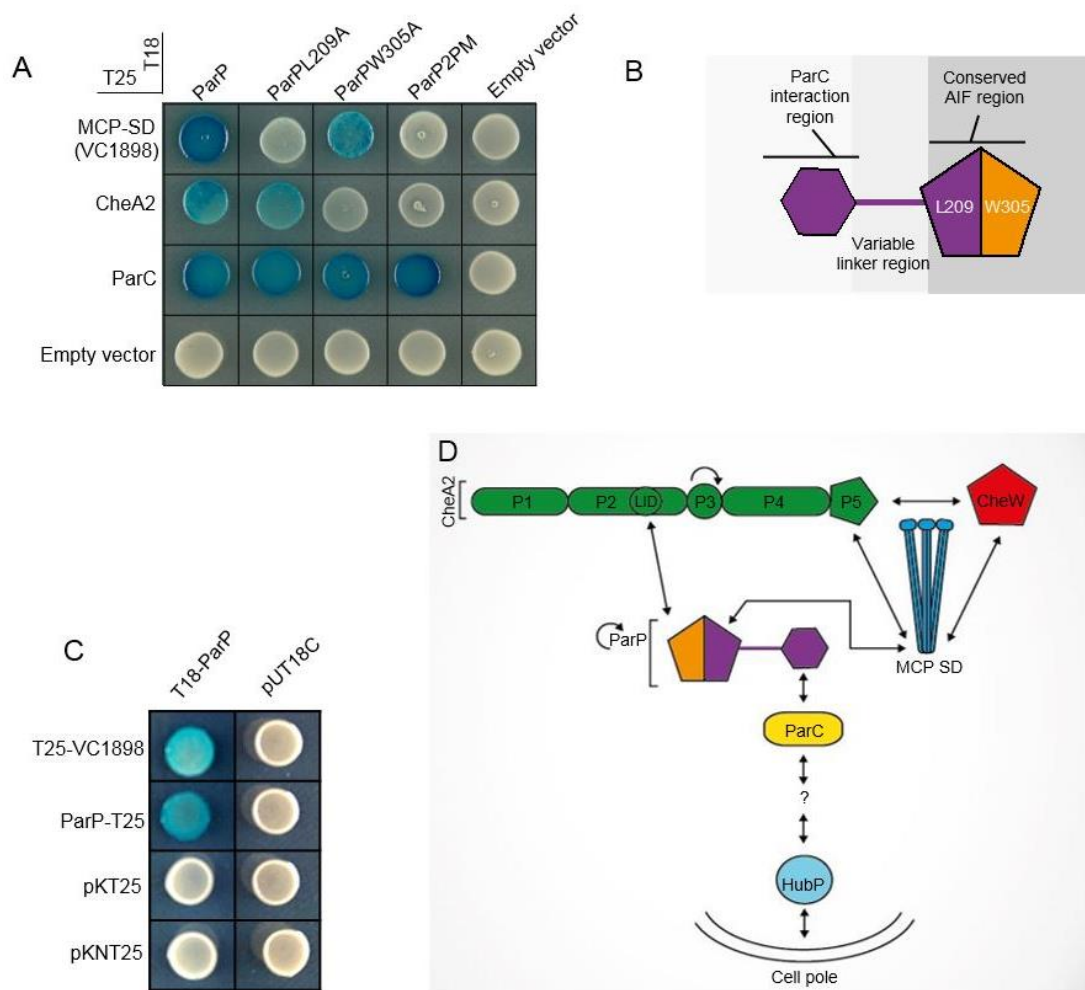


**Figure 24. Two distinct interfaces of ParP-AIF mediate its interaction with MCP and CheA2.** (A) BACTH experiment assaying for interaction between ParP variants and MCP VC1898, CheA2 and ParC. (B) Scheme of ParP's architecture. There are two conserved domains in ParP, the ParC interaction region and the AIF region, the latter contains two interfaces important for ParP interactions with MCP and CheA2. Amino acids L209 and W305 refer to the residues important for ParP-MCP and ParP-CheA2 interactions, respectively. (C) BACTH experiment showing ParP's self-interaction. (D) Schematic depicting ParP's interactions. ParP2PM = ParP with substitutions L209A and W305A. LID = localization and inheritance domain of CheA2. Question mark indicates the still unknown protein or proteins that mediate interaction between HubP and ParC.

### 3.1.6 Interaction with MCPs or CheA2 is required for association of ParP with the chemotaxis signaling arrays

We monitored localization of YFP-ParP and its variants (YFP-ParPL209A, YFP-ParPW305A and YFP-ParP2PM) co-expressed with CFP-CheW1 (a marker of array formation), to address whether ParP interactions with MCPs and/or CheA2 are required for its capacity to associate with signaling arrays. These experiments were done in *V. cholerae*  $\Delta parC$  strain to investigate ParP's association with the arrays without affecting its interaction with ParC. In about 75% of cells, YFP-ParP and CFP-CheW1 formed co-



localized clusters (Figure 25A-B). Meanwhile, for both YFP-ParPL209A and YFP-ParPW305A, between 50 to 55% cells, co-localized with CFP-CheW1 (Figure 25A-B). Thus, we could infer that both interactions provide to ParP the ability to associate with the chemosensory arrays, but likely keeping both interactions (ParP-MCP and ParP-CheA2) enhances ParP's capacity to associate with the arrays. In striking contrast, when YFP-ParP2PM, the variant carrying both substitutions (L209A and W305A), was produced, almost no clusters were observed, despite the presence of CFP-CheW1 clusters in about 55% of the population (Figure 25A-B). These results suggest that ParP's association with the chemotaxis arrays is fully dependent on its interactions with CheA2 and the MCPs. Furthermore, consistent with a function for ParP in stimulating array formation via its interactions with MCPs and CheA2, there was a significant drop from approximately 75% of wild-type cells with YFP-CheW1 clusters, compared to only 50 to 55% in cells expressing either the ParPL209A, ParPW305A or ParP2PM variants (Figure 25B).

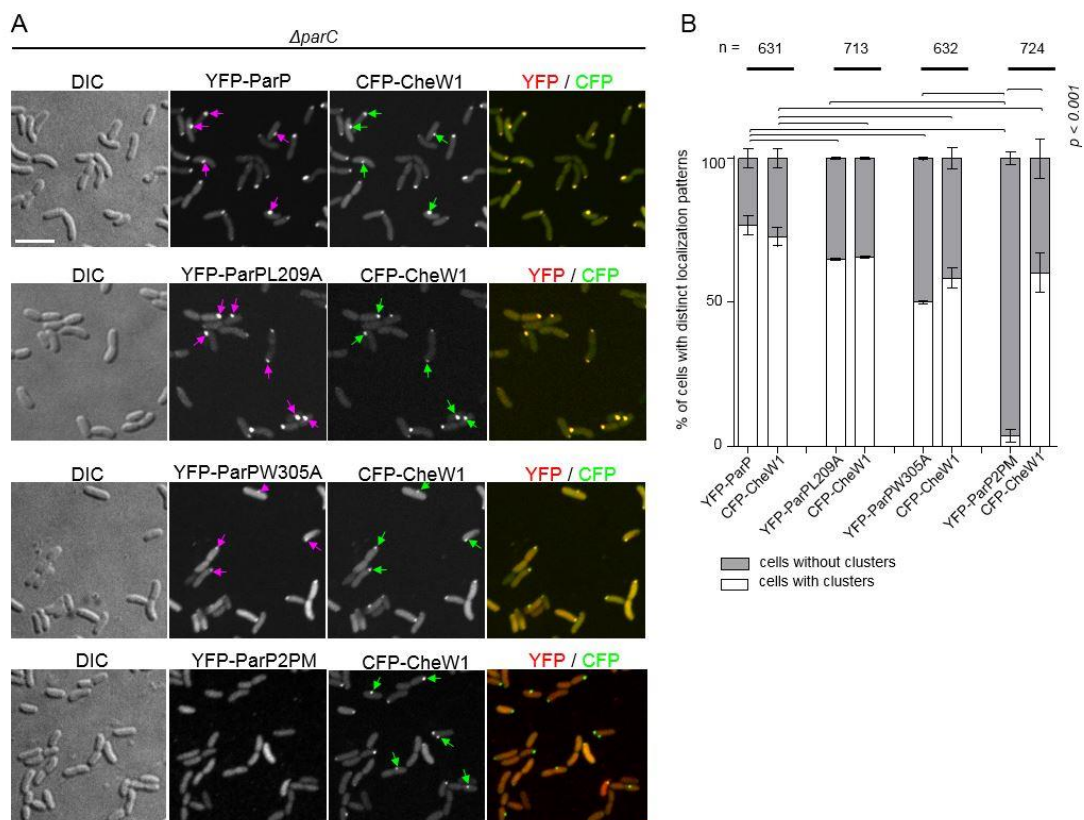


**Figure 25. ParP's interactions with CheA2 and MCPs favor array formation.** (A) Fluorescence microscopy of *V. cholerae*  $\Delta parC$  strain showing the localization of YFP-ParP and its variants along with CFP-CheW1. Purple arrows indicate clusters of YFP-ParP and green arrows point at clusters of CFP-CheW1. Scale bar is 5  $\mu$ m. (B) Bar graph indicate percentages of cells with and without clusters for each protein fusion. Error bars indicate SEM. The n-value shows the total number of cells included in the analyses obtained from three independent experiments. ParP2PM = ParP with substitutions L209A and W305A.

### 3.1.7 The AIF domain of ParP is responsible for promoting signaling array formation

Our data indicate that at least one protein, ParP or CheA2, is required for array formation. Consistent with this idea, in the absence of both *cheA2* and *parP*, chemotaxis clusters (visualized by YFP-CheW1) did not form (Figure 15). However, this was also true when only the region corresponding to the ParP-AIF domain was absent (*parP-ΔAIF/ΔcheA2*) (Figure 26 A-C). Additionally, a strain where ParP is incapable of integrating into the arrays was impaired in its capacity to stimulate array formation in the absence of *cheA2* (*parP2PM/ΔcheA2*) (Figure 26A-C). These experiments agree with the notion that the AIF domain of ParP participates in array formation, in resemblance of the role of CheA2-P5.

We also investigated which domain of CheA2 is needed for its recruitment into signaling arrays, and found that the P5 domain is both required and sufficient (Figure 26D). Furthermore, absence of the P5 domain alone (*cheA2-ΔP5*) did not affect array formation or localization when ParP was present (Figure 26A-C). However, when *parP* was absent (*ΔparP/ cheA2-ΔP5*) YFP-CheW1 was diffused, and thus chemotaxis clusters did not form (Figure 26A-C). Additionally, immunoblot analyses showed that diffuse localization of YFP-CheW1 is not a result of cleavage of the YFP moiety (Figure 26E). Taken together, these data indicate that CheA2 stimulates array formation via its P5 domain, and importantly that the AIF domain of ParP promotes formation of signaling arrays via its interactions with MCPs and CheA2.

### 3.1.8 ParP's N-terminal ParC interaction domain couples array localization and formation

If ParP enables polar localization of chemotaxis clusters by integrating into the core chemotaxis unit, we reasoned that a fusion of ParP's ParC-interaction domain to a different integral component of the core unit might also be capable of recruiting the chemotaxis clusters to the pole. To test this hypothesis, we constructed a ParP variant in which the AIF domain was replaced by the CheA2-P5 domain in a *ΔcheA2* background (*parP-P5/ΔcheA2*), and then we evaluated array localization using YFP-CheW1 (Figure 26B-C). In striking contrast with the double deletion *ΔcheA2/ΔparP* where no YFP-CheW1 clusters formed, the presence of ParP-P5 restored localization of uni- and bi-polar clusters in 65% of cells (Figure 26C). Hence, the ParC-interaction domain is capable of mediating polar localization of signaling arrays when is fused to a protein that is part of the chemotaxis core unit (CheA2-P5), independently of the AIF domain.

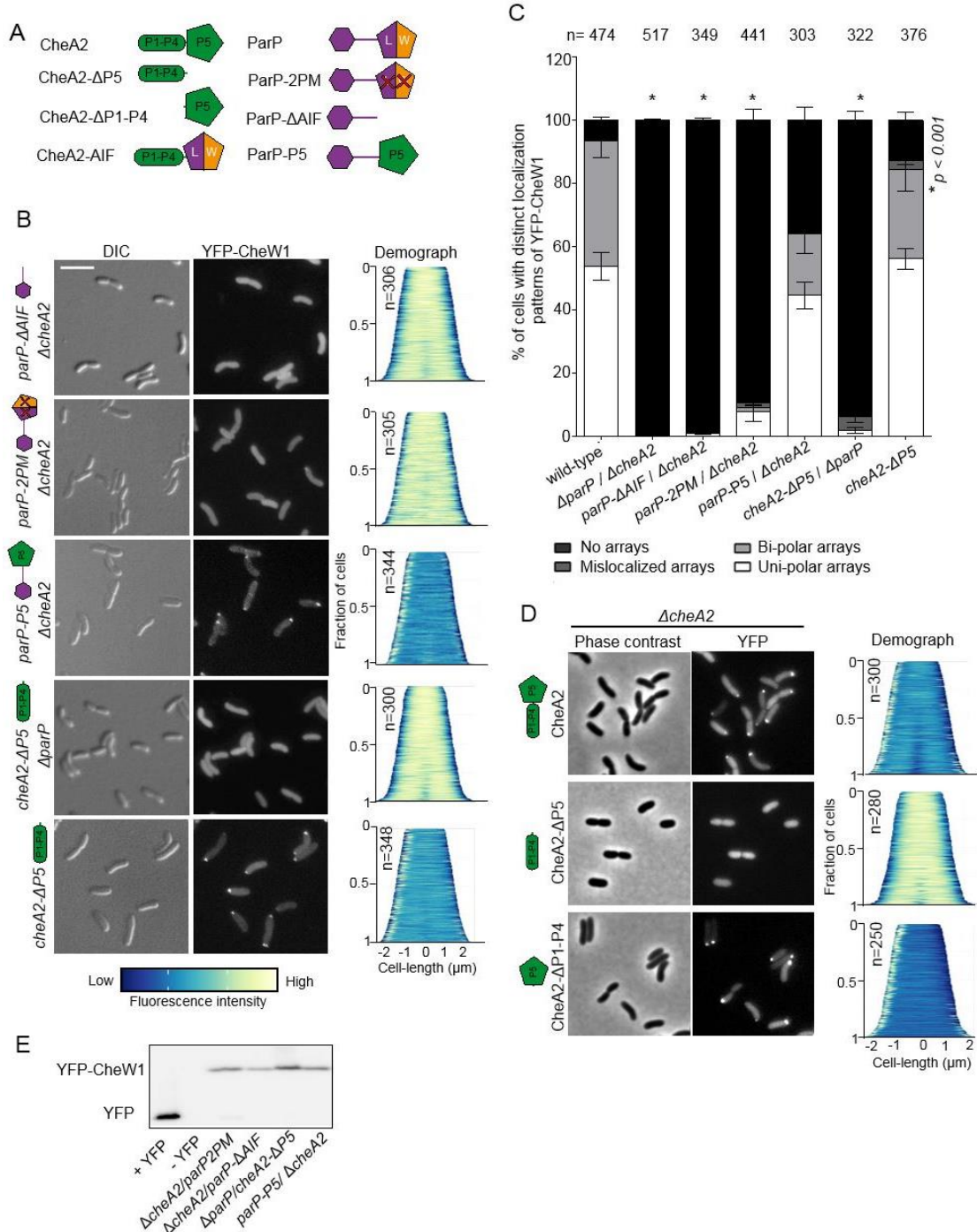


**Figure 26. The ParP-AIF and CheA2-P5 domains promote chemotaxis array formation.** (A) Schematic depicting the various CheA2 and ParP variants analyzed. (B) Fluorescence microscopy showing the intracellular localization of YFP-CheW1 in the indicated *V. cholerae* strain backgrounds. Scale bar is 5  $\mu$ m. (C) Bar graph showing the percentage of cells with distinct YFP-CheW1 localization patterns in the indicated *V. cholerae* strains. Error bars indicate SEM. The n-value indicates the total number of cells analyzed from three independent experiments. Asterisks indicate  $p < 0.001$  compared to wild-type. (D) Fluorescence microscopy showing the intracellular localization of full length and truncated versions of CheA2 fused to YFP in a  $\Delta cheA2$  strain. (E) Immunoblot detecting the presence of YFP using JL8 anti-YFP.

Similar results were observed when simply the AIF domain was replaced by the P5 domain of CheA2 in the wild-type background, where about 60% of cells formed clusters

when arrays were presumably consisting of only CheA2-P5's or AIF domains (Figure 27A-B). Immunoblot analyses indicate that the effects observed in the localization of YFP-CheW1 is not due to variations in its expression level (Figure 26E). Additionally, swimming assays in soft agar plates were carried out to indirectly evaluate the chemotactic ability of the strains where the different domains (AIF and CheA2-P5) were interchanged. Only those strains where the P5 domain of CheA2 was absent showed impaired swimming ability, suggesting that while ParP-AIF contributes to array formation (Figure 26), it does not influence signaling (Figure 27 C-D). Collectively, these observations suggest that ParP's capacity to localize arrays at the cell pole (mediated by its ParC-interaction domain) can operate independently of its capacity to promote array formation (mediated by AIF), and thus that ParP couples two distinct and separable functions.

### 3.1.9 Integration of ParP within signaling arrays is required for their polar localization and inheritance

To test if the incorporation of ParP into signaling arrays and its facilitation of array formation had functional consequences on the polar localization of arrays, the localization of signaling arrays was determined in a set of ParP interaction mutants. In a strain where *parP2PM* replaced *parP* wild-type in its native locus, that is the ParP version deficient in its interaction with CheA2 and MCPs, localization of YFP-CheW1 closely resembled that of the  $\Delta$ *parP* strain, with 65% of cells displaying mislocalized or absent arrays (Figure 28A-C). Meanwhile, strains with ParP variants incapable of interacting with CheA2 or MCPs alone, had a modest increase in mislocalized or absent arrays, 9% and 20% of cells for *parPW305A* and *parPL209A* respectively, compared to 6% in wild-type. Thereby, the marked decreased in polar clusters observed in *parP2PM* is attributed to ParP's lack of interaction with the components of the core chemotaxis unit. Similarly, co-localization studies of CheW1 and ParP wild-type and the different variants showed that if ParP is prevented from its interaction with both CheA2 and MCPs, ParP and CheW do not co-localize as in wild-type (Figure 29 A-B). Altogether, these data suggest that integration of ParP into the arrays occurs via interaction with either CheA2 or the MCPs, but although compromised, one interaction partner seems sufficient for ParP integration and array formation. In other words, disrupting both interactions, CheA2 and MCP together impairs ParP integration and consequently arrays are not recruited to the cell poles.

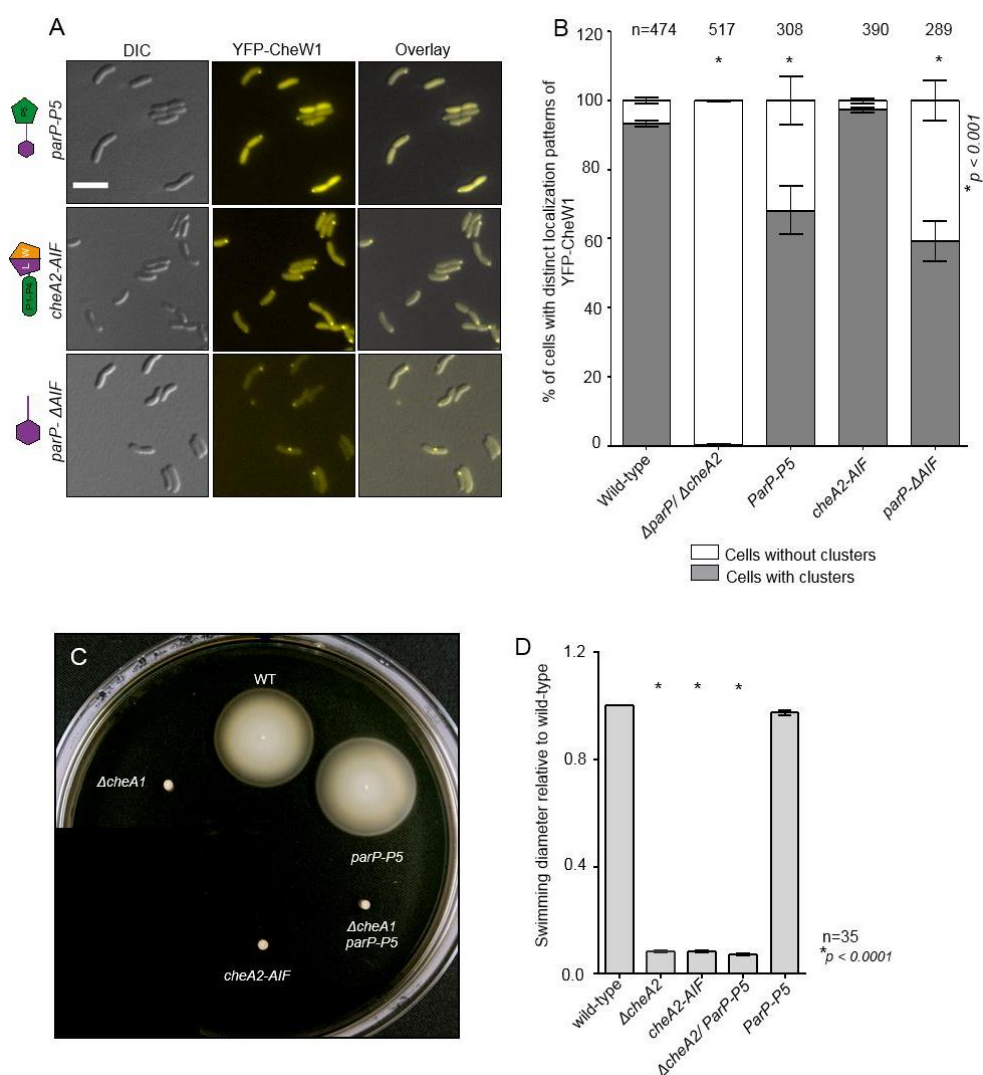


**Figure 27. Only CheA2-P5 is involved in signaling.** (A) Fluorescence microscopy showing the intracellular localization of YFP-CheW1 in the indicated *V. cholerae* strain backgrounds (see also Figure 26A). Scale bar is 5 μm. (B) Bar graph showing the percentage of cells with distinct YFP-CheW1 localization patterns in the indicated *V. cholerae* strains. Error bars indicate SEM. The n-value indicates the total number of cells analyzed from three independent experiments. Asterisks indicate  $p < 0.001$  compared to wild-type. (C) Swimming assay in soft agar (0.3%) plates. (D) Swimming diameter of the indicated strain backgrounds relative to wild-type. For those strains where swimming was not observed, the recorded value corresponds to the size of the colony. The n-value indicates the number of plates. Asterisks indicate  $p < 0.0001$  when compared to wild-type.

### 3.1.10 Interactions between ParP, CheA2 and MCPs regulate polar localization of ParP

We next tested if ParP's interaction with CheA2 and MCPs influenced ParP's own intracellular localization. Wild-type ParP and its variants ParPW305A, ParPL209A and ParP2PM were fused to YFP as N-terminal fusions and expressed ectopically in a  $\Delta parP$  background. Wild-type YFP-ParP displayed a uni- and bi-polar localization in 97% of cells. Meanwhile, YFP-ParPW305A, YFP-ParPL209A and YFP2PM localized as clusters

in about 60% of the cells (Figure 30A-B), consistent with their ability to interact with ParC (Figure 30D). Nonetheless, about 40% of cells for all ParP variants had diffuse localization, whereas for wild-type only 3% of the population had diffuse YFP-ParP (Figure 30A-B). Furthermore, there was a significant increase in the intensity of the cytoplasmic signal for the three ParP variants in the  $\Delta parP$  strain (Figure 30C). Thus, interactions of ParP with both CheA2 and MCPs promote proper polar localization of ParP, and disruption of either interaction results in a decreased proportion of ParP being tethered to the cell pole – even when interactions to recruit chemotaxis arrays to this site appear sufficient to some extent (Figure 28).

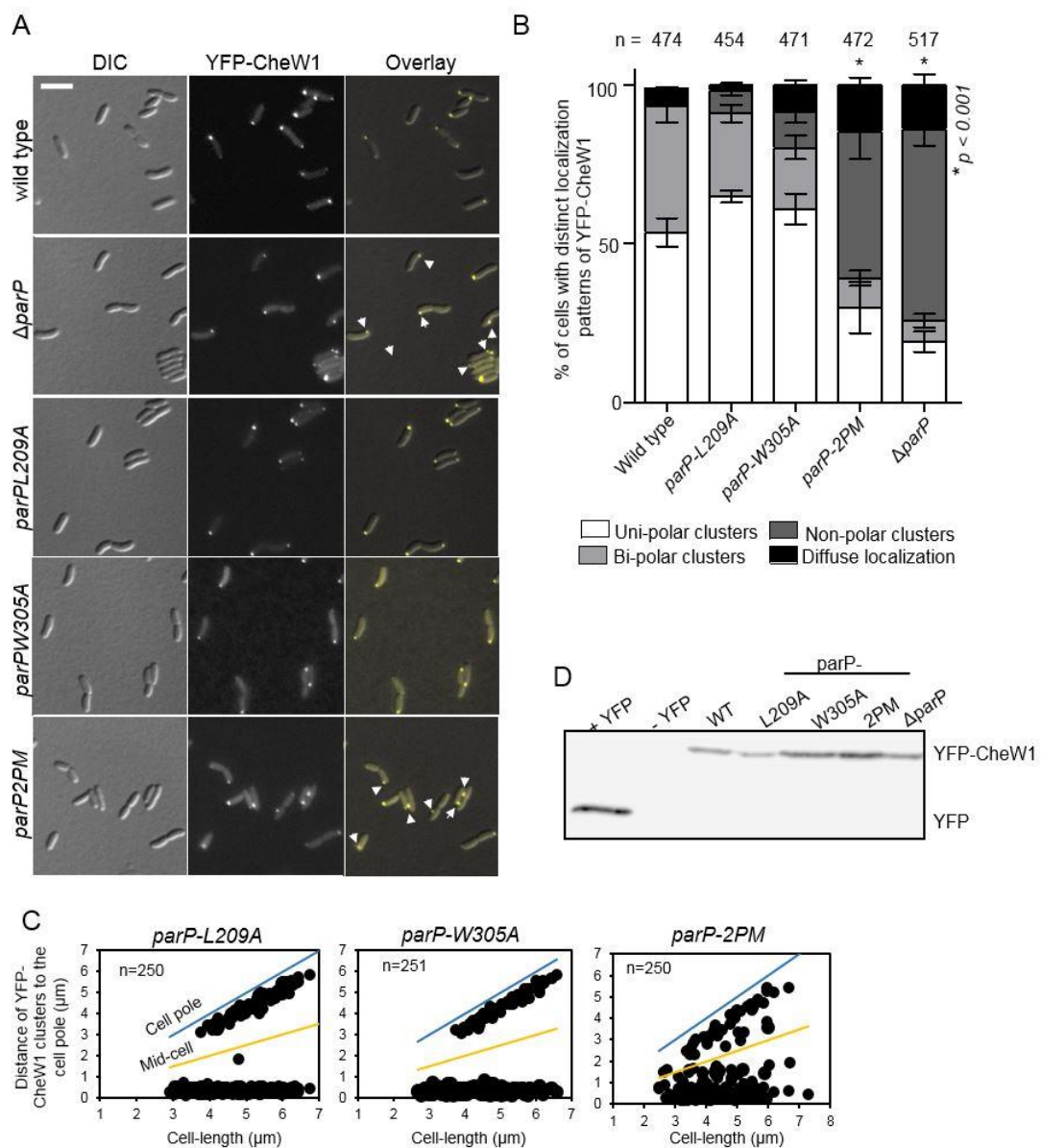


**Figure 28. Interactions between ParP, MCPs and CheA2 ensure polar placement and inheritance of chemotaxis arrays.** (A) Fluorescence microscopy of YFP-CheW1 in different *parP* derivatives and wild-type. Scale bar is 5  $\mu$ m. White arrows point at cells with non-polar clusters. (B) Bar graph showing the percentage of cells with distinct YFP-CheW1 localization patterns. Error bars indicate SEM. Asterisks indicate a  $p < 0.001$  when compared to the wild-type pattern. The n-value indicates the total number of

cells analyzed from three independent experiments. (C) Distance of YFP-CheW1 foci from the cell poles as a function of cell length (See also Figure 15B). (D) Immunoblot detecting the presence of YFP using JL8 anti-YFP antibody.

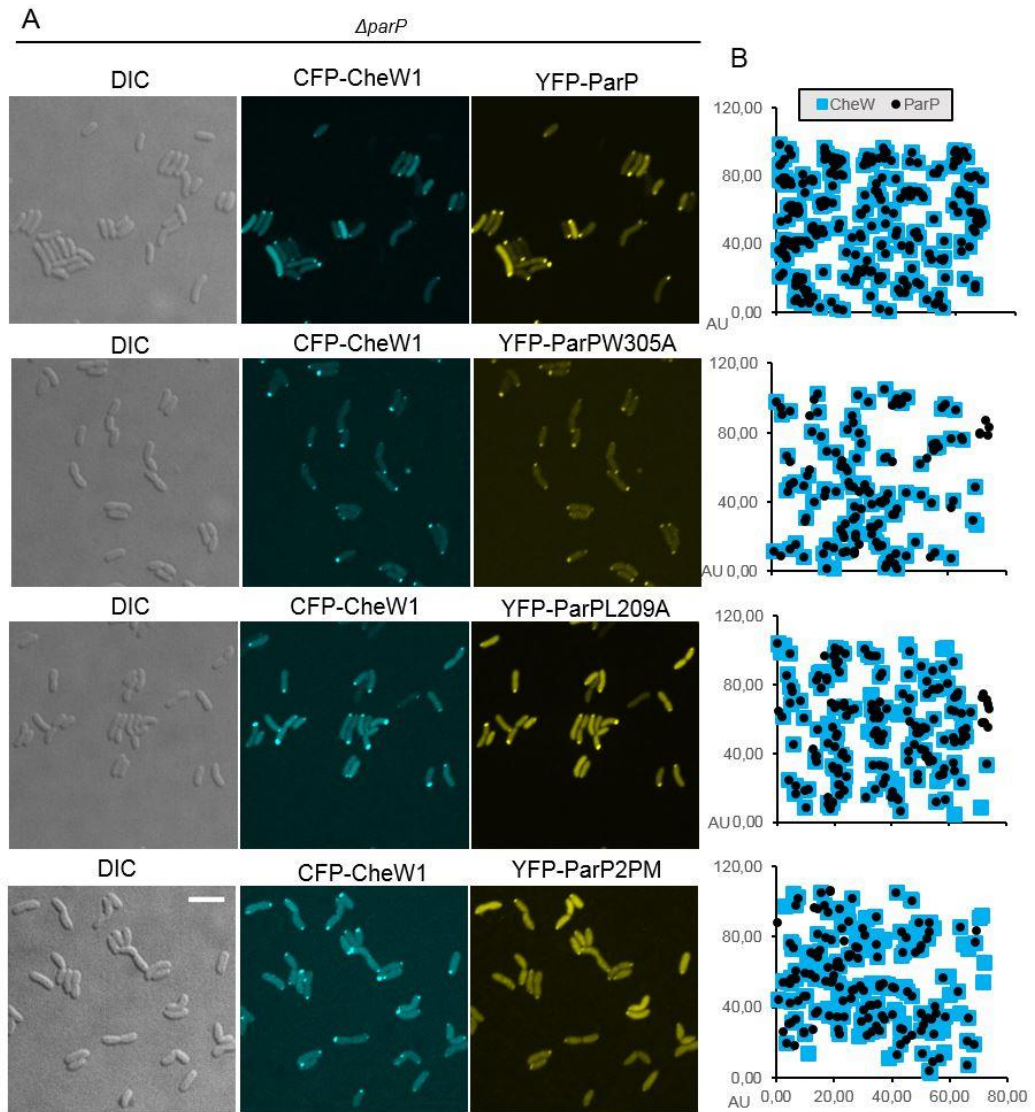


**Figure 29. ParP's interaction with CheA2 and MCPs are important for clustering of CheW.** (A) Fluorescence microscopy of CFP-CheW1 and YFP-ParP derivatives. (B) Graphs showing the coordinates of clusters formed by CFP-CheW1 and YFP-ParP. Scale bar is 5  $\mu\text{m}$ .

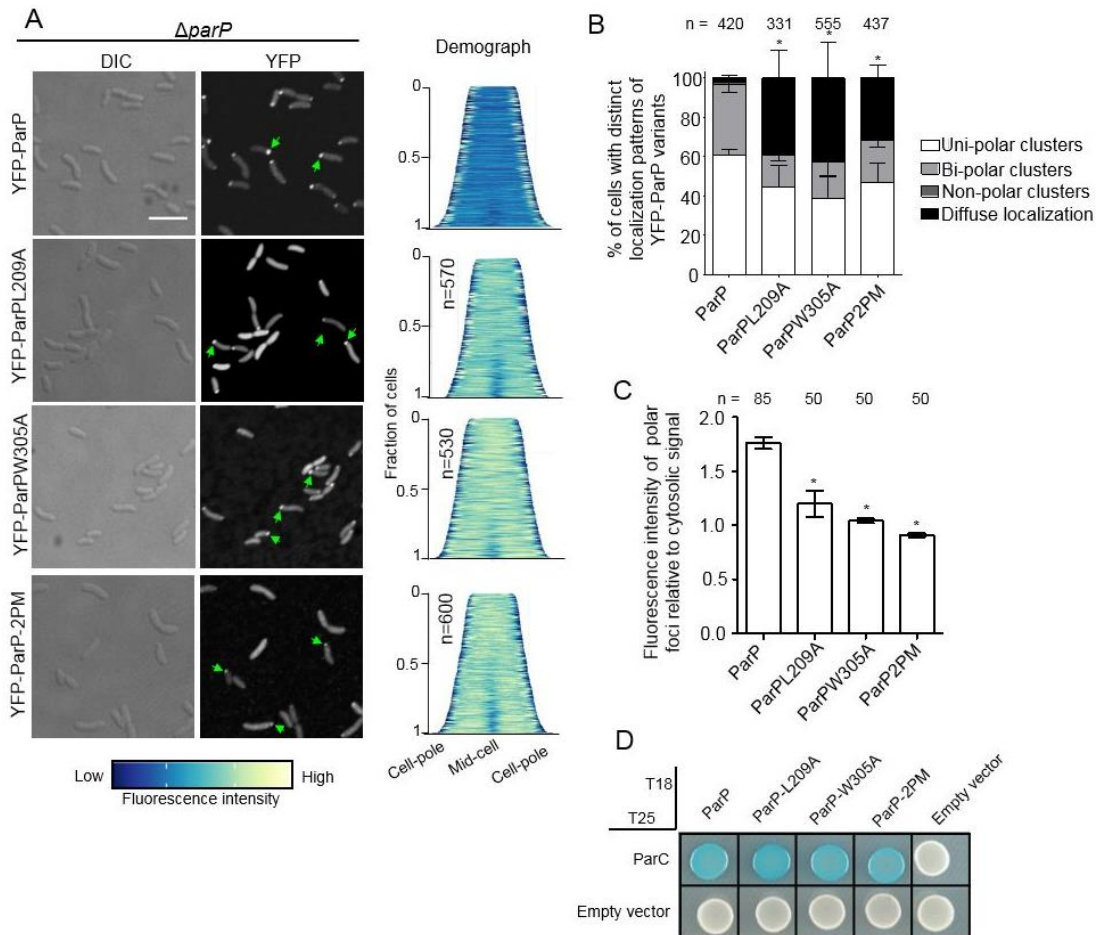


**Figure 30. Integration of ParP within arrays influences ParP polar recruitment.** (A) Fluorescence microscopy showing the localization of YFP-ParP wild-type and its derivatives in  $\Delta parP$  background. Green arrows point at polarly localized clusters. Scale bar is 5  $\mu$ m. (B) Bar graph depicting the fractions of cells with distinct localization patterns. (C) Bar graph showing the fluorescence intensity of polar ParP foci relative to the cytosolic signal. For (B-C) Error bars indicate SEM. The n-values indicate the total number of cells collected for analysis from three independent experiments. Asterisks indicate  $p < 0.0001$  compared to wild-type. (D) BACTH assay testing for interaction between the different ParP variants and ParC.

### 3.1.11 Integration of ParP within signaling arrays promotes ParP's retention at the cell pole

To determine the underlying reason for reduced polar localization of ParP variants incapable of interaction with MCPs and CheA2 (Figure 30C), we analyzed the recruitment and release of ParP and ParP2PM to and from the cell pole. We performed FRAP microscopy experiments to monitor the recruitment of new ParP molecules to cell pole by photobleaching of the polar foci of both ParP versions and measure their fluorescence recovery over time (Figure 31). These experiments showed that there was a continuous recruitment of new ParP and ParP2PM from the cytoplasm to the cell pole (Figure 31A-B).



Subsequently, the release of ParP molecules from the cell pole by bleaching the cytoplasmic signal in cells with uni-polarly localized foci was also analyzed. The intensity of polar clusters was measured and plotted relative to the initial intensity as a function of time (Figure 31C-D). After photobleaching, the intensity of polar YFP-ParP and YFP-ParP2PM clusters decreased, demonstrating that both fusion proteins were continuously released from the poles. However, the decay curves for the two ParP variants were not entirely similar (Figure 31B and D). ParP wild-type reached steady state after about 5 min, while ParP2PM was released at a faster rate, additionally YFP-ParP2PM intensity continued to drop for over 11 min. This suggests that ParP2PM is released from polar clusters to the cytoplasm at a much greater extent than wild-type ParP. Nevertheless, these experiments also suggest that there is a continuous release of ParP molecules from the pole to the cytoplasm as well as recruitment from the cytoplasm to the poles. Moreover, they also reveal that ParP's ability to interact with CheA2 and the MCPs, i.e. its ability to integrate into the arrays, prevents ParP's release from the poles and promotes its retention, consequently stabilizing ParP polar placement.

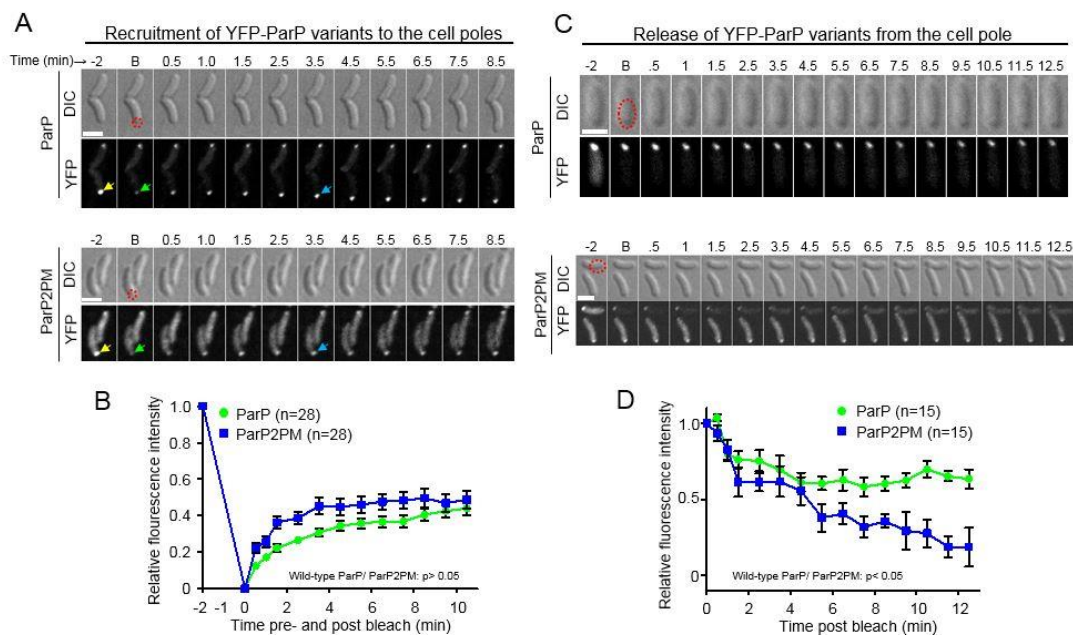


**Figure 31. Integration of ParP within signaling arrays stabilizes recruitment of ParP to the cell pole.** (A) FRAP experiments of YFP-ParP and YFP-ParP2PM clusters at the cell poles. (B) Graph depicting the fluorescence intensity over time of YFP-ParP and YFP-ParP2PM pre- and post-bleaching relative to the intensity of the cluster before photobleaching. (C) Release of YFP-ParP and YFP-ParP2PM from the cell pole post-bleach of the cytoplasmic signal. (D) Graph showing the change in intensity of YFP-ParP and YFP-ParP2PM polar clusters over time. 'B' stands for bleaching. Red dashed circles indicate the bleached region. Yellow arrows indicate the cluster before bleaching, the green arrow points at the post-bleaching clusters, while blue arrows point at the recovered clusters. Error bars indicate SEM and the n-values the number of cells used for data collection. Scale bars are 2  $\mu$ m.

### 3.1.12 Integration of ParP into signaling arrays influences ParC localization

We also studied if ParP's ability to interact with the chemotaxis proteins influenced the intracellular placement of the polar localization determinant ParC. For this, a functional fusion of YFP-ParC was ectopically produced in wild-type and *parP2PM* backgrounds. As previously reported, YFP-ParC localized in foci at the cell poles in wild-type *V. cholerae* (Figure 32A-B) (Ringgaard et al., 2011). Although polar foci were also observed in strain *parP2PM*, a significantly higher fraction (about 20%) of cells exhibited diffuse localization of YFP-ParC when compared to the wild-type (about 4%) (Figure 32A-B). Moreover, in *parP2PM* there was a significant reduction in the intensity of ParC foci (Figure 32C). Hence, integration of ParP within signaling arrays via its AIF-domain influences the retention of ParC at the cell pole. Altogether, these data reveal that integration of ParP within the arrays not only influences array formation and localization, but also affects the dynamic localization of factors that govern cell pole development, such as ParC and ParP itself.

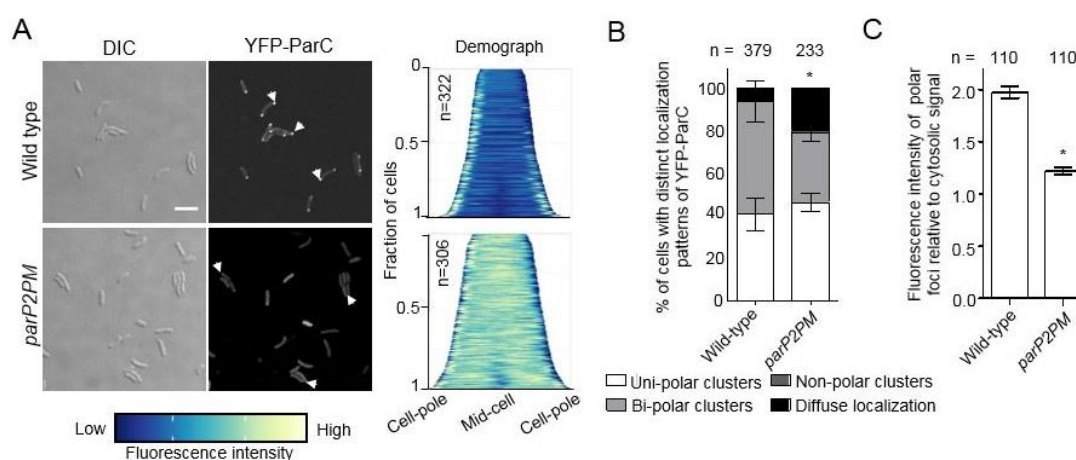


**Figure 32. Integration of ParP within signaling arrays influences ParC polar retention.** (A) Fluorescence microscopy of YFP-ParC in wild-type and *parP2PM* *V. cholerae* strains. Scale bars 5  $\mu$ m. White arrows point at polarly localized YFP-ParC foci. (B) Bar graph depicting the fraction of cells with distinct localization patterns of YFP-ParC and (C) bar graph showing the fluorescence intensity of polar ParC foci relative to the cytoplasmic signal. In (B-C) error bars indicate SEM and asterisks a  $p < 0.001$  in comparison to wild-type. The n-value indicates the total number of cells analyzed from three independent experiments.

## 3.2 **PART II – Base plate variability of chemoreceptor arrays in *V. cholerae***

The genome of *V. cholerae* contains three *cheA* genes; *vca1095*, *vc2063* and *vc1397*, which are distributed in two chromosomes and form three clusters of chemotaxis genes (cluster I, II and III, respectively; Figure 4). It is well known that cluster II proteins form arrays required for chemotaxis in most conditions (Boin et al., 2004; Butler & Camilli, 2004; Gosink et al., 2002; Lee et al., 2001). Interestingly, although proteins from clusters I and III appear to be required for array formation under very specific environmental factors (Briegel et al., 2014a; Ringgaard et al., 2015), arrays formed by proteins encoded from genes in clusters II have been observed under most growth conditions and are correlated with chemotactic behavior in *V. cholerae* (Briegel et al., 2009, 2016).

In part I of results, it is shown that arrays formed by proteins encoded by genes in the chemotaxis operon or cluster II of *V. cholerae*, can form without CheA2, the histidine kinase encoded by *cheA2*, which belongs to cluster II (Figure 4). Similarly, the data presented in part I showed that arrays from cluster II include an additional component, the protein ParP, which serves as a link between the chemotaxis arrays and the protein ParC, ultimately driving correct polar placement of the arrays in *V. cholerae*.

The architecture of bacterial chemosensory arrays has been predominantly studied in *E. coli*, where the structural core of the array is composed of rings formed by alternating P5 domains of CheA and CheW (Figure 8B-C). However, it is unknown how array architecture, particularly the structure of the base plate (Figure 8E), varies among species with ParP and ParC when compared to the model organism *E. coli*, which does not have ParP or ParC. Here, we addressed this question and present the cellular stoichiometry of the different components of the base plate in *V. cholerae* array. Similarly, we compare the ultrastability of arrays from both bacteria, *E. coli* and *V. cholerae* through cryo-EM microscopy experiments. The results presented in this section were generated in a collaborative effort with Prof. Ariane Briegel and Wen Yang, from Leiden University, Netherlands.

### 3.2.1 **Formation and localization of chemoreceptor arrays from cluster II are independent of CheA proteins**

Considering our observations, which indicate that arrays form without CheA2 (VC2063- from cluster II) as long as ParP is present (Figure 15 and Figure 26), we evaluated the formation and localization of arrays from cluster II, by ectopically producing YFP-CheW1 in a strain where *cheA* genes from cluster I, II and III were deleted

(denoted triple *cheA* deletion or  $\Delta vc1397/\Delta vc2063/\Delta vca1095$ ). As it can be observed (Figure 33A-B), in the triple *cheA* deletion strain 52% and 42% of cells had uni- and bi-polarly localized clusters, respectively. This pattern was not different from the one observed in wild-type, where 53% of the population had polarly localized YFP-CheW1 clusters, while 44% of cells had bi-polar localization, which as the demographic analyses show, occurs when the cell elongates in the onset of cell division (Figure 33A-B). Similarly, deletion combinations of one or two of the *cheA* genes gave similar localization results to the wild-type (Figure 34A-B). Altogether, these microscopy experiments indicate that formation and localization of arrays from cluster II are independent of CheA proteins.

Moreover, cryo-EM experiments of the triple *cheA* deletion showed that arrays were still present in the complete absence of CheA proteins. The data revealed that arrays were still present with a 40% reduction in the number of cells with observable arrays compared to the wild-type, supporting the importance of CheA in proper array formation. However, the subtomogram averaging results showed that in the complete absence of CheA proteins, the chemoreceptors were still packed in a hexagonal order with the iconic 12 nm spacing (Briegel et al., 2012; Cassidy et al., 2015; Li et al., 2013; Liu et al., 2012; Piasta et al., 2013), and were indistinguishable in structure from the wild-type cluster II arrays (Figure 33C). Furthermore, complementation of strains with a functional YFP-CheA2 fusion and growth analyses, indicate that the observed effects are not due to the deletion itself or a growth phenotype (Figure 35A-C). While it is beyond doubt that the histidine kinase CheA is required for proper chemotactic activity, as it can be inferred by swimming assays in soft agar (Figure 34 C-D), these data provide additional evidence for the formation of arrays in the complete absence of a kinase. Together, these observations lend support to the claim that CheA proteins are not necessary for the formation of arrays from cluster II proteins or their localization in *V. cholerae*.

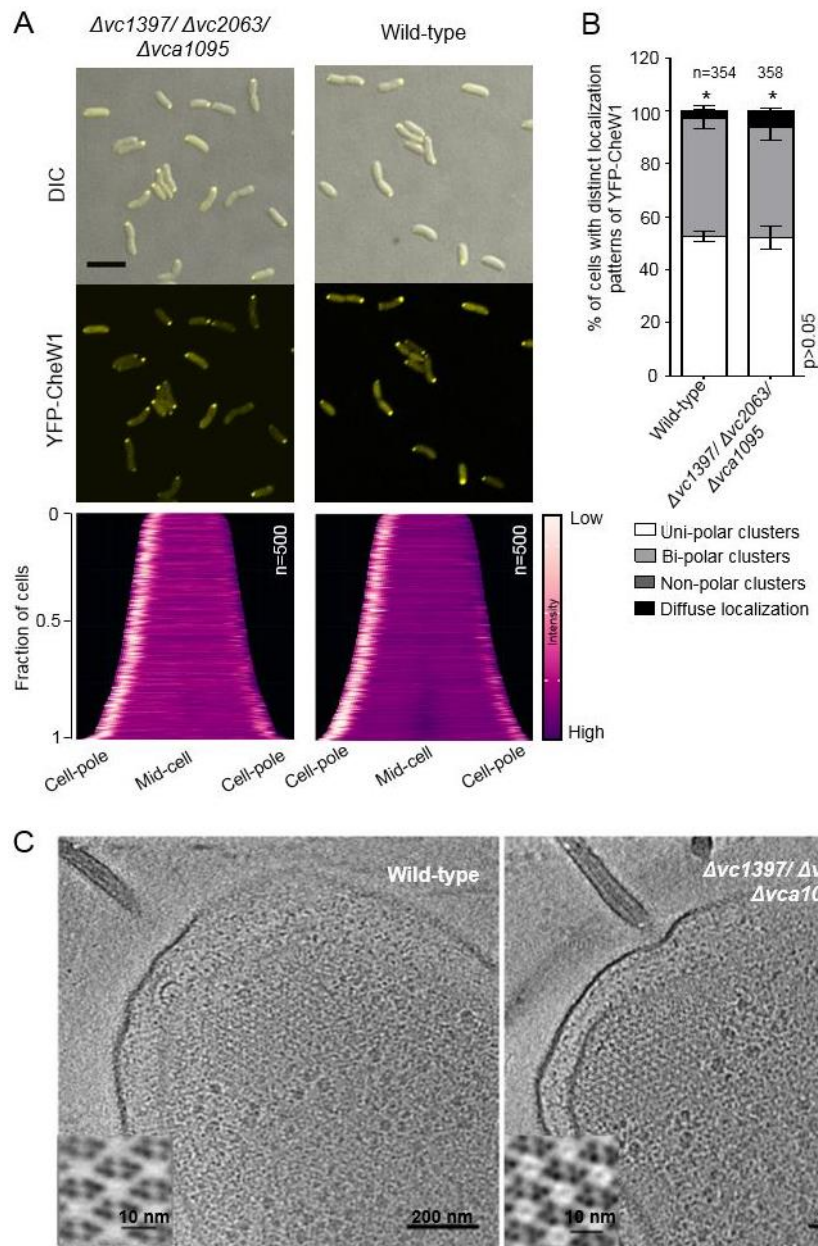


**Figure 33. Chemotaxis signaling arrays of proteins from cluster II form in *V. cholerae* without CheA proteins.** (A) Fluorescence microscopy of YFP-CheW1 as a marker for array formation in wild-type and a strain with deletion of the three *cheA* genes in *V. cholerae*. Demographs indicate the fluorescence intensity along the length of all the indicated cells (n-value). Scale bar is 5  $\mu$ m. (B) Fraction of cells with distinct localization patterns of YFP-CheW1 in the indicated strains. Asterisks indicate a  $p > 0.05$  when comparison is done against the wild-type. The n-values represent the total number of cells taken from three independent experiments. Error bars indicate SEM. (C) Arrays observed in wild-type and the triple *cheA* deletion strain depicting the classical hexagonal arrangement. VCA1095 is CheA3, VC2063 is CheA2 and VC1397 is CheA1 (See Figure 4 for more details on the different chemotaxis operons of *V. cholerae*).

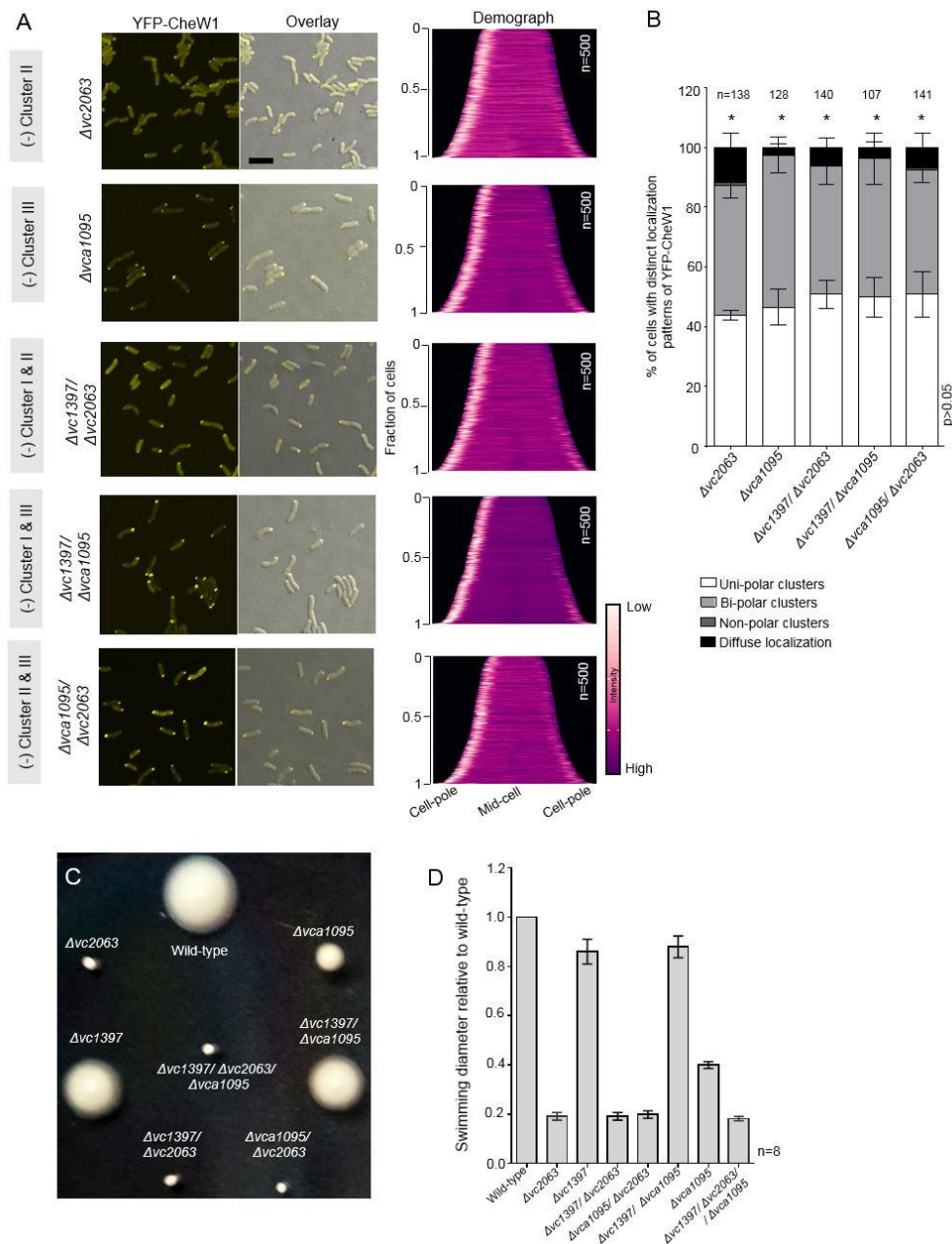


**Figure 34. CheA proteins from clusters I, II or III do not influence formation of arrays.** (A) Fluorescence microscopy of YFP-CheW1 in different deletion backgrounds of *cheA* genes from the indicated cluster. Scale bar is 5  $\mu$ m. (B) Fraction of cells with distinct localization patterns of YFP-CheW1 in the indicated strains. Asterisks indicate a  $p > 0.05$  when compared to wild-type. (C) Swimming assay in soft agar plate of the different strains without *cheA* genes. (D) Swimming diameter of the indicated strain backgrounds relative to wild-type. For those strains without apparent swimming activity, the value plotted indicates the size of the colony. The n-value indicates the number of plates. VCA1095 is CheA3, VC2063 is CheA2 and VC1397 is CheA1 (See Figure 4 for more details on the different chemotaxis operons of *V. cholerae*).

### 3.2.2 Variability of array base plates in *V. cholerae* decreases ultrastability of chemotaxis arrays

We showed previously in section 1 of the results chapter that ParP promotes recruitment of new chemotaxis proteins to chemotactic arrays, where ParP in turn sequesters the chemotaxis proteins, and stabilizes arrays by preventing their release from the cell pole. Hence, to further understand the role of CheA2 in the formation of arrays from cluster II, we performed FRAP microscopy experiments on YFP-CheW1 in wild-type and the triple *cheA* deletion background. Bleached cluster of YFP-CheW1 recovered in fluorescence intensity in both wild-type and the triple *cheA* deletion background, indicating a continuous recruitment of new CheW1 to the chemotaxis arrays. Interestingly, in contrast to ParP, absence of CheAs did not influence the recruitment of new CheW1 to the arrays (Figure 36A-B). Thus, even though CheA2 and ParP are important for proper array formation, our results indicate that integration of both proteins within the chemotaxis base plate have distinct effects on array formation.

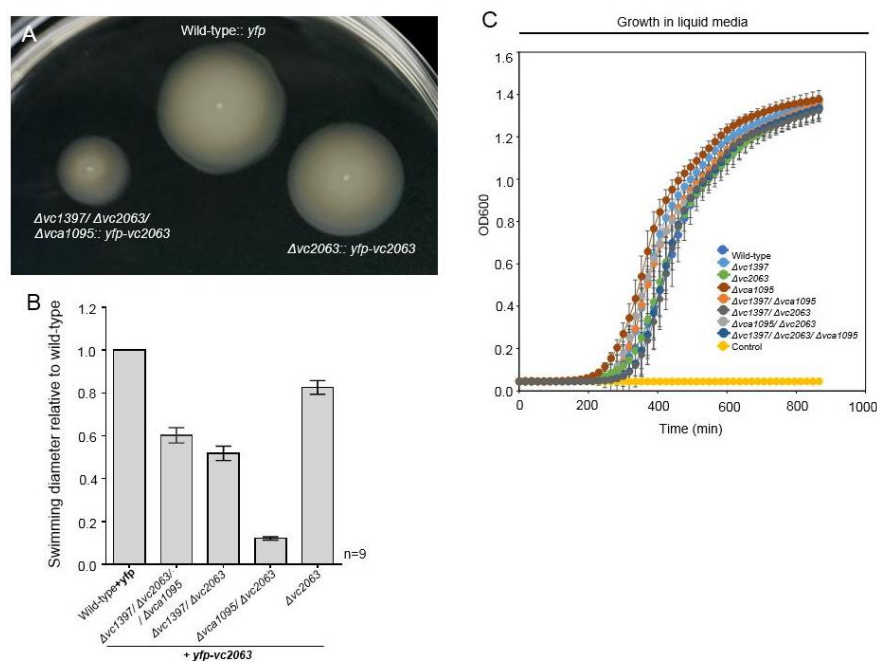


**Figure 35. YFP-CheA2 fluorescent fusion is functional.** (A) Expression of YFP-VC2063 (YFP-CheA2) restores swimming ability in a  $\Delta cheA2$  strain and partially for the triple *cheA* deletion. (B) Swimming diameter when YFP-CheA2 is produced in the different *cheA* deletion backgrounds. The n-value here indicates the number of plates. (C) Growth curve of the different *cheA* deletion *V. cholerae* strains. Control is LB liquid medium alone. VCA1095 is CheA3, VC2063 is CheA2 and VC1397 is CheA1 (See Figure 4 for more details on the different chemotaxis operons of *V. cholerae*).

Particularly, ParP is required for both the formation and the continuous recruitment of new chemotaxis proteins within the arrays where it in turn stabilizes their incorporation into the array structure. Meanwhile, CheA2 does not influence the

continuous recruitment of new chemotaxis proteins within formed arrays, although it is essential for signal transduction. Importantly, FRAP microscopy was carried out in strains where the fluorescent fusion YFP-CheW1 was introduced into the native locus, and thus the observed results are not likely to be attributed to overexpression. Moreover, swimming assays suggest that insertion of *yfp-cheW1* does not impair swimming (Figure 36C), growth (Figure 36D) and thereby, most probably does not affect chemotaxis ability.

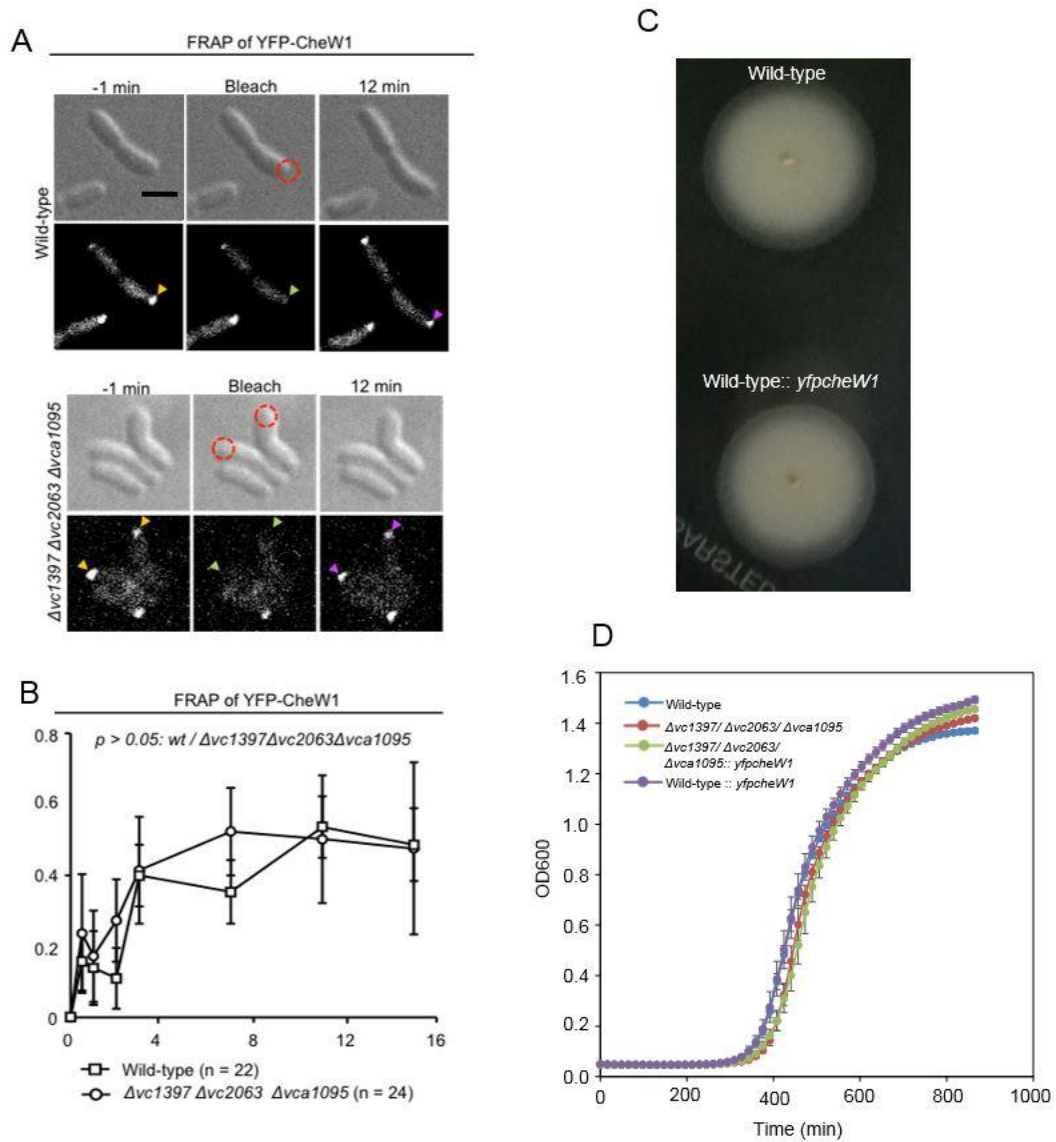


**Figure 36. Polar retention of YFP-CheW1 clusters is independent of CheA proteins at the base plate of arrays.** (A) FRAP microscopy experiments of YFP-CheW1 in wild-type and triple delta *cheA* strain. Clusters of YFP-CheW1 recover post-bleaching in wild-type and the triple *cheA* deletion strain. Numbers indicate minutes pre- and post-bleaching. The dashed red circle outlines the bleached region. Yellow arrows indicate the pre-bleaching cluster, green arrows indicate the bleached cluster. Purple arrows indicate clusters with a recovered YFP signal. Scale bar is 2  $\mu$ m. (B) Graph depicting the fluorescence intensity over time of YFP-CheW1. The n-values indicate the number of cells used to calculate the average intensities. Error bars indicate SEM. (C) Insertion of *yfp-cheW1* in the native locus does not impair swimming or (D) growth in liquid media.



### 3.2.3 *V. cholerae* cluster II arrays show a high degree of instability

In order to achieve an improved resolution (2-3.5 nm) of *E. coli* chemoreceptor arrays by cryo-EM, several laboratories have applied cell lysis either by antibiotic treatment or by inducing a phage lysis gene to flatten the cells (Briegel et al., 2014b, 2015; Fu et al., 2014). Both methods resulted in lysed cells with chemoreceptor arrays that clearly retained their architecture (Figure 37A). In fact, the architecture of the arrays in lysed cells was indistinguishable from that of arrays analyzed in intact minicells (Briegel et al., 2012; Liu et al., 2012). These studies confirmed that the chemoreceptor arrays in *E. coli* exhibit remarkable stability not only as a core unit complex but also as a receptor lattice *in vivo* (Erbse & Falke, 2009). In contrast, the same antibiotic-induced gentle cell lysis resulted in a quick loss of hexagonal packing in the *V. cholerae* chemoreceptor arrays (Figure 37B). Even though the receptors clearly remain localized at the cell pole close to the flagellar motor, their ordered packing is almost completely disrupted.

Furthermore, the base plate was still visible in the side views of lysed *E. coli* (Figure 37C), suggesting that the occupancy of receptors' membrane distal end was not completely lost. Similar observations were made for *V. cholerae* intact (Figure 37D) and lysed (Figure 37E) cells. However, instead of a continuous layer representing the base plate in intact cells, the density of base plate does appear to be discontinuous in the lysed *V. cholerae* (Figure 37E). Tomographic results from lysed *V. cholerae* cells also revealed micelle-like zipper structures where the receptors bend the inner membrane through the association of their membrane distal ends (Figure 37F). Similar structures, which represent a different mode of receptor clustering, were frequently observed in *E. coli* where the chemoreceptors were disproportionally overexpressed relative to CheA and CheW (Briegel et al., 2014b; Weis et al., 2003). Overall, these observations demonstrate that the cluster II array in *V. cholerae* does not exhibit an ultrastable structural integrity like the arrays in *E. coli*. It is noteworthy that this disruption of receptor packing order is only visible with cryo-EM imaging and cannot be detected by fluorescence light microscopy. Ultrastability has generally been thought of as a universal hallmark of chemotaxis arrays (Briegel et al., 2009; Erbse & Falke, 2009), however these results indicate that *V. cholerae* cluster II arrays are unstable and disassemble considerably easier than *E. coli* arrays.

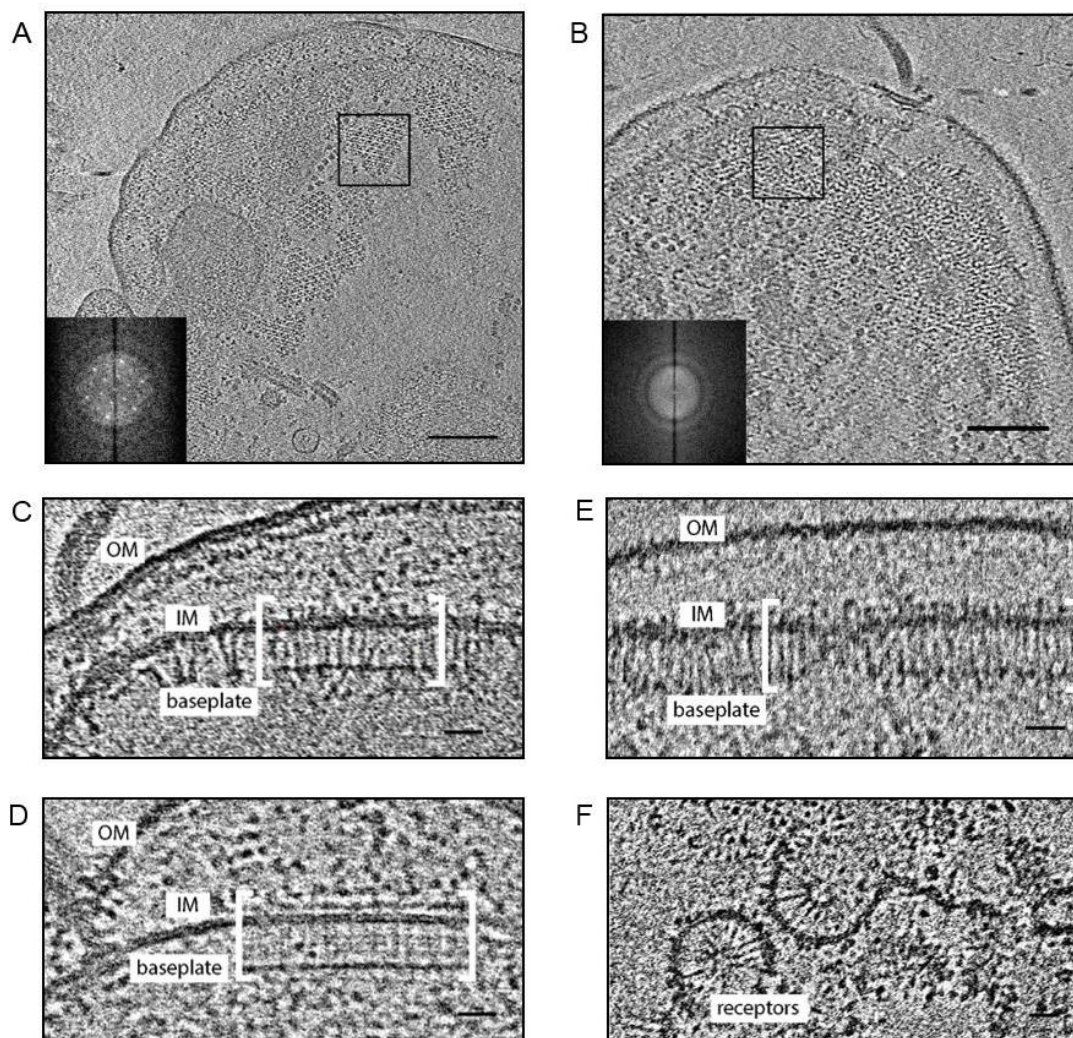


**Figure 37. Hexagonal packing of chemoreceptor arrays in wild-type *V. cholerae* and *E. coli* cells.** (A) The hexagonal packing order can be clearly identified in *E. coli* cells after antibiotic cell lysis treatment. The inset shows the power spectrum that displays a strong diffraction pattern in the boxed region of the receptor array. Scale bar 100 nm. (B) The same lysis procedure disrupts the chemoreceptor array packing order in *V. cholerae*. Strong density representing the receptors is still clustered near the flagellated pole, but there is no hexagonal order in either the cryo-tomograph or the power spectrum (inset). Scale bar is 100 nm. (C) Side view of chemoreceptor array in lysed *E. coli* cell. (D) Side view of cluster II array found in an intact *V. cholerae*. (E) Side view of the cluster II array found in lysed *V. cholerae* showing a discontinuous occupancy at the base plate compare to the continuous density shown in panels C and D for the base plate. OM = outer membrane; IM = inner membrane. White bracket in panels C-E highlights the array. (F) Cryo-tomograph of a lysed *V. cholerae* cell. Chemoreceptors trimmers associate through their membrane distal ends which leads to formation of a micelle-like structure. Scale bar is 20 nm for panels C-F.

### 3.2.4 The composition of the *V. cholerae* cluster II array is variable and it exhibits a distinct stoichiometry of chemotaxis proteins

To understand the high degree of instability of the *V. cholerae* cluster II array, the cellular stoichiometry between the base plate chemotaxis proteins CheW1, CheA2 and

ParP was determined using targeted LC-MS (liquid chromatography mass spectrometry) proteomics on wild-type *V. cholerae* cells. Initial proteomics analysis was used to determine the synthetic heavy peptides used as standards for quantification of CheW1, CheA2 and ParP ratios. Peptide samples were spiked with identical amounts of the heavy peptides in order to calculate the relative ratio between the identical peptides from CheW1, CheA2 and ParP. The analysis revealed a stoichiometry between CheW1:CheA2:ParP of 35:5.3:1 (Figure 38A), showing that CheW1 is highly abundant compared to CheA2 and especially ParP. Thereby, the cluster II base plate is likely to be primarily composed of CheW1, to a lesser extent of CheA2, and with a yet lower level of ParP.

*V. cholerae* genome also encodes four predicted CheV proteins (VC1602 or CheV1, VC2006 which is CheV2, VC2202 is CheV3 and VCA0954 is CheV4). CheV is an important component involved in the assembly of the base plate of arrays in several organisms, and has been defined earlier as a hybrid protein (Abedrabbo et al., 2017; Alexander et al., 2010), for containing a CheW-like domain similar to CheW and ParP-AIF, which in turn mimics the P5 domain of kinase CheA proteins, as well as a REC (or receiver) domain (Fredrick & Helmann, 1994; Ortega & Zhulin, 2016; Rosario et al., 1994). Sequence alignment shows that all four CheVs have the hydrophobic residues that mediate interaction between CheW, CheA-P5 and ParP-AIF with the MCPs (Figure 38C). This alignment suggests that all four CheVs have the potential to integrate into the cluster II array base plate. In a global proteomic analysis, the presence of all CheV proteins was detected (Figure 38B), showing that they are all expressed under the conditions assayed. Additionally, all proteins from cluster II, but no cluster I and III, were detected. These results suggest that CheV proteins are continuously expressed similar to cluster II proteins and thus have the potential to contribute to the structure of the base plate of the cluster II array and consequently, they could also contribute to array formation and stability.

The localization of all four CheV proteins was investigated by ectopically expressing CFP-tagged versions of each protein individually. These fluorescence microscopy experiments showed that, in wild-type cells only CheV2-CFP localized in clusters at the cell poles (Figure 38D), as observed in approximately 62% of cells (Figure 38E). Meanwhile, CheV1-CFP, CheV3-CFP and CheV4-CFP were diffusely localized in the cytoplasm (Figure 38D-E). Thus, CheV2 is the primary CheV integrated into cluster II arrays in wild-type cells. Targeted LC-MS analyses also revealed that the cellular stoichiometry of the base plate proteins, namely CheW1:CheA2:ParP:CheV1:CheV2:CheV3:CheV4, is 50:7.5:1.4:3.8:1:4.3:4.9,

respectively (Figure 38F). CheW1 is the most abundant of the base plate proteins, followed by CheA2. Moreover, CheV2 was also present, although it was also the least abundant of all base plate proteins, even though fluorescence microscopy indicates that CheV2 is the primary CheV protein in the cluster II arrays.

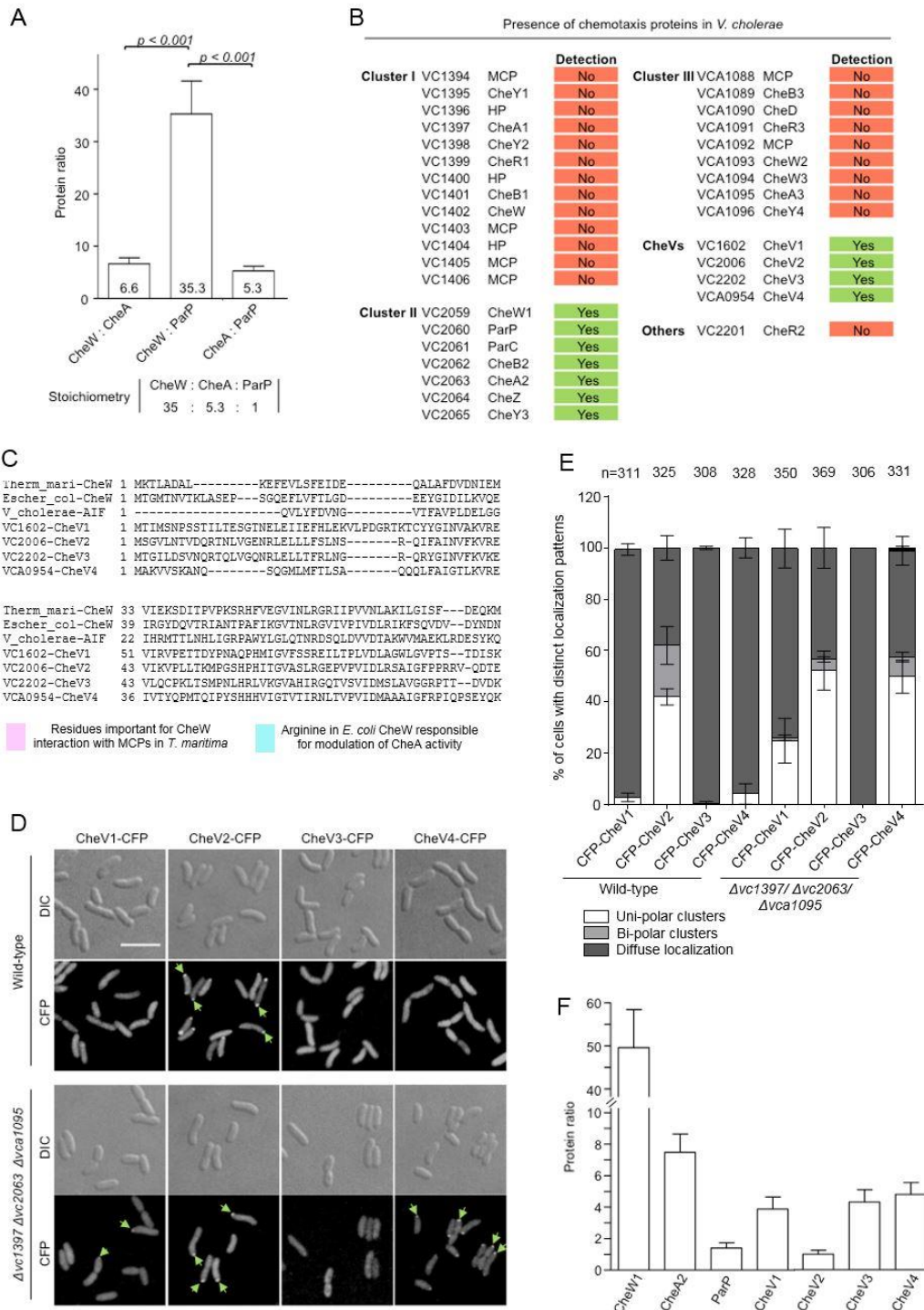


**Figure 38. Cellular stoichiometry and variability of *V. cholerae* base plate proteins.** (A) Bar graph depicting the ratio between the chemotaxis proteins CheW1, CheA2 and ParP from cluster II determined by targeted LC-MS. (B) Table showing the presence of chemotaxis proteins detected by global LC-MS proteomic analysis. (C) Sequence alignment between *T. maritima* CheW (accession number AHD17545.1), *E. coli* CheW (ECK1888), *V. cholerae* AIF domain of ParP (NP\_231692.1) and CheV

proteins of *V. cholerae* (CheV1-NP\_231242.1; CheV2-NP\_231640.1; CheV3-NP\_231833.1; CheV4-NP\_233338.1). The alignment suggest that all four CheVs should be able to integrate into the chemoreceptor array. (D) Fluorescence microscopy of cells ectopically expressing the four CheVs in wild-type *V. cholerae* and the triple *cheA* deletion strain. Scale bar is 5  $\mu\text{m}$ . Green arrows indicate polar clusters of CheV proteins. (E) Bar graph shows the percentage of cells with distinct localization patterns of the four CheV proteins in *V. cholerae* wild-type and the triple *cheA* deletion. (F) Bar graph shows the ratio between chemotaxis proteins CheW1, CheA2, ParP, CheV1, CheV2, CheV3 and CheV4 determined by targeted LC-MS. Error bars indicate SEM in panels (A), (E) and (F).

In the absence of all CheA proteins, it was observed that not only CheV2-CFP formed polar clusters in approximately 56% of cells (a fraction similar to that observed for wild-type), but also CheV4-CFP and CheV1-CFP were polarly localized in about 57% and 25% of the population, respectively (Figure 38D-E). Hence, it appears that both CheV1 and CheV4 are able to integrate into the arrays in the absence of CheA proteins. This recruitment of different CheV proteins under certain conditions suggests that the base plate is a highly variable structure and is capable of adjusting its composition in order to accommodate changes in the dynamic accessibility of different chemotaxis proteins. Indeed, earlier evidence predicted that CheV coordinates with certain receptors to integrate into the array and to modulate receptor function (Ortega et al., 2017).

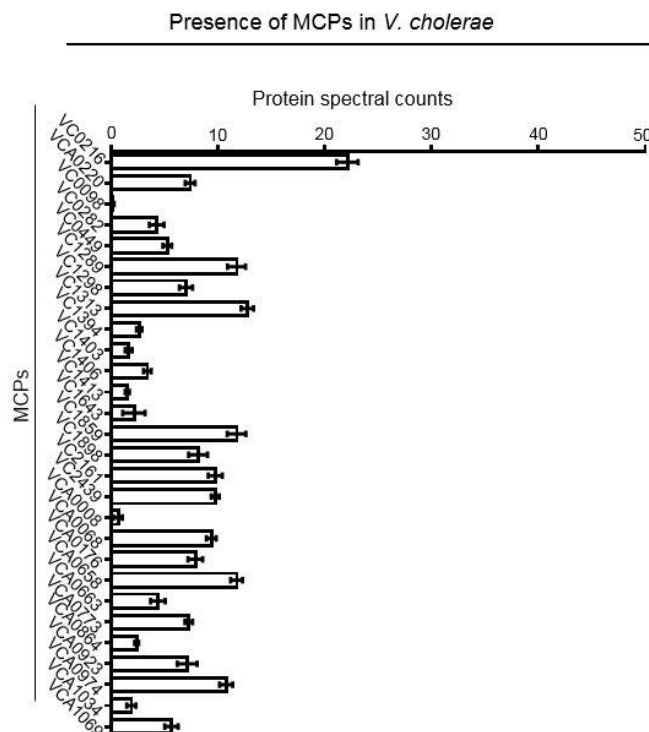


**Figure 39. Methyl-accepting chemotaxis proteins identified in proteomics assay.** Spectral counts of MCPs identified in exponentially growing cells of *V. cholerae* wild-type through proteomics. Spectral counts do not reflect precise quantitative values of the total amount of protein; however, they could be used to judge proteins present in a sample (Lundgren et al., 2010).

While it is unclear if certain MCPs associate with specific arrays or chemotaxis proteins in *V. cholerae*, the total proteomic analyses revealed that approximately half of all MCPs from *V. cholerae* are present in the conditions assayed in this study (Figure 39). Thus, it is a possibility that specific MCPs coordinate activity with particular base plate proteins. However, experimental evidence is still required to evaluate this hypothesis. Altogether, the experiments in this work indicate that *V. cholerae* arrays are less ultrastable than the paradigmatic array structure of *E. coli*, and that this decreased ultrastability could be attributed to the varied composition of the array base plate.

### 3.3 **PART III - Differential diffusion rates of distinct protein states drive protein gradient formation**

The data shown so far reveals how ParP couples array formation and localization (part I) and how the variability of the *V. cholerae* array base plate influences array formation and ultrastability (part II). However, it is still unclear how ParP's interaction with ParC affects the recruitment of the chemotaxis arrays to the cell pole. Moreover, the mechanism that drives ParC's own polar placement is still incompletely understood.

ParC belongs to a family of ParA-like proteins that mediate proper localization of chemotactic signaling arrays to the bacterial cell poles. ParC is localized to the bacterial cell pole via the polar anchoring protein HubP. At the cell pole, ParC recruits ParP. In the absence of ParC, chemotactic signaling arrays are no longer recruited to the poles and instead localize randomly in the cell. Early in the cell cycle, ParC is localized unipolarly at the old flagellated pole where it undergoes a continuous cycle between the cell pole and the cytoplasm. This continuous exchange of ParC between the cell pole and the cytoplasm likely ensures the presence of a constant pool of cytosolic ParC. After completion of chromosome segregation, a ParC anchor develops at the opposite new cell pole. Thus, ParC molecules from the cytoplasmic pool can then be captured at both poles. This diffusion-and-capture mechanism results in a redistribution of ParC from the old to the new cell pole, and over time as equilibrium is reached, it also results in an equal distribution of ParC at both poles. In consequence, chemotaxis arrays are recruited to both cell poles and each daughter cell inherits a ParC cluster and a functional chemotaxis array at their respective old poles upon completion of cell division (Ringgaard et al., 2011).

This section focuses on determining how ParC's own localization is established and how the mechanism behind ParC's cellular placement affects the localization of the chemotaxis arrays. Notably, in this section the model organism *V. parahaemolyticus* was used.

Single particle tracking photo activated localization microscopy (sptPALM) data shown in this work were obtained in collaboration with Dr. Ulrike Endesfelder and Bartosz Turkowyd from the Department of Systems and Synthetic Microbiology of the Max Planck Institute for Terrestrial Microbiology and the LOEWE Center for Synthetic Microbiology (SYNMIKRO), Germany.

### 3.3.1 ParC forms a gradient extending from the cell pole towards mid-cell

To understand the mechanism that regulates ParC's polar localization and its cycle between the cell pole and the cytoplasm, the localization of ParC along the cell length was analyzed by expressing a functional YFP-ParC fusion (Ringgaard et al., 2011) protein in *V. parahaemolyticus*  $\Delta parC$ . Interestingly, line-scan analyses of YFP-ParC signal along the cell length revealed that the YFP-ParC signal was not solely restricted to the polar ParC cluster. Instead, the signal from the YFP-ParC protein fusion extended from the major cluster at the cell pole towards mid-cell, showing its highest intensity at the pole and gradually diminishing towards mid-cell (Figure 40A).

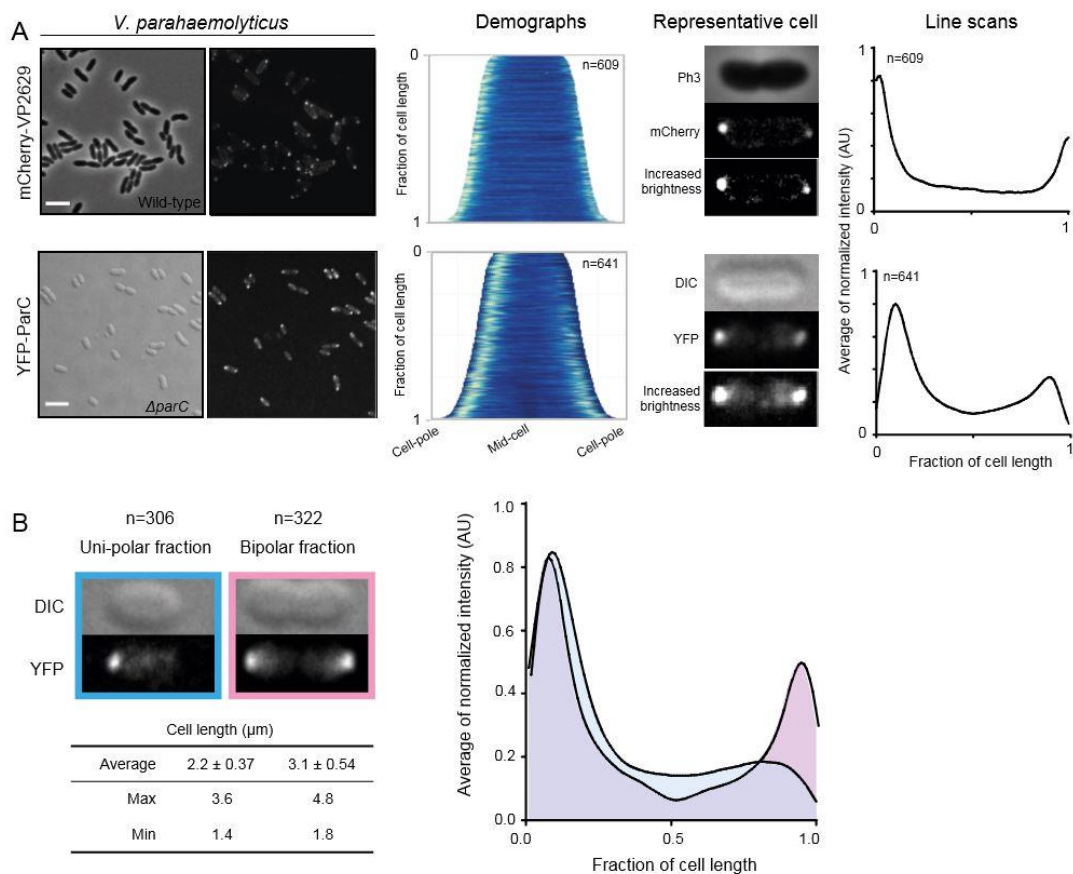


**Figure 40. ParC forms a protein concentration gradient extending from the cell pole to mid-cell.** (A) Localization of mCherry-VP2629 in *V. parahaemolyticus* wild-type and YFP-ParC in *V. parahaemolyticus*  $\Delta parC$ . Demographs show the fluorescence profile along the cell length, cells are arranged according to their lengths, short cells at the top and longer cells at the bottom of the plot. The n-value indicates the total number of cells analyzed. Insets show a representative cell, and graphs are the results of line scans that show the average of the normalized fluorescence profile. Scale bar is 5  $\mu\text{m}$ . (B) Cell length dependent gradient formation of ParC. Short cells have one ParC gradient extending from the cell pole towards mid-cell. Long cells have two ParC gradients extending from each cell pole towards mid-cell. Insets show a representative cell, and graphs are the results of the line scans that show the average fluorescence profile normalized to cell length of short and long cells.



This localization pattern was in contrast to the localization of a fluorescent protein fusion of a MCP, mCherry-VP2629, which represents the fluorescence of chemotaxis arrays (Ringgaard *et al.*, 2014). The fluorescent protein fusion mCherry-VP2629 was primarily concentrated at the cell poles into tight clusters and did not spread further towards mid-cell (Figure 40A). The intensity maxima of mCherry-VP2629 and YFP-ParC signal coincided at the pole, indicating that the main ParC cluster co-localizes with the chemotaxis arrays at the cell pole. Together, these results show that in addition to its main localization at the cell pole, ParC also localizes in a gradient that extends from the cell pole towards mid-cell, with the lowest ParC level at mid-cell.

Moreover, these experiments showed that in cells with one ParC focus, a single ParC gradient extended from the cell pole harboring the ParC cluster, and that the fluorescence signal decreased towards the opposite new pole, which as such experienced the lowest concentration of ParC. Furthermore, in cells with bi-polar localization of ParC, a ParC gradient extending from each pole was observed. These gradients decreased towards mid-cell with the mid-cell position having the lowest ParC concentration (Figure 40B). Thus, the data indicates that ParC not only undergoes a cell cycle-dependent localization from the old pole to the new cell pole, but a second concentration gradient is established, extending from both poles, as redistribution of ParC occurs.

### **3.3.2 DNA binding by ParC is required for its function in mediating polar array localization**

Previous research has demonstrated that ParA-like proteins have sequence non-specific DNA (nsDNA) binding activity, by studies both *in vitro* and *in vivo* (Bouet *et al.*, 2007; Ebersbach & Gerdes, 2004; Erdmann *et al.*, 1999; Hui *et al.*, 2010; Lim *et al.*, 2005; Marston & Errington, 1999; Ptacin *et al.*, 2010; Quisel *et al.*, 1999; Vecchiarelli *et al.*, 2010, 2012). Thereby, ParC's ability to bind DNA was evaluated by ectopically expressing a functional YFP-ParC fusion in *E. coli*, which lacks *parC* homologues. These experiments showed precise co-localization between YFP-ParC and the nucleoid, in contrast to YFP alone, which did not co-localize with the nucleoid and was evenly distributed in the cytoplasm (Figure 41A). Similarly, in artificially elongated *E. coli* cells, nucleoids co-localized with YFP-ParC (Figure 41B). These observations suggest that ParC binds nsDNA, similarly to other ParA-like proteins.

DNA binding by ParA-like proteins occurs through exposed basic residues (Castaing *et al.*, 2008; Hester & Lutkenhaus, 2007; Soberón *et al.*, 2011). Sequence alignment of ParC against other ParA proteins identified residue R191 and K220 in ParC,

which in other ParA proteins have been shown to direct DNA binding (Hester & Lutkenhaus, 2007), an important step in ParA-like proteins cycle (Figure 41C-D). By substituting each residue individually with glutamic acid in YFP-ParC, two variants were created, YFP-ParCR191E and YFP-ParCK220E. These fluorescent fusions were also assayed for their co-localization with respect to the nucleoid in *E. coli*. No change in localization was observed for YFP-ParCK220E. However, YFP-ParCR191E did not co-localize with the nucleoid, an effect also observed in elongated cells. Instead, localization of YFP-ParCR191E resembled the pattern of YFP alone (Figure 41A-B). These results further support the observation that ParC binds DNA and indicate that amino acid R191 is required for its association with nsDNA.

To analyze the importance of ParC DNA binding on its function in mediating polar localization of ParP and chemotaxis arrays, the native *parC* was replaced by *parCR191E*. In the resulting strain, the localization of ParP and the chemotaxis arrays was analyzed. For these experiments, functional fluorescent fusions of YFP-ParP and YFP-CheW (Ringgaard *et al.*, 2014) were employed. As previously shown (Ringgaard *et al.*, 2014), in wild-type YFP-ParP and YFP-CheW formed foci that localized in a uni- and bi-polar manner. However, in strain  $\Delta parC$ , in 75% of the population neither YFP-ParP nor YFP-CheW were properly recruited to the cell poles and instead formed non-polar clusters; in addition, some cells lacked clusters of YFP-ParP and YFP-CheW altogether (Figure 42A-B). Interestingly, in strain *parCR191E*, the fraction of cells with polarly localized YFP-ParP and YFP-CheW decreased by 50% when compared to the wild-type (Figure 42A-B). Hence, these data indicate that the ability of ParC to bind DNA is important for its role in mediating the proper intracellular localization of ParP, and consequently of the chemotaxis arrays.

### 3.3.3 DNA binding by ParC is regulated by its nucleotide-bound state

Studies of the mechanism driving the function of ParA-like ATPases are largely based on mutagenic approaches that rely on several structural features shared by these proteins. Amino acid substitutions permit a dissection of protein function by means of locking the protein in each state of their ATP transition cycle (Koonin, 1993; Lutkenhaus, 2012). Thus, as a ParA-like ATPase, certain characteristics of ParC can be exploited to study the underlying mechanism that allows its subcellular localization and activity. By introducing amino acid substitutions at specific conserved residues positioned within the ATP binding pocket of ParC (Figure 41C-D), it is possible to lock the nucleotide cycle of ParC at different stages (Figure 41C-D) (Hayashi *et al.*, 2001; Hester & Lutkenhaus, 2007; Kiekebusch *et al.*, 2012; Scholefield *et al.*, 2011, 2012).

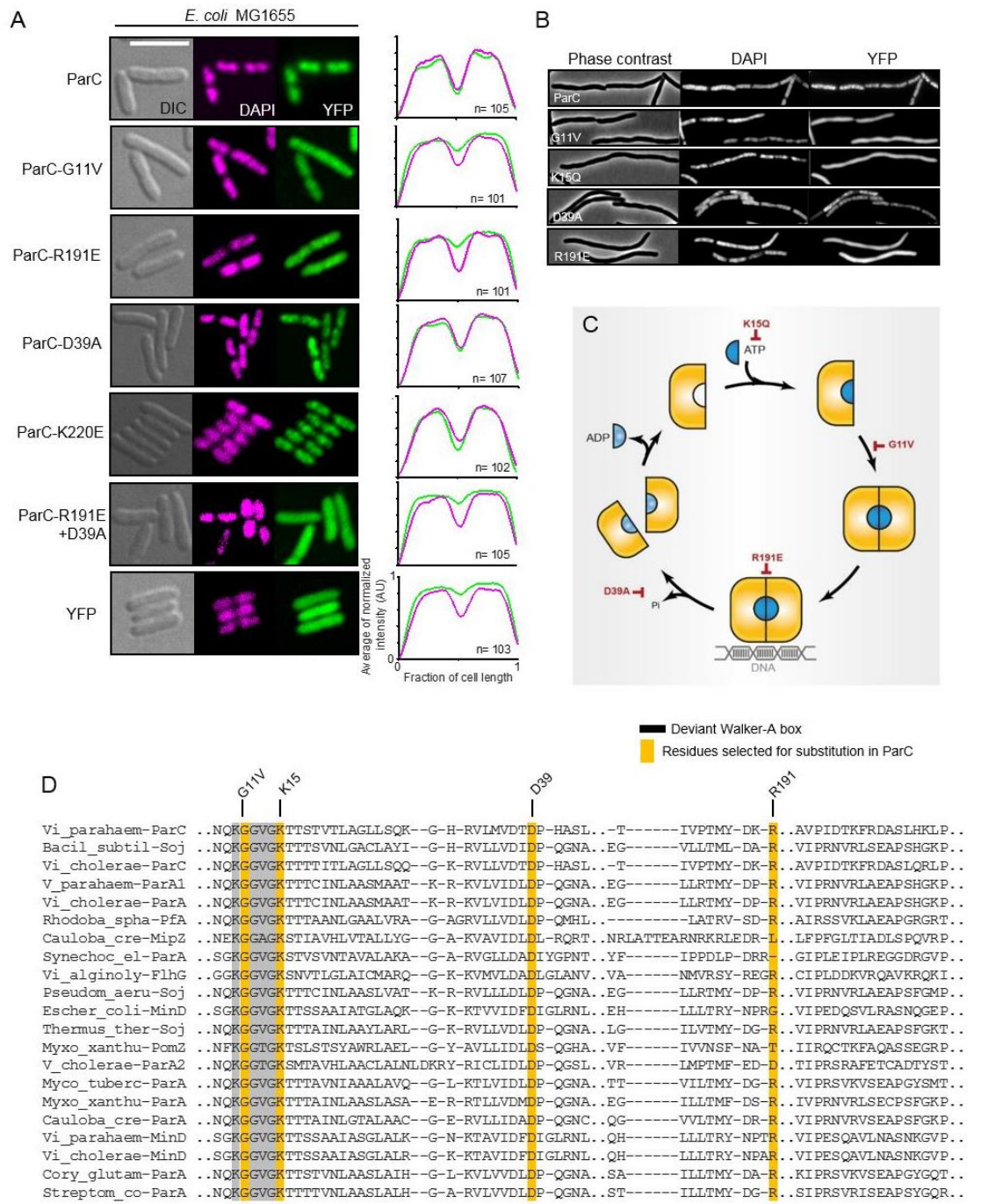


**Figure 41. ParC associates non-specifically to DNA.** (A) Fluorescent protein fusions of YFP-ParC, the indicated protein derivatives, and YFP alone from plasmid pMF390 were ectopically produced in *E. coli*. Their localization was correlated with DAPI stained nucleoids. Line scans of YFP signal along the cell length (green) and the stained nucleoid (magenta) are shown for every protein fusion. The total number of cells analyzed is indicated by the n-value. Scale bar is 5  $\mu$ m. (B) Artificially elongated *E. coli* cells with DAPI stained nucleoids and expressing YFP-ParC wild-type and its variants. (C) ATPase cycle followed by ParA. In red are indicated the amino acid substitutions performed in ParC for dissection of its mechanism. (D) Sequence alignment of several ParA proteins. Highlighted are the residues used for mutagenic studies in ParC based on their effects on ParC's cycle (as shown in C). Accession numbers of the sequences employed for alignment can be found in Table 15.

Based on previous studies we generated several ParC variants, namely i) ParCK15Q, which is predicted to be unable to bind ATP and is locked in the Apo-monomeric form, ii) ParCG11V, which is able to bind but not hydrolyze ATP and is locked in the ATP-bound monomeric form and iii) ParCD39A, which is able to bind but not hydrolyze ATP and is locked in its ATP bound dimeric form. The ability of each variant to associate with DNA was also analyzed by studying their localization relative to the nucleoid in *E. coli*. YFP-ParCK15Q and YFP-ParCG11V were diffuse in the cytoplasm, resembling YFP-ParCR191E (Figure 41A-B). In contrast, YFP-ParCD39A co-localized with the nucleoid similar to wild-type YFP-ParC (Figure 41A-B). These data suggest that the ATP-bound dimeric form of ParC binds DNA while the ATP-bound monomeric form does not have DNA binding activity. To further corroborate these observations, we generated a ParC variant combining the D39A and R191E substitution (ParCD39A+R191E). Indeed, ParCD39A+R191E no longer co-localized with the nucleoid but instead was diffusive in the cytoplasm similar to YFP alone (Figure 41A). Altogether, these data indicate that the Apo-monomeric form and the ATP-bound monomeric form are unable to bind DNA, and that it is the ATP-bound dimeric form of ParC that binds DNA.

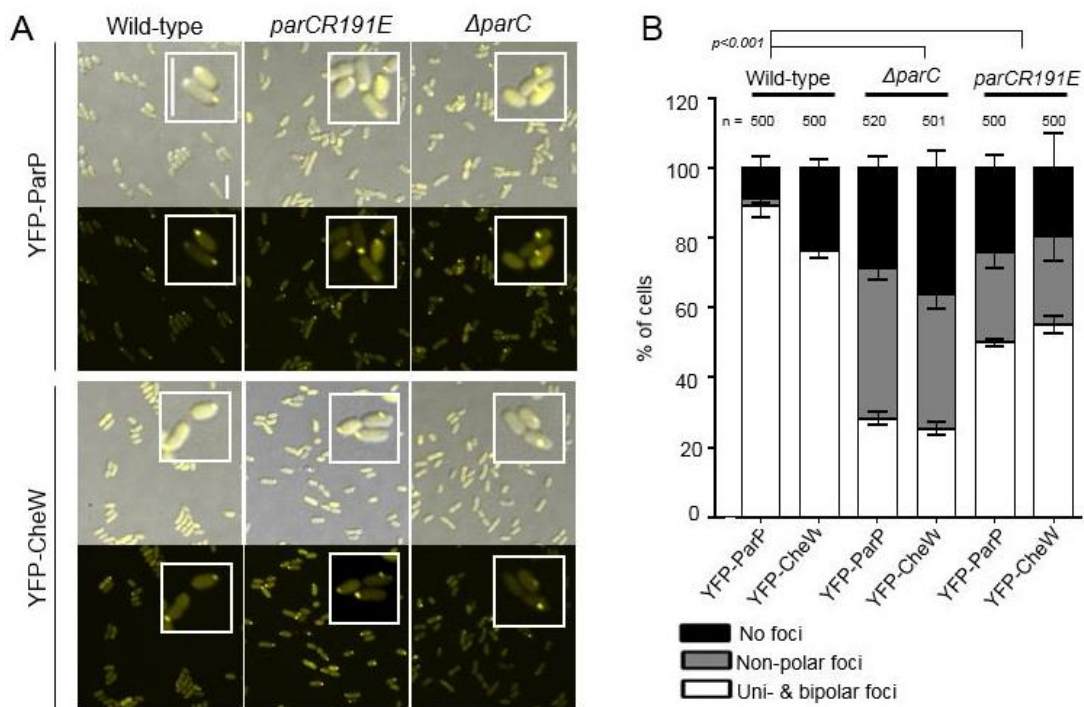


**Figure 42. Association of ParC with nsDNA influences polar placement of chemosensory arrays.** (A) Localization of YFP-ParP and YFP-CheW in *V. parahaemolyticus* wild-type and mutant strains *parCR191E* and  $\Delta parC$ . (B) Percentage of cells with distinct localization patterns of YFP-CheW and YFP-ParP. Error bars indicate SEM. The number of cells analyzed in three independent experiments is the n-number. Scale bars are 5  $\mu$ m.

### 3.3.4 ParC's polar localization is regulated by its ATP-cycle and DNA association

It has been observed that ParC's ATP binding activity is important for its proper function in recruiting chemotaxis arrays to the cell pole and its polar localization in *V. cholerae* (Ringgaard et al., 2011). In order to understand how ParC's nucleotide cycle and DNA binding activity influence its localization dynamics, YFP-ParC and YFP fusions of the different ParC variants (Figure 41C) were individually expressed from plasmids in *V. parahaemolyticus*  $\Delta parC$ , where the localization of each protein fusion was subsequently analyzed. Interestingly, variants YFP-ParCG11V and YFP-ParCR191E localized to the cell poles in a uni- and bi-polar cell length-dependent manner (Figure 43A). In contrast, YFP-ParCK15Q and YFP-ParCD39A were no longer localized to the cell poles but were instead on average evenly distributed in the cytoplasm (Figure 43A). Immunoblot analyses showed that the differences in localization pattern were not due to variations in protein levels nor due to cleavage of the YFP moiety from the ParC variants (Figure 43B). This indicates that it is the ATP-bound monomeric form of ParC being recruited and bound to the cell poles, while the Apo-monomeric and ATP-bound dimeric forms have no affinity for the cell poles.

While ParC, ParCG11V and ParCR191E all localized to the poles, demographic analysis suggested differences in the amount of cytosolic protein, with a higher amount of cytosolic YFP-ParCG11V and a lower amount of cytosolic YFP-ParCR191E compared to wild-type (Figure 43A). To further explore these variations, line-scan analyses of the YFP-signal for all ParC variants were performed. These analyses confirmed that ParCK15Q, ParCD39A and ParCD39A+R191E are diffuse in the cytoplasm and do not localize to the poles (Figure 43C). Furthermore, while YFP-ParCG11V and YFP-ParCR191E showed clear maxima at the poles similar to wild-type ParC, there was a significantly higher cytosolic level of ParCG11V compared to ParC and ParCR191E. Importantly, ParCR191E was almost completely absent from the cytoplasm (Figure 43C). Consistently, polar foci of ParCR191E and ParCG11V were significantly brighter and dimmer, respectively, than wild-type ParC when compared to their respective cytosolic signals (Figure 43D). Even though all three ParC variants are recruited to the cell poles, ParCR191E is the only of them being almost exclusively found at the cell pole and being absent from the cytoplasm. Inversely, YFP-ParCD39A+R191E no longer localized to the cell poles, but was exclusively found in the cytoplasm (Figure 43A-C) – further supporting that the ATP-bound dimeric form of ParC is unable to bind the cell pole.

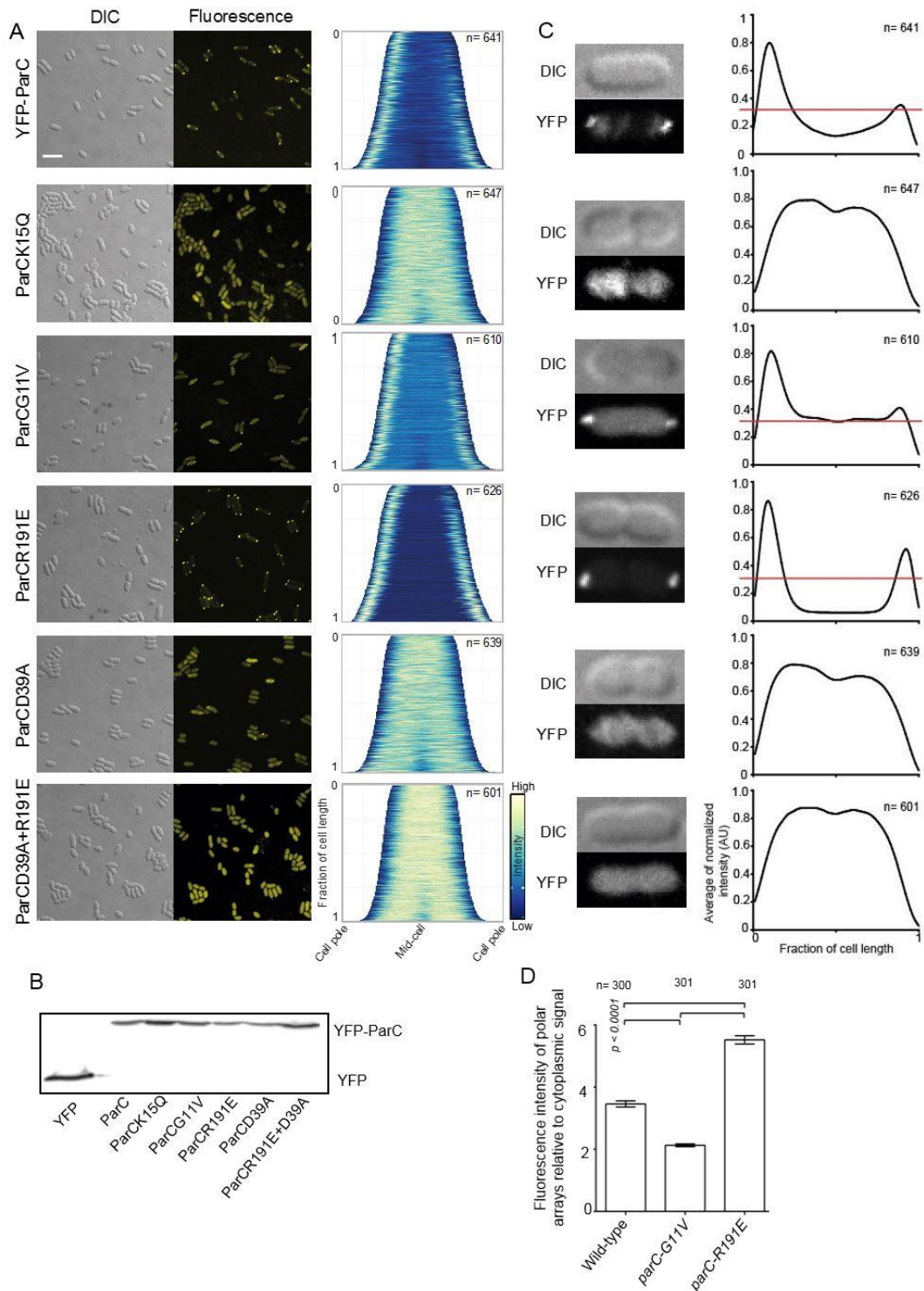


**Figure 43. ParC's polar localization and gradient formation is regulated by its ATP-cycle and DNA association.** (A) Fluorescence microscopy showing the intracellular localization of YFP-ParC wild-type and its variants ectopically expressed in *V. parahaemolyticus*  $\Delta parC$  strain. Demographs show the fluorescence profile along the cell length. In the demographs cells are arranged according to their lengths, short cells at the top and longer at the bottom of the plot. The brightest pole in every cell appears always towards the left side. The n-value indicates the total number of cells analyzed. Scale bar is 5  $\mu$ m. (B) Immunoblot with JL8 anti-YFP antibody to detect YFP and identify the presence of YFP-ParC in strains imaged in (A). (C) Representative cells of microscopy data shown in (A). Graphs are the result of the line scans, representing the average fluorescence profile normalized to the cell length. The red line indicates the level of cytosolic signal of YFP-G11V for comparison with other polarly localized ParC variants. (D) Bar graph showing the fluorescence intensity of polar YFP-ParC, YFP-ParCG11V and YFP-ParCR191E foci relative to the cytoplasmic signal. The n-values in panels (A), (C) and (D) indicate the total number of cells analyzed from three independent experiments.

### 3.3.5 ParC's gradient formation is regulated by its ATP-cycle and is required for ParC's function

Importantly, the line-scan analysis showed that for all ParC variants only wild-type ParC formed a gradient extending from the cell pole. Even YFP-ParCG11V and YFP-ParCR191E, which were polar localized, did not form a gradient extending from the poles towards mid-cell as wild-type ParC (Figure 43C). Furthermore, when the native *parC* locus was replaced with a gene encoding each of the ParC variants, it resulted in a  $\Delta parC$  phenotype in regard to recruitment of ParP and chemotaxis arrays to the cell pole, showing that disruption of either step in ParC's ATP-cycle disrupts ParC function (Figure 44A-B). Altogether, these data indicate that ParC forms a gradient at the polar region, which relies on ParC's ability to interact with nucleoid DNA and bind and hydrolyze ATP and is essential for ParC function.

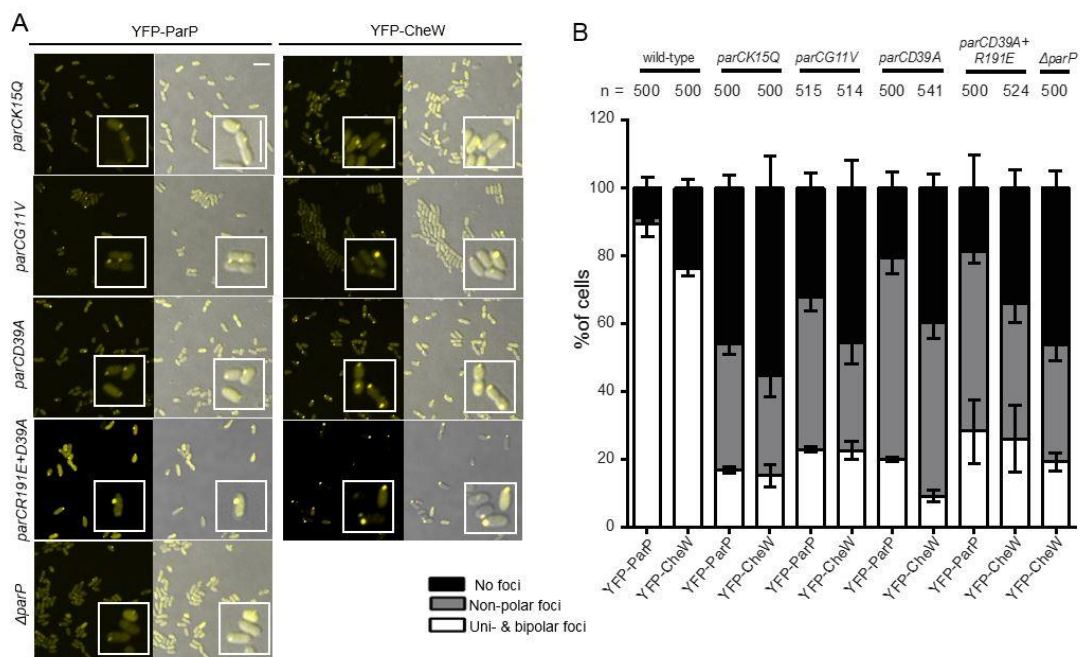


**Figure 44. ParC's nucleotide ATP-dependent cycle influences localization of ParP and CheW.** (A) Localization of YFP-CheW and YFP-ParP in *V. parahaemolyticus* strains where *parC* was replaced in the chromosome by the indicated mutated versions. Scale bars are 5  $\mu$ m. (B) Percentage of cells with distinct localization pattern of YFP-CheW and YFP-ParP in the different strain derivatives. The number of cells analyzed in three independent experiments is the n-number. Error bars indicate SEM. All values of YFP-CheW and YFP-ParP localization in mutated backgrounds are significantly different ( $p < 0.001$ ) from the wild-type. P-values were calculated using student's t-test.

### 3.3.6 Differential diffusion rates of distinct protein states drive protein gradient formation

To further elucidate the mechanism behind ParC's gradient formation, the diffusive behavior of individual ParC protein variants was monitored by fast sptPALM imaging at 33 Hz. As such, it is possible to measure fast single-molecule dynamics, which make up the fluorescence distribution phenotypes of ParC variants. Since these distribution phenotypes indicate distinct binding modes for each individual ParC variant, four different dynamical behaviors of individual ParC molecules were expected from the sptPALM analyses: *i*) ParC interacting with DNA or *ii*) being bound at the pole, both of which should appear as slow or immobile trajectories at fast sptPALM time scales; and *iii*) freely diffusive ParC monomers or (*iv*) dimers, which are both expected to show up as highly mobile trajectories distributed throughout the cellular volume. These multi-state dynamics are already indicated in the images of exemplary cells in (Figure 45A).

During sptPALM imaging, for all trajectories of statistically significant length ( $> 6$  imaging steps), the average jump distance (or JD) was calculated. Jump distance is the average distance between two consecutive localizations in a trajectory. Average JD was then plotted as JD-probability density histograms (Figure 45B). In these, two subpopulations were easily discernable, a red-colored “slow” fraction of molecules with average JD  $\leq 160$  nm and a blue-colored “fast” fraction of molecules with JD  $> 160$  nm (Figure 45A, colored trajectories; Figure 45B, histogram bars). This distinction is nicely verified by the experimental measurement precision  $\sigma$ , which was determined to be 30-35 nm for all measurements (Endesfelder et al., 2014). We then plotted the average JD distributions as cumulative distribution functions (or CDF, integral of the probability density histogram) and fitted them assuming a multi-state Brownian diffusion distribution (Matsuoka et al., 2009) to obtain apparent diffusion coefficients and occupancies for the different molecular states. To test for the number of states present for each protein variant, fitting of 1, 2 and 3 diffusive states was applied. From these, all data showed the best fit-agreement for a two-state Brownian diffusion of each, a mobile and an immobile fraction (Figure 45C).

Moreover, we created average spatial cellular distribution heat maps (Figure 45D) of all cells in the size range of 2.5 to 4  $\mu\text{m}$  length (to exclude already dividing or atypical cells). The coordinates of each cell trajectory's were normalized for cell size and equalized for orientation by projecting them horizontally and vertically along both axes into all four quadrants of the corresponding cell. From these, we created two-dimensional, subcellular heat maps of average JD (Figure 45D, left panel), of molecule density including all trajectories (Figure 45D, middle panel) and filtered for only immobile



trajectories of  $JD \leq 160$  nm (Figure 45D, right panel). For the latter, we made explicit use of the single-molecule resolution of sptPALM imaging, which, in contrast to standard fluorescence microscopy, enabled us to separate fast from slowly diffusing molecules and to visualize their spatial distributions individually.

The results obtained from the sptPALM for the different ParC protein variants, nicely confirmed our observations using standard fluorescence microscopy. Importantly, the sptPALM results showed that ParC wild-type is best fit by a two-state Brownian diffusion of 75% immobile ( $D = 0.03 \mu\text{m}^2/\text{s}$ ) and 25% mobile fraction ( $D = 1.26 \mu\text{m}^2/\text{s}$ ). Here, the immobile fraction of ParC localizes to the poles and on the DNA (Figure 45D, right). In contrast, ParCG11V, which is trapped in its monomeric ATP-bound form, exhibits a slow fraction of 31% (Figure 45A-D), which is almost exclusively localized at the poles (Figure 45D, right panel). For ParCD39A, where the dimeric form is highly stabilized, the immobile fraction of 40% (Figure 45A-D) reconfirms a high binding affinity of the dimer to the DNA, as immobile ParCD39A was almost exclusively restricted to the nucleoid of the cell (Figure 45D, right panel). Interestingly, the slow fraction of ParCG11V shows a diffusion coefficient of zero ( $0 \mu\text{m}^2/\text{s}$ ) (Figure 45C), which indicates that ParCG11V, the monomeric ATP-bound form of ParC, is indeed the ParC variant that is strongly tethered to the pole (apparent displacements caused by the finite localization precision are factored in during the fitting, see materials and methods for details). This is in contrast to ParCD39A, for which the slow fraction exhibits a residual diffusion of  $0.05 \mu\text{m}^2/\text{s}$ . This slow residual diffusion indicates an influence of several, here not further explored, factors during the measurement, for instance the movement of the nucleoid itself as a large, slowly moving macromolecule or the existence of mix-state trajectories due to particles with transient on/off DNA binding dynamics. Furthermore, we can also observe that ParCD39A seems to be mainly bound to the nucleoid surface as mid-cell areas exhibit less ParCD39A in both molecule density heat maps (Figure 45D, middle, right).

The mobile fraction (60%) of ParCD39A exhibits a significantly reduced diffusion of  $0.91 \mu\text{m}^2/\text{s}$  as compared to the mobile fractions of all other variants (Figure 45A-C). This suggests that ParCD39A is indeed predominantly dimeric, as the free monomer should be roughly  $\sqrt{2}$  faster than the dimer with a doubled mass, which is nicely supported by the numbers ( $1.41 \cdot 0.91 \mu\text{m}^2/\text{s} \sim 1.28 \mu\text{m}^2/\text{s}$ ) (Figure 45C, compare to wild-type and ParCG11V mobile fractions). Importantly, as we did not find any significant contribution of a free dimeric diffusive state in all other ParC variants, this indicates that the dimeric form is unstable when is not bound to DNA (Figure 45C-D).

ParCK15Q, being unable to bind ATP, shows a large and highly mobile fraction of 85% of molecules with fast diffusion rate of  $1.29 \mu\text{m}^2/\text{s}$ , indicating that the mobile fraction is in a monomeric state, as expected for the K15Q substitution (Figure 45C). Furthermore, the majority of ParCK15Q is positioned randomly throughout the cell (Figure 45D, middle panel) and only the non-mobile fraction is found at the cell poles (Figure 45D, right panel). As only 15% of ParCK15Q molecules show slow diffusion, this indicates that only 15% of ParCK15Q molecules are able to enter into a binding state of both, either the pole or the DNA. ParCK15Q thus populates the same diffusive states as seen for the wild-type, but at an inverted occupation probability.

For ParCR191E the dimeric form is blocked from binding DNA. Thus, the non-mobile molecules are predominantly found at the cell poles, which can be attributed to the ATP-bound monomeric state of ParC. Furthermore, the high diffusion coefficient of  $D = 1.35 \mu\text{m}^2/\text{s}$  of the freely diffusing fraction indicates that the monomeric form is strongly predominant over the dimeric form in the ParCR191E variant. Importantly, this further indicates that when the dimer is not DNA bound it is unstable and will dissociate into the monomeric freely diffusible form.

For the double mutant ParCD39A-R191E, which prevents DNA binding of the ParC ATP-bound dimer, we can observe two fractions, a 75% mobile fraction with an average  $D$  of  $1.23 \mu\text{m}^2/\text{s}$  and a 25% immobile fraction with an average  $D$  of  $0.00 \mu\text{m}^2/\text{s}$ . The 25% immobile fraction can be spatially resolved to be a mixture of pole-bound monomers and DNA-bound dimers with a ratio of about 1:2 (Figure 45D, right). Nevertheless, for the CDF of ParCD39A-R191E in Figure 45C, a four-state model does not improve fitting accuracy as compared to a two-state model. This seems to be, in case of the two mobile dynamics of freely diffuse monomers and dimers which together yield an average mobile fraction with  $D$  of  $1.23 \mu\text{m}^2/\text{s}$ , due to the strong overlap and the dominance of the freely diffusing monomer, and due to insufficient data size in case of the two immobile fractions. Importantly, in contrast to ParCD39A, ParCD39A-R191E has a high mobile fraction with a  $D$  of  $1.23 \mu\text{m}^2/\text{s}$ , indicating the majority of mobile ParCD39A-R191E is in the monomeric form. Altogether, these data indicate that when the ATP-bound dimer form is prevented from binding to DNA (due to the R191E substitution), it is unstable and either reverts to the ATP-bound monomeric form or continues the cycle and hydrolyses ATP and forms ADP- or Apo-monomeric ParC. In either case, this indicates that DNA binding by ParC stabilizes the ATP-bound dimer and prevents its reversion into a monomeric form. Importantly, in the latter case, DNA binding slows down ATP hydrolysis, and stabilizes the ATP-bound dimer, consequently increasing the time it is associated with DNA.

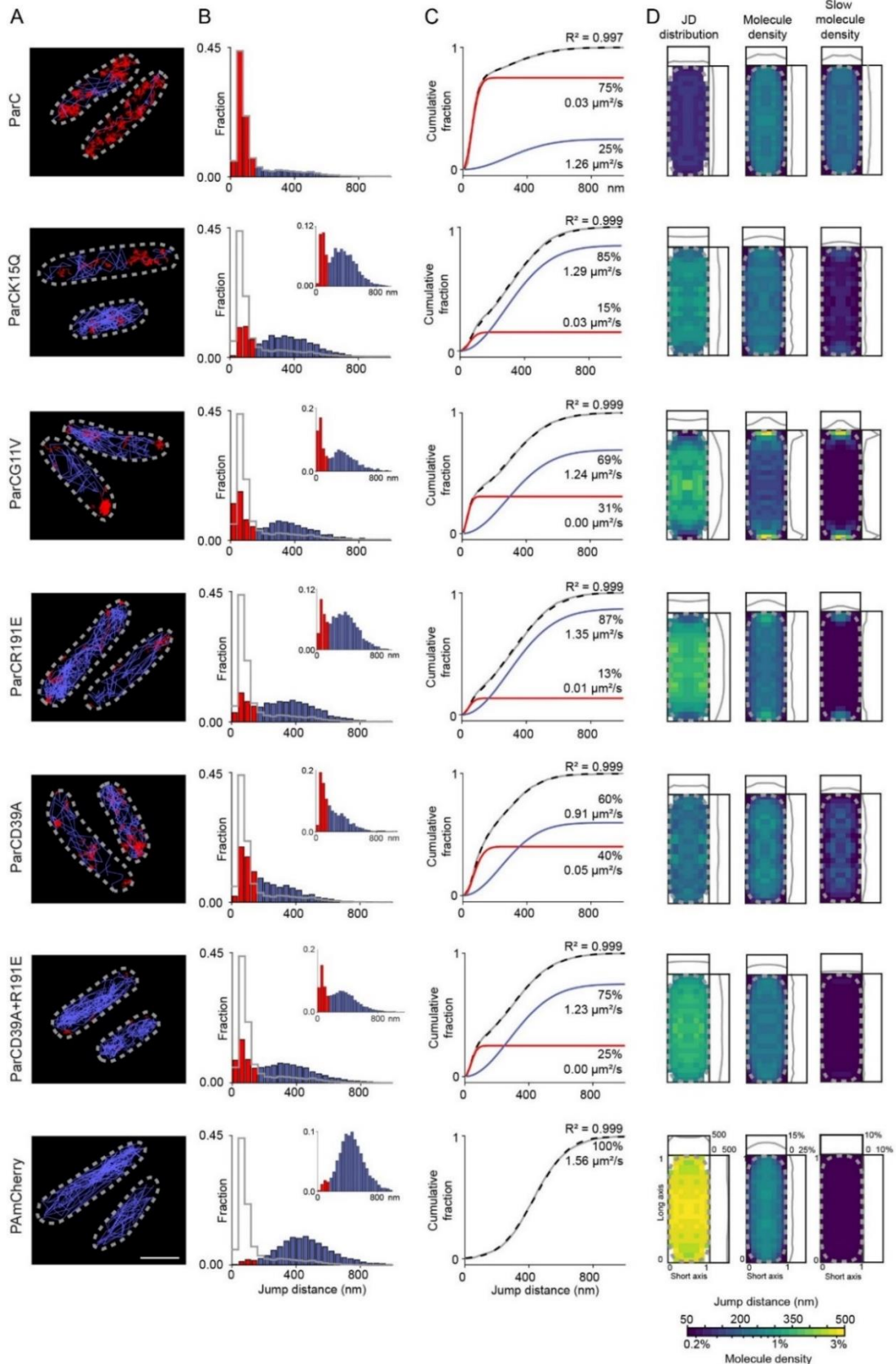


**Figure 45. Differential diffusion rates of distinct ParC protein states.** (A) Exemplary *V. parahaemolyticus*  $\Delta\text{parC}$  cells showing the spatial distribution of trajectories of single PAmCherry-ParC molecules obtained during sptPALM imaging. The label on the left indicates the respective ParC protein variant. Trajectories are color-coded by their average jump distances (JDs) between adjacent frames, “slow” molecules ( $\leq 160$  nm) are in red, “fast” ( $>160$  nm) appear in blue. Cell boundaries are indicated by dashed gray lines. Scale bar is 1  $\mu\text{m}$ . (B) Bar plots showing the distribution of single molecule ParC dynamics represented as a probability density function of average JD per trajectory. Color coding remains

as in (A), i.e. “slow” = red, “fast” = blue. (C) Average JD values per trajectory from (B) represented as cumulative distribution functions (CDFs) and fitted by a two-state diffusion model. Next to the CDF (black), the two-state fit (dotted gray line) and the obtained fit parameters and single-state distributions (slow state in red, fast state in blue) are shown. For more details see materials and methods. (D) 2D 22×8 pixel heatmaps (left) of the spatial distribution of the particles’ average JD per pixel calculated from size and orientation normalized cells (see materials and methods). White pixels denote areas where no average JD is calculated due to low statistics. 2D heatmaps (middle and right) of molecule density showing all trajectories (middle one) or only the slow fraction (average JD  $\leq 160$  nm) of cells normalized as before. Measurement statistics can be found in material and methods in Table 11.

As control, cytosolic PAmCherry shows fast diffusion throughout the whole cellular volume. Correspondingly, the JD distribution can be fitted by one diffusive state (which is slightly skewed by cellular confinement, see materials and methods) with an average apparent diffusion coefficient of  $1.56 \mu\text{m}^2/\text{s}$ .

Finally, when examining the slow diffusive fractions in a more detailed look, it becomes apparent that the ParC variants with only polar slow fractions (ParCG11V, ParCR191E), exhibit completely immobile molecules with  $D = 0.00 \mu\text{m}^2/\text{s}$ , whereas variant ParCD39A with an exclusively DNA-bound but no polar immobile state shows a residual movement of  $D = 0.06 \mu\text{m}^2/\text{s}$ . We therefore speculated that the immobile diffusion of  $0.03 \mu\text{m}^2/\text{s}$  of the ParC wild-type and variant ParCK15Q can be explained by a two-state mixture of a purely immobile polar fraction and a slightly diffusive DNA-bound fraction. We therefore spatially separated and extracted the slow trajectories of the polar volume for all ParC variants (Figure 46, dark red 2×3 pixel box). Indeed, whereas variants ParCG11V and ParCR191E show a 100% immobile polar fraction with  $D = 0.00 \mu\text{m}^2/\text{s}$ , the immobile polar fraction of ParC wild-type could only be fitted by a two-state model which reveals that the polar volume is dominated by a high (86%) fraction of immobile pole-bound ParC with  $D = 0.00 \mu\text{m}^2/\text{s}$  but also contains a minor (14%) second fraction of slightly diffusing molecules with  $D = 0.06 \mu\text{m}^2/\text{s}$  (Figure 46). We would expect a similar distribution for ParCK15Q but could not fit a two-state model due to an overall low sample size of slow ParCK15Q trajectories as ParCK15Q statistics are dominated by the freely diffusing monomer.

Furthermore, as the polar, immobile fraction of all ParC variants is strongly dominated by completely immobile molecules and we did not observe any mixed trajectories that show changes of diffusive state, we can deduce that the bound time of ParC to the pole is significantly longer than several hundreds of milliseconds (typical length of sptPALM trajectories are between 60 – 500 ms). Overall, these data show that ParC’s intracellular localization dynamics depend on its conformational state, regulated by its nucleotide-bound state and ability to bind DNA. Our results indicate that ParC’s intracellular pattern formation (gradient formation) is based on the cycling of ParC protein molecules between distinct conformational states and the redistribution of proteins by

cytosolic diffusion and the formation of a stable ParC sink at the cell pole. Particularly, our data provide evidence that differential diffusion rates of distinct protein states drive gradient formation.

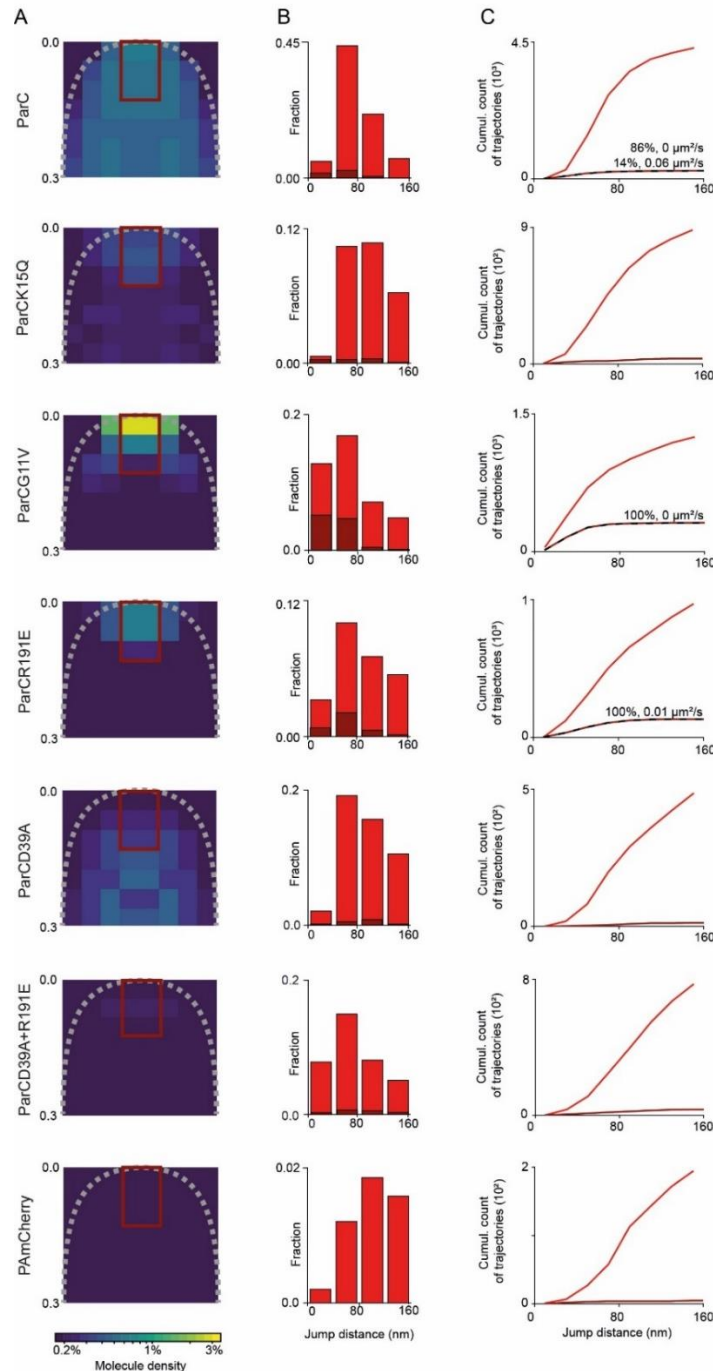


**Figure 46. sptPALM showing the localization and fraction of immobile polar ParC.** (A) A zoom-in of the spatial molecule density heatmap for slow trajectories ( $JD \leq 160$  nm) as shown in Figure 45D (right). The dark red squares mark at the cell pole regions containing the trajectories analyzed in (B) and (C). (B) Zoom-in into the slow part of the average JD per trajectory distribution of Figure 45B. On top of the total fraction of trajectories with  $JD \leq 160$  nm, the JD distribution of only polar molecules from the selected area is overlaid in dark red. (C) Zoom-in the absolute number CDF of average JD distributions (red) and the absolute number CDF (dark red) of the polar fraction from (A, B). Fitting of the relevant (significantly larger than 1% of the total molecule density) polar fractions by CDF models (gray dotted line) for ParC, ParCG11V and ParCR191E reveals a single, immobile state for ParC wild-type, with a dominating immobile state of 86%

---

## CHAPTER 4: DISCUSSION

### 4.1 *PART I* - Coupling chemosensory array formation and localization

The chemosensory arrays have been referred to as the “most prominent signaling structures known in bacteria” (Sourjik & Armitage, 2010). Their ordered architecture and precise localization are essential factors for bacterial chemotaxis. In *V. cholerae* and *V. parahaemolyticus* chemosensory arrays are located at the cell poles and follow a cell cycle dependent localization. The localization of arrays in these bacteria is mediated by the ParC/ParP system. Earlier it was discovered that ParP was required for CheA2’s polar retention in *V. parahaemolyticus* (Ringgaard et al., 2014). In this thesis, ParP’s interaction network was analyzed and reframed into a new model where not just CheA but also the MCP proteins are involved. Importantly, these interactions demonstrate that ParP couples chemosensory array formation and localization.

In this study we identified MCP proteins as important interaction partners for ParP. The BACTH-based genomic screen identified 15 distinct MCPs, and all but two MCPs of *V. cholerae* have the motif within the SD at the most distal tip of the receptors towards the cytoplasm that mediates ParP-MCP interaction. Likely, the screen identified only 15 out of the 45 MCPs because only about 50,000 colonies were screened. Moreover, the screen could only identify those ParP interaction partners which were fused in-frame to the *t18* domain of adenylate cyclase during genomic library generation. While these factors make the analysis not comprehensive, they explain why more MCPs were not found and also why other known interaction partners of ParP, namely CheA2 and ParC (Ringgaard et al., 2011, 2014), were not identified.

Additionally, microscopy experiments revealed that ParP integrates into signaling arrays via its interactions of the AIF domain with the conserved protein interaction tip located at the SD of the MCPs and with CheA2 LID domain. Through these complex interactions, ParP promotes array formation without apparent compromise in array structure. ParP’s AIF domain similarity to CheW and the P5 domain of CheA proteins in residues that mediate interactions with the MCPs, suggest that ParP might compete with CheW and the P5 domain for MCP binding, thereby becoming part of the chemotactic array. Previous studies indicate that other proteins with CheW-like structures can compete with CheW and the P5 to become part of the array in a comparable manner (Asinas & Weis, 2006; Erbse & Falke, 2009; Levit et al., 2002). For instance, CheV can replace CheW (Alexander et al., 2010) or the P5 domain of CheA proteins (Briegel et

al., 2012). Despite of their similar activity, namely the capacity of CheW, P5 domains and ParP-AIF to recognize and bind the MCP interaction tip, all have clearly distinct functions and interestingly, form their own clades of CheW-like domains. These observations suggest that CheW-like domains have evolved to interact with the MCPs within the core unit of arrays to mediate diverse functions, such as signal transduction, array formation and intracellular localization.

Transactions between ParP and its array partners (namely MCPs and CheA2), likely reflect the balancing of the requirement for an additional component that aids array localization, without altering array structure or function. Arrays can still form if one, ParP or CheA2 is absent, due to the presence of the other. However, in the absence of both proteins, the arrays no longer assemble or do so at relatively low levels when compared to the wild-type strain, as observed through fluorescence microscopy as well as cryo-EM experiments. In contrast, arrays are able to form at the level close to the wild-type without CheA2, suggesting that ParP, and likely CheW and CheV proteins, can fully make up for CheA2's absence. However, it is unknown how different in their stability are arrays formed without CheA proteins, nor is clear how much each scaffolding protein, particularly ParP, contribute to array stability in a wild-type scenario.

In the current model of array structure, two CheA2 proteins are present within the core unit, dimerizing through their respective P3 domains (Figure 47), an important interaction that contributes to array stability and signal transduction (Briegel et al., 2011, 2012, 2014b; Li & Hazelbauer, 2011; Li et al., 2013). If ParP-AIF replaces the P5 domain of CheA2 within the arrays, P3 dimerization, and its associated array stabilization, would be lost. Nevertheless, earlier it was shown that ParP-CheA2 interaction (via the LID region) reduces dissociation of CheA from arrays in *V. parahaemolyticus* (Ringgaard et al., 2014) and thereby provides an alternate means of stabilization. Thus, the data in this study favor a model where ParP-AIF replaces some P5 in binding the MCP interaction tip within the chemotaxis core unit, and is tethered there through binding to the LID domain of the remaining monomer CheA2 of the core unit. Presumably, this AIF-LID interaction is able to substitute for the lack of P3 dimerization and hence the array might gain some stability (Figure 47).

Since ParP is able to dimerize via its N-terminus (Ringgaard et al., 2014), it is also possible that ParP dimer is able to replace the CheA2 dimer within the core unit of wild-type cells, resulting in a core unit comprised of two CheWs and a ParP dimer (Figure 47). Core units consisting of only CheW, Par and MCPs reasonably constitute the arrays observed within a CheA2-deficient strain, where arrays formed in levels similar to wild-type. Additional studies will be required to elucidate whether interactions between ParP-

CheW and ParP-P5 occur. Besides, the factors that modulate the MCP interaction tip's accessibility to different partners represent intriguing open questions. In a wild-type background, arrays might include ParP and CheW proteins, whereas in the  $\Delta parP$  and  $\Delta cheA2$  deletion backgrounds, arrays form which contain only scaffolding proteins, not only CheW and ParP but also CheV. Furthermore, it is also a possibility that the dimerization domain of ParP could link ParP from neighboring core units, and in this way promote retention of ParP itself as well as other chemotaxis proteins within the array, thereby contributing to array stability and ultimately their sequestration at the cell pole via ParP's ParC interaction domain.

Previous studies in the  $\alpha$ -proteobacterium *R. sphaeroides* identified a ParA-like protein, with similar activity to ParC. Indeed, PpfA ensures proper segregation and positioning of the cytosolic arrays over the bacterial nucleoid by means similar to that used by proteins involved in plasmid segregation (Ringgaard et al., 2011; Roberts et al., 2012; Thompson et al., 2006). PpfA mediates array localization in concert with TlpT, a predicted cytoplasmic chemoreceptor, which similarly to ParP, links array formation and positioning. In the case of TlpT, its N-terminus interacts with PpfA, likely stimulating PpfA ATPase activity (Roberts et al., 2012; Thompson et al., 2006; Wadhams et al., 2005) which is ultimately required for proper placement and segregation of cytoplasmic chemotaxis in *R. sphaeroides*.

Notably, ParP's interactions with the chemotaxis proteins in the core unit in *V. cholerae* (CheA2 and the MCPs) are also important for ParC-mediated retention of ParP at the cell poles and for polar localization of ParC itself. Disruption of ParP's interactions with MCPs and CheA2 resulted in a much higher percentage of non-polar (cytosolic) ParC and ParP. Thus, although ParC is capable of recruiting ParP to the cell pole, sequestration of ParP and ParC is less efficient when ParP is unable to interact with MCPs and CheA2. As seen earlier with ParC (Ringgaard et al., 2011), here we show that there is a continuous exchange of ParP between the cell pole and the cytoplasm. The photobleaching-based comparisons of ParP and ParP2PM suggest that ParP's capacity to integrate into signaling arrays influence its release from the pole to the cytoplasm. Particularly, that integration of ParP into signaling arrays prevents the release of ParP molecules from the cell pole and consequently promotes its retention at this site. Hence, ParP's integration into arrays modifies its own and likely ParC's subcellular localization dynamics, promoting their polar retention.

Interestingly, ParP retains partial function as long as one of its network connections to the core unit (i.e. either CheA2 or MCPs) exists. Only loss of both ParP's connections to the core unit results in a non-functional ParP variant. Furthermore, when one of its



interactions is altered, the retention of ParP and ParC at the pole is compromised to a similar extent as to when ParP is incapable of interaction with CheA or the MCPs. These observations suggest that when ParP loses a network connection at the core, it can still function in mediating array localization due to the remaining connection. However, the ability of ParP to mediate retention of its network components at the cell poles is severely compromised when only one interaction is halted. This further emphasizes the importance of ParP's interconnectivity within the proteins involved in chemotactic signaling cascade, which ultimately regulate their polar placement and retention.

Taken together, these findings show that ParP's high connectivity allows it to serve as a critical nexus that regulates the temporal dynamics of its network constituents and stabilizes the polar localization of the polar protein ParC and itself. Furthermore, it facilitates the localized assembly and inheritance of signaling arrays at the pole, hereby ensuring proper cell pole development.

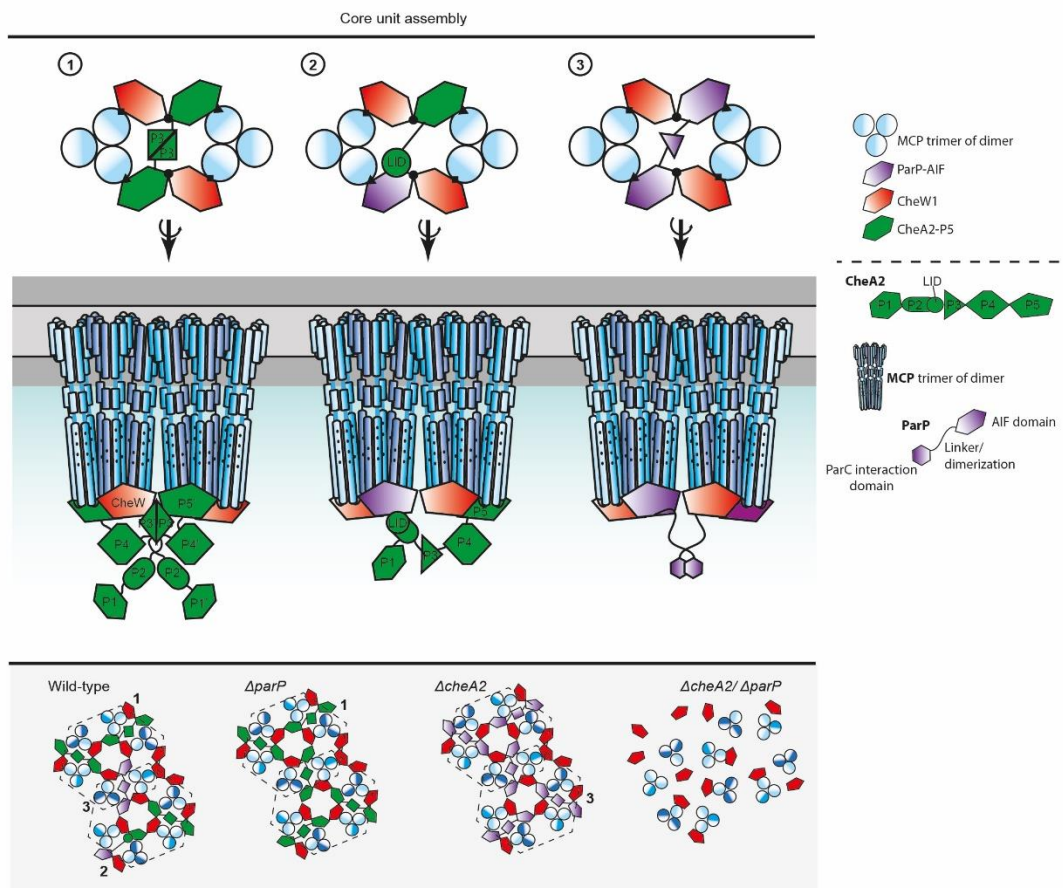


**Figure 47. Model of ParP's integration within the core unit of the chemotactic arrays.** Core units assemble in three types. In type 1 two CheA2 monomers are present, and they dimerize through their P3 domains. Type 2 occurs if ParP-AIF replaces a CheA2 monomer, where possibly the stabilization given by the P3 domains interaction is replaced by the interaction between ParP and the LIP region. Type 3 could take place in the absence of *cheA2*, where ParP, due to its ability to dimerize, replaces CheA2, resulting in a core unit composed of CheW1 proteins and ParP alone. At the bottom of the figure are schemes of the possible arrays formed in different strains. Core units consisting only of CheW1, ParP and MCPs presumably form the arrays observed within the  $\Delta cheA2$  strain. In the wild-type strain, arrays might consist of all three types of core units, whereas in the strain  $\Delta parP$ , arrays consist of type 1 core

units. More experimental work is required to elucidate whether interactions between ParP and CheW1 and ParP and the P5 domain occur; similarly the factors that modulate the MCP's accessibility to different protein partners remain undiscovered. Hexagonal arrangement of MCP trimers of dimers is highlighted by dashed black lines.

## 4.2 PART II - Base plate variability of chemoreceptor arrays in *V. cholerae*

The architecture of bacterial chemotaxis arrays has been predominantly studied in the model organism *E. coli*. It was through studies in this bacterium that the structure of the core unit was determined. In *E. coli*, the structural core of the array is composed of rings formed by alternating P5 domains of CheA and CheW. These rings network the trimers of receptor dimers in the typical hexagonal arrangement. The architecture of these arrays in which six rings of CheA/CheW surround a ring lacking CheA predicts an array stoichiometry of 1:1:6 of CheA:CheW:MCP, or 1:2:6 if the CheA-less hexagons are not empty but instead filled with CheW proteins only (Briegel et al., 2012; Cannistraro et al., 2011; Erbse & Falke, 2009; Li & Hazelbauer, 2004). These proportions roughly agree with the experimentally determined protein ratios previously published for *E. coli* (Erbse & Falke, 2009; Li & Hazelbauer, 2004; Ortega & Zhulin, 2016). It is possible that because of the flexible stoichiometry among the components of the array, the direct visualization of the CheW-only rings *in vivo* has not been reported. Meanwhile, in the recombinant array assembled *in vitro*, array formation was commonly promoted with CheW in molar excess of CheA, typically at the ratio of 1:2 (Cassidy et al., 2015; Haglin et al., 2017). In these studies, such a high concentration of CheW may strongly favor the filling of the empty rings with CheW, which as a result permitted cryo-EM studies and subtomogram to reveal this CheW-only rings *in vitro* (Cassidy et al., 2015). Nevertheless, it is still unclear whether all rings empty of CheA are filled up with six CheW monomers to create a complete ring structure *in vivo*.

In this study, we analyzed a *V. cholerae* strain without any *cheA* genes, which provided an extreme case in which the majority of the receptor trimers of dimers bind to CheW at the base plate. Previous data suggest that expression of genes in cluster II as well as formation and localization of arrays composed of proteins encoded by the genes in this cluster were independent of cluster I and III genes (Ringgaard et al., 2015). In agreement with these observations, here we show that hexagonal packing of arrays consisting of proteins from cluster II do not require kinases from cluster I and III. Interestingly, arrays without CheA proteins maintain the classical hexagonal architecture, with an approximated 12 nm spacing, a property deemed to be universal for all arrays (Briegel et al., 2009). Moreover, the data in this study also show that although CheA2 from cluster II is essential for proper chemotaxis activity, it is not required for localization of cluster II arrays. These data indicate that in the absence of CheA proteins, *V. cholera* arrays retain their hexagonal packing and polar localization of arrays is not affected.

However, even though arrays formed and retained their classical architecture without CheA in *V. cholerae*, it is important to notice that previous experimental evidence showed that CheA is important for maintaining the overall structural integrity of the chemoreceptor arrays. The CheA homodimer integrates into two neighboring receptor hexagons which are then linked by the dimerization of the P3 domains (Bilwes et al., 1999). Thus, CheA dimerization is crucial for interlinking neighboring CheA/CheW rings and also for establishing the entire allosteric network of the complex (Piñas et al., 2016). In *E. coli*, the total ratio of CheA dimer to the total amount of coupling proteins is 1:4, assuming that all CheA-free rings are filled with CheWs. This high CheA occupancy ensures that at least each trimer of receptor dimers directly binds to a P5 domain of CheA. Consequently, the hexagonal packing is ensured regardless of the presence of the CheW-only rings. The stoichiometry data show that the ratio of CheA dimer to other coupling proteins in *V. cholerae* is 1:14, which is remarkably different than in *E. coli*. Therefore, this could mean that there are considerably fewer CheA dimers in the base plate to function as “structural staples” to interlink the rings, which are predominantly formed by CheW. It is worth mentioning that the low abundance of CheA does not translate in a complete absence of CheA/CheW rings in cluster II arrays. Yet, this structure is likely to be interspersed in the lattice given the low abundance of CheA. Conversely, interspersed CheA/CheW rings would not provide an equivalent stability to the array architecture as extensively networked CheA/CheW in rings do.

Ultrastability has been assumed to be one of the hallmarks of chemoreceptor arrays among different species, a characteristic that is based on the universal appearance of the array lattice and the stability studies in the arrays of the model organism *E. coli* (Briegel et al., 2009; Erbse & Falke, 2009). The cellular stoichiometry of the proteins in the array of *V. cholerae*, namely CheW1, CheA2, ParP and the four CheV proteins, provides a plausible explanation of why cluster II array is not as stable as the array in *E. coli*. We further expect a variance of the chemoreceptor array stability among species in which stoichiometry of the base plate components may also deviate from the one observed in *E. coli*.

ParP from *V. parahaemolyticus* forms dimers (Ringgaard et al., 2014) similar to those formed by ParP from *V. cholerae*, as suggested by BACTH assays. ParP may form dimers through its flexible linker between its C-terminal AIF domain and the N-terminal ParC interaction domain. Thus, ParP may substitute for the CheA homodimer in the base plate instead of competing with the CheW monomer. If this is the case, ParP is potentially capable of contributing to array stability in a similar manner to CheA dimers, despite its comparatively low levels.

The stoichiometry of the *V. cholerae* cluster II base plate components reported in this study suggest a high level of dynamics in base plate architecture during array formation. Due to a more diverse composition of the base plate, it is conceivable that the array develops at the cell pole through a dynamic recruitment of receptors that bind CheA2, ParP, CheV and predominantly CheW. This is contrasting to *E. coli*, where the core units are thought to assemble first, and subsequently associate to form the extended receptor arrays with a strict stoichiometry and ordered arrangement of both the receptors and the base plate protein CheA and CheW (Briegel et al., 2014b). This assembly process may reflect the relative simplicity of the *E. coli* chemotaxis system. This compositional diversity of base plates can also be found in other organisms for which the ratios of chemotaxis proteins have been determined. For example, in *B. subtilis*, the base plate also contains CheV, and array stoichiometry was determined to be 1:1:3:23 for CheA:CheW:CheV:MCP (Cannistraro et al., 2011). These differences in protein ratios indicate that the protein arrangement in the base plate varies significantly depending on the organism, even though the receptors are packed in a 12 nm hexagonal lattice-like structure (Briegel et al., 2009, 2012). It seems that the composition of the base plate tolerates different levels of base plate proteins. This statement is supported by previous results that show the loss of ordered CheA distribution in arrays when the array components are overexpressed from different plasmids (Briegel et al., 2014b).

Overall, the results in this work emphasize that there are significant differences in the composition and architecture of the chemotaxis arrays between bacteria species. In the case of *V. cholerae*, the less stable arrays are the result of the variable composition of the base plate proteins. This observation is consistent with the high number of MCP predicted for *V. cholerae*. MCPs integration into the array is believed to depend on the presence of specific coupling proteins (Ortega & Zhulin, 2016). Additionally, a recent study indicates that the P5 domain of CheA is not directly controlled by the receptors; rather the MCPs manipulate CheW, which in turn influence the P5 regulatory activity (Piñas et al., 2018). Considering all this information, *V. cholerae* arrays may employ several scaffolding proteins to integrate the signals captured by different MCPs and influence kinase activity accordingly.

The model proposed in this work implies that different coupling proteins can participate in array formation and are influenced by certain MCPs, depending on the environmental cue detected. Furthermore, the array variability may enable a swift adaptation exchange of different chemoreceptors within the existing array lattice in response to alterations in the environmental conditions. The capacity to include other coupling proteins in the base plate is a property that has been previously studied in several organisms. For instance, in *Helicobacter pylori*, CheV1 and CheW are required

to form functional arrays, although CheW had greater influence in kinase activation than CheV (Abedrabbo et al., 2017). On the other hand, in *B. subtilis* CheV can modify (i.e. increase or decrease) kinase activity depending on the methylation state of the MCP proteins (Walukiewicz et al., 2014). In contrast, the *E. coli* system might have evolved to form ultrastable arrays, which likely provide a robust more generic chemotaxis response without the need for adding or exchanging array components once they are assembled. Finally, our findings highlight the need to study chemoreceptor array structure and composition in different bacteria to properly understand the diversity and biological significance of chemotaxis signaling.

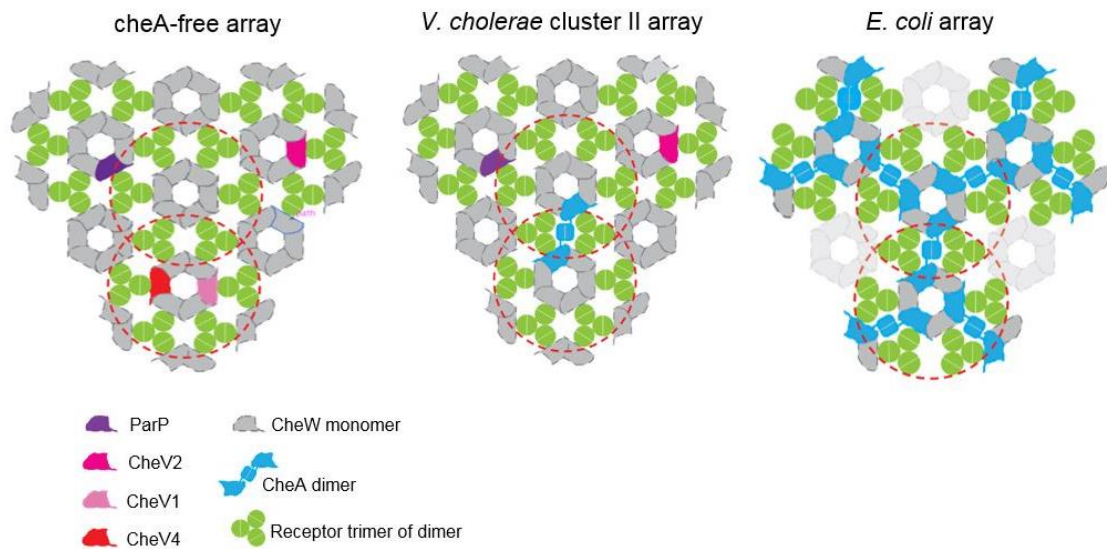


**Figure 48. Different arrangement of CheA dimer occupancy in different arrays.** (Left) In the CheA-free array in *V. cholerae*, the base plate is predicted to be composed of CheW-only rings with sporadic insertion of ParP, CheV1 and CheV4. The absence of CheA dimer results in no networks of the CheW dominant rings in the base plate. (Center) In the wild-type *V. cholerae* array, CheA serves as a “structural staple” that interlinks the ring networks in the base plate to increase the overall stability of the chemoreceptor array. Because of the low occupancy of CheA to other coupling proteins, only a few neighboring receptor hexagons are structurally interlinked by CheA dimers. For (Left) and (Center) CheA refers to protein CheA2. (Right) In *E. coli*, the ratio of CheA dimer to CheW ensures that the hexagonal packing of the receptors is secured, mainly by the CheA/CheW rings with less reliance on CheA-empty rings. The dashed red circles outline individual receptor hexagons in the receptor array structure. This scheme does not represent the accurate proportion of coupling proteins for *V. cholerae* arrays, see main text for details.

### 4.3 **PART III - Differential diffusion rates of distinct protein states drive protein gradient formation**

Earlier, ParC proteins were identified as a new sub-family of Mrp/MinD P-loop ATPases present in  $\gamma$ -proteobacteria, where it mediates the positioning of chemosensory arrays in the human pathogens *V. cholerae* and *V. parahaemolyticus* (Ringgaard et al., 2011). In a former study, it was showed that homologues of *parC* are present in more than 50% of chemotaxis operons (Ringgaard et al., 2011). However, most of the current knowledge of ParA-like systems relies on the research of several paradigmatic model proteins with well-characterized cognate protein interaction partners. This thesis work builds upon the existing knowledge of ParA-like ATPases, and employs fluorescence and quantitative sptPALM to provide new insights into the mechanism behind ParC's subcellular localization and to explore how protein cellular gradients are formed.

The data presented here shows that ParC forms a protein gradient with a concentration maximum at cell-pole and a minimum at mid-cell. Furthermore, it can be observed that ParC's intracellular localization-dynamics depends on its conformational states, regulated by its nucleotide-bound state and ability to bind DNA. The results indicate that ParC's intracellular pattern formation (the gradient) is based on the cycling of ParC protein molecules between distinct conformational states and the redistribution of proteins by cytosolic diffusion and the formation of a stable ParC sink at the cell pole. Particularly, the data provide evidence that differential diffusion rates of distinct protein states drive gradient formation.

The data obtained in this study support a model where the ATP-bound monomeric form of ParC (ParCG11V) is unable to bind DNA and is freely diffusible when present in the cytoplasm. However, due to its high affinity for the cell pole, freely diffusing ATP-bound monomeric ParC molecules are captured, sequestered and importantly highly stabilized at the pole, where they experience a diffusion rate of zero – hence the “diffusion-and-capture” mechanism for ParC sequestration at the pole. Consequently, the cell pole acts as a sink and ensures the formation of a significant concentration maxima of stable monomeric ATP-bound ParC molecules in the cell pole (Figure 49). We suggest that this high concentration of monomeric ATP-bound ParC at the cell pole shifts the equilibrium between ATP-bound monomer and dimer towards dimer formation. As a result, ATP-bound dimer formation is stimulated at the cell pole. Recently formed dimers have no affinity for the cell pole, thus diffuse freely in the cytoplasm and are unstable. Due to their high instability they quickly dissociate if they are not bound to DNA. However, the ParC dimer has high affinity for DNA and will associate with the bacterial

nucleoid, significantly slowing down its diffusion rate. The data indicate that the ParC dimer is unstable when it exists in its freely diffusing form (i.e. not associated with DNA). Consequently, the dimer density will decrease as a function of distance from the pole, due to the increasing time period, the freely diffusing dimer decreases as the travel distance from the pole increases. That is, the likelihood of dimer dissociation increases with increasing distance from the pole towards mid-cell. In consequence only dimers that associate with DNA will remain stably associated to the DNA. In summary, as a consequence of the reduced diffusion caused by DNA binding, and the instability of non-DNA associated dimers, the dimers are retained in close proximity of the cell pole and as mentioned earlier, the dimer density will decrease as a function of distance from the pole (Figure 49).

How ATP-dimer dissociation by ATP hydrolysis is regulated in ParA-like proteins is still not clear; however, ParC itself has a weak intrinsic ATPase activity (Ringgaard et al., 2011, 2014). Since the ParC dimer is primarily associated with the DNA and unstable in its freely diffusing form, this suggests that DNA binding has a stabilizing effect on dimer association, and thus likely decreases the probability of ATP hydrolysis. Furthermore, since the ParC dimer has no affinity for the cell pole it is absent from this region, where ParC's partner protein ParP is exclusively positioned (Alvarado et al., 2017; Ringgaard et al., 2014). In addition it is unlikely that ParP is able to stimulate ParC's ATP hydrolysis due to the spatial exclusions of ParP and the ParC dimer in the cell.

Earlier, we showed that ParP acts to sequester and stabilize ParC at the cell pole and ensures its association with the large macromolecular complex of chemotaxis signaling arrays (Alvarado et al., 2017; Ringgaard et al., 2014). Indeed, ParC's tight association, via ParP, to such a large rigid structure could explain the very stable, non-diffusive ( $D = 0.00 \mu\text{m}^2/\text{s}$ ) behavior of ParC molecules bound at the cell pole. Taken together, these observations suggest that it is the intrinsic ATPase activity of ParC that drives ATP hydrolysis and its consequential dissociation as a dimer from the nucleoid space, in the formation of its free and highly diffusible monomeric form. These monomers eventually undergo nucleotide exchange, are recaptured and sequestered at the cell pole and the cycle is restarted. Furthermore, this supports a model where ParP acts to ensure the formation and stabilization of the sink of ParC at the cell pole, this is ensuring the ParC concentration maxima at the pole, which is essential for gradient formation. Thus, a combination of reduced diffusion by association with chromosomal DNA, and instability of non-DNA bound dimers, ensures that a higher concentration of ParC dimers is retained in close proximity to the cell pole, with a decreasing concentration towards mid-cell (Figure 49).



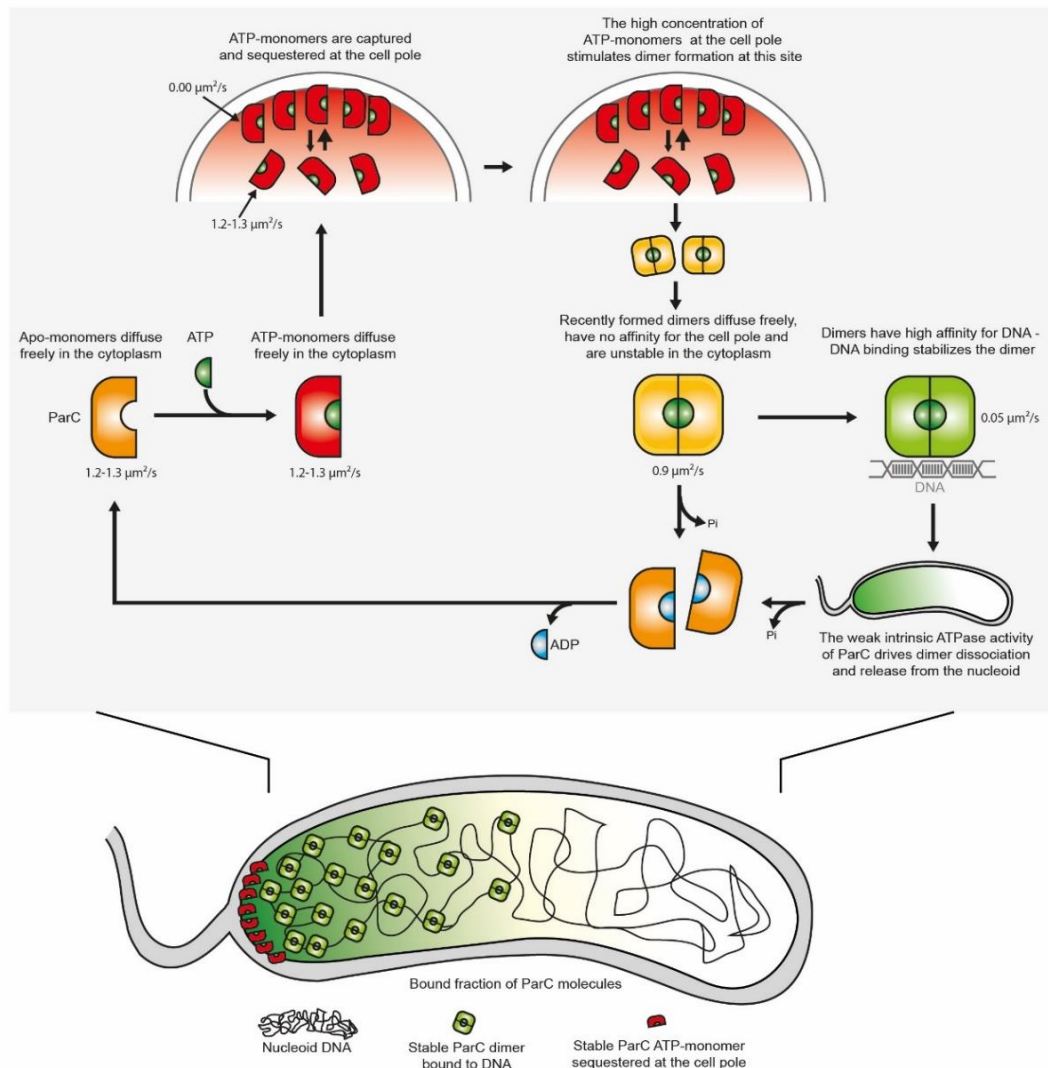


**Figure 49. Differential diffusion rates of distinct protein states in a diffusion-and-capture mechanism drive protein gradient formation.** Schematic showing the intracellular localizations and localization dynamics of different ParC protein variants. Localization site and dynamics are regulated by differential diffusion rates of distinct ParC's protein states, ultimately driving ParC protein gradient formation. Numbers indicate the specific diffusion rate of the corresponding ParC protein state. The ATP-bound monomeric form of ParC is unable to bind DNA and is freely diffusible in the cytoplasm. Due to its high affinity for the cell pole, diffusing ATP-bound monomeric ParC molecules are captured, sequestered and highly stabilized at the pole, thus the "diffusion-and-capture" mechanism. Due to the high affinity of the ATP-bound monomer for the cell pole, the pole acts as a sink and ensures the formation of a significant concentration maxima of monomeric ATP-bound ParC molecules at the pole. The high polar concentration of monomeric ATP-bound ParC stimulates ATP-bound dimer formation in the polar region. Recently formed dimers diffuse freely, have no affinity for the cell pole but are unstable in the cytoplasm, thereby they quickly dissociate if not bound to DNA. However, the ParC dimer has high affinity for the DNA and will associate with the bacterial nucleoid, significantly slowing down its diffusion rate. As a consequence of the reduced diffusion due to DNA binding, and the instability of non-DNA associated dimers, the dimers are retained in close proximity to the cell pole and the dimer density will decrease as a function of the distance from the pole towards mid-cell. Weak intrinsic ATPase activity of ParC drives dimer ATP hydrolysis and its consequential dissociation to its freely diffusible monomeric form and release from the nucleoid space. Released monomers eventually undergo nucleotide exchange, are recaptured and sequestered at the cell pole and the cycle is repeated. In this way, a combination of the reduced diffusion and association with chromosomal DNA, and the instability of non-DNA associated dimers, ensures that a higher concentration of ParC dimers is kept at a close proximity to the cell pole cytoplasm, with a decreasing concentration towards mid-cell.

Furthermore, this constant exchange of ParC molecules between the cell pole and the cytoplasm ensures a continuous pool of cytosolic ParC throughout the cell cycle. As a consequence, once the HubP-dependent ParC anchor develops at the new cell pole, freely diffusing ATP-bound monomeric ParC molecules from the cytoplasmic pool can then be captured at both poles and a new ParC concentration sink is generated at the new pole. As a consequence of the continuous release of ParC dimers from the old pole and their turnover to monomeric ParC in the cytosolic space, a redistribution of ParC from the old to the new cell pole occurs. Over time, an equilibrium is reached resulting in two equal concentration sinks at both cell poles with two ParC gradients extending towards mid-cell.

Several spatiotemporal positioning systems in bacteria have been shown to rely on the characteristic property of ParA-like proteins to be able to switch between distinct protein stages depending on their nucleotide-bound state, examples include the MinCDE system (de Boer et al., 1989; De Boer et al., 1992; Hu et al., 1999, 2002; Lackner et al., 2003; Lutkenhaus, 2012; Meinhardt & de Boer, 2001; Raskin & de Boer, 1999), the ParABS systems (Briegel et al., 2009; Gerdes et al., 2010), the PomXYZ complex (Schumacher et al., 2017; Treuner-Lange et al., 2013) and the MipZ system (Kiekebusch et al., 2012; Thanbichler & Shapiro, 2006). The molecular mechanism for ParC mediated gradient formation is similar to that indicated for MipZ of *C. crescentus*, where it was proposed that different diffusion rates of MipZ protein variants regulate its gradient formation. Indeed, it seems that it is a fundamental, essential prerequisite that the generation of such gradients, as observed for ParC and MipZ, is driven by distinct protein diffusion rates. Here, using conventional fluorescence microscopy and sptPALM, we show for the first time that ParC molecules experience differential diffusion rates depending on its distinct protein state, and thus provide evidence for what was believed to be one of the underlying essential principles in the establishment and maintenance of such gradients that extend from the cell pole towards mid-cell.

---

## CHAPTER 5: CONCLUSIONS AND FUTURE PROSPECTS

In this work we identified a new interaction partner of ParP, the MCPs. Furthermore we provided evidence showing that ParP targets conserved residues found at the protein interaction tip of the SD of MCPs, residues that are also required for MCP interaction with CheW and CheA. Additionally, we showed that the AIF domain of ParP, which is related to CheW and P5 of CheA, coordinates the interaction of ParP with CheA and the SD. Thus, the presence of two interaction regions within the AIF domain is proposed. More interestingly, the data suggests that ParP, through its AIF domain, participates in array formation. Thereby, when combining the roles of the AIF domain at the N-terminus to the activity of the ParC interaction domain at the C-terminus, it is possible to appreciate how ParP couples array positioning and formation. Notably, our experiments suggest that ParP performs these two activities independently of each other. While there is no evidence of ParP's influence in the signaling activity of the arrays in *V. cholerae*, it is clear from our data that ParP's interactions with CheA, MCPs and ParC, promote their retention at the poles.

Additionally, in this work we showed that the array base plate in *V. cholerae* has the ability to localize properly at the cell poles and assemble in the classical hexagonal packing in the absence of all putative kinases. These observations suggest that arrays' architecture relies more on the scaffolding proteins, namely ParP, CheV and CheW. Moreover, while previous research showed that all CheV proteins form part of cluster II arrays, others have suggested that only CheV2 participates in array formation. Our data is in agreement with the latter proposal since we observed that only CheV2 associates with polarly localized clusters in conditions that favor formation of arrays from cluster II proteins. However, we also observed that in the absence of CheA proteins, other CheVs formed polarly localized foci, suggesting their possible involvement in array formation when one component of the arrays is absent. Altogether, the data indicate that the base plate is a variable structure, which can include several proteins. Interestingly, this variability seems to account for the decreased ultrastability displayed by *V. cholerae* arrays.

Moreover, we showed that ParC, an ATPase involved in the subcellular placement of chemotaxis arrays in *V. cholerae* and *V. parahaemolyticus*, forms an intracellular gradient. In addition, the observations presented here indicate that this gradient is regulated by ParC's ability to associate with DNA and bind ATP. The data

---

suggest that the gradient responds to varied displacement capabilities of the distinct protein states that ParC goes through. Hence, ParC forms a cellular gradient from the cell poles towards the cytoplasmic region, with ATP-bound monomers that are released from the poles to the nucleoid. Following dimerization, dimers of ParC are capable of associating with nucleoid DNA. This interaction stabilizes the dimer which eventually, due to ATPase intrinsic activity, hydrolyzes ATP to ultimately return to the pole. At last, the results indicate that ParC undergoes a continuous cycle between the cell pole and the cytoplasm, and disruption of this cycle rendered misplaced chemotactic arrays as well as ParP foci.

With all this information, we can summarize how the ParC/ ParP system mediates the proper polar placement of the chemotactic signaling arrays in *Vibrio*. In short cells, ParC, ParP and the chemosensory arrays are located at the flagellated cell pole (Figure 50 – number 1). In the pole, ParP prevents dissociation of the arrays by its interactions with the protein interaction tip located at the SD of the MCPs and with the LID region of CheA. These interactions occur through the AIF domain at the C-terminus of ParP. At the same time, ParP interacts with ParC via its N-terminus conserved region (the ParC-interaction domain). Thereby, ParC is also positioned at the poles, where it undergoes a capture and release process driven by its ATP-dependent cycle. These three components, ParC, ParP and the arrays, are placed at the cell poles by a still unknown protein (or proteins) that serves as a linker to the marker of the cell pole HubP. As the cell cycle progresses, HubP is recruited to the new pole, this also permits the polar placement of the unknown linker (Figure 50– number 2). Once the polar linker is placed at the new pole, ParC is recruited to this site. This redistribution of ParC takes place thanks to its ATP-dependent cycle, most likely free diffuse monomers reach the pole where they are captured. Polar localization of ParC in the new pole permits ParP's polar placement (Figure 50– number 3), which in turn drives the correct localization of a new chemotactic array (Figure 50– number 4). And once arrays are formed, they could vary in the composition of their base plates, at least in the case of *V. cholerae*, where different coupling proteins can be included in array composition.

At this point, more experiments are required to understand the reasons behind base plate variability, if it responds to the need to associate different proteins to specific MCPs or if different scaffolding proteins belong to specific arrays. Furthermore, more work is still required to understand how this variability is accomplished. Likewise, more research is still needed to address ParP's contribution to array stability and overall activity. Furthermore, it is not clear how ParP associates with ParC to ultimately recruit arrays to the cell poles. Finally, more investigation is required to understand how the

gradient is maintained, what other proteins influence ParC's polar placement and how the gradient, if at all, is influenced by ParP.

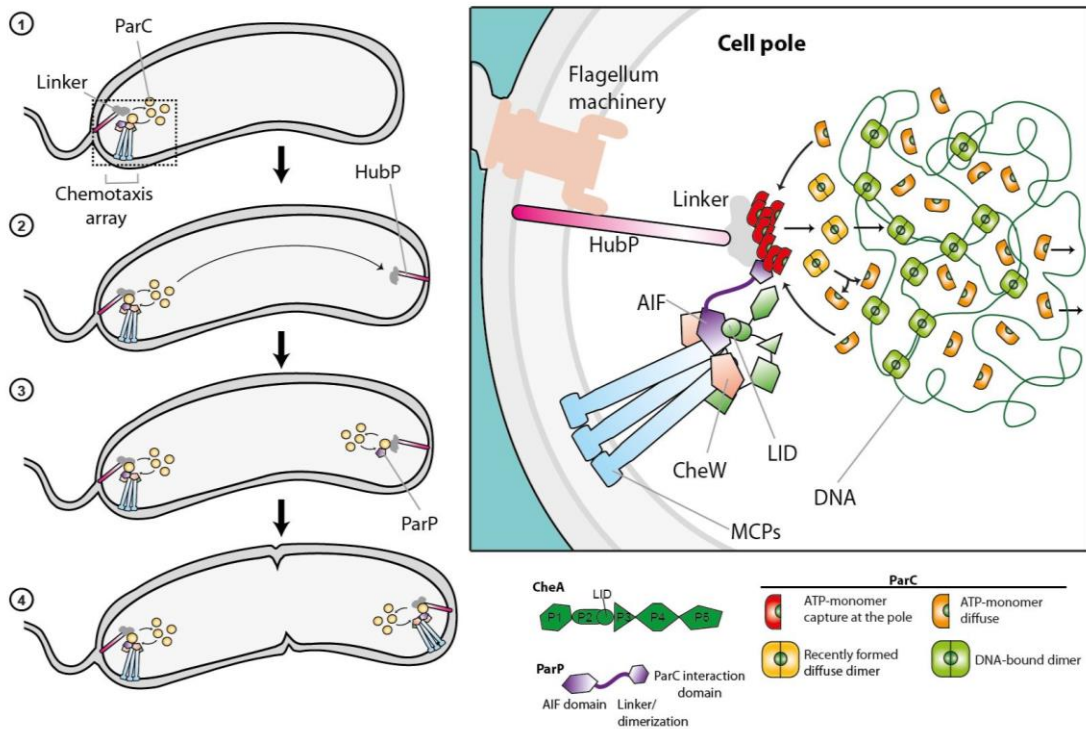


**Figure 50. Scheme summarizing the current model of the ParC/ParP system.** (Right) (1) ParC, ParP and the proteins from the chemotactic arrays localize at the flagellated cell pole in *Vibrio* species. (2) As the cell cycle progresses HubP and the unknown linker locate in the new pole. This permits ParC's recruitment (arrow). (3) Once ParC is at the new pole, ParP is also polarly placed, and this permits (4) the formation of a new array. Dotted square represents the region shown in the (left) panel. (Left) During ParC's cycling, the ATP-bound monomer is retained at the poles while the dimeric state of the protein remains away from the polar region. In the cell pole, it is likely ParP does not interact with the dimeric form of ParC, simply because dimers are spatially excluded from ParP. Thus, we could hypothesize that ParP's domain responsible for interaction with ParC has a higher affinity for the ATP-bound monomeric form of ParC, which is the most abundant protein state in the polar region. The monomers of ParC (in red) at the pole are subsequently released as they form dimers, which will diffuse (yellow) until they bind DNA (green). The dimers could also dissociate and form monomers, which will either be recruited to the old pole or to the new pole, depending where in is the cell its cell cycle. For clarity, other protein states of ParC are not shown. For more details see main text.

# CHAPTER 6: MATERIALS AND METHODS

## 6.1 Chemicals, equipment and software

Essential resources, including reagents (Table 1), kits (Table 2), equipment (Table 3) and software (Table 4) are listed below along their supplier and/or manufacturer. When available an identifier number is also provided. If microbiological or molecular techniques required the work with biosafety level 2 organisms or materials, the corresponding assays were performed following the guidelines set in place for this biosecurity level.

**Table 1. Reagents**

Reagents	Supplier	Identifier
<b>Genetic reagents</b>		
Restriction enzymes	New England Biolabs (NEB) (Frankfurt a.M.)	
2-Log DNA Ladder (0.1-10.0KB)	New England Biolabs (NEB) (Frankfurt a.M.)	NEB Cat#: N3200S
Color Pre-stained Protein Standard Broad Range (11-245 KDA)	New England Biolabs (NEB) (Frankfurt a.M.)	NEB Cat#: P7712S
T4 Ligase	New England Biolabs (NEB) (Frankfurt a.M.)	NEB Cat#: M0202L
10X Buffer for T4 DNA Ligase with 10mM ATP	New England Biolabs (NEB) (Frankfurt a.M.)	NEB Cat#: B0202S
Q5 Hot Start High Fidelity DNA Polymerase	New England Biolabs (NEB) (Frankfurt a.M.)	NEB Cat#: M0493S
Q5 High GC Enhancer	New England Biolabs (NEB) (Frankfurt a.M.)	NEB Cat#: B9028A
Q5 Reaction buffer	New England Biolabs (NEB) (Frankfurt a.M.)	NEB Cat#: B9027S
Desoxyribonucleotide (dNTP) Solution Mix	New England Biolabs (NEB) (Frankfurt a.M.)	NEB Cat#: N04475
Alkaline Phosphatase Calf Intestinal (CIP)	New England Biolabs (NEB) (Frankfurt a.M.)	NEB Cat#: M0290L
<b>Antibody</b>		
Living Colors A.v. Monoclonal Antibody (JL-8) (Mouse monoclonal anti-GFP)	Clontech Laboratories, Inc. (USA)	Cat#: 632381
<b>Chemical compound, drug</b>		
Antibiotics: Chloramphenicol; Ampicillin sodium salt; Streptomycin sulfate; kanamycin sulfate	Carl Roth GmbH + Co KG (Karlsruhe)	Art.-Nr: 3886.3; k029.3; 0236.2

Isopropyl $\beta$ -D-1 thiogalactopyranoside (IPTG)	Peqlab (Erlangen)	Nr.: 35-2030
Difco Agar, Granulated LB-Medium (Luria/Miller)	BD Carl Roth GmbH + Co KG (Karlsruhe)	Ref#: 214510 Art.-Nr: X968,3
L(+)-Arabinose	Carl Roth GmbH + Co KG (Karlsruhe)	Art.-Nr: 5118.3
peqGOLD Universal Agarose Agarose NEEP Ultra-Quality	Peqlab (Erlangen) Carl Roth GmbH + Co KG (Karlsruhe)	Nr.: 35-1020 Art.-Nr: 2267.3
D(+) Saccharose	Carl Roth GmbH + Co KG (Karlsruhe)	Art.-Nr: 4621.1
Bacto Yeast Extract Tryptone	BD Carl Roth GmbH + Co KG (Karlsruhe)	Ref#: 212750 Carl Roth GmbH + Co KG (Karlsruhe)
Instant Blue	Expedeon (United Kingdom)	
EZ rich defined liquid medium	EZRDM, VWR, Germany	
Gel loading dye purple 6X	New England Biolabs (NEB) (Frankfurt a.M.)	#B7025S
5-Bromo-4-Chloro-3-Indolyl- $\beta$ -D-Galactopyranoside (X-Gal)	Carl Roth GmbH + Co KG (Karlsruhe)	Art.-Nr: 2315.4
<b>Materials</b>		
96-well plates	Greiner Bio-One GmbH, Frickenhausen	
Microscopy slides	Carl Roth GmbH + Co KG (Karlsruhe)	Art.-Nr: 0656
Cover slips	Carl Roth GmbH + Co KG (Karlsruhe)	Art.-Nr: H875
Petri dish 92x16mm	Sarstedt	Cat#: 82.1472.001

**Table 2. Commercial kits and assays**

Name	Manufacturer	Identifier
NucleoSpin Gel and PCR Clean-up kit	Macherey-Nagel (Düren)	Ref.: 740609.250
NucleoSpin Plasmid Kit	Macherey-Nagel (Düren)	Ref.: 740588.250
Bacterial Two Hybrid Kit	Euromedex (Souddelweyersheim, France)	Cat#: EUK001

**Table 3. Software and on-line resources**

Name	Source/Reference	Additional information
MetaMorph v7.5	Molecular Devices (Union City, CA)	
SeqBuilder v12.3.1	DNASTAR Software for Life Scientists (Madison, WI)	

SeqMan Pro v12.3.1	DNASTAR Software for Life Scientists (Madison, WI)	
ImageJ-Fiji	(Schindelin et al., 2012)	<a href="http://rsbweb.nih.gov/ij">http://rsbweb.nih.gov/ij</a>
R studio version 3.0.1		<a href="http://www.rstudio.com/">http://www.rstudio.com/</a>
GraphPad Prism version 6.07	GraphPad Software (La Jolla CA)	<a href="https://www.graphpad.com/">https://www.graphpad.com/</a>
Customized script for cell sorting	(Cameron et al., 2014)	<a href="http://github.com/ta-cameron/Cell-Profiles">http://github.com/ta-cameron/Cell-Profiles</a>
ggplot2 version 0.9.3.1	Hadley Wickham, Department of Statistics, Rice University	<a href="http://ggplot2.org">http://ggplot2.org</a>
NIS-Elements Software AR 4.60.00 (Nikon)	NIS-Elements Software AR 4.60.00 (Nikon)	
STRING-known and predicted protein-protein interactions	(Jensen et al., 2009)	<a href="http://string-db.org/">http://string-db.org/</a>
Phyre: Protein Homology/analogy Recognition Engine V 2.0	(Kelley & Sternberg, 2009)	<a href="http://www.sbg.bio.ic.ac.uk/phyre/html/">http://www.sbg.bio.ic.ac.uk/phyre/html/</a>
Oligo Calc: Oligonucleotide Properties Calculator	(Kibbe, 2007)	<a href="http://biotoools.nubic.northwestern.edu/OligoCalc.html">http://biotoools.nubic.northwestern.edu/OligoCalc.html</a>
Conserved Domain Architecture Retrieval Tool (CDART)	(Geer et al., 2002)	<a href="https://www.ncbi.nlm.nih.gov/Structure/lexington/lexington.cgi">https://www.ncbi.nlm.nih.gov/Structure/lexington/lexington.cgi</a>
SMART: EMBL-Heidelberg	(Letunic & Bork, 2018)	<a href="http://smart.embl-heidelberg.de/">http://smart.embl-heidelberg.de/</a>

**Table 4. Essential equipment**

Application	Device	Manufacturer
Electroporation	MicroPulser electroporator	Bio-rad (München)
PCR	Mastercycler nexus PCR System	Eppendorf (Hamburg)
Centrifugation	Centrifuge 5424 and 5424R. Multifuge 1 S-R, Biofuge Pico17, multifuge X1R	Eppendorf (Hamburg) Heraeus/Thermo Scientific (Dreieich)
Thermomixing	Thermomixer compact	Eppendorf (Hamburg)
DNA illumination and documentation	E-BOX VX2 imaging system	PeqLab (Eberhardzell)
DNA illumination	UVT_20 LE	Herolab (Wiesloch)
Protein electrophoresis	Mini-PROTEAN 3 cell	Bio-rad (München)
Western blotting	Transfer system from PeqLab	PeqLab (Eberhardzell)
Chemical-luminescence detection	Luminescent image analyzer LAS-4000	Fujifilm (Düsseldorf)
Microscopy*	Ziess Axio Imager M1 fluorescence microscope, Zeiss Axioplan 2 fluorescence microscope, Nikon eclipse Ti inverted microscope, Talos	



---

L120C transmission electron microscope.

---

\*for details of the microscopes set-up see section "Microscopy methods"

## 6.2 Media, buffers and solutions

Mostly cells were grown in LB media. However, certain assays required TB medium or EZ rich defined liquid medium (EZRDM, VWR, Germany). The composition of growth media as well as buffers employed in this work is listed below.

**Table 5. Media, buffers and solutions**

Media/Buffer	Composition
Luria-Bertani (LB)	1% (w/v) tryptone; 0.5% (w/v) yeast extract; 1% (w/v) NaCl
Terrific Broth (TB)	For 1 L: 20g tryptone; 4ml glycerol; 100ml phosphate buffer
Phosphate buffered saline (PBS)	For 10x solution: 25.6 g Na <sub>2</sub> HPO <sub>4</sub> ·7H <sub>2</sub> O 80 g NaCl 2 g KCl 2 g KH <sub>2</sub> PO <sub>4</sub> Bring to 1 liter with H <sub>2</sub> O. Autoclave for 40 minutes at 121°C.
Phosphate buffer	0.017 M KH <sub>2</sub> PO <sub>4</sub> & 0.072 M K <sub>2</sub> HPO <sub>4</sub>

## 6.3 Microbiological methods

### 6.3.1 Growth conditions

For the majority of experiments *V. cholerae*, *V. parahaemolyticus* and *E. coli* strains were grown in LB media on LB agar plates at 30°C or 37°C. For sptPALM *V. parahaemolyticus* strains were grown in TB media and EZ rich defined liquid medium (EZRDM, VWR, Germany). When required, antibiotics were added in the following concentrations: streptomycin 200 µg/ml; kanamycin 50 µg/ml; ampicillin 100 µg/ml; chloramphenicol 20 and 30 µg/ml for *E. coli* and 5 µg/ml for *V. cholerae* and *V. parahaemolyticus*. Similarly, when induction of plasmids containing an arabinose inducible promoter was needed, L-arabinose was added to a final concentration of 0.2% w/v. When IPTG was required for induction a final concentration of 1mM.

### 6.3.2 Strains

*E. coli* strains DH5α<sub>pir</sub> and TOP10 were used for cloning. *E. coli* strain SM10λ<sub>pir</sub> was used to transfer plasmid DNA by conjugation from *E. coli* to *V. cholerae* and *V. parahaemolyticus* (Miller & Mekalanos, 1988). *E. coli* strain MG1655 was used for co-localization studies where nucleoid DNA was stained with DAPI. Additionally, two *V.*

*cholerae* strains were employed in this work, El Tor clinical isolate N16961 and C6706 *lacZ*-. *V. parahaemolyticus* strains used in this stud are derivatives of strain RIMD 2210633. A comprehensive list of all strains used for this work can be found in Table 6.

**Table 6. Strains**

Strain name	Genotype	Reference
<i>Escherichia coli</i> BTH101	F <sup>-</sup> <i>cya</i> -99 <i>araD</i> 139 <i>galE</i> 15 <i>galK</i> 16 <i>rpsL</i> 1 <i>hsdR</i> 2 <i>mcrA</i> 1 <i>mcrB</i> 1	
<i>Escherichia coli</i> DH5αλpir	<i>sup</i> E44, Δ <i>lacU</i> 169 (Φ <i>lacZ</i> Δ <i>M</i> 15), <i>recA</i> 1, <i>endA</i> 1, <i>hsdR</i> 17, <i>thi</i> -1, <i>gyrA</i> 96, <i>relA</i> 1, λpir	
<i>Escherichia coli</i> K-12 MG1655	F <sup>-</sup> , lambda <sup>-</sup> , rph-1	
<i>Escherichia coli</i> SM10λpir	KmR, <i>thi</i> -1, <i>thr</i> , <i>leu</i> , <i>tonA</i> , <i>lacY</i> , <i>supE</i> , <i>recA</i> ::RP4-2-Tc::Mu, λpir	
<i>Escherichia coli</i> TOP10	F <sup>-</sup> <i>mcrA</i> Δ( <i>mrr</i> - <i>hsdRMS</i> - <i>mcrBC</i> ) φ80 <i>lacZ</i> Δ <i>M</i> 15 Δ <i>lacX</i> 74 <i>recA</i> 1 <i>araD</i> 139 Δ( <i>ara-leu</i> )7697 <i>galU</i> <i>galK</i> λ <sup>-</sup> <i>rpsL</i> (Str <sup>R</sup> ) <i>endA</i> 1 <i>nupG</i>	
<i>Escherichia coli</i> VS296	Δ <i>cheR</i> Δ <i>cheB</i> Δ <i>cheW</i> Δ <i>cheA</i> Δ <i>cheY</i> Δ <i>cheZ</i> Δ <i>tar</i> Δ <i>tsr</i> Δ <i>tap</i>	Provided by Dr. Victor Sourjik
<i>Vibrio cholerae</i> AA13	Δ <i>vc</i> 2063 (Δ <i>cheA</i> 2)	(Alvarado et al., 2017)
<i>Vibrio cholerae</i> AA15	Δ <i>vc</i> 2060 Δ <i>vc</i> 2063 (Δ <i>parP</i> / Δ <i>cheA</i> 2)	(Alvarado et al., 2017)
<i>Vibrio cholerae</i> AA17	<i>vc</i> 2060 <i>L</i> 209A- <i>W</i> 305A:: <i>vc</i> 2063 ( <i>parP</i> - <i>L</i> 209A- <i>W</i> 305A Δ <i>cheA</i> 2)	(Alvarado et al., 2017)
<i>Vibrio cholerae</i> AA18	Δ <i>vc</i> 2063:: <i>vc</i> 2063-Δ <i>P</i> 5 (Δ <i>cheA</i> 2-Δ <i>P</i> 5)	(Alvarado et al., 2017)
<i>Vibrio cholerae</i> AA20	Δ <i>vc</i> 2060:: <i>vc</i> 2060- Δ <i>AIF</i> (Δ <i>parP</i> :: <i>parP</i> -Δ <i>AIF</i> ) <sup>+</sup>	This work
<i>Vibrio cholerae</i> AA21	Δ <i>vc</i> 2060:: <i>vc</i> 2060-Δ <i>AIF</i> Δ <i>vc</i> 2063 (Δ <i>parP</i> :: <i>parP</i> - Δ <i>AIF</i> Δ <i>cheA</i> 2)	(Alvarado et al., 2017)
<i>Vibrio cholerae</i> AA24	Δ <i>vc</i> a1095 <sup>+</sup>	This work
<i>Vibrio cholerae</i> AA25	Δ <i>vc</i> 1397/ Δ <i>vc</i> 2063 <sup>+</sup>	This work
<i>Vibrio cholerae</i> AA26	Δ <i>vc</i> 1397 / Δ <i>vc</i> 2063 / Δ <i>vc</i> a1095 <sup>+</sup>	This work
<i>Vibrio cholerae</i> AA27	Δ <i>vc</i> 2063 (Δ <i>cheA</i> 2) <sup>+</sup>	This work
<i>Vibrio cholerae</i> AA28	Δ <i>vc</i> 1397/ Δ <i>vc</i> a1095 <sup>+</sup>	This work
<i>Vibrio cholerae</i> AA29	Δ <i>vc</i> a1095/ <sup>+</sup>	This work
<i>Vibrio cholerae</i> C6706	<i>lacZ</i> -, clinical isolate, wild type	This work
<i>Vibrio cholerae</i> N16961	Clinical isolate, wild type	This work
<i>Vibrio cholerae</i> PM2	<i>vc</i> 2060 <i>W</i> 305A ( <i>parPW</i> 305A)	(Alvarado et al., 2017)
<i>Vibrio cholerae</i> PM3	<i>vc</i> 2060 <i>L</i> 209A ( <i>parPL</i> 209A)	(Alvarado et al., 2017)
<i>Vibrio cholerae</i> PM33	Δ <i>vc</i> 2060:: <i>vc</i> 2060- <i>P</i> 5 (Δ <i>parP</i> :: <i>parP</i> - <i>P</i> 5) <sup>+</sup>	This work
<i>Vibrio cholerae</i> PM34	Δ <i>vc</i> 2060:: <i>vc</i> 2060- <i>P</i> 5 Δ <i>vc</i> 2063 (Δ <i>parP</i> :: <i>parP</i> - <i>P</i> 5 Δ <i>cheA</i> 2)	(Alvarado et al., 2017)
<i>Vibrio cholerae</i> PM35	Δ <i>vc</i> 2063:: <i>vc</i> 2063-Δ <i>P</i> 5 Δ <i>vc</i> 2060 ( <i>cheA</i> 2-Δ <i>P</i> 5 Δ <i>parP</i> )	(Alvarado et al., 2017)

<i>Vibrio cholerae</i> PM4	<i>vc2060L209A-W305A (parP-L209A-W305A)</i>	(Alvarado et al., 2017)
<i>Vibrio cholerae</i> PM48	$\Delta vc2063::vc2063-AIF$ ( $\Delta cheA2::cheA2-AIF$ ) <sup>+</sup>	This work
<i>Vibrio cholerae</i> SR70	$\Delta vc2060 (\Delta parP)$	(Alvarado et al., 2017)
<i>Vibrio cholerae</i> $\Delta parC$	$\Delta vc2061 (\Delta parC)$ <sup>+</sup>	(Ringgaard et al., 2011)
<i>V. parahaemolyticus</i> AA01	RIMD 2210633 $\Delta parC::parCG11V$	(Alvarado et al., 2017)
<i>V. parahaemolyticus</i> AA02	RIMD 2210633 $\Delta parC::parCR191E$	(Alvarado et al., 2017)
<i>V. parahaemolyticus</i> AA03	RIMD 2210633 $\Delta parC::parCD39A$	(Alvarado et al., 2017)
<i>V. parahaemolyticus</i> AA04	RIMD 2210633 $\Delta parC::parCR191E+D39A$	(Alvarado et al., 2017)
<i>V. parahaemolyticus</i> AA05	RIMD 2210633 $\Delta parC::parCK15Q$	(Alvarado et al., 2017)
<i>V. parahaemolyticus</i> MZ01	RIMD 2210633 $\Delta vp2227 (\Delta parC)$	(Ringgaard et al., 2011)
<i>V. parahaemolyticus</i> RIMD 2210633	Clinical isolate	This work
<i>V. parahaemolyticus</i> SR58	RIMD 2210633 $\Delta vp2225 (\Delta cheW)$	(Ringgaard et al., 2014)
<i>V. parahaemolyticus</i> SR59	RIMD 2210633 $\Delta vp2226 (\Delta cheP)$	(Ringgaard et al., 2014)

<sup>+</sup>Derivatives of *V. cholerae* C6706 (*lacZ*<sup>-</sup>). Otherwise, *V. cholerae* strains are derivatives of strain N16961.

### 6.3.3 Swimming assays

For *V. cholerae* strains, cells were grown overnight in 5ml LB at 37° C with shaking. A sterile toothpick was used to prick cells into LB 0.3% agar plates containing 200 µg/ml of streptomycin and if required, the antibiotic for plasmid selection. Plates were incubated at 30° C for 8-10 hours. The diameter of the swimming colony was then manually recorded and plotted against wild-type normalized to 1. A similar approach was followed for swimming assays of *V. parahaemolyticus* strains. However, in this case plates did not contain antibiotic, unless needed for plasmid selection.

### 6.3.4 Growth curves

In all cases, cells were grown in agar plates, antibiotics were added when required. A colony was subsequently grown until stationary phase was reached (OD600 ≥3.0) in LB liquid media. Then 10 µl were taken and re-suspended in 1 ml LB. From here 1-2 µl were used to inoculate a 200 µl aliquot in a microtiter plate. Plates were kept at 37° C and OD600 was recorded every 15 minutes for 18 to 24 hours in a TECAN

Microplate Reader (Infinite 200 PRO). As a rule, 8 to 12 replicates were kept per strain. Average of the OD600 was plotted over time. Error bars indicate one standard deviation.

### 6.3.5 Bacterial-two-hybrid assays

The bacterial adenylate cyclase two-hybrid system (BACTH) (Karimova et al., 1998) was employed to detect direct protein-protein interactions using strain *E. coli* BTH101. Genes encoding for the proteins of interest were fused to plasmid containing the genes that encode for the T18 (pUT18C or pUT18) or the T25 domain (pKT25 or pKNT25) of adenylate cyclase of *Bordetella pertussis*. Plasmids were provided by the manufacturer (Euromedex, Soouddelweyersheim, France). Competent BTH101 cells were co-transformed with two plasmids, having a C or N-terminus fusion of the gene of interest to *t25* or *t18*. BTH101 lacks the *cyaA* gene, which encodes the catalytic domain of the adenylate cyclase; thereby, they do not produce cyclic adenosine monophosphate (cAMP). If the transformed plasmids encode for proteins that interact, the T25 and T18 come closer to each other, reconstituting the catalytic domain of adenylate cyclase, and thus the strain is capable of producing cAMP. This secondary messenger activates the expression of the *lac* operon and the consequent production of  $\beta$ -galactosidase. This enzyme in turn cleaves X-gal, which is added to the growth media. Subsequently, X-gal cleavage permits the screening of blue-white colonies.

For the screening were three plasmid were used, strains were additionally transformed with a plasmid containing an YFP protein fusion. For transformation in all cases, 20 to 25 ng of plasmid DNA were used. Cells were transformed and plated on selective agar plates containing 100  $\mu$ g/ml of ampicillin, 50  $\mu$ g/ml of kanamycin and in the case of the three-hybrid approach, 20  $\mu$ g/ml of chloramphenicol. Plates also contained 0.5 mM IPTG and 40  $\mu$ g/ml X-gal, and for induction of the YFP protein fusions, L-arabinose in a final concentration of 30% was also included. Subsequently, plates were incubated at 30° for no longer than 48 h. Plates where colonies turned blue were kept at 4° C. Next, three colonies were taken per plate, grown in LB added with the respective antibiotics and plated in three indicator plates, which were also incubated at 30° for no longer than 48 h. Pictures were taken of the three replicates at different intervals during the incubation time. As a negative control in all cases cells were transformed with empty vectors, and as a positive control, cells were transformed with plasmid pUT18C-*zip* and pKNT25-*zip* (Euromedex, Soouddelweyersheim, France). While not shown in every case, all BACTH assays in this thesis were plated with their respective positive and negative controls.

### 6.3.6 Protein interaction-partner screening based on the bacterial-two-hybrid system

As shown in (Figure 17), *V. cholerae* chromosomal DNA was digested with rate-cutter restriction enzymes (NlaIII and Sau3AI). Fragments in the size range of 1000 to 5000 bp were subsequently purified and fused to the gene encoding the T25 domain of adenylate cyclase in vector pKT25. This resulted in the construction of a genetic library of chromosomal DNA fragments. The library was transformed into *E. coli* strain BTH101 harboring a plasmid where *parP* (*vc2060*) was fused to the region encoding for domain T18 of adenylate cyclase (plasmid pAK2). Transformants were spread on indicator plates. One hundred blue colonies were chosen randomly, their plasmids were eluted and the fragment of chromosomal DNA in plasmid pKT25 was identified by sequencing.

## 6.4 Molecular biology methods

### 6.4.1 Preparation of competent cells

To prepare chemically competent *E. coli*, a single colony was taken and incubated in 5ml LB liquid media (relevant antibiotic added) at 37° C with shaking until OD600 reached 0.7-1.0. Then, a larger volume was inoculated, normally at a 1:50 volume unit ratio. The larger liquid culture was grown until OD600 reached 0.5-0.7. Subsequently cells were pelleted down by centrifugation for 10 min at 4700rpm at 4° C. After decanting the supernatant, the pelleted cells were washed twice with ice-cold 50mM CaCl<sub>2</sub>. After the second centrifugation cells were suspended using 50mM CaCl<sub>2</sub> with added glycerol to 1/10 of the original volume. Aliquots of 50µl were snap-frozen in liquid nitrogen and later kept for extended time storage at -80° C.

To prepare electro-competent cells of both *V. cholerae* and *V. parahaemolyticus* 200 ml liquid LB was inoculated with a single colony. The liquid culture was then incubated at 37° C with shaking until OD600 reached 1.0. Cells were then pelletized by centrifugation for 10 min at 4700rpm at 4° C. Immediately, cells were kept on ice. The pellet was washed twice with ice-cold freshly prepared 273mM sucrose solution. The sucrose solution was buffered using KOH to keep pH at 7.2-7.4. After the two centrifugations, the cells were re-suspended in sucrose solution with glycerol added to 1/10 of the original cell culture volume. Aliquots of 50µl were snap-frozen in liquid nitrogen and later kept for extended time storage at -80° C.

### 6.4.2 Transformation of competent cells

To transform *E. coli* competent cells, a 50µl aliquot of CaCl<sub>2</sub> competent cells was added with the corresponding volume of plasmid to a concentration of 50-100 ng. Cells were kept on ice for 20-30 min, at which point they were heat shock for 2 minutes by incubating the tubes in a water bath at 42° C. Immediately after removal from the water bath, cells were kept on ice, and 1ml of LB liquid media was added. Subsequently, cells were incubated at 37° C with shaking for recovery. Cells were harvested after 45 min, the supernatant was decanted and an approximate volume of 50 µl of cells were plated onto LB-agar plates added with the relevant antibiotic(s).

To transform electro-competent *Vibrio* cells, an aliquot of competent cells was mixed with the corresponding volume of plasmid to a concentration of 100-1000 ng. Cells were kept on ice for about 30 minutes. Subsequently, the plasmid and cell mixture was transferred onto a pre-cooled electroporation cuvette (Bio-Rad) and immediately electroporated using a MicroPulser electroporator (Bio-Rad) at the appropriate calibration (voltage 2200, µF 25 and 200 Ω). Afterwards, 1 ml of LB-liquid media was added and the cells were incubated at 37° C with shaking for recovery for about 3-4 hours. Later, cells were harvested and plated on LB-agar plates containing the relevant antibiotic.

### 6.4.3 Construction of strains and domains exchange

Construction of *V. cholerae* and *V. parahaemolyticus* deletions or gene replacements with mutated versions, was performed with standard allele exchange techniques using derivatives of plasmid pCVD442 for *V. cholerae* and of pDM4 (Donnenberg & Kaper, 1991) for *V. parahaemolyticus*.

Strain AA26 was constructed by sequential in-frame deletions of *vc1397*, *vc2063* and finally *vc1095*.

For strains where the P5 domain of CheA was swapped by the AIF domain of ParP, or viceversa, the corresponding region of P5 consisted of 130 amino acids, from L649 to Q778 in CheA of *V. cholerae* (accession number NP\_231596). While the AIF domain of ParP is 133 amino acids long, from position Q195 to M327 in ParP of *V. cholerae* (accession number NP\_231692.1). These regions were determined using SMART (<http://smart.embl-heidelberg.de/>) (Letunic & Bork, 2018).

### 6.4.4 Plasmids and oligonucleotides

The list of all plasmids and primers used in this study is shown below. Relevant information is also provided.

Table 7. Plasmids

Plasmid name	Relevant genotype/description	Reference
mcherry-vc1898L512R	<i>PBAD::mCherry-vc1898L518R</i>	(Alvarado et al., 2017)
del-vc2060	<i>Plasmid for deletion of vc2060 (parP)</i>	(Alvarado et al., 2017)
pAA02	Plasmid for insertion of <i>vp2227K15Q</i>	This work
pAA03	Plasmid for insertion of <i>vp2227G11V</i>	This work
pAA04	Plasmid for insertion of <i>vp2227R191E</i>	This work
pAA05	Plasmid for insertion of <i>vp2227D39A</i>	This work
pAA100	<i>PBAD::vc1602-cfp (CheV1)</i>	This work
pAA101	<i>PBAD::vc2006-cfp (CheV2)</i>	This work
pAA102	<i>PBAD::vc2202-cfp (CheV3)</i>	This work
pAA103	<i>PBAD::vca0954-cfp (CheV4)</i>	This work
pAA20	Plasmid for insertion of <i>vp2227R191E+D39A</i>	This work
pAA43	<i>Plasmid for deletion of vc2063-P5 (cheA2-P5)</i>	(Alvarado et al., 2017)
pAA44	<i>Plasmid for insertion of vc2060-P5 (parP-P5) on the chromosome replacing the native vc2060 locus</i>	(Alvarado et al., 2017)
pAA48	<i>Plac::T18-vc1898L521R</i>	(Alvarado et al., 2017)
pAA49	<i>Plac::T25-vc1898L521R</i>	This work
pAA50	<i>Plac::T18-vc1898N522R</i>	(Alvarado et al., 2017)
pAA51	<i>Plac::T18-vc1898A524R</i>	(Alvarado et al., 2017)
pAA52	<i>Plac::T25-vc1898A524R</i>	This work
pAA53	<i>Plac::T25-vc1898I525R</i>	This work
pAA54	<i>Plac::T25-vc1898A528R</i>	This work
pAA55	<i>Plac::T25-vc1898L518R</i>	This work
pAA56	<i>Plac::T18-vc1898L518R</i>	(Alvarado et al., 2017)
pAA60	<i>PBAD::mCherry-vc1898</i>	(Alvarado et al., 2017)
pAA74	<i>Plac::mCherry-vc1898</i>	(Alvarado et al., 2017)
pAA75	<i>PBAD::cfp-vc2059 (cheW1)</i>	(Alvarado et al., 2017)
pAA76	<i>PBAD::yfp-vc20602PM-cfp-vc2059 (parP2PM, cheW1)</i>	(Alvarado et al., 2017)
pAA77	<i>PBAD::yfp-vc2060-cfp-vc2059 (parP, cheW1)</i>	(Alvarado et al., 2017)
pAA78	<i>PBAD::yfp-vc2060W305A-cfp-vc2059 (parPW305A, cheW1)</i>	(Alvarado et al., 2017)
pAA79	<i>PBAD::yfp-vc2060L209A-cfp-vc2059 (parPL209A, cheW1)</i>	(Alvarado et al., 2017)
pAA84	<i>PBAD::PAmCherry-vp2227R191E</i>	This work
pAA85	<i>PBAD::PAmCherry-vp2227G11V</i>	This work
pAA86	<i>PBAD::PAmCherry-vp2227K15Q</i>	This work
pAA87	<i>PBAD::PAmCherry-vp2227D39A</i>	This work
pAA88	<i>PBAD::yfp-vc2227K220E</i>	This work
pAA91	<i>PBAD::yfp-vc2227R191E+D39A</i>	This work
pAA98	<i>PBAD::mCherry-vc2227R191E+D39A</i>	This work

pAK10	<i>Plac::T25-vc2063 (cheA2)</i>	(Alvarado et al., 2017)
pAK105	<i>PBAD::yfp-vc2060L209A (parPL209A)</i>	(Alvarado et al., 2017)
pAK13	<i>Plasmid for deletion of vc2063 (cheA2)</i>	(Alvarado et al., 2017)
pAK13	Plasmid to delete <i>vc2063</i>	(Alvarado et al., 2017)
pAK14	<i>PBAD::yfp-vc2063</i>	(Alvarado et al., 2017)
pAK2	<i>Plac::T18-vc2060 (parP)</i>	(Alvarado et al., 2017)
pAK63	<i>PBAD::yfp-vc2063-(P1-P4)</i>	(Alvarado et al., 2017)
pAK7	<i>Plac::T25-vc2059 (cheW1)</i>	(Alvarado et al., 2017)
pAK72	<i>PBAD::yfp-vc2063-P5</i>	(Alvarado et al., 2017)
pAK76	<i>Plac::T25-vca00658</i>	This work
pAK78	<i>Plac::T25-vc1868</i>	This work
pAK8	<i>Plac::T25-vc2060 (parP)</i>	(Alvarado et al., 2017)
pAK80	<i>Plac::T25-vc1898</i>	(Alvarado et al., 2017)
pAK84	<i>Plac::T18-vca0068</i>	(Alvarado et al., 2017)
pAK86	<i>Plac::T18-vca0658</i>	(Alvarado et al., 2017)
pAK88	<i>Plac::T18-vc1868</i>	(Alvarado et al., 2017)
pAK9	<i>Plac::T25-vc2061 (parC)</i>	(Alvarado et al., 2017)
pAK90	<i>Plac::T18-vc1898</i>	(Alvarado et al., 2017)
pAmCherry- vp2227-#50	<i>PBAD::PAmCherry-vp2227</i>	This work
pBAD33	Arabinose induced expression vector	(Guzman et al., 1995)
pCVD442	Suicide vector for gene deletion	(Donnenberg & Kaper, 1991)
pDM4	Suicide vector for strain construction	(Donnenberg & Kaper, 1991)
pKT25	<i>Plac::T25</i>	(Karimova et al., 1998)
pMF390	<i>PBAD::yfp</i>	(Yamaichi et al., 2012)
pMF391	<i>PBAD::cfp</i>	(Yamaichi et al., 2012)
pMZ03	<i>PBAD::yfp-vp2225</i>	This work
pMZ05	<i>PBAD::yfp-vp2226</i>	(Ringgaard et al., 2014)
pPM010	<i>Plac::T18-vc2060W305A (parPW305A)</i>	(Alvarado et al., 2017)
pPM011	<i>Plac::T18-vc20602PM (parP2PM)</i>	(Alvarado et al., 2017)



pPM014	<i>PBAD::yfp-vc2060W305A (parPW305A)</i>	(Alvarado et al., 2017)
pPM015	<i>PBAD::yfp-vc20602PM (parP2PM)</i>	(Alvarado et al., 2017)
pPM020	<i>Plasmid for insertion of vc2060W305A (parPW305A) on the chromosome replacing the native vc2060 locus</i>	(Alvarado et al., 2017)
pPM021	<i>Plasmid for insertion of vc2060L209A (parPL209A) on the chromosome replacing the native vc2060 locus</i>	(Alvarado et al., 2017)
pPM027	<i>Plasmid for insertion of vc2060-2PM (parP2PM) on the chromosome replacing the native vc2060 locus</i>	(Alvarado et al., 2017)
pPM041	Plasmid to delete <i>vc1397</i>	(Briegel et al., 2016)
pSR1033	<i>PBAD::yfp-vc2059 (cheW1)</i>	(Ringgaard et al., 2011)
pSR1035	<i>PBAD::yfp-vp2227</i>	(Ringgaard et al., 2014)
pSR1084	<i>PBAD::yfp- vp2227K15Q</i>	(Ringgaard et al., 2014)
pSR1089	<i>PBAD::yfp- vp2227G11V</i>	(Ringgaard et al., 2014)
pSR1102	<i>PBAD::yfp-vc2060 (parP)</i>	(Ringgaard et al., 2014)
pSR1120	<i>PBAD::mCherry-vp2629</i>	(Ringgaard et al., 2014)
pSR1159	<i>PBAD::yfp- vp2227R191E</i>	This work
pSR1164	<i>PBAD::yfp- vp2227D39A</i>	This work
pSR1218	<i>Plac::T18-vc2060L196A (parPL196A)</i>	(Alvarado et al., 2017)
pSR1219	<i>Plac::T18-vc2060L209A (parPL209A)</i>	(Alvarado et al., 2017)
pSR1220	<i>Plac::T18-vc2060L212A (parPL212A)</i>	(Alvarado et al., 2017)
pSR1221	<i>Plac::T18-vc2060L215A (parPL215A)</i>	(Alvarado et al., 2017)
pSR1233	Plasmid to delete <i>vca1095</i>	(Alvarado et al., 2017)
pUC19	<i>Plac::</i>	
pUT18C	<i>Plac::T18</i>	(Karimova et al., 1998)
pSR1024	<i>PBAD::yfp-vc2061 (parC)</i>	(Ringgaard et al., 2011)

**Table 8. Primers**

Primer name	Primer sequence
VC2063-BTH-CW	CCCCCTCTAGAGGCAGCTATGAGCTACGAATTAGACGAAGAC
VC2063-BTH-CCW	CCCCCGGTACCGCGGCCGCTCAGACGCGAGAAGCAGCTG
VC2059-BTH-CW	CCCCCGGATCCGGCAGCTATGTCGGAAACGACTCAGAGAG
VC2059-BTH-CCW	CCCCCGGTACCGCGGCCGCTTACATATGAGCCATTTTCGTCCCA
VC2060-BTH-CW	CCCCCGGATCCGGCAGCTATGAGTAGTGCATTGATATCCAGC
VC2060-BTH-CCW	CCCCGAATTCGCGGCCGCTTAATTTTCCAGTGCTTTTACATCAAG

VC2061-BTH-CW	CCCCCGGATCCGGCAGCTATGATCGTTTGGAGTGTAGCAAACC
VC2061-BTH-CCW	CCCCCGGTACCGCGGCCGCTACTCATCGATAGCGAGCCTC
VC1898-CW2	CCCCCTCTAGAGGCAGCTATGGAAACCGCATCGGAGTCAGG
VC1898-CCW1	CCCCGGTACCGCGGCCGCTTAGAGTTTAAACCTATGGACTAACTC
VCA0068-CW2	CCCCCGGATCCGGCAGCTATGGGCGCAGCACAACAAGCCA
VCA0068-CCW1	CCCCCGGTACCGCGGCCGCTTACACGCGAAAATACTGGAGCTG
VC1868-CW2	CCCCCGGATCCGGCAGCTATGGTTATTAGTGCTGCGATTGGCTCT
VC1868-CCW1	CCCCCGGTACCGCGGCCGCTACAACGTAAAGCGTCGGCAAT
VCA0658-CW2	CCCCCGGATCCGGCAGCTATGAATGTCACCCATCAGAATTTACAG
VCA0658-CCW1	CCCCCGGTACCGCGGCCGCTATTTTTGTGCAAACCTGCTTCGA
VC2063del-a	CCCCCTCTAGATCTGCCAATAACCCTATGTTTAAAG
VC2063del-b	TTCGTAGCTCATACGTTACCCCT
VC2063del-c	AGGGGTAACGTATGAGCTACGAATCTCGCGTCTGATTAGCTGCAC
VC2063del-d	CCCCCTCTAGATTTCCCAAAGGTGAGGTAGCTG
VC2060-L196A-CW	GATCCGTGAAAAAGATTTCCAAGTCGCTTATTTTGATGTCAATGGT
VC2060-L196A-CCW	GTCAC GTGACACCATTGACATCAAATAAGCGACTTGAAATCTTTTTTAC
VC2060-L209A-CW	GGATC CAATGGTGTCACTTTCGCAGTGCCAGCTGATGAGTTAGGTGGGAT
VC2060-L209A-CCW	TCATCG CGATGAATCCCACCTAACTCATCAGCTGGCACTGCGAAAGTGACA
VC2060-L212A-CW	CCATTG CTTTCGCAGTGCCACTCGATGAGGCAGGTGGGATTCATCGTATGA
VC2060-L212A-CCW	CC GGTCATACGATGAATCCCACCTGCCTCATCGAGTGGCACTGCGAA
VC2060-I215A-CW	AG GCCACTCGATGAGTTAGGTGGGGCTCATCGTATGACCACACTTAA
VC2060-I215A-CCW	C GTTAAGTGTGGTCATACGATGAGCCCCACCTAACTCATCGAGTGG
VC2060-W305-cw	C GCGTGAGCAAGTCGGTAAACGGCCTGCGCTCGCGGGCATGGTGA
VC2060-W305-ccw	AAGAAAAA TTTTTCTTTCACCATGCCCGCGAGCGCAGGCCGTTTACCGACTTG
VC1898-L518R-cw	CTCACGC CAATATTGCTGAGCAGACCAACCGTTTGGCGCTCAATGCTGCGAT
VC1898-L518R-ccw	TGA TCAATCGCAGCATTGAGCGCCAAACGGTTGGTCTGCTCAGCAATA
VC1898-L521R-cw	TTG CTGAGCAGACCAACCTTTTGGCGCGCAATGCTGCGATTGAAGCGG
VC1898-L521R-ccw	C GCCGCTTCAATCGCAGCATTGCGCGCCAAAAGGTTGGTCTGCTCA
VC1898-N522R-cw	G GAGCAGACCAACCTTTTGGCGCTCCGTGCTGCGATTGAAGCGGC
VC1898-N522R-ccw	GCGTG CACGCGCCGCTTCAATCGCAGCACGGAGCGCCAAAAGGTTGGTC
VC1898-A524R-cw	TGCTC ACCAACCTTTTGGCGCTCAATGCTCGGATTGAAGCGGCGGTGCA
VC1898-A524R-ccw	GGAG CTCCTGCACGCGCCGCTTCAATCCGAGCATTGAGCGCCAAAAGGT
VC2060-PM-ins-a	TGGT CCCCCCCCGGGATCCCTGCCCATATGTCTCTTG
VC2060-PM-ins-b	GCTGGATATCAATGCACTACTCAT
VC2060-PM-ins-c	ATGAGTAGTGCATTGATATCCAGC
VC2060-PM-ins-d	TTAATTTTCCAGTGCTTTTACATCAAG
VC2060-PM-ins-e	CTTGATGTAAGCACTGGAAAATTAA
VC2060-PM-ins-f	CCCCCCCCGGGAACCGACCCTCCTGCGATTAC
VC2060-1-cw	CCCCGAGCTCTGTACAAGATGAGTAGTGCATTGATATCCAGC
VC2060-1-ccw	CCCCGTGACTTAATTTTCCAGTGCTTTTACATCAAG
VC2060_CheWlike-c	CAAGTCCTCTATTTTGTATGTCA
VC2060_CheWlike-d	CATAGCTATCAATGCTTGAACA
VC2060_CheWlike-Xba1-a1	CCCCCTCTAGAATATCCAGCGAACAAGCGCTG

---

VC2060-VC2063-b1	CGCGACGCCAACCATCAAGAAATCTTTTTACGGATCGT
VC2063_P5-c1	TTGATGGTTGGCGTCGCG
VC2063_P5-d1	CTGCTTGAGCAGATCCGG
VC2060-VC2063-e1	CCGGATCTGCTCAAGCAGCTTAATGCAGGGCTTGATGTA
VC2060_CheWlike-XbaI-f1	CCCCCTAGATTTTCGTCCCATTCTTCATCGG
VC2063-1-cw	CCCCCTCTAGAGACATCCTCGAGCTCATGAGCTACGAATTAGACG AAGAC
VC2063-1-ccw	CCCCCGCATGCTCAGACGCGAGAAGCAGCTG
VC2063-7-ccw	CCCCCGCATGCTCAGGTAGAGTCAATATCGATCGAGC
VC2063-8-cw	CCCCCTCTAGAGACATCCTCGAGCTCCTGGCTATTCTTCCTACCT GAT
Vc1898-cw	CCCCCGCATGCCTAGCCGTTTCATCGGATTAGAGT
Vc1898-ccw	CCCCCGCATGCCTAGCCGTTTCATCGGATTAGAGT
Vc1898-cherry-2-cw	CCCCCGCATGCATGGTGAGCAAGGGCGAGGAGGAT
Vc1898-Xmal-ccw	CCCCCCCCGGGCTAGCCGTTTCATCGGATTAGAGT
CFP-VC2059-cw	CCCCCTGTACAGGGTGTGCGAAACGACTCA
CFP-VC2059-ccw	CCCCCGCATGCTTACATATGAGCCATTTTCGTCCCA
ShDo-Spc-CFP-CheW	CCCCCGTCTGACTAAGGAGGATTTATAAAGATGGTGAGCAAGGGCG AGGA
VP2227-R191E-cw	ACCAACCATGTACGACAAGGAAACTCGCGCTTCGTTGCAG
VP2227-R191E-ccw	CTGCAACGAAGCGCGAGTTTTCTTGTCGTACATGGTTGGT
VP2227-G11V-cw	AGTGTAGCTAACCAAAAAGTTGGGGTAGGTAACCACA
VP2227-G11V-ccw	TGTGGTTTTACCTACCCCAACTTTTTGGTTAGCTACACT
VP2227-K15Q-cw	ACCAAAAAGGTGGGGTAGGTCAAACCACATCAACAGTGAC
VP2227-K15Q-ccw	GTCCTGTTGATGTGGTTTGACCTACCCACCTTTTTGGT
P2227-D39A-cw	GTATTGATGGTCGACACCGCTCCTCATGCGTCACTGACG
VP2227-D39A-ccw	CGTCAGTGACGCATGAGGAGCGGTGTGACCATCAATAC
VP2227-K220E-cw	GCAGTACCGATTGAGACGCAAGTTTG
VP2227-K220E-ccw	CAAACCTGCGTCTCAATCGGTACTION
VP2227-del-a	CCCCCTCTAGATGAAGATATTGCACGTAACCGC
VP-2227-del-b	TTGGTTAGCTACACTCCAAACGAT
VP2227-PM-ins-cw	CGTACCAACCATGTACGACAAGGCACTCGCGCTTCGTTGCA GAC
VP2227-PM-ins-ccw	GTCTGCAACGAAGCGCGAGTGCCTTGTCGTACATGGTTGG TACG
VP2227-del-cc	AGGTTAGCGTTCGATGAGCAGTAA
VP2227-del-d	CCCCCTCTAGATCTTCACTTCTTTGCGTGCTTC
PAGFP-VP2227-cw	CCCCCGCATGCTCACTTGTACAGCTCGTCCATGCC
VC1062-2	TCTCGCCCTTGCTCACCAT GAGCTCGAGGATGTC CATATTCAGGATATATTTATCCAT GACATCCTCGAGCTC ATGGTGAGCAAGGGCGAGGA
CFP-3	CCCCC TCTAGA ATGTCAGGTGTTTTGAACACGGTA
VC2006-1-XbaI	TCTCGCCCTTGCTCACCAT GAGCTCGAGGATGTC
VC2006-2	GGAAAGCACTTCTCGCAATCTT
VC2202-1-XbaI	CCCCC TCTAGA ATGACGGGTATTCTTGATT
VCA0954-1-XbaI	CCCCC TCTAGA ATGGCTAAAGTCGTACAGTAA
VC2202-2-new	TCTCGCCCTTGCTCACCAT GAGCTCGAGGATGTC TTAACTAGCGCAGCTTTTAC
VCA0954-2-new	TCTCGCCCTTGCTCACCAT GAGCTCGAGGATGTC CGATTTTTGCAAACGCTGCGTCT
VCA1062-1-XbaI-new	CCCCC TCTAGA ATG AGCAACCCAAGCAGTACTA

---

#### 6.4.4.1 Construction of plasmids

*Plasmids pAK2 and pAK8.* The gene for *vc2060* was PCR amplified from *V. cholerae* using primers VC2060-BTH-cw/VC2060-BTH-ccw. The PCR product was digested with BamHI and EcoRI and was inserted into the equivalent sites of plasmids pUT18C and pKT25 resulting in plasmids pAK2 and pAK8 respectively.

*Plasmid pAK7.* The gene for *vc2059* was PCR amplified from *V. cholerae* using primers VC2059-BTH-cw/VC2059-BTH-ccw. The PCR product was digested with BamHI and KpnI and was inserted into the equivalent sites of plasmid pKT25 resulting in plasmid pAK7.

*Plasmid pAK9.* The gene for *vc2061* was PCR amplified from *V. cholerae* using primers VC2061-BTH-cw/VC2061-BTH-ccw. The PCR product was digested with BamHI and KpnI and was inserted into the equivalent sites of plasmid pKT25 resulting in plasmid pAK9.

*Plasmid pAK10.* The gene for *vc2063* was PCR amplified from *V. cholerae* using primers VC2063-BTH-cw/VC2063-BTH-ccw. The PCR product was digested with XbaI and KpnI and was inserted into the equivalent sites of plasmid pKT25 resulting in plasmid pAK10.

*Plasmid pAK14.* The gene for *vc2063* was PCR amplified from *V. cholerae* using primers VC2063-1-cw/VC2063-1-ccw. The PCR product was digested with XbaI and SphI and was inserted into the equivalent sites of plasmid pMF390 resulting in plasmid pAK14.

*Plasmid pAK63.* The gene coding for amino acids 1-628 of CheA2, which constitutes domains P1 to P4 (*vc2063*, base pairs 1-1884) was PCR amplified from *V. cholerae* using primers VC2063-1-cw/VC2063-7-ccw. The PCR product was digested with XbaI and SphI and was inserted into the equivalent sites of plasmid pMF390 resulting in plasmid pAK63.

*Plasmid pAK72.* The gene coding for amino acids 643-785 of CheA2, which constitutes domain P% (*vc2063*, base pairs 1929-2355) was PCR amplified from *V. cholerae* using primers VC2063-8-cw/VC2063-1-ccw. The PCR product was digested with XbaI and SphI and was inserted into the equivalent sites of plasmid pMF390 resulting in plasmid pAK72.

*Plasmid pAK13.* The up- and downstream regions flanking *vc2063* were amplified using primer pairs *vc2063-del-a/vc2063-del-b* and *vc2063-del-c/vc2063-del-d*, respectively, using *V. cholerae* chromosomal DNA as template. In a third PCR, using primers *vc2063-del-a/vc2063-del-d* and products of the first two PCR reactions as template, the flanking regions were stitched together. The resulting product was digested with XbaI and was inserted into the equivalent site of pCVD442, resulting in plasmid pAK13.

*Plasmids pAK80 and pAK90.* The gene coding for amino acids 461-672 of MCP VC1898 (*vc1898*, base pairs 1383-2016) was PCR amplified from *V. cholerae* using primers VC1898-cw2/VC1898-ccw1. The PCR product was digested with XbaI and KpnI and was inserted into the equivalent sites of plasmids pKT25 and pUT18C resulting in plasmids pAK80 and pAK90 respectively.

*Plasmid pAK84.* The gene coding for amino acids 330-547 of MCP VCA0068 (*vca0068*, base pairs 990-1641) was PCR amplified from *V. cholerae* using primers VCA0068-cw2/VCA0068-ccw1. The PCR product

was digested with BamHI and KpnI and was inserted into the equivalent sites of plasmid pUT18C resulting in plasmid pAK84.

*Plasmid pAK86.* The gene coding for amino acids 335-536 of MCP VA0658 (*vca0658*, base pairs 1005-1608) was PCR amplified from *V. cholerae* using primers VCA0658-cw2/VCA0658-ccw1. The PCR product was digested with BamHI and KpnI and was inserted into the equivalent sites of plasmid pUT18C resulting in plasmid pAK86.

*Plasmid pAK88.* The gene coding for amino acids 424-626 of MCP VC1868 (*vc1868*, base pairs 1272-1878) was PCR amplified from *V. cholerae* using primers VC1868-cw2/VC1868-ccw1. The PCR product was digested with BamHI and KpnI and was inserted into the equivalent sites of plasmid pUT18C resulting in plasmid pAK88.

*Plasmid pSR1218.* Amino acid substitution L196A was introduced in ParP using plasmid pAK2 as template and rolling circle PCR using primers vc2060-L196A-cw/vc2060-L196A-ccw, resulting in plasmid pSR1218.

*Plasmid pSR1219.* Amino acid substitution L209A was introduced in ParP using plasmid pAK2 as template and rolling circle PCR using primers vc2060-L209A-cw/vc2060-L209A-ccw, resulting in plasmid pSR1219.

*Plasmid pSR1220.* Amino acid substitution L212A was introduced in ParP using plasmid pAK2 as template and rolling circle PCR using primers vc2060-L212A-cw/vc2060-L212A-ccw, resulting in plasmid pSR1220.

*Plasmid pSR1221.* Amino acid substitution I215A was introduced in ParP using plasmid pAK2 as template and rolling circle PCR using primers vc2060-I215A-cw/vc2060-I215A-ccw, resulting in plasmid pSR1221.

*Plasmid pAA44.* Plasmid pAA44 was constructed by PCR amplification of the up- and down-stream regions of *vc2060* encoding the AIF domain using *V. cholerae* chromosomal DNA as template. In a third PCR reaction, the part of *vc2063* encoding the P5 domain was amplified using *V. cholerae* chromosomal DNA as template. PCR1 and PCR2 were performed with primer pairs VC2060\_CheWlike-XbaI-a1/VC2060-VC2063-b1 and VC2060-VC2063-e1/VC2060\_CheWlike-XbaI-f1 respectively. PCR3 was performed with primer pair VC2063\_P5-c1/VC2063\_P5-d1. A fourth PCR was then performed using primer pair VC2060\_CheWlike-XbaI-a1/VC2060\_CheWlike-XbaI-f1 and the products of PCR1, PCR2, and PCR3 as template. The resulting PCR product was digested with XbaI and ligated into the equivalent site in pCVD442 resulting in plasmid pAA44.

*Plasmid pAA48.* Amino acid substitution L521R was introduced in VC1898 using plasmid pAK90 as template and rolling circle PCR using primers VC1898-L521R-cw/VC1898-L521R-ccw, resulting in plasmid pAA48.

*Plasmid pAA50.* Amino acid substitution N522R was introduced in VC1898 using plasmid pAK90 as template and rolling circle PCR using primers VC1898-N522R-cw/VC1898-N522R-ccw, resulting in plasmid pAA50.

*Plasmid pAA51.* Amino acid substitution A524R was introduced in VC1898 using plasmid pAK90 as template and rolling circle PCR using primers VC1898-A524R-cw/VC1898-A524R-ccw, resulting in plasmid pAA51.

*Plasmid pAA56.* Amino acid substitution L518R was introduced in VC1898 using plasmid pAK90 as template and rolling circle PCR using primers VC1898-L518R-cw/VC1898-L518R-ccw, resulting in plasmid pAA56.

*Plasmid pAA60.* The gene encoding for *vc1898* was amplified using primers *vc1898-cw* and *vc1898-ccw* using genomic DNA from *Vibrio cholerae* N16961. The resulting PCR fragment was digested with enzymes BsrGI and SphI. Subsequently, the digested fragment was inserted into the equivalent sites of plasmids pJH37 resulting in plasmid pAA60.

*Plasmid pAA74.* The genes encoding for *mCherry* and *vc1898* were amplified using primers *vc1998-cherry-2-cw* and *vc1898-Xmal-ccw* using plasmid pAA60 as template. The resulting PCR fragment was digested with SphI and XmaI and then inserted into the equivalent sites in plasmid pUC19, resulting in plasmid pAA74.

*Plasmid pAA75.* The gene encoding for *cheW1* was PCR amplified from plasmid pSR1033 using primers CFP-VC2059-cw and CFP-VC2059-ccw, the resulting fragment was then digested with BsrGI and SphI. Then the digested fragment was inserted in the corresponding sites of plasmid pMF391, finally resulting in plasmid pAA75.

*Plasmids pAA76, pAA77, pAA78, and pAA79.* The gene encoding for *cfp-cheW1* was amplified using primers ShDo-Spc-CFP-CheW and CFP-VC2059-ccw from plasmid pAA75. The resulting fragment was digested with HincII and SphI and inserted into the corresponding sites of plasmids pPM15, pSR1102, pPM14 and pAK105, resulting in plasmids pAA76, pAA77, pAA78 and pAA79, respectively.

*Plasmid pPM010.* Amino acid substitution W305A was introduced in ParP using plasmid pAK2 as template and rolling circle PCR using primers *vc2060-W305A-cw/vc2060-W305A-ccw*, resulting in plasmid pPM010.

*Plasmid pPM011.* Amino acid substitution W305A was introduced in ParP using plasmid pSR1219 as template and rolling circle PCR using primers *vc2060-W305A-cw/vc2060-W305A-ccw*, resulting in plasmid pPM011.

*Plasmid pPM014.* The gene for *vc2060W305A* was PCR amplified from plasmid pPM010, using primers VC2060-1-cw/VC2060-1-ccw. The PCR product was digested with BsrGI and HincII and was inserted into the equivalent sites of plasmid pMF390, resulting in plasmid pPM014.

*Plasmid pPM015.* The gene for *vc2060W305A* was PCR amplified from plasmid pPM011, using primers VC2060-1-cw/VC2060-1-ccw. The PCR product was digested with BsrGI and HincII and was inserted into the equivalent sites of plasmid pMF390, resulting in plasmid pPM014.

*Plasmid pPM020.* Plasmid pPM020 was constructed by PCR amplification of the up- and down-stream regions of *vc2060* using *V. cholerae* chromosomal DNA as template. In a third PCR reaction *vc2060W305A* was amplified using plasmid pPM010 as template. PCR1 and PCR2 were performed with primer pairs VC2060-PM-ins-a/VC2060-PM-ins-b and VC2060-PM-ins-e/VC2060-PM-ins-f respectively. PCR3 was performed with primer pair VC2060-PM-ins-c/VC2060-PM-ins-d. A fourth PCR was then performed using primer pair VC2060-PM-ins-a/VC2060-PM-ins-f and the products of PCR1, PCR2, and PCR3 as template. The resulting PCR product was digested with SacI and ligated into the equivalent site in pCVD442 resulting in plasmid pPM020.

*Plasmid pPM021.* Plasmid pPM021 was constructed by PCR amplification of the up- and down-stream regions of *vc2060* using *V. cholerae* chromosomal DNA as template. In a third PCR reaction *vc2060L209A*

was amplified using plasmid pSR1219 as template. PCR1 and PCR2 were performed with primer pairs VC2060-PM-ins-a/VC2060-PM-ins-b and VC2060-PM-ins-e/VC2060-PM-ins-f respectively. PCR3 was performed with primer pair VC2060-PM-ins-c/VC2060-PM-ins-d. A fourth PCR was then performed using primer pair VC2060-PM-ins-a/VC2060-PM-ins-f and the products of PCR1, PCR2, and PCR3 as template. The resulting PCR product was digested with *SacI* and ligated into the equivalent site in pCVD442 resulting in plasmid pPM021.

*Plasmid pPM027.* Plasmid pPM027 was constructed by PCR amplification of the up- and down-stream regions of *vc2060* using *V. cholerae* chromosomal DNA as template. In a third PCR reaction *vc2060L209A-W305A* was amplified using plasmid pPM011 as template. PCR1 and PCR2 were performed with primer pairs VC2060-PM-ins-a/VC2060-PM-ins-b and VC2060-PM-ins-e/VC2060-PM-ins-f respectively. PCR3 was performed with primer pair VC2060-PM-ins-c/VC2060-PM-ins-d. A fourth PCR was then performed using primer pair VC2060-PM-ins-a/VC2060-PM-ins-f and the products of PCR1, PCR2, and PCR3 as template. The resulting PCR product was digested with *SacI* and ligated into the equivalent site in pCVD442 resulting in plasmid pPM027.

*Plasmids pAA84, pAA85, pAA86, pAA87 and pAA88.* Plasmid pAmCherry-*vp2227*-#50 was used as template for rolling circle PCR using primer pair VP2227-R191E-cw/ VP2227-R191E-ccw in order to introduce amino acid substitution R191E, primer pair VP2227-G11V-cw and VP2227-G11V-ccw to introduce G11V, VP2227-K15Q-cw/ VP2227-K15Q-ccw for K15Q, VP2227-D39A-cw/ VP2227-D39A-ccw to introduce substitution D39A and primer pair VP2227-K220E-cw / VP2227-K220E-ccw to introduce substitution K220E. The resulting plasmids were pAA84, pAA85, pAA86, pAA87 and pAA88, respectively.

*Plasmid pAA98.* Plasmid pAA84 was used as template for rolling circle PCR using primers VP2227-D39A-cw and VP2227-D39A-ccw in order to introduce amino acid substitution D39A. The resulting plasmid was pAA98.

*Plasmid pAA91.* Plasmid pSR1164 was used as template for rolling circle PCR using primers VP2227-R191E-cw and VP2227-R191E-ccw in order to introduce amino acid substitution D39A. The resulting plasmid was pAA91.

*Plasmid pAA02, pAA03, pAA04, pAA05 and pAA20.* Genomic DNA of *V. parahaemolyticus* wild-type was used for PCR using primers VP2227-del-a and VP-2227-del-b. Similarly, plasmids pSR1084, pSR1089, pSR1159, pSR1164 and pAA91 were used as templates for PCR with primers VP2227-PM-ins-cw and VP2227-PM-ins-ccw. A third PCR product was generated using genomic DNA with primers VP2227-del-cc and VP2227-del-d. The first and last PCR products were mixed with each resulting PCR product from each plasmid template and ran in another PCR with primers VP2227-de-a and VP-2227-del-d. The resulting products were digested with *XbaI* and cloned into the corresponding site of vector pDM4, resulting in *pAA02*, *pAA03*, *pAA04*, *pAA05* and *pAA20*.

*Plasmid pAA100.* Genomic DNA of *V. cholerae* was used to amplify *vc1602* gene with primers VCA1062-1-*XbaI*-new and VC1062-2. Similarly, *cfp* was amplified from plasmid pMF391 using primers CFP-3 and PAGFP-VP2227-cw. Both PCR products were used as template for a third PCR using primers using primers VCA1062-1-*XbaI*-new and PAGFP-VP2227-cw. The resulting product was digested with enzymes *XbaI* and *SphI* and inserted in the corresponding sites of vector pBAD33, resulting in plasmid pAA100.

*Plasmid pAA101.* The gene *vc2006* was amplified using genomic DNA as template with primers VC2006-1-XbaI and VC2006-2. Using vector pMF391, *cfp* was amplified using primers CFP-3 and PAGFP-VP2227-cw. Both PCR products were used as template for a third PCR using primers using primers VC2006-1-XbaI and PAGFP-VP2227-cw. The resulting product was digested with enzymes XbaI and SphI and inserted in the corresponding sites of vector pBAD33, resulting in plasmid pAA101.

*Plasmid pAA102.* To create this plasmid *vc2202* was amplified from genomic DNA using primers VC2202-1-XbaI and VC2202-2-new. Vector pMF391 was used for template of *cfp* amplified using primers CFP-3 and PAGFP-VP2227-cw. Both PCR products were used as template for a third PCR using primers using primers VC2202-1-XbaI and PAGFP-VP2227-cw. The resulting product was digested with enzymes XbaI and SphI and inserted in the corresponding sites of vector pBAD33.

*Plasmid pAA103.* Similarly, *vca0954* was amplified from genomic DNA with primers VCA0954-1-XbaI and VCA0954-2-new. Vector pMF391 was used for template of *cfp* amplified using primers CFP-3 and PAGFP-VP2227-cw. Both PCR products were used as template for a third PCR using primers using primers VCA0954-1-XbaI and PAGFP-VP2227-cw. The resulting product was digested with enzymes XbaI and SphI and inserted in the corresponding sites of vector pBAD33 giving pAA102.

#### **6.4.5 Site-directed mutagenesis**

For site-directed mutagenesis of plasmid DNA using the rolling-circle amplification method (Lizardi et al., 1998). Briefly, PCR of vector DNA was conducted using Q5 Hot Start High Fidelity DNA Polymerase. Subsequently, the resulting reaction was cleaned with NucleoSpin Gel and PCR Clean-up kit (Machery-Nagel) and a restriction digestion reaction was set up with DpnI. The digested product was then cleaned again using the aforementioned kit. The resulting DNA was transformed in an *E. coli* strain. To confirm the introduction of mutations, all plasmids were sent for sequencing.

#### **6.4.6 Polymerase chain reaction (PCR) and agarose gel electrophoresis**

For the amplification of DNA fragments, Q5 Hot Start High Fidelity DNA Polymerase or Phusion High-Fidelity DNA Polymerase were used in a total reaction volume of 50 µl. Colony PCR was performed in a total volume of 25 µl. Composition of the PCR reaction is shown below in Table 9. PCR conditions (denaturation, annealing and elongation temperatures and times) were modified depending on the expected product size. The standard PCR program from where conditions were modified is shown in Table 10.



**Table 9. Components of the PCR mix**

Component	Volume ( $\mu$ l)
5X Q5 reaction buffer	10
10mM dNTPs	1
10 $\mu$ l primer forward	0.5
10 $\mu$ l primer reverse	0.5
DNA	0.5 (final concentration <1000ng)
Polymerase	0.5
High GC enhancer	10
Nuclease-free water	Up to 50 $\mu$ l

**Table 10. Standard PCR program**

Step	Temperature ( $^{\circ}$ C)	Time
Initial denaturation	95	3 min
Denaturation	95	30 sec
Annealing	5 below the primer meting temperature (normally values were 55 to 62)	30 sec
Elongation	72	1 min per kilobase
Final elongation	72	3 min
Hold	4	$\infty$

Nucleic acid fragments were separated based on their size using 1% agarose gels. Agarose solution contained 0.01% (v/v) ethidium bromide in TBE buffer (Invitrogen) at 130 Volts. Before loading the DNA onto the gel, samples were mixed with Gel loading dye purple 6X (no SDS) (New England Biolabs). As a marker the 2-log DNA ladder (New England Biolabs) was also used. Gels were visualized using a E-BOX VX2 imaging system from PeqLab.

#### 6.4.7 Restriction digestion and ligation

Restriction of DNA fragments was performed using the corresponding restriction endonuclease, unless otherwise specified by the enzyme manufacturer, the restriction reaction was carried out at 37 $^{\circ}$  C for 2h. Restricted DNA was purified by running a gel and then eluting the band corresponding to the desired fragment size. Gel was then eluted using the NucleoSpin Gel and PCR Clean-up kit (Machery-Nagel) following the manufacturer's protocol.

Ligation reactions were performed using the T4 DNA ligase (New England Biolabs). Approximately 50 ng of vector DNA and 3 to 5-fold molar excess of insert DNA were mixed and kept at room temperature for 1 h minimum. Ligation mixtures were then used to transform *E. coli* strains DH5 $\alpha$ pir, SM10 $\lambda$ pir or MG1655.

## 6.5 Biochemical and proteomics methods

### 6.5.1 Immunoblot analyses

To test for stability and expression of YFP-CheW1, YFP-ParP and YFP-ParC variants, bacterial samples were collected from cultures ready for fluorescence microscopy imaging. Samples from different strains were normalized to equal optical density and subjected to western blot analysis using JL8 anti-GFP antibodies (which also recognize YFP). For positive control, strains were kept with plasmid pMF390 expressing YFP alone. Moreover, a strain not expressing any YFP was used as negative control.

### 6.5.2 Determination of isotopically labeled reference peptides for CheA, CheW, ParP and CheV proteins

*Vibrio cholerae* C6706 *lacZ*- was grown at 37°C in liquid LB until OD600 reached 0.5-0.7. Cells were pelleted by centrifugation and washed twice with PBS buffer (20%). Sample preparation, LC-MS and data analysis were carried out as described previously (Glatter et al., 2015; Yuan et al., 2017) with the exception of the proteolytic digest, which was carried out using a tandem LysC/trypsin digest. Following protein solubilization using 2% Sodiumlauroylsarcosinate (SLS) the detergent concentration was diluted to 0.5% with 100mM Ammoniumbicarbonate. To 50  $\mu$ g total protein extract, 500 ng LysC (Wako) was added and incubated for 4h at 37 °C. Then digest was continued by adding 1  $\mu$ g trypsin (Promega) for overnight at 30 °C. Detergent depletion and preparation of peptides for LC-MS analysis was carried out as described previously (Yuan et al., 2017).

The peptides were then analyzed using liquid-chromatography-mass spectrometry carried out on a Q-Exactive Plus instrument connected to an Ultimate 3000 RSLC nano and a nanospray flex ion source (all Thermo Scientific). Peptide separation was performed on a reverse phase HPLC column (75  $\mu$ m x 42 cm) packed in-house with C18 resin (2.4  $\mu$ m; Dr. Maisch). The following separating gradient was used: 98 % solvent A (0.15 % formic acid) and 2 % solvent B (99.85 % acetonitrile, 0.15 % formic acid) to 32 % solvent B over 90 minutes at a flow rate of 300 nl/min.

In order to identify the most suitable peptides for peptide standard synthesis digests from *Vibrio cholera* lysates were analyzed using data-dependent acquisition

(Yuan et al., 2017). In brief, the MS parameters were set as follows: MS1 resolution of 60 000 ( $m/z$  200), scan range from 375 to 1500  $m/z$ , MS/MS scans of the 10 most intense ions with 17 500 ( $m/z$  200). The ion accumulation time was set to 50 ms (both MS and MS/MS). The automatic gain control (AGC) was set to  $3 \times 10^6$  for MS survey scans and  $1 \times 10^5$  for MS/MS scans. MS raw files were searched using MASCOT (v 2.5, Matrix Science) with the following criteria: semitryptic tryptic specificity; two missed cleavages were allowed; carbamidomethylation (C) was set as a fixed modification; and oxidation (M) and deamidation (N, Q) were set as a variable modification. The mass tolerance was set to 10 ppm for precursor ions and 0.02. Search results were loaded into Scaffold 4 (Proteome software) and peptides were chosen as candidates for peptides synthesis when only fully cleaved and no miscleaved version of this peptide was observed.

### **6.5.3 Targeted Liquid chromatography-mass spectrometry (LC-MS)**

Sample and peptide preparation was carried out as described in previous section. Before solid-phase extraction, isotopically labeled reference peptides (TQL, JPT Peptide Technologies) for CheA, CheW and ParP were prepared according to the manufactures' instruction and added to the digested lysate with a concentration of 20 fmol/ $\mu$ l.

For targeted-MS analysis the mass spectrometer first acquired a full MS-SIM scan with an MS1 resolution of 70.000, ACG target setting of 1e6 and 100 ms max injection time. Then PRM scans were carried out with a MS2 resolution of 35.000, AGC target settings of 2e5, 100 ms and an isolation window of 2  $m/z$ . Normalized collision energy was set to 27%. The analysis was performed unscheduled. For data analysis, the results were imported into Skyline (v. 4.1.0.111714) (MacLean et al., 2010).

## **6.6 Microscopy methods**

### **6.6.1 Fluorescence microscopy**

#### **6.6.1.1 Sample preparation**

For fluorescence microscopy in El Tor clinical isolate N16961 and C6706 *lacZ*-, fluorescent fusion proteins were ectopically expressed from plasmids. Cells were grown for 12 hours in LB medium at 37° C with shaking. Ten microliters were then used to inoculate 5 milliliter cultures. When OD600  $\approx$  1.0, protein expression was induced by addition of 0.2% w/v final concentration of L-arabinose. The cultures were incubated for one additional hour, at which point cells were ready for microcopy analysis.

For fluorescence microscopy of *E. coli* strain VS296, a strain carrying the relevant plasmid for fluorescent protein expression was inoculated in 5 mL 10 % LB in PBS buffer. Expression of fluorescence proteins was induced by addition of 0.4% w/v final concentration of L-arabinose and 1 mM IPTG. Cultures were incubated 8-10 hours, at which time-point cells were ready for microscopy analysis.

To conduct fluorescence microscopy of *V. parahaemolyticus*, protein fusions were ectopically produce from plasmids. Cell were grown in agar plates containing 5 µg/ml of chloramphenicol overnight at 37° C. A colony was taken to inoculate 5 ml of liquid LB media with 5 µg/ml of chloramphenicol. When OD600 reached 0.1-0.2, protein expression was induced by adding 0.2% w/v final concentration of L-arabinose. The cells were then grown for 2 hours, until OD600 was 1.6-1.9. Cells were then collected for image acquisition.

To image DNA-stained nucleoids, *E. coli* MG1655 cells harboring their respective plasmids were grown 12 hours in LB liquid media containing 20 µg/ml of chloramphenicol at 30° C. Subsequently 50 µl were taken to inoculate 5 ml of liquid LB with 30 µg/ml of chloramphenicol. Cells were then incubated for 2 hours at 30° C with shaking, at which point 0.2% of w/v final concentration of L-arabinose was added to induce protein production. Cell cultures were incubated an additional 2 hours. Prior image collection cells were stained with 1 µg/ml of DNA stain 4',6-diamidino-2-phenylindole (DAPI) for 10 minutes.

### 6.6.1.2 Image acquisition

Cells ready for microscopy analysis were mounted onto 1% agarose pad. For imaging of *V. cholerae* and *V. parahaemolyticus* strains, agarose pad included 10 % PBS buffer. Microscopy of YFP-CheW1 was performed using a Zeiss Axio Imager M1 fluorescence microscope. Images were collected with a Cascade:1K CCD camera (Photometrics), using a Zeiss αPlan-Fluar 100x/1.45 Oil DIC objective. Imaging of YFP-CheA2 (Figure 26D) variants was performed using a Zeiss Axioplan 2 microscope equipped with a 100x a-plan lens and Hamamatsu cooled CCD camera. Microscopy of mCherry-VP2629 was conducted using a Zeiss Axioplan 2 microscope equipped with a 100x Plan lens and a Hamamatsu cooled CCD camera (Figure 40A). Every other microscopy experiment was performed using a Nikon eclipse Ti inverted Andor spinning-disc confocal microscope equipped with a 100x lens and an Andor Zyla sCMOS cooled camera and an Andor FRAPPA system. For comparison, in every experiment all mutant strains were imaged with the same exposure time and laser intensity as the wild-type.

### 6.6.1.3 Sample size and image analysis

Microscopy images were analyzed using Fiji (Schindelin et al., 2012). Demographs and line scan profiles were generated using a modified script from the previously published in (Cameron et al., 2014). R-studio v 3.0.1 (<http://www.rstudio.com/>) was employed to generate plots. In fluorescence microscopy experiments, the counting of the percentage of cells with distinct localization patterns was conducted manually. Minimum three experiments were considered for all analyses. From each experiment cells were taken for counting randomly, the total number of cells per strain included in every experiment appears in the figures. The mean of the three or more experiments is always plotted with error bars indicating the standard error of the mean (SEM). When required, a t-test was performed to calculate the  $p$  value. When an  $n$ -value is given for analyses of fluorescence microscopy images, this indicates the total number of cells analyzed of the three or more independent experiments.

For microscopy experiments measuring the fluorescence intensity of polar foci relative to the cytosolic signal (Figure 32), relative intensity was measured in the total number of cells indicated ( $n$ ) in the respective figures. The mean was then plotted with error bars representing the SEM. The  $p$ -value was calculated performing a Student's t-test.

For demographic analysis, the data from three or more biological experiments were pooled. If needed, the average of the normalized intensity from the demographs was calculated and plotted as a line scan. The total number of cells included ( $n$ ) is mentioned for each demograph in the corresponding figure. Statistical analyses and plots were generated using GraphPad Prism, v6.07, software (Prism Software, Irvine, CA).

To plot the distance of clusters from the cell poles, the values of the distance between foci was collected using MetaMorph Offline 7.7.5.0 (Universal Imaging Corporation, West Chester, PA, USA). Scatter plots were generated using Excel.

### 6.6.2 Photobleaching time-lapse experiments

Photobleaching time-lapse experiments were performed using the Andor FRAPPA system. Cells were treated and mounted on agarose pads as described for fluorescence microscopy of *V. cholerae* and *V. parahaemolyticus* cells. Firstly, a point-of-interest was bleached using a 515-nm laser at 7% intensity. In case of bleaching of the cytoplasm (for *V. cholerae* – Figure 31), a region-of-interest corresponding to 2/3 of the cell length was chosen and bleached with 1 pulse using a 515-nm laser at 7 % intensity. Cells were then imaged over time. For each time-point the fluorescence intensity at the cell pole was then calculated relative to the pre-bleach intensity and plotted as a function of time. Graphs represent the average intensity of the indicated

number of cells analyzed, with error-bars representing SEM. The total number of cells analyzed ( $n$ ) is mentioned in the figures.

### 6.6.3 Cryo-electron microscopy

For imaging of *V. cholerae* strains to determine the formation of arrays in  $\Delta cheA2$ , cells were cultured overnight in 5 ml LB media at 37°C with 200rpm shaking. For each strain, 3  $\mu$ l cell culture were applied to a freshly plasma-cleaned R2/2 copper Quantifoil grid (Quantifoil Micro Tools, Jena, Germany). Plunge freezing was carried out with a Leica EMGP (Leica microsystems, Wetzlar, Germany). Excessive liquid was wicked off from the grid by 1 second blotting inside the chamber set at room temperature and 95% humidity. Grids were plunge frozen in liquid ethane at -183°C and then stored in liquid nitrogen until imaging. Cryo-EM images were collected on a Talos L120C transmission electron microscope (Thermo Fisher Scientific (formerly FEI), Hillsboro, OR, USA) operating at 120 kV. All targets were randomly picked, manually located and imaged in low dose mode.

For imaging of lysed cells, lysis of *V. cholerae* and *E. coli* was performed using overnight cultures kept at 30°C shaking at 200 rpm, cells were grown in LB and TB media, respectively. Subsequently, cells were diluted 1:500 using fresh media. These cells were incubated at 30°C for additional 3 hours. Then 2000 UI/ml of penicillin was added to the cultures when they reached exponential phase. After addition of the antibiotic, cells were incubated one more hour and then harvested by centrifugation. The lysis process was monitored under a light microscope.

After lysis, a protein A-treated 10 nm colloidal gold solution (Cell Microscopy Core, Utrecht University, Utrecht, The Netherlands) was added into the lysed-cells mixture. After vortexing, aliquots of 3  $\mu$ l mixture was applied to freshly plasma-cleaned R2/2, 200mesh copper Quantifoil grids (Quantifoil Micro Tools GmbH, Germany). Plunge freezing was carried out in liquid ethane using a Leica EMGP (Leica microsystems, Wetzlar, Germany). During 1s blotting time, the blotting chamber was set at room temperature (20°C) with 95% humidity. Data acquisition was performed on a Titan Krios transmission electron microscope (Thermo Fisher Scientific (formerly FEI), Hillsboro, OR, USA) operating at 300 kV. Images were recorded with a Gatan K2 Summit direct electron detector (Gatan, Pleasanton, CA) equipped with a GIF-quantum energy filter (Gatan) operating with a slit width of 20eV to remove inelastically scattered electrons. Images were taken at a nominal magnification of 42,000 x, which corresponded to a pixel size of 3.513 Å. Under UCSFtomomo software, all tilt series were collected using a bidirectional tilt scheme which started with 0° to -60° followed by 0° to 60° tilting with a

2° increment. Defocus was set to -8  $\mu\text{m}$ . For unlysed bacteria cells and lysed cells, the cumulative dosage was 120  $\text{e}^-/\text{Å}^2$  and 80  $\text{e}^-/\text{Å}^2$ , respectively.

### **6.6.3.1 Tomogram Reconstruction and Subtomogram Averaging**

Drift correction, bead-tracking based tilt series alignment were done using software package IMOD (Mastronarde, 1997). CTFplotter was employed for CTF determination and correction (Xiong et al., 2009). Tomograms were reconstructed using both weighted back-projection simultaneous iterative reconstruction (SIRT) with iteration number set to 9. Dynamo was used for particle picking and subtomogram averaging (Castaño-Díez et al., 2012; Lutkenhaus et al., 2017).

## **6.6.4 sptPALM microscopy**

### **6.6.4.1 Sample preparation**

A colony of *V. parahaemolyticus* harboring the corresponding plasmid was inoculated in 5 ml liquid TB media with 5  $\mu\text{g}/\text{ml}$  of chloramphenicol. Cells were grown until OD600 reached 0.1-0.2, protein expression was then induced by adding 0.2% w/v final concentration of L-arabinose for one hour. Subsequently, cells were washed using 20% PBS twice by centrifugation at 4700 rpm. The pelletized cells were then suspended in EZ rich defined liquid medium (EZRDM, VWR, Germany) added with 10% PBS. Cells were incubated for additional 30 minutes, then an aliquot was washed by centrifugation and suspended in 10% PBS alone, from which 1-2  $\mu\text{l}$  were spotted onto an agarose pad.

### **6.6.4.2 Agarose slide preparation**

Low-temperature gelling agarose (Sigma-Aldrich, Germany) was suspended in freshly prepared EZ rich defined medium (EZRDM, VWR, Germany) with 10% PBS to a final concentration 1% (w/v) and heated up to 70°C until agarose melted completely, and stored later at 37°C. Cooled, but not gelled agarose was placed on the microscope slide inside the gene frame (Thermo Fisher, Germany) and sealed with a cleaned overnight in 1M KOH (Sigma-Aldrich, Germany) coverslip. After two hours coverslip was removed, cells were loaded on the agarose pad and covered with a new cleaned coverslip.

### **6.6.4.3 Microscope set-up**

Imaging was performed as described in detail earlier (Virant et al., 2017). Briefly, the microscope is a customized setup based on an automated Nikon Ti Eclipse microscope, equipped with appropriate dichroic and filters (ET dapi/Fitc/cy3 dichroic, ZT405/488/561rpc rejection filter, ET610/75 bandpass, all AHF Analysentechnik,

Germany), and a CFI Apo TIRF 100× oil objective (NA 1.49, Nikon). 405 and 561 nm laser devices (OBIS, Coherent Inc., Santa Clara, California USA) were modulated via an acousto-optical tunable filter (AOTF, Gooch & Housego, UK). Fluorescence was detected by an emCCD (iXON Ultra 888; Andor, UK) adjusted to 129 nm pixel size. The z-focus was controlled by a commercial perfect focus system (Nikon, Düsseldorf, Germany). Acquisitions were controlled by a customized version of the open source software  $\mu$ Manager (Edelstein et al., 2010). Live cell experiments were performed using a customized heating stage and heated objective at 25°C.

#### 6.6.4.4 sptPALM image acquisition

Living *V. parahaemolyticus* cells placed on the 1% agarose pads were imaged with the 33 Hz image acquisition rate for 15.000 frames in highly inclined and laminated optical sheet (HILO) mode (Tokunaga et al., 2008). The 561 nm laser irradiation was continuous with an intensity of 800 W/cm<sup>2</sup>, while the 405 nm laser was pulsed every 10<sup>th</sup> imaging frame with an intensity of 1-3 W/cm<sup>2</sup>. Before sptPALM imaging, bright-light snapshots of cell shapes were taken for cell segmentation required in data analysis.

#### 6.6.4.5 sptPALM data analysis

In a first step, cells were segmented manually from the bright-light images using Fiji (Schindelin et al., 2012) and stored as ROIs. Localizations were obtained using rapidSTORM 3.3 (Wolter et al., 2012) and split into single cell regions using the set of ROIs. Single-molecule trajectories were obtained and visualized using customized software written in C++, and filtered by their characteristics: trajectories shorter than 6 steps and longer than 20 steps were filtered out. Additionally, highly autofluorescent cells and obvious noise (e.g. from inclusion bodies) were manually discarded from the dataset. For remaining cells, the average displacement between adjacent frames for each trajectory ("jump distance JD" (Weimann et al., 2013)) was extracted for all trajectories and visualized in a histogram using OriginPro 2017 (Origin LAB Corporation). Color coding of the trajectories in the exemplarily shown cells (Figure 45A) and in the JD histograms (Figure 45B) reflects slow/immobile (red, JD  $\leq$  160 nm) and fast/free (blue, JD > 160 nm) diffusing molecules.

Detailed statistics of the data shown in (Figure 45) can be found below in Table 11.



### 6.6.4.5.1 Extracting diffusive states, their occupancies and apparent diffusion coefficients

Average JD values were represented as cumulative distribution function (CDF) using OriginPro 2017 for each ParC variant (Figure 45C). We then explored the number of underlying diffusive states in the CDFs using single-state, two-states and three-states CDFs. For all ParC variants, the CDF model for two diffusive states to each CDF gave the best performance:

$$CDF(r, t) = A_1(1 - \exp\left(-\frac{r^2}{4(D_1t + \sigma^2)}\right)) + A_2(1 - \exp\left(-\frac{r^2}{4(D_2t + \sigma^2)}\right)) \quad (1)$$

$A_1$  and  $A_2$  represent the occupancy of each diffusive state with apparent diffusion coefficients  $D_1$  and  $D_2$  respectively and localization precision  $\sigma$ , time interval  $t$ . Here, localization precision  $\sigma$  was explicitly left as a free parameter during fitting and for all CDF fits reproduced the experimental localization precision calculated from the rapidSTORM localizations using NeNA (Endesfelder et al., 2014). Obtained numbers for  $D_1$ ,  $D_2$  and occupancies  $A_1$ ,  $A_2$  as well as the  $R^2$ -value of each fit are shown in Figure 45C. Further, the single distributions for both diffusive states are plotted (red, slow, blue fast).

The two state diffusion model fails to fit the CDF for the freely diffusing PAmCherry control as (i) PAmCherry only exhibits one diffusive state freely diffusing through the cytoplasm and therefore (ii) shows a fast diffusion which in its distribution tail (fraction of JDs of 600 nm and higher), is already restricted by the cellular confinement under our imaging conditions (30 ms per frame). The PDF and CDF distribution thus is symmetrized by quenching the higher JD values due to confinement and is best fitted by the integral of the normal distribution:

$$C\ CDF(\mu, \omega) = \frac{1}{2} [1 + \operatorname{erf}\left(\frac{JD - \mu}{\sqrt{2\omega}}\right)] \quad (2)$$

with  $\mu$  and  $\omega$  being mean and variance of the normal distribution.

The apparent diffusion coefficient can then be obtained from:

$$JD^2 = 4D\Delta t + 4\sigma^2 \quad (3)$$

For (Figure 45A), where we were explicitly interested in the slow ( $JD \leq 160$  nm) fraction of molecules at the cell poles, we selected an area we consider as the “core polar region” (Figure 46, dark red inset) and extracted the trajectories which were (i) inside this area and (ii) fulfilled the criterion of average  $JD \leq 160$  nm. The obtained CDF plots were fitted using equation (2).

### 6.6.4.5.2 Generation of average cellular distribution heatmaps

Heatmaps of average cellular distributions (Figure 45, average JD (left)) of molecule density for all trajectories (middle) and of molecule density of trajectories with average JD  $\leq 160$  nm (to visualize the slow fraction only) (right) were generated by a customized Python 3 script (Python Software Foundation). Here, cells were filtered for 2.5-4  $\mu\text{m}$  cell length to remove already dividing or atypical cells. Each single cell was then rotated into the same orientation along its long axis; localization coordinates were normalized and mirrored vertically and horizontally along both axes into all four cellular quadrants. 2D histograms were generated using 22 and 8 pixels for the long and short cell axis, respectively and color-coded for average JD or molecule density. For JD heatmaps only pixels with at least 0.2% of the total amount of localizations and more than 30 localizations were filled with averaged values, pixels with insufficient statistics were left white. Profiles were generated by collapsing the distributions along both axes, respectively and smoothed with the Savitzky-Golay filter (Savitzky & Golay, 1964).

**Table 11. sptPALM data and statistics of different PA-mcherry ParC variants**

ParC variant	Cells analyzed	Total trajectories recorded
Wild-type	117	5600
K15Q	193	3322
G11V	78	3007
D39A	62	1285
R191E	129	3389
R191E+D39	129	4702
A		
PA-mcherry	106	5895

## 6.7 Bioinformatic analyses

### 6.7.1 Multiple sequence alignment

In generation of multiple sequence alignments of *V. cholerae* MCPs and ParP orthologues, respectively, we used the MUSCLE tool at default settings (Edgar, 2004).

ParP orthologues, in generation of the sequence alignment and phylogenetic tree in were chosen based on a STRING (Jensen et al., 2009) analysis of ParP and ParC from *V. cholerae*, using default settings. Thus, all ParP orthologues included in the analysis are encoded by predicted *parP* genes, located within a chemotaxis operon, and with an associated *parC* gene immediately upstream. Thus, indicating that all ParPs included in the analysis are part of a ParC/ParP-system.

ParP from *V. parahaemolyticus* was aligned against CheW from *T. maritima* MSB8. *T. maritima* MSB8 CheW was chosen as reference for the alignment as amino acid residues from *T. maritima* MSB8 CheW important for mediating interactions to MCPs have been solved (Briegel et al., 2012; Griswold et al., 2002; Li et al., 2013; Park et al., 2006).

To generate multiple sequence alignments of ParC and ParA protein sequences, T-coffee was used with the default settings (Notredame, C., Higgins, D. G., & Heringa et al., 2000) and BoxShade v3.2 was used for figure generation ([https://embnet.vital-it.ch/software/BOX\\_form.html](https://embnet.vital-it.ch/software/BOX_form.html)).

To obtain ParP sequences of different organisms (Figure 22), the NCBI Conserved Domain Architecture Retrieval Tool (CDART) (Geer et al., 2002) was surveyed for all ParP orthologous sequences. Subsequently, the retrieved sequences were manually pruned to remove redundant organisms. The selected sequences (Table 13) were used for multiple sequence alignment.

### 6.7.2 Phylogenetic tree

Phylogenetic trees were generated based on MUSCLE sequence alignments using Jalview Average Distance BLOSUM62 with default settings. Phylogenetic trees generated in Jalview were displayed and colored using iTOL (Letunic & Bork, 2011).

Furthermore, to generate the phylogenetic tree (Figure 23A) CheWs and CheAs from chemotaxis operons that have an associated ParC/ParP-system were included. These sequences were chosen based on a STRING analysis of ParP and ParC from *V. cholerae*.

### 6.7.3 Lists of sequences

Tables below include all genomic and protein sequences employed in this work.

**Table 12. Methyl-accepting chemotaxis proteins of *V. cholerae***

	<b>MCP locus number</b>	<b>Protein accession number</b>
1	VCA0008	NP_232409
2	VCA0031	NP_232432
3	VCA0068	NP_232469
4	VCA0176	NP_232576
5	VCA0220	NP_232619
6	VCA0268	NP_232666
7	VCA0658	NP_233047
8	VCA0663	NP_233052
9	VCA0773	NP_233159
10	VCA0864	NP_233250
11	VCA0906	NP_233291
12	VCA0923	NP_233308
13	VCA0974	NP_233358

---

14	VCA0988	NP_233372
15	VCA0979	AAF96875
16	VCA1034	NP_233417
17	VCA1056	NP_233438
18	VCA1069	NP_233451
19	VCA1088	NP_233469
20	VCA1092	NP_233472
21	VC0098	NP_229757
22	VC0216	NP_229873
23	VC0282	NP_229938
24	VC0449	NP_230103
25	VC0512	NP_230163
26	VC0514	NP_230165
27	VC0825	NP_230473
28	VC0840	NP_230488
29	VC1248	NP_230893
30	VC1289	NP_230934
31	VC1298	NP_230943
32	VC1313	NP_230957
33	VC1394	NP_231038
34	VC1403	NP_231046
35	VC1405	NP_231048
36	VC1406	NP_231049
37	VC1413	NP_231056
38	VC1535	AAF94689
39	VC1643	NP_231280
40	VC1859	NP_231493
41	VC1868	NP_231502
42	VC1898	NP_231532
43	VC1967	NP_231601
44	VC2161	NP_231792
45	VC2439	NP_232068

---

VCA-second chromosome, VC- first chromosome

**Table 13. ParP sequences employed for alignment**

Strain name	ParP Protein identifier
<i>Vibrio cholerae</i> _El_Tor_N16961	NP_231692.1
<i>Vibrio parahaemolyticus</i> _RIMD_2210633	NP_798605.1
<i>Aeromonas allosaccharophila</i>	WP_042658718.1
<i>Aeromonas bestiarum</i>	WP-WP103472014.1
<i>Aeromonas enteropelogenes</i>	WP_061475569.1
<i>Aeromonas jandaei</i>	WP_041208905.1
<i>Aeromonas lacus</i>	WP_033114442.1
<i>Aeromonas piscicola</i>	AAZ95864.1
<i>Aeromonas rivuli</i>	WP_042043842.1
<i>Aeromonas salmonicida</i>	WP_017412743.1
<i>Aeromonas sanarellii</i>	WP_042076857.1
<i>Aeromonas simiae</i>	WP_042045803.1
<i>Aeromonas veronii</i>	WP_005362044.1
<i>Aliagarivorans taiwanensis</i>	WP_026958074.1
<i>Alishewanella agri</i>	WP_008983085.1
<i>Alishewanella jeotgali</i>	WP_008949660.1
<i>Alteromonas confluentis</i>	WP_070127015.1
<i>Alteromonas lipolytica</i>	WP_070175550.1

---

<i>Anaerobiospirillum_succiniciproducens</i>	WP_052338870.1
<i>Bacterioplanes_sanyensis</i>	WP_094061726.1
<i>Enterovibrio_norvegicus</i>	WP_102391966.1
<i>Ferrimonas_futtsuensis</i>	WP_084644006.1
<i>Idiomarina_xiamenensis</i>	WP_008489642.1
<i>Marinobacterium_georgiense</i> DSM_11526	SEA09389.1
<i>Marinomonas_aquimarina</i>	SBS24862.1
<i>Marinospirillum_alkaliphilum</i>	WP_072325129.1
<i>Marinospirillum_insulare</i>	WP_027850719.1
<i>Oceanisphaera_profunda</i>	WP_087037911.1
<i>Oceanospirillaceae_bacterium_TMED276</i>	OUX65223.1
<i>Oceanospirillum_beijerinckii</i>	WP_051228069.1
<i>Oceanospirillum_maris</i>	WP_051206390.1
<i>Oceanospirillum_sanctuarii</i>	WP_086480803.1
<i>Pararheinheimera_texasensis</i>	WP_031571284.1
<i>Photobacterium_galatheae</i>	WP_081819538.1
<i>Photobacterium_halotolerans</i>	WP_081669340.1
<i>Photobacterium_leiognathi</i>	WP_023933112.1
<i>Photobacterium_marinum</i>	WP_086004399.1
<i>Pseudoalteromonas_luteoviolacea</i>	WP_039609440.1
<i>Pseudoalteromonas_phenolica</i>	WP_058029215.1
<i>Pseudoalteromonas_rubra</i>	WP_010385705.1
<i>Pseudomonas_aeruginosa</i>	WP_012076401.1
<i>Pseudomonas_chlororaphis</i>	WP_009042752.1
<i>Pseudomonas_congelans</i>	WP_096126117.1
<i>Pseudomonas_corrugata</i>	WP_024778680.1
<i>Pseudomonas_entomophila</i>	WP_011534881.1
<i>Pseudomonas_flexibilis</i>	KHL69861.1
<i>Pseudomonas_fluorescens</i>	WP_046037686.1
<i>Pseudomonas_fragi</i>	WP_095028713.1
<i>Pseudomonas_gingeri</i>	WP_042934655.1
<i>Pseudomonas_indica</i>	WP_084336178.1
<i>Pseudomonas_jessenii</i>	WP_090453851.1
<i>Pseudomonas_mendocina</i>	WP_003243240.1
<i>Pseudomonas_montellii</i>	WP_060394372.1
<i>Pseudomonas_moorei</i>	WP_090324247.1
<i>Pseudomonas_mosselii</i>	WP_028691012.1
<i>Pseudomonas_panipatensis</i>	WP_090262549.1
<i>Pseudomonas_psychrophila</i>	SDU69812.1
<i>Pseudomonas_punonensis</i>	WP_070882938.1
<i>Pseudomonas_putida</i>	WP_016498572.1
<i>Pseudomonas_reinekei</i>	WP_075948874.1
<i>Pseudomonas_seleniipraecipitans</i>	WP_092365155.1
<i>Pseudomonas_straminea</i>	WP_093503470.1
<i>Pseudomonas_synxantha</i>	WP_078821960.1
<i>Pseudomonas_syringae</i>	WP_024665776.1
<i>Pseudomonas_syringae_pv.-maculicola</i>	KPB68734.1
<i>Pseudomonas_syringae_pv._pisi_str.1704B</i>	EGH43690.1
<i>Pseudomonas_umsongensis</i>	WP_083348440.1
<i>Pseudomonas_vancouverensis</i>	WP_093225071.1
<i>Ruminobacter_amylophilus</i>	WP_093141449.1
<i>Ruminobacter_sp.RM87</i>	WP_051621752.1
<i>Salinivibrio_costicola</i>	WP_077662861.1
<i>Salinivibrio_kushneri</i>	WP_077456359.1
<i>Salinivibrio_proteolyticus</i>	WP_077674297.1
<i>Salinivibrio_sharmensis</i>	WP_077771506.1

<i>Salinivibrio_siamensis</i>	WP_077667784.1
<i>Shewanella_algae</i>	WP_025011080.1
<i>Shewanella_amazonensis</i>	WP_011760386.1
<i>Shewanella_decolorationis</i>	WP_023267150.1
<i>Shewanella_mangrovi</i>	WP_037443833.1
<i>Shewanella_putrefaciens</i>	WP_028761169.1
<i>Stenotrophomonas_maltophilia</i>	WP_049448934.1
<i>Succinimonas_amylolytica</i>	WP_019001110.1
<i>Succinivibrio_dextrinosolvens</i>	WP_037972713.1
<i>Teredinibacter_turnerae</i>	WP_018015569.1
<i>Thaumasiovibrio_subtropicus</i>	WP_087021619.1
<i>Vibrio_aerogenes</i>	WP_073605689.1
<i>Vibrio_albensis</i>	WP_000092961.1
<i>Vibrio_chagasii</i>	WP_105024519.1
<i>Vibrio_coralliilyticus</i>	WP_006959437.1
<i>Vibrio_diazotrophicus</i>	WP_042483829.1
<i>Vibrio_fluvialis</i>	WP_044365807.1
<i>Vibrio_fujianensis</i>	WP_099611467.1
<i>Vibrio_gazogenes</i>	WP_072956712.1
<i>Vibrio_hepatarius</i>	WP_053410728.1
<i>Vibrio_mangrovi</i>	WP_087480566.1
<i>Vibrio_mimicus</i>	WP_061052940.1
<i>Vibrio_neptunius</i>	WP_045975289.1
<i>Vibrio_orientalis</i>	WP_004413311.1
<i>Vibrio_ruber</i>	WP_077333788.1
<i>Vibrio_spartinae</i>	WP_074371532.1
<i>Vibrio_splendidus</i>	WP_004739871.1
<i>Vibrio_tritonius</i>	WP_068712699.1
<i>Vibrio_tubiashii</i>	WP_038205570.1
<i>Vibrio_vulnificus</i>	WP_080933302.1
<i>Vibrio_xiamenensis</i>	SDH70912.1
<i>Xanthomonas_axonopodis</i>	WP_015463129.1
<i>Xanthomonas_campestris</i>	WP_075287683.1
<i>Xanthomonas_codiaei</i>	WP_104540869.1

Table 14. Sequences employed for phylogenetic tree

Organism	LOCUS		
	CheA	ParP	CheW
<i>Vibrio parahaemolyticus</i> RIMD 2210633*	VP2229	VP2226	VP2225
<i>Virbio harveyi</i> *	VIBHAR_03141	VIBHAR_03138	VIBHAR_03137
<i>Vibrio vulnificus</i> CMCP6*	VV1_1955	VV1_1958	VV1_1959
<i>Vibrio splendidus</i> LGP32	VS_0843	VS_0849	VS_0847
<i>Vibrio cholerae</i> O395*	VC0395_A1651	VC0395_A1648	VC0395_A1647
<i>Vibrio fischeri</i> MJ11*	VFMJ11_1963	VFMJ11_1960	VFMJ11_1959
<i>Aliivibrio salmonicida</i>	VSAL_I2287	VSAL_I2284	VSAL_I2283
<i>Photobacterium profundum</i> SS9	PBPRA0942	PBPRA0945	PBPRA0946
<i>Idiomarina loihiensis</i> L2TR	IL1114	IL1111	IL1110

<i>Idiomarina loihiensis</i> GSL 199	K734_05605	K734_05590	K734_05585
<i>Pseudoalteromonas haloplanktis</i> TAC125	PSHAa0812	PSHAa0817	PSHAa0818
<i>Aeromonas hydrophila</i> ATCC 7966	AHA_1385	AHA_1390	AHA_1391
<i>Aeromonas hydrophila</i> ML09-119*	AHML_07500	AHML_07525	AHML_07530
<i>Aeromonas salmonicida</i>	ASA_1357	ASA_1362	ASA_1363
<i>Alteromonas macleodii</i>	MADE_02867		
<i>Alteromonas macleodii</i> ATCC 27126*	MASE_14110	MASE_04970	MASE_04975
<i>Pseudoalteromonas atlantica</i> T6c	Patl_3027	Patl_3024	Patl_3023
<i>Shewanella denitrificans</i> OS217	Sden_1346	Sden_1350	Sden_1351
<i>Shewanella frigidimarina</i> NCIMB400	Sfri_1202	Sfri_1206	Sfri_1207
<i>Shewanella woodyi</i> ATCC 51908	Swoo_1638	Swoo_1642	Swoo_1643
<i>Shewanella loihica</i> PV-4	Shew_1386	Shew_1390	Shew_1391
<i>Shewanella halifaxensis</i> HAW-EB4	Shal_1468	Shal_1472	Shal_1473
<i>Colwellia psychrerythraea</i> 34H	CPS_1522	CPS_1527	CPS_1528
<i>Pseudomonas aeruginosa</i> LESB58	PLES_39551	PLES_39501	PLES_39491
<i>Pseudomonas aeruginosa</i> PAO1	PA1458	PA1463	PA1464
<i>Pseudomonas aeruginosa</i> UCBPP-PA14	PA14_45590	PA14_45510	PA14_45500
<i>Pseudomonas aeruginosa</i> PA7	PSPA7_3868	PSPA7_3863	PSPA7_3862
<i>Pseudomonas mendocina</i> ymp	Pmen_2802	Pmen_2797	Pmen_2796
<i>Pseudomonas stutzeri</i> A1501	PST_2566	PST_2561	PST_2560
<i>Pseudomonas putida</i> F1	Pput_1529	Pput_1534	Pput_1535
<i>Pseudomonas entomophila</i> L48	PSEEN3793	PSEEN3788	PSEEN3787
<i>Pseudomonas fluorescens</i> SBW25	PFLU4414	PFLU4408	PFLU4407
<i>Pseudomonas syringae</i> DC3000	PSPTO_1982	PSPTO_1987	PSPTO_1988
<i>Cellvibrio japonicus</i>	CJA_2138	CJA_2133	CJA_2132
<i>Marinomonas</i> sp MWYL1	Mmwl1_3425	Mmwyl1_3420	Mmwyl1_3428
<i>Saccharophagus degradans</i>	Sde_2161	Sde_2156	Sde_2155
<i>Teredinibacter tumerae</i>	TERTU_1367	TERTU_1374	TERTU_1340
<i>Hahella chejuensis</i>	HCH_05168	HCH_05162	HCH_05161
<i>Marinobacter aquaeolei</i>	Maqu_1972	Maqu_1967	Maqu_1966
<i>Thioalkalivibrio sulfidophilus</i> HLEbGR7	Tgr7_1341	Tgr7_1346	Tgr7_1347
<i>Halorhodospira halophila</i> SL1	Hhal_0474	Hhal_0471	Hhal_0470

<i>Alkalilimnicola ehrlichii</i> MLHE-1	Mlg_0988	Mlg_0991	Mlg_0992
--	----------	----------	----------

\* When more than one CheA was found in the genome, the closest to ParP and ParC was taken.

**Table 15. ParA sequences**

Organism	Protein	NCBI identifier
<i>Vibrio parahaemolyticus</i>	ParC	NP_798606.1
<i>Vibrio cholerae</i>	ParC	AAF95207.1
<i>Vibrio parahaemolyticus</i>	ParA	NP_799457.1
<i>Vibrio cholerae</i>	ParA	AAF95912.1
<i>Rhodobacter sphaeroides</i>	PpfA	WP_011337952.1
<i>Caulobacter crescentus</i>	MipZ	AAK24136
<i>Synechococcus elongates</i>	ParA	BAD78634
<i>Vibrio alginolyticus</i>	FlhG	WP_009696006
<i>Pseudomonas aeruginosa</i>	Soj	WP_003097243.1
<i>Escherichia coli</i>	MinD	WP_103433148.1
<i>Thermus thermophilus</i>	Soj	WP_011173976

**Table 16. Other sequences used in this work**

Organism	Protein	Accession number/ Protein data bank ID	Relevant reference(s)
<i>Thermotoga maritima</i>	CheW	AHD17545.1/ 3UR1	(Griswold et al., 2002)
<i>Thermotoga maritima</i>	MCP TM1143	NP_228949.1	(Park et al., 2006)
<i>Escherichia coli</i>	CheW	ECK1888	
<i>Vibrio cholerae</i>	CheV1	NP_231242.1	
<i>Vibrio cholerae</i>	CheV2	NP_231640.1	
<i>Vibrio cholerae</i>	CheV3	NP_231833.1	
<i>Vibrio cholerae</i>	CheV4	NP_233338.1	



# REFERENCES

- Abedrabbo, S., Castellon, J., Collins, K. D., Johnson, K. S., & Ottemann, K. M. (2017). Cooperation of two distinct coupling proteins creates chemosensory network connections. *Proceedings of the National Academy of Sciences*, *114*(11), 2970–2975.
- Adler, J. (1966a). Chemotaxis in Bacteria. *Science*, *153*(3737), 708 LP-716.
- Adler, J. (1966b). Effect of amino acids and oxygen on chemotaxis in *Escherichia coli*. *Journal of Bacteriology*, *92*(1), 121–129.
- Adler, J. (1976). The sensing of chemicals by bacteria. *Scientific American*, *234*(4), 40–47.
- Alexander, R. P., Lowenthal, A. C., Harshey, R. M., & Ottemann, K. M. (2010). CheV: CheW-like coupling proteins at the core of the chemotaxis signaling network. *Trends in Microbiology*, *18*(11), 494–503.
- Alexander, R. P., & Zhulin, I. B. (2007). Evolutionary genomics reveals conserved structural determinants of signaling and adaptation in microbial chemoreceptors. *Proceedings of the National Academy of Sciences*, *104*(8), 2885–2890.
- Alexandre, G., Greer-Phillips, S., & Zhulin, I. B. (2004). Ecological role of energy taxis in microorganisms. *FEMS Microbiology Reviews*, *28*(1), 113–126.
- Ali, M., Nelson, A. R., Lopez, A. L., & Sack, D. A. (2015). Updated global burden of cholera in endemic countries. *PLoS Neglected Tropical Diseases*, *9*(6), e0003832.
- Alm, R. A., & Manning, P. A. (1990). Characterization of the hlyB gene and its role in the production of the El Tor haemolysin of *Vibrio cholerae* O1. *Molecular Microbiology*, *4*(3), 413–425.
- Almagro-Moreno, S., Pruss, K., & Taylor, R. K. (2015). Intestinal Colonization Dynamics of *Vibrio cholerae*. *PLoS Pathogens*, *11*(5), e1004787.
- Alon, U., Surette, M. G., Barkai, N., & Leibler, S. (1999). Robustness in bacterial chemotaxis. *Nature*, *397*(6715), 168–171.
- Alvarado, A., Kjær, A., Yang, W., Mann, P., Briegel, A., Waldor, M. K., & Ringgaard, S. (2017). Coupling chemosensory array formation and localization. *eLife*, *6*.
- Antúnez-Lamas, M., Cabrera-Ordóñez, E., López-Solanilla, E., Raposo, R., Trelles-Salazar, O., Rodríguez-Moreno, A., & Rodríguez-Palenzuela, P. (2009). Role of motility and chemotaxis in the pathogenesis of *Dickeya dadantii* 3937 (ex *Erwinia chrysanthemi* 3937). *Microbiology*, *155*(2), 434–442.
- Armitage, J. (1997). Behavioural responses of bacteria to light and oxygen. *Archives of Microbiology*.
- Armitage, J. P. (1999). *Bacterial tactic responses*. *Advances in microbial physiology* (Vol. 41).
- Armitage, J. P., Pitta, T. P., Vigeant, M. A. S., Packer, H. L., & Ford, R. M. (1999). Transformations in flagellar structure of *Rhodobacter sphaeroides* and possible relationship to changes in swimming speed. *Journal of Bacteriology*, *181*(16), 4825–4833.
- Asinas, A. E., & Weis, R. M. (2006). Competitive and cooperative interactions in receptor signaling complexes. *The Journal of Biological Chemistry*, *281*(41), 30512–30523.
- Avram Sanders, D., Mendez, B., & Koshland, D. E. (1989). Role of the CheW protein in bacterial chemotaxis: Overexpression is equivalent to absence. *Journal of Bacteriology*, *171*(11), 6271–6278.
- Bandyopadhyaya, A., & Chaudhuri, K. (2009). Differential modulation of NF-kappaB-mediated pro-inflammatory response in human intestinal epithelial cells by cheY homologues of *Vibrio cholerae*. *Innate Immunity*, *15*(3), 131–142.
- Banerjee, R., Das, S., Mukhopadhyay, K., Nag, S., Chakraborty, A., & Chaudhuri, K. (2002). Involvement of in vivo induced cheY-4 gene of *Vibrio cholerae* in motility, early adherence to intestinal epithelial cells and regulation of virulence factors. *FEBS Letters*, *532*(1–2), 221–226.
- Berg, H. C. (1991). Bacterial motility: handedness and symmetry. *Ciba Foundation Symposium*, *162*(1884), 58–69–72.
- Berg, H. C., & Berry, R. M. (2005). *E. coli* in motion. *Physics Today*, *58*(2), 64–65.
- Bilwes, A. M., Alex, L. A., Crane, B. R., & Simon, M. I. (1999). Structure of CheA, a signal-transducing histidine kinase. *Cell*, *96*(1), 131–141.
- Bischoff, D. S., & Ordal, G. W. (1991). Sequence and characterization of Bacillus subtilis CheB, a homolog of *Escherichia coli* CheY, and its role in a different mechanism of chemotaxis. *Journal of Biological Chemistry*, *266*(19), 12301–12305.
- Bischoff, D. S., & Ordal, G. W. (1992). Bacillus subtilis chemotaxis: a deviation from the *Escherichia coli* paradigm. *Molecular Microbiology*, *6*(1), 23–28.
- Boin, M. A., Austin, M. J., & Häse, C. C. (2004). Chemotaxis in *Vibrio cholerae*. *FEMS Microbiology Letters*.
- Boles, B. R., & McCarter, L. L. (2002). *Vibrio parahaemolyticus* scrABC, a novel operon affecting swarming and capsular polysaccharide regulation. *Journal of Bacteriology*, *184*(21), 5946–5954.
- Borkovich, K. A., Kaplan, N., Hess, J. F., & Simon, M. I. (1989). Transmembrane signal transduction in bacterial chemotaxis involves ligand-dependent activation of phosphate group transfer. *Proceedings of the National Academy of Sciences*, *86*(4), 1208–1212.
- Bornhorst, J. A., & Falke, J. J. (2000). Attractant regulation of the aspartate receptor - Kinase complex: Limited cooperative interactions between receptors and effects of the receptor modification state. *Biochemistry*, *39*(31), 9486–9493.

- Bouet, J. Y., Ah-Seng, Y., Benmeradi, N., & Lane, D. (2007). Polymerization of SopA partition ATPase: Regulation by DNA binding and SopB. *Molecular Microbiology*, 63(2), 468–481.
- Briegel, A., Beeby, M., Thanbichler, M., & Jensen, G. J. (2011). Activated chemoreceptor arrays remain intact and hexagonally packed. *Molecular Microbiology*, 82(3), 748–757.
- Briegel, A., Ladinsky, M. S., Oikonomou, C., Jones, C. W., Harris, M. J., Fowler, D. J., ... Jensen, G. J. (2014a). Structure of bacterial cytoplasmic chemoreceptor arrays and implications for chemotactic signaling. *eLife*, 2014(3), 1–16.
- Briegel, A., Li, X. X., Bilwes, A. M., Hughes, K. T., Jensen, G. J., & Crane, B. R. (2012). Bacterial chemoreceptor arrays are hexagonally packed trimers of receptor dimers networked by rings of kinase and coupling proteins. *Proceedings of the National Academy of Sciences*, 109(10), 3766–3771.
- Briegel, A., Ortega, D. R., Huang, A. N., Oikonomou, C. M., Gunsalus, R. P., & Jensen, G. J. (2015). Structural conservation of chemotaxis machinery across Archaea and Bacteria. *Environmental Microbiology Reports*, 7(3), 414–419.
- Briegel, A., Ortega, D. R., Mann, P., Kjær, A., Ringgaard, S., & Jensen, G. J. (2016). Chemotaxis cluster 1 proteins form cytoplasmic arrays in *Vibrio cholerae* and are stabilized by a double signaling domain receptor DosM. *Proceedings of the National Academy of Sciences*, 113(37), 10412–10417.
- Briegel, A., Ortega, D. R., Tocheva, E. I., Wuichet, K., Li, Z., Chen, S. Y., ... Jensen, G. J. (2009). Universal architecture of bacterial chemoreceptor arrays. *Proceedings of the National Academy of Sciences*, 106(40), 17181–17186.
- Briegel, A., Wong, M. L., Hodges, H. L., Oikonomou, C. M., Piasta, K. N., Harris, M. J., ... Jensen, G. J. (2014b). New Insights into Bacterial Chemoreceptor Array Structure and Assembly from Electron Cryotomography. *Biochemistry*, 53(10), 1575–1585.
- Burke, A. K., Guthrie, L. T. C., Modise, T., Cormier, G., Jensen, R. V., McCarter, L. L., & Stevens, A. M. (2015). OpaR controls a network of downstream transcription factors in *Vibrio parahaemolyticus* BB22OP. *PLoS ONE*, 10(4).
- Butler, S. M., & Camilli, A. (2004). Both chemotaxis and net motility greatly influence the infectivity of *Vibrio cholerae*. *Proceedings of the National Academy of Sciences*, 101(14), 5018–5023.
- Cameron, T. A., Anderson-Furgeson, J., Zupan, J. R., Zik, J. J., & Zambryski, P. C. (2014). Peptidoglycan synthesis machinery in *Agrobacterium tumefaciens* during unipolar growth and cell division. *mBio*, 5(3), e01219-14.
- Cannistraro, V. J., Glekas, G. D., Rao, C. V., & Ordal, G. W. (2011). Cellular stoichiometry of the chemotaxis proteins in *Bacillus subtilis*. *Journal of Bacteriology*, 193(13), 3220–3227.
- Cassidy, C. K., Himes, B. A., Alvarez, F. J., Ma, J., Zhao, G., Perilla, J. R., ... Zhang, P. (2015). CryoEM and computer simulations reveal a novel kinase conformational switch in bacterial chemotaxis signaling. *eLife*, 4.
- Castaing, J. P., Bouet, J. Y., & Lane, D. (2008). F plasmid partition depends on interaction of SopA with non-specific DNA. *Molecular Microbiology*, 70(4), 1000–1011.
- Castaño-Díez, D., Kudryashev, M., Arheit, M., & Stahlberg, H. (2012). Dynamo: A flexible, user-friendly development tool for subtomogram averaging of cryo-EM data in high-performance computing environments. *Journal of Structural Biology*.
- Chaparro, A. P., Ali, S. K., & Klose, K. E. (2010). The ToxT-dependent methyl-accepting chemoreceptors AcfB and Tcpl contribute to *Vibrio cholerae* intestinal colonization. *FEMS Microbiology Letters*, 302(2), 99–105.
- Clemens, J. D., Nair, G. B., Ahmed, T., Qadri, F., & Holmgren, J. (2017). Cholera. *The Lancet*, 390(10101), 1539–1549.
- Collins, K. D., Lacial, J., & Ottemann, K. M. (2014). Internal Sense of Direction: Sensing and Signaling from Cytoplasmic Chemoreceptors. *Microbiology and Molecular Biology Reviews*, 78(4), 672–684.
- Correa, N. E., Peng, F., & Klose, K. E. (2005). Roles of the regulatory proteins FlhF and FlhG in the *Vibrio cholerae* flagellar transcription hierarchy. *Journal of Bacteriology*, 187(18), 6324–6332.
- Davis, B. M., & Waldor, M. K. (2013). Establishing polar identity in gram-negative rods. *Current Opinion in Microbiology*, 16(6), 752–759.
- de Boer, P. A. J., Crossley, R. E., & Rothfield, L. I. (1989). A division inhibitor and a topological specificity factor coded for by the minicell locus determine proper placement of the division septum in *E. coli*. *Cell*, 56(4), 641–649.
- De Boer, P. A. J., Crossley, R. E., & Rothfield, L. I. (1992). Roles of MinC and MinD in the site-specific septation block mediated by the MinCDE system of *Escherichia coli*. *Journal of Bacteriology*, 174(1), 63–70.
- Donnenberg, M. S., & Kaper, J. B. (1991). Construction of an Eae Deletion Mutant of Enteropathogenic *Escherichia coli* by Using a Positive-Selection Suicide Vector. *Infection and Immunity*, 59(12), 4310–4317.
- Draper, W., & Liphardt, J. (2017). Origins of chemoreceptor curvature sorting in *Escherichia coli*. *Nature Communications*, 8.
- Duke, T., & Bray, D. (1999). Heightened sensitivity of a lattice of membrane receptors. *Proceedings of the National Academy of Sciences*, 96(18), 10104–10108.
- Ebersbach, G., & Gerdes, K. (2004). Bacterial mitosis: Partitioning protein ParA oscillates in spiral-shaped structures and positions plasmids at mid-cell. *Molecular Microbiology*, 52(2), 385–398.
- Edelstein, A., Amodaj, N., Hoover, K., Vale, R., & Stuurman, N. (2010). Computer control of microscopes using manager. *Current Protocols in Molecular Biology*, (SUPPL. 92), 1–22.
- Edgar, R. C. (2004). MUSCLE: multiple sequence alignment with high accuracy and high throughput. *Nucleic Acids Res*, 32(5), 1792–1797.
- Endesfelder, U., Malkusch, S., Fricke, F., & Heilemann, M. (2014). A simple method to estimate the average localization

- precision of a single-molecule localization microscopy experiment. *Histochemistry and Cell Biology*, 141(6), 629–638.
- Endres, R. G., & Wingreen, N. S. (2006). Precise adaptation in bacterial chemotaxis through “assistance neighborhoods.” *Proceedings of the National Academy of Sciences*, 103(35), 13040–13044.
- Engelmann, T. W. (1883). Bacterium photometricum - Ein Beitrag zur vergleichenden Physiologie des Licht- und Farbensinnes. *Pfleger, Archiv Für Die Gesamte Physiologie Des Menschen Und Der Thiere*, 30(1), 95–124.
- Englert, D. L., Adase, C. A., Jayaraman, A., & Manson, M. D. (2010). Repellent taxis in response to nickel ion requires neither Ni<sup>2+</sup> transport nor the periplasmic NikA binding protein. *Journal of Bacteriology*, 192(10), 2633–2637.
- Erbse, A. H., & Falke, J. J. (2009). The Core Signaling Proteins of Bacterial Chemotaxis Assemble To Form an Ultrastable Complex. *Biochemistry*, 48(29), 6975–6987.
- Erdmann, N., Petroff, T., & Funnell, B. E. (1999). Intracellular localization of P1 ParB protein depends on ParA and parS. *Proceedings of the National Academy of Sciences*, 96(26), 14905–14910.
- Everiss, K. D., Hughes, K. J., Kovach, M. E., & Peterson, K. M. (1994). The *Vibrio cholerae* acfB colonization determinant encodes an inner membrane protein that is related to a family of signal-transducing proteins. *Infection and Immunity*, 62(8), 3289–3298.
- Faguy, D. M., & Jarrell, K. F. (1999). A twisted tale: The origin and evolution of motility and chemotaxis in prokaryotes. *Microbiology*.
- Falke, J. J., & Hazelbauer, G. L. (2001). Transmembrane signaling in bacterial chemoreceptors. *Trends in Biochemical Sciences*.
- Ferris, H. U., Dunin-Horkawicz, S., Mondjar, L. G., Hulko, M., Hantke, K., Martin, J., ... Coles, M. (2011). The mechanisms of HAMP-mediated signaling in transmembrane receptors. *Structure*, 19(3), 378–385.
- Fogel, M. A., & Waldor, M. K. (2006). A dynamic, mitotic-like mechanism for bacterial chromosome segregation. *Genes and Development*, 20(23), 3269–3282.
- Fredrick, K. L., & Helmann, J. D. (1994). Dual chemotaxis signaling pathways in *Bacillus subtilis*: A  $\sigma$ (D)-dependent gene encodes a novel protein with both CheW and CheY homologous domains. *Journal of Bacteriology*, 176(9), 2727–2735.
- Freter, R., & O'Brien, P. C. M. (1981a). Role of chemotaxis in the association of motile bacteria with intestinal mucosa: Chemotactic responses of *Vibrio cholerae* and description of motile nonchemotactic mutants. *Infection and Immunity*, 34(1), 215–221.
- Freter, R., & O'Brien, P. C. M. (1981b). Role of chemotaxis in the association of motile bacteria with intestinal mucosa: Fitness and virulence of nonchemotactic *Vibrio cholerae* mutants in infant mice. *Infection and Immunity*, 34(1), 222–233.
- Freter, R., O'Brien, P. C. M., & Macsai, M. S. (1981). Role of chemotaxis in the association of motile bacteria with intestinal mucosa: *In vivo* studies. *Infection and Immunity*, 34(1), 234–240.
- Fu, X., Himes, B. A., Ke, D., Rice, W. J., Ning, J., & Zhang, P. (2014). Controlled bacterial lysis for electron tomography of native cell membranes. *Structure*, 22(12), 1875–1882.
- Fukuoka, H., Sagawa, T., Inoue, Y., Takahashi, H., & Ishijima, A. (2014). Direct imaging of intracellular signaling components that regulate bacterial chemotaxis. *Sci Signal*, 7(319), ra32.
- Galli, E., Paly, E., & Barre, F. X. (2017). Late assembly of the *Vibrio cholerae* cell division machinery postpones septation to the last 10% of the cell cycle. *Scientific Reports*, 7.
- Geer, L. Y., Domrachev, M., Lipman, D. J., & Bryant, S. H. (2002). CDART: Protein homology by domain architecture. *Genome Research*.
- Gegner, J. A., & Dahlquist, F. W. (1991). Signal transduction in bacteria: CheW forms a reversible complex with the protein kinase CheA. *Proc Natl Acad Sci U S A*, 88(3), 750–754.
- Gegner, J. A., Graham, D. R., Roth, A. F., & Dahlquist, F. W. (1992). Assembly of an MCP receptor, CheW, and kinase CheA complex in the bacterial chemotaxis signal transduction pathway. *Cell*, 70(6), 975–982.
- Gerdes, K., Howard, M., & Szardenings, F. (2010). Pushing and pulling in prokaryotic DNA segregation. *Cell*, 141(6), 927–942.
- Gestwicki, J. E., Lamanna, A. C., Harshey, R. M., McCarter, L. L., Kiessling, L. L., & Adler, J. (2000). Evolutionary Conservation of Methyl-Accepting Chemotaxis Protein Location in Bacteria and Archaea Evolutionary Conservation of Methyl-Accepting Chemotaxis Protein Location in Bacteria and Archaea. *Journal of Bacteriology*, 182(22), 6499–6502.
- Gill, D. M., & Meren, R. (1978). ADP-ribosylation of membrane proteins catalyzed by cholera toxin: basis of the activation of adenylate cyclase. *Proc Natl Acad Sci U S A*, 75(7), 3050–3054.
- Glatter, T., Ahrné, E., & Schmidt, A. (2015). Comparison of different sample preparation protocols reveals lysis buffer-specific extraction biases in gram-negative bacteria and human cells. *Journal of Proteome Research*.
- Goldman, D. J., & Ordal, G. W. (1984). In Vitro Methylation and Demethylation of Methyl-Accepting Chemotaxis Proteins in *Bacillus subtilis*. *Biochemistry*, 23(12), 2600–2606.
- Gosink, K. K., Kobayashi, R., Kawagishi, I., & Häse, C. C. (2002). Analyses of the roles of the three cheA homologs in chemotaxis of *Vibrio cholerae*. *Journal of Bacteriology*, 184(6), 1767–1771.
- Greenfield, D., McEvoy, A. L., Shroff, H., Crooks, G. E., Wingreen, N. S., Betzig, E., & Liphardt, J. (2009). Self-organization of the *Escherichia coli* chemotaxis network imaged with super-resolution light microscopy. *PLoS Biology*, 7(6).

- <https://doi.org/10.1371/journal.pbio.1000137>
- Griswold, I. J., Zhou, H., Matison, M., Swanson, R. V., McIntosh, L. P., Simon, M. I., & Dahlquist, F. W. (2002). The solution structure and interactions of CheW from *Thermotoga maritima*. *Nature Structural Biology*, *9*(2), 121–125.
- Guentzel, M. N., & Berry, L. J. (1975). Motility as a virulence factor for *Vibrio cholerae*. *Infection and Immunity*, *11*(5), 890–897.
- Gupta, S., & Chowdhury, R. (1997). Bile affects production of virulence factors and motility of *Vibrio cholerae*. *Infection and Immunity*, *65*(3), 1131–1134.
- Guzman, L. M., Belin, D., Carson, M. J., & Beckwith, J. (1995). Tight regulation, modulation, and high-level expression by vectors containing the arabinose P(BAD) promoter. *Journal of Bacteriology*.
- Haglin, E. R., Yang, W., Briegel, A., & Thompson, L. K. (2017). His-Tag-Mediated Dimerization of Chemoreceptors Leads to Assembly of Functional Nanoarrays. *Biochemistry*, *56*(44), 5874–5885.
- Hamblin, P. a, Maguire, B. a, Grishanin, R. N., & Armitage, J. P. (1997). Evidence for two chemosensory pathways in *Rhodobacter sphaeroides*. *Molecular Microbiology*, *26*(5), 1083–1096.
- Hamer, R., Chen, P.-Y., Armitage, J. P., Reinert, G., & Deane, C. M. (2010). Deciphering chemotaxis pathways using cross species comparisons. *BMC Systems Biology*, *4*(1), 3.
- Hang, L., John, M., Asaduzzaman, M., Bridges, E. A., Vanderspurt, C., Kirn, T. J., ... Calderwood, S. B. (2003). Use of in vivo-induced antigen technology (IVIAT) to identify genes uniquely expressed during human infection with *Vibrio cholerae*. *Proceedings of the National Academy of Sciences*, *100*(14), 8508–8513.
- Hanlon, D. W., Márquez-Magaña, L. M., Carpenter, P. B., Chamberlin, M. J., & Ordal, G. W. (1992). Sequence and characterization of *Bacillus subtilis* CheW. *The Journal of Biological Chemistry*, *267*(17), 12055–12060.
- Harkey, C. W., Everiss, K. D., & Peterson, K. M. (1994). The *Vibrio cholerae* toxin-coregulated-pilus gene *tcpI* encodes a homolog of methyl-accepting chemotaxis proteins. *Infection and Immunity*, *62*(7), 2669–2678.
- Harris, J. B., LaRocque, R. C., Qadri, F., Ryan, E. T., & Calderwood, S. B. (2012). Cholera. In *The Lancet* (Vol. 379, pp. 2466–2476).
- Hayashi, I., Oyama, T., & Morikawa, K. (2001). Structural and functional studies of MinD ATPase: implications for the molecular recognition of the bacterial cell division apparatus. *Embo Journal*, *20*(8), 1819–1828.
- Hazelbauer, G. L., Falke, J. J., & Parkinson, J. S. (2008). Bacterial chemoreceptors: high-performance signaling in networked arrays. *Trends in Biochemical Sciences*, *33*(1), 9–19.
- Heering, J., & Ringgaard, S. (2016). Differential localization of chemotactic signaling arrays during the lifecycle of *Vibrio parahaemolyticus*. *Frontiers in Microbiology*, *7*(November), 1–12.
- Hegde, M., Englert, D. L., Schrock, S., Cohn, W. B., Vogt, C., Wood, T. K., ... Jayaraman, A. (2011). Chemotaxis to the quorum-sensing signal AI-2 requires the Tsr chemoreceptor and the periplasmic LsrB AI-2-binding protein. *Journal of Bacteriology*, *193*(3), 768–773.
- Hernandez-Valle, J., Domenzain, C., de la Mora, J., Poggio, S., Dreyfus, G., & Camarena, L. (2017). The master regulators of the *fla1* and *fla2* flagella of *Rhodobacter sphaeroides* control the expression of their cognate chey proteins. *Journal of Bacteriology*, *199*(5).
- Hester, C. M., & Lutkenhaus, J. (2007). Soj (ParA) DNA binding is mediated by conserved arginines and is essential for plasmid segregation. *Proceedings of the National Academy of Sciences*, *104*(51), 20326–20331.
- Hickman, J. W., Tifrea, D. F., & Harwood, C. S. (2005). A chemosensory system that regulates biofilm formation through modulation of cyclic diguanylate levels. *Proceedings of the National Academy of Sciences*, *102*(40), 14422–14427.
- Hiremath, G., Hyakutake, A., Yamamoto, K., Ebisawa, T., Nakamura, T., Nishiyama, S. ichiro, ... Kawagishi, I. (2015). Hypoxia-induced localization of chemotaxis-related signaling proteins in *Vibrio cholerae*. *Molecular Microbiology*, *95*(5), 780–790.
- Hu, Z., Gogol, E. P., & Lutkenhaus, J. (2002). Dynamic assembly of MinD on phospholipid vesicles regulated by ATP and MinE. *Proceedings of the National Academy of Sciences*, *99*(10), 6761–6766.
- Hu, Z., Mukherjee, A., Pichoff, S., & Lutkenhaus, J. (1999). The MinC component of the division site selection system in *Escherichia coli* interacts with FtsZ to prevent polymerization. *Proceedings of the National Academy of Sciences*, *96*(26), 14819–14824.
- Hui, M. P., Galkin, V. E., Yu, X., Stasiak, A. Z., Stasiak, A., Waldor, M. K., & Egelman, E. H. (2010). ParA2, a *Vibrio cholerae* chromosome partitioning protein, forms left-handed helical filaments on DNA. *Proceedings of the National Academy of Sciences*, *107*(10), 4590–4595.
- Hulko, M., Berndt, F., Gruber, M., Linder, J. U., Truffault, V., Schultz, A., ... Coles, M. (2006). The HAMP Domain Structure Implies Helix Rotation in Transmembrane Signaling. *Cell*, *126*(5), 929–940. <https://doi.org/10.1016/j.cell.2006.06.058>
- Hyakutake, A., Homma, M., Austin, M. J., Boin, M. A., Häse, C. C., & Kawagishi, I. (2005). Only one of the five CheY homologs in *Vibrio cholerae* directly switches flagellar rotation. *Journal of Bacteriology*, *187*(24), 8403–8410.
- Inaba, S., Nishigaki, T., Takekawa, N., Kojima, S., & Homma, M. (2017). Localization and domain characterization of the SfiA regulator of flagellar formation in *Vibrio alginolyticus*. *Genes to Cells*, *22*(7), 619–627. <https://doi.org/10.1111/gtc.12501>
- Jensen, L. J., Kuhn, M., Stark, M., Chaffron, S., Creevey, C., Muller, J., ... von Mering, C. (2009). STRING 8—a global view on proteins and their functional interactions in 630 organisms. *Nucleic Acids Research* *37*(Database issue), D412–6.

- Jones, C. W., & Armitage, J. P. (2015). Positioning of bacterial chemoreceptors. *Trends Microbiol*, 23(5), 247–256.
- Jones, C. W., & Armitage, J. P. (2017). Essential role of the cytoplasmic chemoreceptor TlpT in the de novo formation of chemosensory complexes in *Rhodobacter sphaeroides*. *Journal of Bacteriology*, JB--00366.
- Karatan, E., Saulmon, M. M., Bunn, M. W., & Ordal, G. W. (2001). Phosphorylation of the Response Regulator CheV Is Required for Adaptation to Attractants during *Bacillus subtilis* Chemotaxis. *Journal of Biological Chemistry*, 276(47), 43618–43626.
- Karimova, G., Pidoux, J., Ullmann, A., & Ladant, D. (1998). A bacterial two-hybrid system based on a reconstituted signal transduction pathway. *Proceedings of the National Academy of Sciences*, 95(10), 5752–5756.
- Kearns, D. B. (2010). A field guide to bacterial swarming motility. *Nature Reviews Microbiology*.
- Kelley, L. A., & Sternberg, M. J. (2009). Protein structure prediction on the Web: a case study using the Phyre server. *Nature Protocols*, 4(3), 363.
- Kibbe, W. A. (2007). OligoCalc: An online oligonucleotide properties calculator. *Nucleic Acids Research*, 35(2), W43–W46.
- Kiekeley, D., Michie, K. A., Essen, L. O., Löwe, J., & Thanbichler, M. (2012). Localized Dimerization and Nucleoid Binding Drive Gradient Formation by the Bacterial Cell Division Inhibitor MipZ. *Molecular Cell*, 46(3), 245–259.
- Kihara, M., & Macnab, R. M. (1981). Cytoplasmic pH mediated pH taxis and weak-acid repellent taxis of bacteria. *Journal of Bacteriology*, 145(3), 1209–1221.
- Kim, H.-E., Shitashiro, M., Kuroda, A., Takiguchi, N., & Kato, J. (2007). Ethylene Chemotaxis in *Pseudomonas aeruginosa* and Other *Pseudomonas* Species. *Microbes and Environments*, 22(2), 186–189.
- Kim, K. K., Yokota, H., & Kim, S. H. (1999). Four-helical-bundle structure of the cytoplasmic domain of a serine chemotaxis receptor. *Nature*, 400(6746), 787–792.
- Kim, Y. K., & McCarter, L. L. (2000). Analysis of the polar flagellar gene system of *Vibrio parahaemolyticus*. *Journal of Bacteriology*, 182(13), 3693–3704.
- Kirsch, M. L., Peters, P. D., Hanlon, D. W., Kirby, J. R., & Ordal, G. W. (1993a). Chemotactic methyltransferase promotes adaptation to high concentrations of attractant in *Bacillus subtilis*. *Journal of Biological Chemistry*, 268(25), 18610–18616.
- Kirsch, M. L., Zuberi, A. R., Henner, D., Peters, P. D., Yazdi, M. A., & Ordal, G. W. (1993b). Chemotactic methyltransferase promotes adaptation to repellents in *Bacillus subtilis*. *Journal of Biological Chemistry*, 268(34), 25350–25356.
- Koonin, E. V. (1993). A superfamily of ATPases with diverse functions containing either classical or deviant ATP-binding motif. *Journal of Molecular Biology*, 229(4), 1165–1174.
- Krembel, A. K., Neumann, S., & Sourjik, V. (2015). Universal Response-Adaptation Relation in Bacterial Chemotaxis. *Journal of Bacteriology*, 197(2), 307–313.
- Kremer, J. R., Mastrorade, D. N., & McIntosh, J. R. (1996). Computer visualization of three-dimensional image data using IMOD. *Journal of Structural Biology*, 116(1), 71–76.
- Kusumoto, A., Shinohara, A., Terashima, H., Kojima, S., Yakushi, T., & Homma, M. (2008). Collaboration of FlhF and FlhG to regulate polar flagella number and localization in *Vibrio alginolyticus*. *Microbiology*, 154(5), 1390–1399.
- Lacal, J., Garcia-Fontana, C., Muñoz-Martínez, F., Ramos, J. L., & Krell, T. (2010). Sensing of environmental signals: Classification of chemoreceptors according to the size of their ligand binding regions. *Environmental Microbiology*, 12(11), 2873–2884.
- Lackner, L. L., Raskin, D. M., & De Boer, P. A. J. (2003). ATP-dependent interactions between *Escherichia coli* Min proteins and the phospholipid membrane in vitro. *Journal of Bacteriology*, 185(3), 735–749.
- Laganenka, L., Colin, R., & Sourjik, V. (2016). Chemotaxis towards autoinducer 2 mediates autoaggregation in *Escherichia coli*. *Nature Communications*, 7.
- Lazzaroni, J. C., Germon, P., Ray, M. C., & Vianney, A. (1999). The Tol proteins of *Escherichia coli* and their involvement in the uptake of biomolecules and outer membrane stability. *FEMS Microbiology Letters*, 177(2), 191–197.
- Lee, S. H., Butler, S. M., & Camilli, A. (2001). Selection for in vivo regulators of bacterial virulence. *Proceedings of the National Academy of Sciences*, 98(12), 6889–6894.
- Leonard, T. A., Butler, P. J., & Löwe, J. (2005). Bacterial chromosome segregation: structure and DNA binding of the Soj dimer--a conserved biological switch. *The EMBO Journal*, 24(2), 270–282.
- Letunic, I., & Bork, P. (2011). Interactive Tree Of Life v2: online annotation and display of phylogenetic trees made easy. *Nucleic Acids Research*, 39(Web Server issue), W475–8.
- Letunic, I., & Bork, P. (2018). 20 years of the SMART protein domain annotation resource. *Nucleic Acids Research*, 46(d1), D493–D496.
- Levit, M. N., Grebe, T. W., & Stock, J. B. (2002). Organization of the receptor-kinase signaling array that regulates *Escherichia coli* chemotaxis. *Journal of Biological Chemistry*, 277(39), 36748–36754.
- Li, G., & Weis, R. M. (2000). Covalent modification regulates ligand binding to receptor complexes in the chemosensory system of *Escherichia coli*. *Cell*, 100(3), 357–365.
- Li, M., & Hazelbauer, G. L. (2004). Cellular stoichiometry of the components of the chemotaxis signaling complex. *Journal of Bacteriology*, 186(12), 3687–3694.
- Li, M., & Hazelbauer, G. L. (2005). Adaptational assistance in clusters of bacterial chemoreceptors. *Molecular Microbiology*, 56(6), 1617–1626.

- Li, M., & Hazelbauer, G. L. (2014). Selective allosteric coupling in core chemotaxis signaling complexes. *Proceedings of the National Academy of Sciences*, 2014(6), 1–6.
- Li, M., Khursigara, C. M., Subramaniam, S., & Hazelbauer, G. L. (2011). Chemotaxis kinase CheA is activated by three neighbouring chemoreceptor dimers as effectively as by receptor clusters. *Molecular Microbiology*, 79(3), 677–685.
- Li, M. S., & Hazelbauer, G. L. (2011). Core unit of chemotaxis signaling complexes. *Proc Natl Acad Sci U S A*, 108(23), 9390–9395.
- Li, X. X., Fleetwood, A. D., Bayas, C., Bilwes, A. M., Ortega, D. R., Falke, J. J., ... Crane, B. R. (2013). The 3.2 angstrom Resolution Structure of a Receptor:CheA:CheW Signaling Complex Defines Overlapping Binding Sites and Key Residue Interactions within Bacterial Chemosensory Arrays. *Biochemistry*, 52(22), 3852–3865.
- Li, Y., Hu, Y., Fu, W., Xia, B., & Jin, C. (2007). Solution structure of the bacterial chemotaxis adaptor protein CheW from *Escherichia coli*. *Biochemical and Biophysical Research Communications*, 360(4), 863–867.
- Lim, G. E., Derman, A. I., & Pogliano, J. (2005). Bacterial DNA segregation by dynamic SopA polymers. *Proceedings of the National Academy of Sciences*, 102(49), 17658–17663.
- Liu, J., Hu, B., Morado, D. R., Jani, S., Manson, M. D., & Margolin, W. (2012). Molecular architecture of chemoreceptor arrays revealed by cryoelectron tomography of *Escherichia coli* minicells. *Proceedings of the National Academy of Sciences*, 109(23), E1481–E1488.
- Lizardi, P. M., Huang, X., Zhu, Z., Bray-Ward, P., Thomas, D. C., & Ward, D. C. (1998). Mutation detection and single-molecule counting using isothermal rolling-circle amplification. *Nature Genetics*, 19(3), 225.
- Lopes, J. G., & Sourjik, V. (2018). Chemotaxis of *Escherichia coli* to major hormones and polyamines present in human gut. *The ISME Journal*, 1.
- Lundgren, D. H., Hwang, S. II, Wu, L., & Han, D. K. (2010). Role of spectral counting in quantitative proteomics. *Expert Review of Proteomics*, 7(1), 39–53.
- Lutkenhaus, J. (2012). The ParA/MinD family puts things in their place. *Trends in Microbiology*, 20(9), 411–418.
- Lutkenhaus, Kudryashev, M., & Stahlberg, H. (2017). Dynamo Catalogue: Geometrical tools and data management for particle picking in subtomogram averaging of cryo-electron tomograms. *Journal of Structural Biology*, 197(2), 135–144.
- MacCready, J. S., Hakim, P., Young, E. J., Hu, L., Liu, J., Osteryoung, K. W., ... Ducat, D. C. (2018). Protein Gradients on the Nucleoid Position the Carbon-fixing Organelles of Cyanobacteria. *bioRxiv*. <https://doi.org/10.1101/334813>
- Mackenzie, C., Choudhary, M., Larimer, F. W., Predki, P. F., Stilwagen, S., Armitage, J. P., ... Kaplan, S. (2001). The home stretch, a first analysis of the nearly completed genome of *Rhodobacter sphaeroides* 2.4.1. *Photosynthesis Research*, 70(1), 19–41.
- MacLean, B., Tomazela, D. M., Shulman, N., Chambers, M., Finney, G. L., Frewen, B., ... MacCoss, M. J. (2010). Skyline: An open source document editor for creating and analyzing targeted proteomics experiments. *Bioinformatics*, 26(7), 966–968.
- Macnab, R. M., & Koshland, D. E. (1972). The Gradient-Sensing Mechanism in Bacterial Chemotaxis. *Proceedings of the National Academy of Sciences*, 69(9), 2509–2512.
- Maddock, J. R., & Shapiro, L. (1993). Polar localization of the chemotaxis receptor complex in *Escherichia coli* cell. *Science*, 259(5102), 1717–1723.
- Maeda, K., Imae, Y., Shioi, J. I., & Oosawa, F. (1976). Effect of temperature on motility and chemotaxis of *Escherichia coli*. *Journal of Bacteriology*, 127(3), 1039–1046.
- Marston, a L., & Errington, J. (1999). Dynamic movement of the ParA-like Soj protein of *B. subtilis* and its dual role in nucleoid organization and developmental regulation. *Molecular Cell*, 4(5), 673–682.
- Mastrorarde, D. N. (1997). Dual-axis tomography: An approach with alignment methods that preserve resolution. *Journal of Structural Biology*, 120(3), 343–352.
- Matilla, M. A., & Krell, T. (2017). Chemoreceptor-based signal sensing. *Current Opinion in Biotechnology*, 45, 8–14.
- Matilla, M. A., & Krell, T. (2018). The effect of bacterial chemotaxis on host infection and pathogenicity. *FEMS Microbiology Reviews*, 42(1), p.fux052.
- Matsuoka, S., Shibata, T., & Ueda, M. (2009). Statistical analysis of lateral diffusion and multistate kinetics in single-molecule imaging. *Biophysical Journal*, 97(4), 1115–1124.
- Mauriello, E. M. F., Jones, C., Moine, A., & Armitage, J. P. (2018). Cellular targeting and segregation of bacterial chemosensory systems. *FEMS Microbiology Reviews*, 42(4), 462–476
- McCarter, L. (1999). The multiple identities of *Vibrio parahaemolyticus*. *J Mol Microbiol Biotechnol*, 1(1), 51–57.
- McCarter, L., Hilmen, M., & Silverman, M. (1988). Flagellar dynamometer controls swarmer cell differentiation of *V. parahaemolyticus*. *Cell*, 54(3), 345–351.
- McCarter, L., & Silverman, M. (1990). Surface-induced swarmer cell differentiation of *Vibrio parahaemolyticus*. *Molecular Microbiology*, 4(7), 1057–1062.
- Meinhardt, H., & de Boer, P. A. J. (2001). Pattern formation in *Escherichia coli*: A model for the pole-to-pole oscillations of Min proteins and the localization of the division site. *Proceedings of the National Academy of Sciences*, 98(25), 14202–14207.
- Mekalanos, J. J. (1985). Cholera toxin: genetic analysis, regulation, and role in pathogenesis. In *Genetic Approaches to*

- Microbial Pathogenicity* (pp. 97–118). Springer.
- Micali, G., & Endres, R. G. (2016). Bacterial chemotaxis: Information processing, thermodynamics, and behavior. *Current Opinion in Microbiology*, 30, 8-15.
- Miller, V. L., & Mekalanos, J. J. (1988). A novel suicide vector and its use in construction of insertion mutations: osmoregulation of outer membrane proteins and virulence determinants in *Vibrio cholerae* requires *toxR*. *J Bacteriol*, 170(6), 2575–2583.
- Millet, Y. A., Alvarez, D., Ringgaard, S., von Andrian, U. H., Davis, B. M., & Waldor, M. K. (2014). Insights into *Vibrio cholerae* Intestinal Colonization from Monitoring Fluorescently Labeled Bacteria. *PLoS Pathogens*, 10(10), e1004405.
- Morgan, D. G., Baumgartner, J. W., & Hazelbauer, G. L. (1993). Proteins antigenically related to methyl-accepting chemotaxis proteins of *Escherichia coli* detected in a wide range of bacterial species. *Journal of Bacteriology*, 175(1), 133–140.
- Morris, J. G., & Acheson, D. (2003). Cholera and Other Types of Vibriosis: A Story of Human Pandemics and Oysters on the Half Shell. *Clinical Infectious Diseases*, 37(2), 272–280.
- Morrison, T. O. M. B., & Parkinson, J. S. (1994). Liberation of an interaction domain from the phosphotransfer region of CheA, a signaling kinase of *Escherichia coli*. *Biochemistry*, 91(June), 5485–5489.
- Mowery, P., Ostler, J. B., & Parkinson, J. S. (2008). Different signaling roles of two conserved residues in the cytoplasmic hairpin tip of Tsr, the *Escherichia coli* serine chemoreceptor. *Journal of Bacteriology*, 190(24), 8065–8074.
- Muff, T. J., & Ordal, G. W. (2007). The CheC phosphatase regulates chemotactic adaptation through CheD. *Journal of Biological Chemistry*, 282(47), 34120–34128.
- Nair, G. B., Ramamurthy, T., Bhattacharya, S. K., Dutta, B., Takeda, Y., & Sack, D. A. (2007). Global dissemination of *Vibrio parahaemolyticus* serotype O3:K6 and its serovariants. *Clinical Microbiology Reviews*.
- Nelson, E. J., Harris, J. B., Morris, J. G., Calderwood, S. B., & Camilli, A. (2009). Cholera transmission: The host, pathogen and bacteriophage dynamic. *Nature Reviews Microbiology*, 7(10), 693.
- Nishiyama, S. I., Suzuki, D., Itoh, Y., Suzuki, K., Tajima, H., Hyakutake, A., ... Kawagishi, I. (2012). Mlp24 (McpX) of *Vibrio cholerae* implicated in pathogenicity functions as a chemoreceptor for multiple amino acids. *Infection and Immunity*, 80(9), 3170–3178.
- Nishiyama, S. I., Takahashi, Y., Yamamoto, K., Suzuki, D., Itoh, Y., Sumita, K., ... Kawagishi, I. (2016). Identification of a *Vibrio cholerae* chemoreceptor that senses taurine and amino acids as attractants. *Scientific Reports*, 6.
- Notredame, C., Higgins, D. G., & Heringa, J., Notredame, C., Higgins, D. G., & Heringa, J. (2000). T-coffee: a novel method for fast and accurate multiple sequence alignment. *Journal of Molecular Biology*, 302(1), 205–217.
- Ortega, Á., Zhulin, I. B., & Krell, T. (2017). Sensory Repertoire of Bacterial Chemoreceptors. *Microbiology and Molecular Biology Reviews*, 81(4), e00033-17.
- Ortega, D. R., & Zhulin, I. B. (2016). Evolutionary Genomics Suggests That CheV Is an Additional Adaptor for Accommodating Specific Chemoreceptors within the Chemotaxis Signaling Complex. *PLoS Computational Biology*, 12(2).
- Packer, H. L., & Armitage, J. P. (2000a). Behavioral responses of *Rhodobacter sphaeroides* to linear gradients of the nutrients succinate and acetate. *Applied and Environmental Microbiology*, 66(12), 5186–5191.
- Packer, H. L., & Armitage, J. P. (2000b). Inverted behavioural responses in wild-type *Rhodobacter sphaeroides* to temporal stimuli. *FEMS Microbiology Letters*, 189(2), 299–304.
- Parales, R. E., Luu, R. A., Hughes, J. G., & Ditty, J. L. (2015). Bacterial chemotaxis to xenobiotic chemicals and naturally-occurring analogs. *Current Opinion in Biotechnology*.
- Park, S. Y., Borbat, P. P., Gonzalez-Bonet, G., Bhatnagar, J., Pollard, A. M., Freed, J. H., ... Crane, B. R. (2006). Reconstruction of the chemotaxis receptor-kinase assembly. *Nat Struct Mol Biol*, 13(5), 400–407.
- Pasupuleti, S., Sule, N., Cohn, W. B., MacKenzie, D. S., Jayaraman, A., & Manson, M. D. (2014). Chemotaxis of *Escherichia coli* to norepinephrine (NE) requires conversion of NE to 3,4-dihydroxymandelic acid. *Journal of Bacteriology*, 196(23), 3992–4000.
- Peterson, K. M., & Gellings, P. S. (2018). Multiple intrainestinal signals coordinate the regulation of *Vibrio cholerae* virulence determinants. *Pathogens and Disease*, 76(1), ftx126.
- Peterson, K. M., & Mekalanos, J. J. (1988). Characterization of the *Vibrio cholerae* ToxR regulon: Identification of novel genes involved in intestinal colonization. *Infection and Immunity*, 56(11), 2822–2829.
- Piasta, K. N., & Falke, J. J. (2014). Increasing and Decreasing the Ultraprecise Stability of Bacterial Chemotaxis Core Signaling Complexes by Modifying Protein-Protein Contacts. *Biochemistry*, 53(35), 5592–5600.
- Piasta, K. N., Ulliman, C. J., Slivka, P. F., Crane, B. R., & Falke, J. J. (2013). Defining a key receptor-CheA kinase contact and elucidating its function in the membrane-bound bacterial chemosensory array: A disulfide mapping and TAM-IDS study. *Biochemistry*, 52(22), 3866–3880.
- Piñas, G. E., DeSantis, M. D., & Parkinson, J. S. (2018). Noncritical Signaling Role of a Kinase–Receptor Interaction Surface in the *Escherichia coli* Chemosensory Core Complex. *Journal of Molecular Biology*, 430(7), 1051–1064.
- Piñas, G. E., Frank, V., Vaknin, A., & Parkinson, J. S. (2016). The source of high signal cooperativity in bacterial chemosensory arrays. *Proceedings of the National Academy of Sciences*, 113(12), 3335–3340.
- Pollard, A. M., & Sourjik, V. (2018). Transmembrane region of bacterial chemoreceptor is capable of promoting protein clustering. *Journal of Biological Chemistry*, 293(6), 2149–2158.

- Porter, S. L., & Armitage, J. P. (2002). Phosphotransfer in *Rhodobacter sphaeroides* chemotaxis. *Journal of Molecular Biology*, 324(1), 35–45.
- Porter, S. L., & Armitage, J. P. (2004). Chemotaxis in *Rhodobacter sphaeroides* requires an atypical histidine protein kinase. *Journal of Biological Chemistry*, 279(52), 54573–54580.
- Porter, S. L., Wadhams, G. H., & Armitage, J. P. (2008). *Rhodobacter sphaeroides*: complexity in chemotactic signalling. *Trends in Microbiology*, 16(6), 251–260.
- Porter, S. L., Wadhams, G. H., & Armitage, J. P. (2011). Signal processing in complex chemotaxis pathways. *Nature Reviews Microbiology*, 9(3), 153.
- Porter, S. L., Wadhams, G. H., Martin, A. C., Byles, E. D., Lancaster, D. E., & Armitage, J. P. (2006). The CheYs of *Rhodobacter sphaeroides*. *Journal of Biological Chemistry*, 281(43), 32694–32704.
- Porter, S. L., Warren, A. V., Martin, A. C., & Armitage, J. P. (2002). The third chemotaxis locus of *Rhodobacter sphaeroides* is essential for chemotaxis. *Molecular Microbiology*, 46(4), 1081–1094.
- Ptacin, J. L., Lee, S. F., Garner, E. C., Toro, E., Eckart, M., Comolli, L. R., ... Shapiro, L. (2010). A spindle-like apparatus guides bacterial chromosome segregation. *Nature Cell Biology*, 12(8), 791–798.
- Quisel, J. D., Lin, D. C., & Grossman, A. D. (1999). Control of development by altered localization of a transcription factor in *B. subtilis*. *Molecular Cell*, 4(5), 665–672.
- Rao, C. V., Glekas, G. D., & Ordal, G. W. (2008). The three adaptation systems of *Bacillus subtilis* chemotaxis. *Trends in Microbiology*, 16(10), 480–487.
- Raskin, D. M., & de Boer, P. A. J. (1999). Rapid pole-to-pole oscillation of a protein required for directing division to the middle of *Escherichia coli*. *Proceedings of the National Academy of Sciences*, 96(9), 4971–4976.
- Reinhardt, J. M., & Bardy, S. L. (2018). Partitioning protein ParP directly links chemotaxis to biofilm dispersal in *Pseudomonas aeruginosa*. *bioRxiv*. <https://doi.org/10.1101/330878>
- Repaske, D. R., & Adler, J. (1981). Change in intracellular pH of *Escherichia coli* mediates the chemotactic response to certain attractants and repellents. *Journal of Bacteriology*, 145(3), 1196–1208.
- Ringgaard, S., Hubbard, T., Mandlik, A., Davis, B. M., & Waldor, M. K. (2015). RpoS and quorum sensing control expression and polar localization of *Vibrio cholerae* chemotaxis cluster III proteins *in vitro* and *in vivo*. *Molecular Microbiology*, 97(4), 660–675.
- Ringgaard, S., Schirner, K., Davis, B. M., & Waldor, M. K. (2011). A family of ParA-like ATPases promotes cell pole maturation by facilitating polar localization of chemotaxis proteins. *Genes Dev*, 25(14), 1544–1555.
- Ringgaard, S., Zepeda-Rivera, M., Wu, X., Schirner, K., Davis, B. M., & Waldor, M. K. (2014). ParP prevents dissociation of CheA from chemotactic signaling arrays and tethers them to a polar anchor. *Proceedings of the National Academy of Sciences*, 111(2), E255–E264.
- Roberts, M. A. J., Wadhams, G. H., Hadfield, K. A., Tickner, S., & Armitage, J. P. (2012). ParA-like protein uses nonspecific chromosomal DNA binding to partition protein complexes. *Proceedings of the National Academy of Sciences*, 109(17), 6698–6703.
- Rosario, M. M. L., Fredrick, K. L., Ordal, G. W., & Helmann, J. D. (1994). Chemotaxis in *Bacillus subtilis* requires either of two functionally redundant CheW homologs. *Journal of Bacteriology*, 176(9), 2736–2739.
- Rosario, M. M. L., Kirby, J. R., Ordal, G. W., & Bochar, D. A. (1995). Chemotactic Methylation and Behavior in *Bacillus Subtilis*: Role of Two Unique Proteins, CheC and CheD. *Biochemistry*, 34(11), 3823–3831.
- Rosario, M. M. L., & Ordal, G. W. (1996). CheC and CheD interact to regulate methylation of *Bacillus subtilis* methyl-accepting chemotaxis proteins. *Molecular Microbiology*, 21(3), 511–518.
- Rossmann, F., Brenzinger, S., Knauer, C., Dörrich, A. K., Bubendorfer, S., Ruppert, U., ... Thormann, K. M. (2015). The role of FlhF and HubP as polar landmark proteins in *Shewanella putrefaciens* CN-32. *Molecular Microbiology*, 98(4), 727–742.
- Saaki, T. N. V., Strahl, H., & Hamoen, L. W. (2018). Membrane curvature and the Tol-Pal complex determine polar localization of the chemoreceptor Tar in *Escherichia coli*. *Journal of Bacteriology*, 200(9), JB-00658.
- Sack, D. A., Sack, R. B., Nair, G. B., & Siddique, A. (2004). Cholera. *The Lancet*, 363(9404), 223–233.
- Salah Ud-Din, A. I. M., & Roujeinikova, A. (2017). Methyl-accepting chemotaxis proteins: a core sensing element in prokaryotes and archaea. *Cellular and Molecular Life Sciences*, 74(18), 3293–3303.
- Sampedro, I., Parales, R. E., Krell, T., & Hill, J. E. (2015). *Pseudomonas* chemotaxis. *FEMS Microbiology Reviews*, 39(1), 17–46.
- Sang, N. N., Soda, S., Inoue, D., Sei, K., & Ike, M. (2009). Effects of intermittent and continuous aeration on accelerative stabilization and microbial population dynamics in landfill bioreactors. *Journal of Bioscience and Bioengineering*, 108(4), 336–343.
- Santos, T. M. A., Lin, T. Y., Rajendran, M., Anderson, S. M., & Weibel, D. B. (2014). Polar localization of *Escherichia coli* chemoreceptors requires an intact Tol-Pal complex. *Molecular Microbiology*, 92(5), 985–1004.
- Savage, D. F., Afonso, B., Chen, A. H., & Silver, P. a. (2010). Spatially ordered dynamics of the bacterial carbon fixation machinery. *Science (New York, N.Y.)*, 327(5970), 1258–1261.
- Savitzky, A., & Golay, M. J. E. (1964). Smoothing and Differentiation of Data by Simplified Least Squares Procedures. *Analytical Chemistry*, 36(8), 1627–1639.
- Schindelin, J., Arganda-Carreras, I., Frise, E., Kaynig, V., Longair, M., Pietzsch, T., ... Cardona, A. (2012). Fiji: An open-



- source platform for biological-image analysis. *Nature Methods*, 9(7), 676.
- Scholefield, G., Errington, J., & Murray, H. (2012). Soj/ParA stalls DNA replication by inhibiting helix formation of the initiator protein DnaA. *The EMBO Journal*, 31(6), 1542–1555.
- Scholefield, G., Whiting, R., Errington, J., & Murray, H. (2011). Spo0J regulates the oligomeric state of Soj to trigger its switch from an activator to an inhibitor of DNA replication initiation. *Molecular Microbiology*, 79(4), 1089–1100.
- Schumacher, D., Bergeler, S., Harms, A., Vonck, J., Huneke-Vogt, S., Frey, E., & Søggaard-Andersen, L. (2017). The PomXYZ Proteins Self-Organize on the Bacterial Nucleoid to Stimulate Cell Division. *Developmental Cell*, 41(3), 299–314.e13.
- Selvaraj, P., Gupta, R., Peterson, K. M. (2015). The *Vibrio cholerae* ToxR Regulon Encodes Host-Specific Chemotaxis Proteins that Function in Intestinal Colonization. *SOJ Microbiol Infect Dis.*, 6(2), 356–372.
- Shah, D. S. H., Porter, S. L., Harris, D. C., Wadhams, G. H., Hamblin, P. A., & Armitage, J. P. (2000). Identification of a fourth cheY gene in *Rhodobacter sphaeroides* and interspecies interaction within the bacterial chemotaxis signal transduction pathway. *Molecular Microbiology*, 35(1), 101–112.
- Shinoda, S., & Okamoto, K. (1977). Formation and function of *Vibrio parahaemolyticus* lateral flagella. *Journal of Bacteriology*, 129(3), 1266–1271.
- Shiomi, D., Yoshimoto, M., Homma, M., & Kawagishi, I. (2006). Helical distribution of the bacterial chemoreceptor via colocalization with the Sec protein translocation machinery. *Molecular Microbiology*, 60(4), 894–906.
- Slivka, P. F., & Falke, J. J. (2012). Isolated Bacterial Chemosensory Array Possesses Quasi- and Ultrastable Components: Functional Links between Array Stability, Cooperativity, and Order. *Biochemistry*, 51(51), 10218–10228.
- Soberón, N. E., Lioy, V. S., Pratto, F., Volante, A., & Alonso, J. C. (2011). Molecular anatomy of the *Streptococcus pyogenes* pSM19035 partition and segrosome complexes. *Nucleic Acids Research*, 39(7), 2624–2637.
- Son, K., Guasto, J. S., & Stocker, R. (2013). Bacteria can exploit a flagellar buckling instability to change direction. *Nature Physics*, 9(8), 494–498.
- Sourjik, V., & Armitage, J. P. (2010). Spatial organization in bacterial chemotaxis. *EMBO J*, 29(16), 2724–2733.
- Sourjik, V., & Berg, H. C. (2002). Receptor sensitivity in bacterial chemotaxis. *Proceedings of the National Academy of Sciences*, 99(1), 123–127.
- Sourjik, V., & Berg, H. C. (2004). Functional interactions between receptors in bacterial chemotaxis. *Nature*, 428(6981), 437–441.
- Sourjik, V., & Wingreen, N. S. (2012). Responding to chemical gradients: bacterial chemotaxis. *Current Opinion in Cell Biology*, 24(2), 262–268.
- Springer, W. R., & Koshland, D. E. (1977). Identification of a protein methyltransferase as the cheR gene product in the bacterial sensing system. *Proceedings of the National Academy of Sciences*, 74(2), 533–537.
- Stock, J. B., & Koshland, D. E. (1978). A protein methylesterase involved in bacterial sensing. *Proceedings of the National Academy of Sciences*, 75(8), 3659–3663.
- Stocker, R. (2011). Reverse and flick: Hybrid locomotion in bacteria. *Proceedings of the National Academy of Sciences*, 108(7), 2635–2636.
- Strahl, H., Ronneau, S., González, B. S., Klutsch, D., Schaffner-Barbero, C., & Hamoen, L. W. (2015). Transmembrane protein sorting driven by membrane curvature. *Nature Communications*, 6, 8728.
- Studdert, C. a., & Parkinson, J. S. (2005). Insights into the organization and dynamics of bacterial chemoreceptor clusters through in vivo crosslinking studies. *Proceedings of the National Academy of Sciences*, 102(43), 15623–15628.
- Su, Y. C., & Liu, C. (2007). *Vibrio parahaemolyticus*: A concern of seafood safety. *Food Microbiology*, 24(6), 549–558.
- Swain, K. E., & Falke, J. J. (2007). Structure of the conserved HAMP domain in an intact, membrane-bound chemoreceptor: A disulfide mapping study. *Biochemistry*, 46(48), 13684–13695.
- Swanson, R. V., Schuster, S. C., & Simon, M. I. (1993). Expression of CheA fragments which define domains encoding kinase, phosphotransfer, and CheY binding activities. *Biochemistry*, 32(30), 7623–7629.
- Szurmant, H., Muff, T. J., & Ordal, G. W. (2004). *Bacillus subtilis* CheC and FliY are members of a novel class of CheY-P-hydrolyzing proteins in the chemotactic signal transduction cascade. *Journal of Biological Chemistry*, 279(21), 21787–21792.
- Szurmant, H., & Ordal, G. W. (2004). Diversity in Chemotaxis Mechanisms among the Bacteria and Archaea. *Microbiology and Molecular Biology Reviews*, 68(2), 301–319.
- Takekawa, N., Kwon, S., Nishioka, N., Kojima, S., & Homma, M. (2016). HubP, a polar landmark protein, regulates flagellar number by assisting in the proper polar localization of FliG in *Vibrio alginolyticus*. *Journal of Bacteriology*, 198(22), 3091–3098.
- Thanbichler, M., & Shapiro, L. (2006). MipZ, a Spatial Regulator Coordinating Chromosome Segregation with Cell Division in *Caulobacter*. *Cell*, 126(1), 147–162.
- Thar, R., & Kuhl, M. (2003). Bacteria are not too small for spatial sensing of chemical gradients: an experimental evidence. *Proceedings of the National Academy of Sciences*, 100(10), 5748–5753.
- Thiem, S., & Sourjik, V. (2008). Stochastic assembly of chemoreceptor clusters in *Escherichia coli*. *Mol Microbiol*, 68(5), 1228–1236.
- Thoelke, M. S., Kirby, J. R., & Ordal, G. W. (1989). Novel Methyl Transfer during Chemotaxis in *Bacillus subtilis*.

- Biochemistry*, 28(13), 5585–5589.
- Thompson, S. R., Wadhams, G. H., & Armitage, J. P. (2006). The positioning of cytoplasmic protein clusters in bacteria. *Proc Natl Acad Sci U S A*, 103(21), 8209–8214.
- Tokunaga, M., Imamoto, N., & Sakata-Sogawa, K. (2008). Highly inclined thin illumination enables clear single-molecule imaging in cells. *Nature Methods*, 5(2), 159–161.
- Treuner-Lange, A., Aguiluz, K., van der Does, C., Gomez-Santos, N., Harms, A., Schumacher, D., Lenz, P., Kahnt, J., Munoz-Dorado, J., Sogaard-Andersen, L. (2013). PomZ, a ParA-like protein, regulates Z-ring formation and cell division in *Myxococcus xanthus*. *Molecular Microbiology*, 87(2), 235–253.
- Vecchiarelli, A. G., Han, Y. W., Tan, X., Mizuuchi, M., Ghirlando, R., Biertümpfel, C., ... Mizuuchi, K. (2010). ATP control of dynamic P1 ParA-DNA interactions: A key role for the nucleoid in plasmid partition. *Molecular Microbiology*, 78(1), 78–91.
- Vecchiarelli, A. G., Mizuuchi, K., & Funnell, B. E. (2012). Surfing biological surfaces: Exploiting the nucleoid for partition and transport in bacteria. *Molecular Microbiology*, 86(3), 513–523.
- Virant, D., Turkowyd, B., Balinovic, A., & Endesfelder, U. (2017). Combining primed photoconversion and UV-photoactivation for aberration-free, live-cell compliant multi-color single-molecule localization microscopy imaging. *International Journal of Molecular Sciences*, 18(7).
- Vu, A., Wang, X., Zhou, H., & Dahlquist, F. W. (2012). The receptor-CheW binding interface in bacterial chemotaxis. *Journal of Molecular Biology*, 415(4), 759–767.
- Wadhams, G. H., & Armitage, J. P. (2004). Making sense of it all: bacterial chemotaxis. *Nat Rev Mol Cell Biol*, 5(12), 1024–1037.
- Wadhams, G. H., Martin, A. C., & Armitage, J. P. (2000). Identification and localization of a methyl-accepting chemotaxis protein in *Rhodobacter sphaeroides*. *Molecular Microbiology*, 36(6), 1222–1233.
- Wadhams, G. H., Martin, A. C., Porter, S. L., Maddock, J. R., Mantotta, J. C., King, H. M., & Armitage, J. P. (2002). TlpC, a novel chemotaxis protein in *Rhodobacter sphaeroides*, localizes to a discrete region in the cytoplasm. *Molecular Microbiology*, 46(5), 1211–1221.
- Wadhams, G. H., Martin, A. C., Warren, A. V., & Armitage, J. P. (2005). Requirements for chemotaxis protein localization in *Rhodobacter sphaeroides*. *Molecular Microbiology*, 58(3), 895–902.
- Wadhams, G. H., Warren, A. V., Martin, A. C., & Armitage, J. P. (2003). Targeting of two signal transduction pathways to different regions of the bacterial cell. *Mol Microbiol*, 50(3), 763–770.
- Walukiewicz, H. E., Tohidifar, P., Ordal, G. W., & Rao, C. V. (2014). Interactions among the three adaptation systems of *Bacillus subtilis* chemotaxis as revealed by an in vitro receptor-kinase assay. *Molecular Microbiology*, 93(6), 1104–1118.
- Wang, H., Wingreen, N. S., & Mukhopadhyay, R. (2008). Self-organized periodicity of protein clusters in growing bacteria. *Physical Review Letters*, 101(21).
- Ward, M. J., Bell, A. W., Hamblin, P. A., Packer, H. L., & Armitage, J. P. (1995). Identification of a chemotaxis operon with two cheY genes in *Rhodobacter sphaeroides*. *Molecular Microbiology*, 17(2), 357–366.
- Weimann, L., Ganzinger, K. A., McColl, J., Irvine, K. L., Davis, S. J., Gay, N. J., ... Klenerman, D. (2013). A Quantitative Comparison of Single-Dye Tracking Analysis Tools Using Monte Carlo Simulations. *PLoS ONE*, 8(5).
- Weis, R. M., Hirai, T., Chalah, A., Kessel, M., Peters, P. J., & Subramaniam, S. (2003). Electron microscopic analysis of membrane assemblies formed by the bacterial chemotaxis receptor Tsr. *Journal of Bacteriology*, 185(12), 3636–3643.
- Wolter, S., Löschberger, A., Holm, T., Aufmkolk, S., Dabauvalle, M. C., Van De Linde, S., & Sauer, M. (2012). RapidSTORM: Accurate, fast open-source software for localization microscopy. *Nature Methods*, 9(11), 1040.
- Wuichet, K., & Zhulin, I. B. (2010). Origins and diversification of a complex signal transduction system in prokaryotes. *Science Signaling*, 3(128), ra50.
- Xie, L., Altindal, T., Chattopadhyay, S., & Wu, X.-L. (2011). Bacterial flagellum as a propeller and as a rudder for efficient chemotaxis. *Proceedings of the National Academy of Sciences*, 108(6), 2246–2251.
- Xiong, Q., Morphew, M. K., Schwartz, C. L., Hoenger, A. H., & Mastrorarde, D. N. (2009). CTF determination and correction for low dose tomographic tilt series. *Journal of Structural Biology*, 168(3), 378–387.
- Yamaichi, Y., Bruckner, R., Ringgaard, S., Moll, A., Cameron, D. E., Briegel, A., ... Waldor, M. K. (2012). A multidomain hub anchors the chromosome segregation and chemotactic machinery to the bacterial pole. *Genes Dev*, 26(20), 2348–2360.
- Yeung, P. S. M., & Boor, K. J. (2004). Epidemiology, pathogenesis, and prevention of foodborne *Vibrio parahaemolyticus* infections. *Foodborne Pathogens and Disease*, 1(2), 74–88.
- Yuan, J., Jin, F., Glatter, T., & Sourjik, V. (2017). Osmosensing by the bacterial PhoQ/PhoP two-component system. *Proceedings of the National Academy of Sciences*, 114(50), E10792 LP-E10798.
- Yuan, W., Glekas, G. D., Allen, G. M., Walukiewicz, H. E., Rao, C. V., & Ordal, G. W. (2012). The Importance of the Interaction of CheD with CheC and the Chemoreceptors Compared to Its Enzymatic Activity during Chemotaxis in *Bacillus subtilis*. *PLoS ONE*, 7(12).
- Zhang, P., Khursigara, C. M., Hartnell, L. M., & Subramaniam, S. (2007). Direct visualization of *Escherichia coli* chemotaxis receptor arrays using cryo-electron microscopy. *Proceedings of the National Academy of Sciences*, 104(10), 3777–3781.

- 
- Zhao, J., & Parkinson, J. S. (2006). Cysteine-scanning analysis of the chemoreceptor-coupling domain of the *Escherichia coli* chemotaxis signaling kinase CheA. *Journal of Bacteriology*, 188(12), 4321–4330.
- Zimmer, M. A., Tiu, J., Collins, M. A., & Ordal, G. W. (2000). Selective methylation changes on the *Bacillus subtilis* chemotaxis receptor McpB promote adaptation. *Journal of Biological Chemistry*, 275(32), 24264–24272.
- Zusman, D. R., Scott, A. E., Yang, Z., & Kirby, J. R. (2007). Chemosensory pathways, motility and development in *Myxococcus xanthus*. *Nature Reviews Microbiology*, 5(11), 862.

---

# ACKNOWLEDGEMENTS

I would like to acknowledge my supervisor Dr. Simon Ringgaard for giving me the chance to learn and work in his lab. Your work provided the springboard for this thesis and I will always be grateful for the opportunity. I also want to thank my doctoral thesis committee, Prof. Dr. Martin Thanbichler, Prof. Dr. Victor Sourjik, Prof. Dr. Michael Bölker and Prof. Dr. Johann Heider. In addition, my sincere gratitude goes to the members of my IMPRS committee, Prof. Thanbichler, Prof. Sourjik and Prof. Sogaard-Andersen, for their input and feedback during the thesis advisory meetings. Similarly, a very special thank-you to Dr. Dorota Skotnicka for proofreading this work, and Dr. Kathrin Schirner for translation of the abstract.

I am also thankful to Prof. Dr. Ariane Briegel and Wen Yang for their input in our understanding of the structure of chemotaxis arrays in *Vibrio* using cryo-electron microscopy. To Dr. Ulrike Endesfelder and Bartosz Turkowyd for their contribution to our views of ParC's localization mechanism through sptPALM microscopy, and to Dr. Timo Glatter, for his input and assistance with the proteomics work. Your expertise and contributions to our research are invaluable, thank you for helping us make these stories better.

I also would like to thank Prof. Dr. Nagamani Balagurusamy. Your dedication to science and teaching made a strong impression. Even today, your teachings continue to be a source of inspiration. Thank you very much. I also want to extend my acknowledgments to Dr. Padma Nimmalayala and Prof. Dr. Umesh Reddy for their support and advice during my masters' work.

Furthermore, my deepest gratitude goes to all the past and present members of the Ringgaard lab. Especially to Samada Muraleedharan, thank you for your friendship and help during the last four years; and to Petra Mann, thank you so much for all your help and all the patience. To Carlolina Freitas, Shankar Chandrashekar Iyer and Jan Heering, it is great to call you my colleagues, but it is even greater to call you my friends. And last but not least, thank you to Stephan Wimmi and Barbara Ritzl, your perseverance was inspiring. To all members of the Ringgaard lab, thank you very much! It was a great privilege to have worked with you.

Equally great was being at the Department of Ecophysiology, and I would like to thank those in A1 and the members of the Diepold lab with whom we share A2. I was very fortunate to work in such a great scientific community.

---

To my friends in this continent, especially Rehab, Shadaan, Cathy and Bailey, thank you. My stay here was so much fun because you were with me. To Sarahi, thank you for all the support and for sharing your family with me; it was always helpful and super fun. I also would like to thank my friends in Mexico and the US. In particular, a HUGE thank-you goes to my dearest Yuli, who was there at all times.

Finally and most importantly, none of this would have happened without my family: muchísimas gracias a todos, en especial a mi madre, Laura, Luis, André, Jesu y Jesús y desde luego, Nito. Los quiero mucho.

---

# CURRICULIM VITAE

## Alejandra Alvarado

### PERSONAL INFORMATION

---

Complete given name Alejandra Guadalupe Alvarado Rodríguez  
Place of birth Torreón, Coahuila, México

### EDUCATION

---

- OCT 2014 - | PhD (Dr. rer. nat)  
Max Planck Institute for Terrestrial Microbiology. Department of Ecophysiology. Marburg, Germany.
- Thesis: The ParC/ParP system in localization and segregation of chemotaxis signaling arrays in *Vibrio cholerae* and *Vibrio parahaemolyticus*.
- AUG 2012 - AUG 2014 | Masters in Biotechnology  
West Virginia State University, College of Natural Sciences and Mathematics. West Virginia, USA.
- Thesis: Small RNA regulation in response to drought and high CO<sub>2</sub> concentrations in sweet potato *Ipomoea batatas* (L.) Lam. variety beauregard (B14)
- JUL 2009 – DEC 2009 | Internship  
University of Georgia, College of Engineering. Athens Georgia, USA.
- Research Internship for bachelor thesis. USAID-TIES program.
- AUG 2006 - JUL 2010 | BSc. Biochemical Engineering  
School of Biological Sciences, Autonomous University of Coahuila. Torreón, Coahuila, Mexico.
- Thesis: Evaluating the biomethanation potential of agricultural residues and crude glycerol-poultry litter mixture at high solid concentrations

### LIST OF PUBLICATIONS

---

- Saminathan, T.<sup>#</sup>, **Alvarado, A.**<sup>#</sup>, Lopez, C., Shinde, S., Gajanayake, B., Abburi, V.L., Vajja, V.G., Jagadeeswaran, G., Reddy, K.R., Nimmakayala, P. and Reddy, U.K., **2018**. Elevated carbon dioxide and drought modulate physiology and storage-root development in sweet potato by regulating microRNAs. *Functional & integrative genomics*, pp.1-20. (<sup>#</sup>equal contribution).
- Ringgaard, S., Yang, W., **Alvarado, A.**, Schirmer, K. and Briegel, A., **2018**. Chemotaxis arrays in *Vibrio* species and their intracellular positioning by the ParC/ParP system. *Journal of bacteriology*, pp.JB-00793.
- Alvarado, A.**, Kjær, A., Yang, W., Mann, P., Briegel, A., Waldor, M.K. and Ringgaard, S., **2017**. Coupling chemosensory array formation and localization. *eLife*, 6.
- Heering, J., **Alvarado, A.** and Ringgaard, S., **2017**. Induction of Cellular Differentiation and Single Cell Imaging of *Vibrio parahaemolyticus* Swimmer and Swarmer Cells. *Journal of visualized experiments: JoVE*, (123).
- Nimmakayala, P., Tomason, Y.R., Abburi, V.L., **Alvarado, A.**, Saminathan, T., Vajja, V.G., Salazar, G., Panicker, G.K., Levi, A., Wechter, W.P. and McCreight, J.D., **2016**. Genome-wide differentiation of various melon horticultural groups for use in GWAS for fruit firmness and construction of a high resolution genetic map. *Frontiers in plant science*, 7, p.1437.
- Alvarado, A.**, Montañez-Hernández, L.E., Palacio-Molina, S.L., Oropeza-Navarro, R., Luévanos-Escareño, M.P. and Balagurusamy, N., **2014**. Microbial trophic interactions and *mcrA* gene expression in monitoring of anaerobic digesters. *Frontiers in microbiology*, 5, p.597.

---

# ERKLÄRUNG

Hermit versichere ich, dass ich die vorliegende Dissertation mit dem **Titel „The ParC/ParP system in the localization and segregation of chemotaxis signaling arrays in *Vibrio cholerae* and *Vibrio parahaemolyticus*“** selbstständig verfasst, keine anderen als die Text angegebenen Hilfsmittel verwendet und sämtliche Stellen, die im Wortlaut oder dem Sinn nach anderen Werken entnommen sind, mit Quellenangaben kenntlich gemachth habe.

Die Dissertation wurde in der jetzigen oder einer ähnlichen Form noch bei keiner anderen Hochschule eingereicht und hat noch keinen sonstigen Prüfungswegzengedient.

---

October 9th, 2018

Ort, Datum

---

Alejandra Guadalupe  
Alvarado Rodriguez

---

# EINVERSTÄNDNISERKLÄRUNG

Ich erkläre mich dam einverstanden, dass die vorliegende Dissertation

**„The ParC/ParP system in the localization and segregation of chemotaxis signaling arrays in *Vibrio cholerae* and *Vibrio parahaemolyticus*“**

in Bibliotheken allgemein zugänglich gemacht wird. Dazu gehört, dass sie

- von der Bibliothek der Einrichtung, in der ich meine Arbeit anfertig habe, zur Benutzung in ihren Räumen bereitgehalten wird;
- in konventionellen und maschinenlesbaren Katalogen, Verzeichnissen und Datenbanken verzeichnet wird;
- im Rahmen der urheberrechtlichen Bestimmungen für Kopierzwecke genutzt werden kann.

Marburg, den 13.12.2018

---

Alejandra Guadalupe  
Alvarado Rodriguez

---

Dr. Simon Ringgaard